Nonequilibrium emergent phenomena in organic molecular solids

Dissertation

zur Erlangung des Doktorgrades

des Department Physik

der Universität Hamburg

vorgelegt von

Matteo Mitrano

aus Rom, Italien

Hamburg

2015

Gutachter der Dissertation:	Prof. Dr. Andrea Cavalleri Prof. Dr. Alexander Lichtenstein
Gutachter der Disputation:	Prof. Dr. Andrea Cavalleri Prof. Dr. Henning Moritz
Datum der Disputation:	15/07/2015
Vorsitzender des Prüfungsausschusses:	Prof. Dr. Ludwig Mathey
Vorsitzender des Promotionssausschusses:	Prof. Dr. Jan Louis
Dekan der MIN Fakultät:	Prof. Dr. Heinrich Graener
Leiter des Fachbereich Physik:	Prof. Dr. Peter Hauschildt

"Pulchra sunt quae videntur,
pulchriora quae sciuntur,
longe pulcherrima quae ignorantur"
Nicolaus Steno (1673)

Dedicated to all the people that are forced to drift away from their natural aspirations and their childhood dreams

Abstract

The manipulation of matter with ultrashort laser pulses is a relevant research field from both a fundamental and an applied perspective, owing to the efficient coupling to the electronic degrees of freedom on femtosecond timescales and the ability to induce transient phases that cannot be realized in equilibrium scenarios. Strongly correlated materials are a natural environment for the observation of such novel and emergent out-of-equilibrium physics because small modifications to the electron-electron interactions can induce transitions between remarkably different macroscopic phases. One of the most effective means of modifying the effective electron-electron interactions is to perturb the crystal structure through pressure, strain or even light. However, it remains largely unexplored how perturbing the structural degrees of freedom affects the electron dynamics of the transiently driven states and how the interplay of correlations and electron-lattice interactions determine the intrinsic timescales of these nonequilibrium states.

This thesis investigates how to control the light-induced nonequilibrium electronic properties in strongly correlated organics, that are highly tunable with moderate variations of external parameters, by perturbing their structural degrees of freedom, either via static pressures or vibrational excitation. We study the role of correlations in determining the relaxation rate of holes (holons) and double occupancies (doublons) in a solid state Mott insulator, the ET-F_2TCNQ, driven across a transient insulator-to-metal transition. By mapping holon-doublon lifetimes onto the ground-state electronic interactions, we found that the decay rate of the photoinjected quasiparticles depends on the degree of correlation between carriers and is affected by the presence of a competition between local recombination and delocalization of holon-doublon pairs.

By optically controlling the effective correlations in organic molecular crystals through vibrational excitations, we then show the possibility of driving a superconducting phase transition by transiently perturbing those degrees of freedom that mediate the pairing interaction. We select the molecular solid K_3C_{60}, a well characterized superconductor at relatively high temperatures (T_c=19.8 K) in which high-energy intramolecular vibrations are considered as key for the Cooper pairing. When driven with strong midinfrared fields resonantly tuned to infrared active *intra*molecular vibrations, we induce a short-lived transient state with striking superconducting-like optical properties above the equilibrium transition temperature and up to 100 K, five times the equilibrium T_c. We explain the appearance of

this superconducting-like behavior in terms of light-induced structural distortions capable to induce changes in the onsite Coulomb correlation and in the electron-phonon coupling.

Zusammenfassung

Die Manipulation und Kontrolle kondensierter Materie mittels ultrakurzer Laserpulse entwickelt sich zu einem immer wichtigeren Forschungsfeld. Seine Relevanz zeigt sich sowohl in der Grundlagenforschung zu fundamentalen und intrinsischen Zeitskalen von Anregungen in Festkörpern, als auch aus der angewandten Perspektive optisch geschalteter Zustände, deren Mechanismen neue funktionelle Materialien erlauben. Dies liegt zum einen an der effizienten Kopplung der Lichtpulse an die elektronischen Freiheitsgrade im Festkörper auf einer Femtosekunden-Zeitskala, die ultraschnelle Schaltvorgänge ermöglicht, und zum Anderen an der Möglichkeit, neue transiente Phasen zu stabilisieren, die sich als Gleichgewichtszustände nicht realisieren lassen.

Stark korrelierte Materialien bieten ideale Voraussetzungen für die Beobachtung und Realisierung solch neuartiger Nichtgleichgewichtsphänomene, da bereits kleinste Änderungen der dominierenden Elektron-Elektron-Wechselwirkung Übergänge zwischen unterschiedlichen makroskopischen Phasen (isolierend, metallisch, supraleitend, anti-, oder ferromagnetisch, ...) induzieren können.

Im thermodynamischen Gleichgewicht lässt sich die effektive Elektron-Elektron-Wechselwirkung durch externe Parameter wie Druck, Dehnung, oder magnetische und elektrische Felder sowie durch eine chemische Dotierung der Kristallstruktur und im Nichtgleichgewicht auch durch optische Anregung beeinflussen. Dabei ist der Einfluss der strukturellen und vibronischen Freiheitsgrade auf die elektronische Dynamik der transienten Zuständen und die transienten effektiven elektronischen Wechselwirkungen noch weitestgehend unverstanden.

Diese Arbeit befasst sich mit der lichtinduzierten Nichtgleichwichtsdynamik und neuartigen dynamisch induzierten Zuständen in stark korrelierten organischen Quantenmaterialien. Dazu werden die elektronischen sowie strukturellen Wechselwirkungen in Molekülkristallen sowohl durch statischen Druck als auch dynamisch mittels Anregung bestimmter Molekülschwingungen kontrolliert. Der Einfluss der elektronischen Wechselwirkungen auf diese Dynamik wird dabei durch die Relaxationsrate photoinduzierter Quasiteilchen, so genannten Dublonen-(doppelt besetzter Elektronenzustände) Loch-Paare in dem Mott-Isolator ET-F_2TCNQ bestimmt. Dieser wird mittels Photodotierung durch angeregte Elektronen von einem Isolator zu einem transienten Metall getrieben. Das Anlegen eines äußeren Drucks führt zu einer gezielten Variation der elektronischen Wechselwirkungen des Grundzustandes durch den die Lebensdauer des photoinduzierten Zustandes beeinflusst

werden kann. Damit lässt sich nachweisen, dass die Zerfallsrate der angeregten Quasiteilchen von der Stärke der elektronischen Wechselwirkungen zwischen den Ladungsträgern abhängt, und dass dadurch maßgeblich das Verhältnis zwischen lokaler Rekombination und Delokalisierung der angeregten Dublonen-Loch Paare bestimmt wird.

Eine direkte optische Kontrolle solch effektiver Wechselwirkungen in organischen molekularen Kristallen lässt sich durch Anregung lokaler Molekülschwingungen erreichen. Dies zeigt neue Möglichkeiten für lichtinduzierte Phasenübergänge, insbesondere in supraleitende Phasen, auf. Letztere lassen sich durch eine dynamische Modulation der elektronischen und vibronischen Freiheitsgrade erreichen, die für die Bildung supraleitendender Cooper-Paare relevant sind. Hierfür wählen wir den supraleitenden organischen Molekülkristall K_3C_{60}. Für seine, im Rahmen der BCS-Theorie, relativ hohe Sprungtemperatur von T_c=19.8 K werden hochenergetische Molekülschwingungen verantwortlich gemacht. Es wird gezeigt, dass eine resonante Anregung bestimmter molekularer Schwingungen mit ultrakurzen Lichtpulsen hoher Feldstärke das induzieren eines kurzlebigen transienten Zustandes mit eindrucksvollen Supraleiter-artigen optischen Eigenschaften oberhalb der Sprungtemperatur erlaubt. Dieser transiente supraleitende Zustand kann bis zu 100K, der fünffachen Sprungtemperatur des Gleichgewichts-Grundzustand, induziert werden. Das Auftreten dieses spektakulären Nichtsgleichgewichtszustandes wird im Sinne einer lichtinduzierten strukturellen und nichtlinearen Verzerrung des Kristallgitters diskutiert, die fähig ist, eine Veränderung der lokalen elektronischen Wechselwirkungen und der Elektron-Phonon Wechselwirkung zu generieren.

Hiermit erkläre ich an Eides statt, dass ich die vorliegende Dissertationsschrift selbst verfasst und keine anderen als die angegebenen Quellen und Hilfsmittel benutzt habe. Diese Arbeit lag noch keiner anderen Person oder Prüfungsbehörde im Rahmen einer Prüfung vor.

I hereby declare, on oath, that I have written the present dissertation on my own and have not used other than the mentioned resources and aids. This work has never been presented to other persons or evaluation panels in the context of an examination.

Matteo Mitrano
Hamburg, den 27/04/2015

Unterschrift (Signed):

Datum (Date):

Publications List

This thesis is based on my work as a graduate student at the Max Planck Institute for the Structure and Dynamics of Matter (Hamburg, Germany) within the Quantum Condensed Matter Division and at the University of Hamburg.
The results presented in this manuscript are based on the following papers:

(1) **M. Mitrano**, G. Cotugno, S. R. Clark, R. Singla, S. Kaiser, J. Stähler, R. Beyer, M. Dressel, L. Baldassarre, D. Nicoletti, A. Perucchi, T. Hasegawa, H. Okamoto, D. Jaksch, and A. Cavalleri, *Pressure-Dependent Relaxation in the Photoexcited Mott Insulator ET-F_2TCNQ: Influence of Hopping and Correlations on Quasiparticle Recombination Rates*, Physical Review Letters, **112**, 117801 (2014)

(2) **M. Mitrano**, A. Cantaluppi, D. Nicoletti, S. Kaiser, A. Perucchi, S. Lupi, P. Di Pietro, D. Pontiroli, M. Riccò, A. Subedi, S. R. Clark, D. Jaksch, and A. Cavalleri, *An optically stimulated superconducting-like phase in K_3C_{60} far above equilibrium T_c*, submitted (2015).

Role of the author

This thesis work is the result of complex collaborations involving diverse experimental techniques, as well as different theoretical methods.
The experimental work described in Chapter 4, has been conceived by A. Cavalleri. The samples have been provided by T. Hasegawa and H. Okamoto. Equilibrium optical measurements have been performed by the author, together with R. Beyer, A. Dengl and M. Dressel (University of Stuttgart, Stuttgart, Germany) and with L. Baldassare, P. Di Pietro and A. Perucchi (Elettra Synchrotron, Trieste, Italy). The corresponding data analysis has been completed by the author with the helful support of S. Kaiser and D. Nicoletti. Ultrafast optical measurements under pressure have been performed by the author, together with R. Singla and with the support of S. Kaiser, D. Nicoletti and J. Stähler. The data analysis of the time-resolved data has been carried out exclusively by the author. The theoretical modeling and numerical simulations associated to this experiment were performed by G. Cotugno and S. R. Clark, with the help of D. Jaksch. The author together with G. Cotugno, S. R. Clark, D. Jaksch, S. Kaiser, D. Nicoletti, and A. Cavalleri contributed to the development of the interpretation of the experimental findings that resulted in the publication [1] of the previous list.
The experimental work described in Chapter 5, has been conceived by the author, with helpful feedback from A. Cavalleri and S. Kaiser. Samples have been grown and characterized by D. Pontiroli and M. Riccò. Equilibrium optical measurements and the respective data analysis have been carried out by the author and A. Cantaluppi, with help from A. Perucchi and P. Di Pietro. The author and A. Cantaluppi, with the helpful support of H. Bromberger (OPA design and construction), built the optical apparatus for THz time-resolved measurements. These measurements and their data analysis have been performed by the author and A. Cantaluppi, with the helpful support of S. Kaiser and D. Nicoletti. The MATLAB analysis code for the THz time-resolved measurements has been written by Cassandra R. Hunt. A. Subedi performed DFT band-structure and electron-phonon (phonon-phonon) coupling calculations, while S. R. Clark and D. Jaksch estimated the correlation changes in the driven state of the K_3C_{60} superconductor. The author, together with A. Cantaluppi, S. Kaiser, D. Nicoletti, A. Cavalleri, A. Subedi, S. R. Clark and D. Jaksch, contributed to the interpretation of the experiments that are now part of the manuscript [2] of the previous list.
The author would like to acknowledge help by J. Harms for the realization of the

figures 1.1, 2.1, 2.3b, 3.1, 5.1b, A.4, A.6 in the present manuscript. The format of this thesis manuscript is based on a LATEX template originally written by Steven Gunn and Sunil Patel and distributed under a CC BY-NC-SA 3.0 license.

List of additional publications

During the development of this thesis work, I had the opportunity to work on other research topics that are not (or are only marginally) part of this dissertation. The following list accounts for these scientific contributions and completes the previously reported publications list:

(1) **M. Mitrano**, B. Maroni, C. Marini, M. Hanfland, B. Joseph, P. Postorino, and L. Malavasi. *Anisotropic compression in the high-pressure regime of pure and chromium-doped vanadium dioxide* Physical Review B, **85**, 184108 (2012).

(2) I. Gierz, J. C. Petersen, **M. Mitrano**, C. Cacho, I. C. E. Turcu, E. Springate, A. Stöhr, A. Köhler, U. Starke, and A. Cavalleri. *Snapshots of non-equilibrium Dirac carrier distributions in graphene*, Nature Materials, **12**, 1119 (2013).

(3) I. Gierz, **M. Mitrano**, H. Bromberger, C. Cacho, R. Chapman, E. Springate, S. Link, U. Starke, B. Sachs, M. Eckstein, T. O. Wehling, M. I. Katsnelson, A. Lichtenstein, and A. Cavalleri, *Phonon-pump extreme-ultraviolet-photoemission probe in graphene: Anomalous heating of Dirac carriers by lattice deformation.*, Physical Review Letters **114**, 125503 (2015).

(4) A. Caviglia, R. Scherwitzl, P. Popovich, W. Hu, H. Bromberger, R. Singla, **M. Mitrano**, M. C. Hoffmann, S. Kaiser, P. Zubko, S. Gariglio, J. M. Triscone, M. Först, and A. Cavalleri, *Ultrafast Strain Engineering in Complex Oxide Heterostructures*, Physical Review Letters, **108**, 136801 (2012).

(5) I. Gierz, **M. Mitrano**, J. C. Petersen, C. Cacho, I. C. E. Turcu, E. Springate, A. Stöhr, A. Köhler, U. Starke, and A. Cavalleri. *Population Inversion in Monolayer and Bilayer Graphene*, Journal of Physics: Condensed Matter **27**, 164204 (2015).

(6) C. Marini, B. Joseph, S. Caramazza, F. Capitani, M. Bendele, **M. Mitrano**, D. Chermisi, S. Mangialardo, B. Pal, M. Goyal, A. Iadecola, O. Mathon, S. Pascarelli, D. D. Sarma, and P. Postorino, *Local disorder investigation in $NiS_{2-x}Se_x$ using Raman and Ni K-edge x-ray absorption spectroscopies*, Journal of Physics: Condensed Matter, **26**, 452201 (2014).

(7) C. Marini, M. Bendele, B. Joseph, I. Kantor, **M. Mitrano**, O. Mathon, M. Baldini, L. Malavasi, S. Pascarelli, and P. Postorino, *Probing the electronic*

and local structural changes across the pressure-induced insulator-to-metal transition in VO_2, EPL (Europhysics Letters), **108**, 36003 (2014).

(8) R. Singla, G. Cotugno, S. Kaiser, M. Först, **M. Mitrano**, H. Y. Liu, A. Cartella, C. Manzoni, H. Okamoto, T. Hasegawa, S. R. Clark, D. Jaksch, and A. Cavalleri, *Correlation-gap oscillations in an organic Mott-insulator induced by phase locked excitation of local molecular vibrations*, submitted (2014).

(9) L. Baldassarre, A. Perucchi, **M. Mitrano**, D. Nicoletti, C. Marini, D. Pontiroli, M. Mazzani, M. Aramini, M. Riccó, G. Giovannetti, M. Capone and S. Lupi, *The strength of electron correlation in Cs_3C_{60}*, submitted (2015).

Contents

Contents **xv**

Introduction **1**
Emergent dynamics in strongly correlated solids 1
Phase transition timescales in strongly correlated solids 3
Manipulating the superconducting phase transition boundary 6
Structure of the Thesis 7

1 Organics as model systems for strongly correlated materials **9**
1.1 Organic molecular crystals and their phase diagrams 9
1.2 Understanding the phase diagrams of strongly correlated electron systems 14
1.3 Ultrafast dynamics in organic molecular solids 17

2 The ET-F_2TCNQ as a prototypical Mott insulator **25**
2.1 The ET-F_2TCNQ Mott Insulator 25
2.1.1 Crystal structure 25
2.1.2 Electronic properties 27
2.2 Nonequilibrium states and dynamical control of the ET-F_2TCNQ Mott insulator 29
2.2.1 Mott gap dynamics and transient insulator-to-metal transition 30
2.2.2 Vibrational control of the electronic interactions 33
2.3 Excitations of a 1D Mott insulator 33
2.3.1 Systematics of the excitations 34
2.3.2 Relevance of holon-doublon excitations in describing a metal-to-insulator transition 35
2.3.3 Holon-Doublon decay 37
2.4 Summary 39

3 The K_3C_{60} molecular superconductor **41**
3.1 Structure of K_3C_{60} 41
3.2 Phonons and molecular vibrations of K_3C_{60} 43
3.3 Electronic properties of K_3C_{60} 45
3.3.1 Band structure 45

3.3.2 Correlation and metal-insulator transition in A_3C_{60} 47
3.4 Strongly correlated superconductivity in K_3C_{60} 48
3.4.1 Phenomenology of the superconducting state in K_3C_{60} . . . 48
3.4.2 Optical signatures of the superconducting state in K_3C_{60} . . 52
3.4.3 Relevance of correlations in the superconducting dynamics . 56
3.5 Nonequilibrium states and photoinduced dynamics in K_3C_{60} 59
3.6 Summary 62

4 Nonequilibrium dynamics of the ET-F_2TCNQ under pressure 65
4.1 Nonequilibrium quasiparticle recombination in metals and semiconductors 66
4.2 Equilibrium optical properties at ambient conditions 68
4.2.1 Extraction of the Hubbard parameters from the optical conductivity 70
4.3 Equilibrium optical properties under pressure 73
4.4 Hubbard parameters of the ET-F_2TCNQ under pressure 77
4.5 Pump-probe measurements under pressure 80
4.6 Modeling holon-doublon dynamics 83
4.7 Summary 88

5 An optically stimulated superconducting-like phase in K_3C_{60} far above T_c 91
5.1 Light control of the superconducting state 91
5.2 Characterization of the K_3C_{60} powders equilibrium optical properties 94
5.2.1 Normal state optical properties 94
5.2.2 Temperature dependence of the optical properties in the superconducting state 98
5.3 Nonequilibrium dynamics below T_c 102
5.4 Nonequilibrium dynamics above T_c 105
5.5 Characterization of the photoinduced response above T_c 108
5.5.1 Temperature dependence of the transient response above T_c 109
5.5.2 Fluence and pump energy dependence of the transient response above T_c 112
5.6 Considerations on the origin of the excited state above T_c 114
5.7 Summary 119

6 Conclusions and outlook 123
6.1 Conclusions 123
6.2 Outlook 126

A Experimental Methods 129
A.1 Ultrafast NIR and MIR light generation 129
A.1.1 Difference frequency generation and optical parametric amplification 129

A.1.2 Experimental realization of the OPA and DFG units 132
A.2 High pressure techniques 135
A.2.1 The Diamond Anvil Cell as a tool for high pressure generation 135
A.2.2 High pressure measurement 139
A.3 Equilibrium infrared spectroscopy under pressure 142
A.3.1 Infrared optical measurements at SISSI beamline 142
A.3.2 Infrared optical measurements at 1. Physikalisches Institut of the University of Stuttgart 145
A.4 Near-infrared pump-probe measurements on ET-F_2TCNQ under pressure 146
A.5 THz Time-Resolved Spectroscopy (THz-TRS) 150
A.5.1 THz light generation and detection techniques 151
A.5.2 Experimental realization of a MIR pump-THz probe setup . 153
A.5.3 Retrieval of transient optical properties from THz-TRS data 158
A.5.4 Experimental protocol 163

B Kramers-Kronig relations for reflection data taken through a transparent window 167

C ET-F_2TCNQ equilibrium optical properties: supplementary data 169

D Ultrafast pulse propagation through a Diamond window 171

E The Mott metal-to-insulator transition 175

Bibliography 181

Acknowledgements 181

Introduction

Emergent dynamics in strongly correlated solids

The development of ultrashort laser pulses, with typical durations ranging from hundreds of femtoseconds down to the attosecond regime [1–3], opened new routes towards the control of condensed matter. Ultrafast laser light can indeed be used to induce phase transitions, like insulator-to-metal [4–10], superconductor-to-normal state [11, 12] and order-disorder ones [13–16], that are of interest from both an applied and a fundamental point of view. These phase transitions are often differing from their equilibrium analogues because they happen on timescales that are limited by the response of the electronic/lattice subsystem and they can involve transient states that are not encountered in equilibrium conditions [7, 17–19].
From an applied point of view, the capability to induce phase transitions and to control the electronic properties of solids on ultrashort timescales is of importance towards the realization of an *ultrafast bi-directional switch* with a response time of a few fs, that could improve by several orders of magnitude our current computational capabilities and impact on our lives like the invention of the transistor did [20]. Light pulses can nowadays match these timescales and some important steps have been taken towards this goal [19, 21, 22], making it a realistic target in the coming years.
From a basic perspective, the perturbation of electronic states on their fundamental timescales led to a variety of emergent phenomena. Photo-excited states are emergent when resulting from a transient change of the many-body interactions within the electronic subsystem and exhibiting properties at variance with the ones normally present in their equilibrium phase diagrams. A natural testbed for the exploration of this non-equilibrium physics is represented by strongly correlated materials, where the interplay between charge, spin, and lattice degrees of freedom produces various competing ground states already in equilibrium conditions, and

where the possibilities of material engineering are enormous. In these materials, unlike band insulators and semiconductors, the electronic properties are derived from strong interactions among electrons and this usually leads to cooperative and colossal responses [23–26].

In the equilibrium physics of strongly correlated materials, the main procedure to access broken symmetry states emerging from collective electronic interactions such as Mott insulating, antiferromagnetic or superconducting states, is to tune external parameters like pressure (acting on the lattice spacing), temperature (acting on thermal fluctuations), chemical doping or gating (modifying the band filling). In non-equilibrium phase transitions, changes in these parameters are often induced in the form of abrupt quantum quenches, that involve a dramatic change of the many-body interactions on very short timescales, and only recently adequate tools for their theoretical understanding (like nonequilibrium Dynamical Mean Field Theory, time-dependent Density Matrix Renormalization Group or quantum Boltzmann equations) have been developed [27–35]. A crucial open problem in this field is, for example, to understand under which conditions it is possible to stabilize a long range order (like a charge ordered state or superconductivity) starting from a higher symmetry state. While the converse is relatively simple, the need for a bidirectional switch requires a complete control of the capability to break a symmetry transiently and on demand.

An important example of light-induced emergent behavior are the so called "hidden phases", namely transient states that are not accessible through adiabatic variation of parameters like temperature and pressure in their ground state phase diagram [17–19]. Photo-induced phase transitions can be achieved through different mechanisms, that involve different excitation energies. A very common one is based on heating the electrons and move them from an already broken symmetry state towards a different symmetry. This procedure, also referred as photodoping, requires photon energies high enough to induce electronic hopping above possible gap energies and a very practical choice is to use visible or near infrared light [10, 36–42]

An alternative and more intriguing route is, instead, to induce a collective motion of both the electrons and the lattice through vibrational degrees of freedom. Structural modes can indeed be used as means to trigger photoinduced phase transitions and act as additional tuning knobs for the macroscopic control of the electronic properties [43–52]. The pump-light in this case has to be resonant to the phonon frequencies and is, therefore, falling in the midinfrared/THz region of

the electromagnetic spectrum. Being the energies involved much lower than the ones used in photodoping, these pulses are not directly heating the material as in most optical experiments [53]. This method was proved particularly effective in inducing transient phase transitions in strongly correlated materials like cuprates [46, 48, 49, 54], manganites [43, 44], oxide heterostructures [47] and organic compounds [51].

A third novel protocol for the control of solids is the gating with strong quasi-static fields in the THz region that is of obvious interest for the development of faster and more efficient electronics. Recent experiments in cuprates [21, 55] showed that strong THz pulses can bidirectionally trigger the superconducting transition while in conventional superconductor allowed the observation of nonthermal superconductor-to-normal transitions and of the amplitude mode associated with these transitions [12, 56, 57].

We now introduce the two main problems investigated in this thesis work.

Phase transition timescales in strongly correlated solids

A first important problem in photoinduced phenomena is to determine the connection between the decay of the transient phase and the effective interactions (like Coulomb repulsion, exchange interaction and electronic hopping) of the ground state. Its solution is essential in order to stabilize the photoinduced states and allow predictive knowledge of their timescales.

A rough estimate of the timescales associated to relevant phenomena in condensed matter directly follows from an analogy with the Heisenberg uncertainty principle [58, 59]

$$\Delta E \Delta \tau \sim \hbar, \tag{1}$$

where ΔE indicates the magnitude of the energy scale involved in a physical process, while $\Delta \tau$ quantifies its characteristic time scale.

Low energy electronic phenomena, like collective modes and orderings, have intrinsically slower timescales than electron hopping or exchange phenomena, which involve instead much higher energy scales. A simplified overview of typical energy- and time-scales in strongly correlated solids, that constitute the main focus of this thesis work, is reported in Fig. 1.

This estimate can be particularly useful in order to rationalize the timescales associated with processes, like the photo-induced melting of a gap, and is beautifully

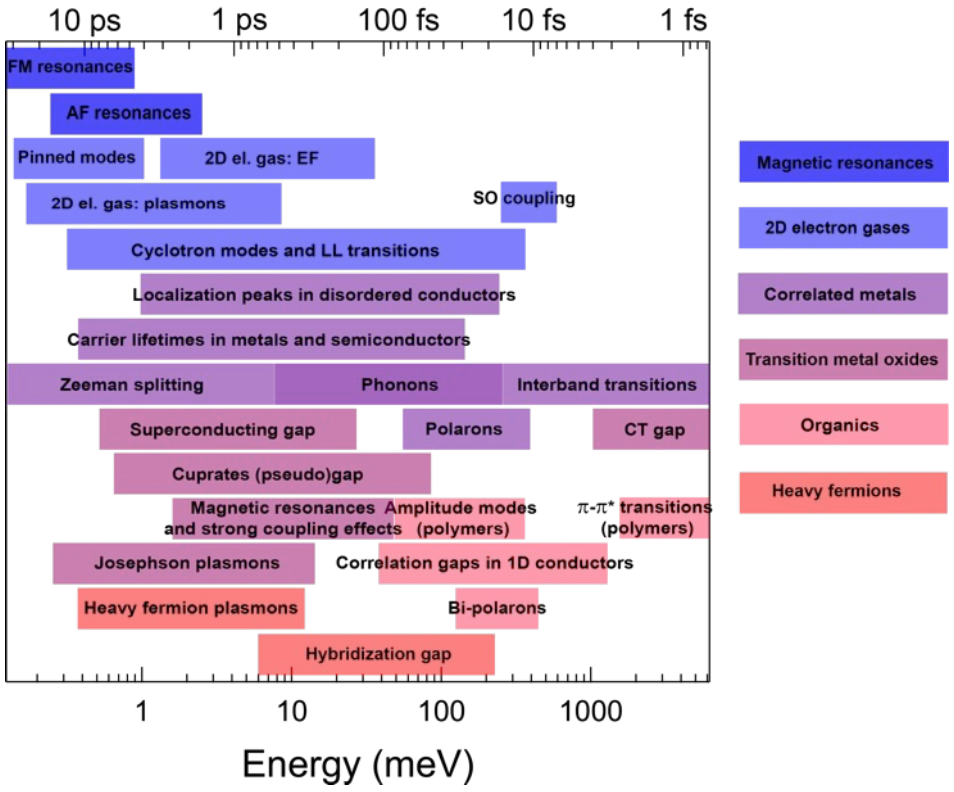

FIGURE 1: **Characteristic energy and time scales in strongly correlated materials**. Schematic summary of energy and time scales associated with selected relevant physical phenomena in strongly correlated solids. The following abbreviations are used: FM-ferromagnetic, AF-antiferromagnetic, EF-Fermi energy, LL-Landau level, SO-spin-orbit, CT- charge transfer. (Adapted from Ref. [26])

verified in multiple experiments where it is found that gaps with lower energies (e.g. superconducting or charge density wave) have a melting timescale orders of magnitude longer than the faster timescales associated to the higher energy Mott gaps (see Fig. 2) [1]. One has to consider that eq. (1) also represents a lower limit to the switching process and emergent effects like competition of different electronic configurations and couplings between diverse degrees of freedom (like the electron-phonon one) can significantly modify the relaxation of the transient phase towards equilibrium.

A prototypical case where the relaxation dynamics is affected by the magnitude of the electron-electron interactions is the decay of holon-doublon quasiparticles (holons are empty sites, while doublons are double occupancies in the lattice) in Mott insulators. So far this problem has been investigated with theoretical methods [61], that suggested a prominent role of the Coulomb correlation in slowing the decay of these high-energy excitations, and in pioneering experiments with

[1] The gap energy is roughly proportional to the excitation density needed in order to melt it.

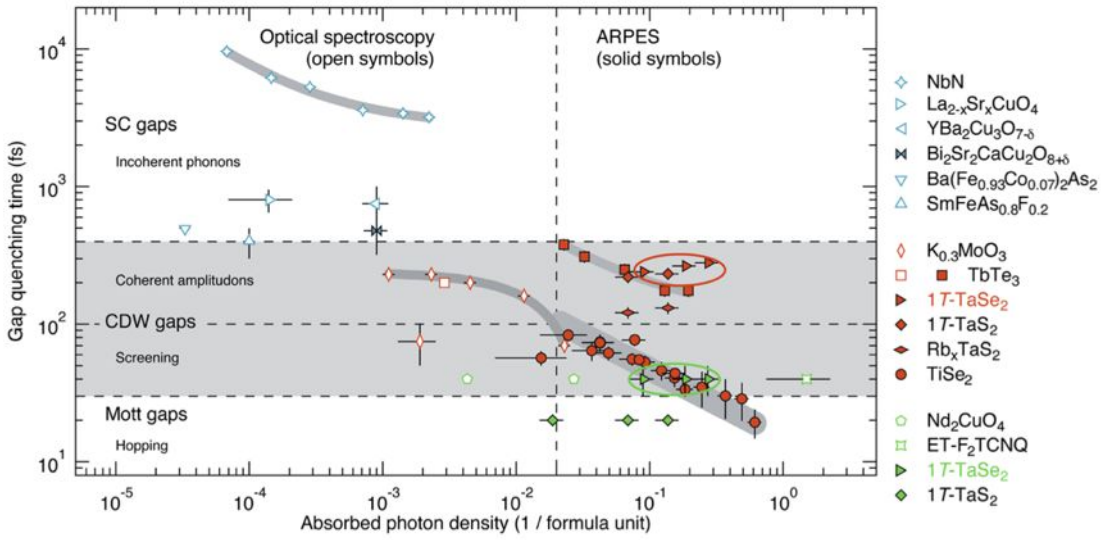

FIGURE 2: **Melting timescales of electronic gaps as a function of excitation density**. Melting timescales of electronic gaps as a function of excitation density, as measured by time-resolved optical and photoemission spectroscopy for various superconductors, charge-density–wave systems, and Mott insulators. From Ref. [60]. Published by The Royal Society of Chemistry.

cold atoms in optical lattices [62, 63] that found evidence for an exponential scaling of the decay times in the ratio between electronic bandwidth (W) and onsite Coulomb correlation (U).

In this thesis, we report the first experimental observation of the holon-doublon recombination rate dependence upon variation of the ratio U/W in a quasi-one dimensional solid state Mott insulator, the ET-F_2TCNQ. The variation of the electronic parameters is achieved by means of pressure-tuning of the lattice (and therefore of the bandwidth W and of the intersite correlation energy V) and we are able to observe a clear decrease of the holon-doublon recombination rate with the increasing ratio $(U - V)/W$. This experiment, carried out in a solid-state system where electron-molecular vibrations are important and where Coulomb correlations are longer ranged with respect to cold atoms experiments, constituted not only a verification of the quantum simulation in a real solid state system, but also unveiled the relevance of tunneling between different holon-doublon states in affecting the global decay of the photoexcited state.

Manipulating the superconducting phase transition boundary

A promising direction for the development of devices operating on ultrafast timescales is that associated with the ultrafast control of the superconducting transition. Besides the fascinating properties of this phase of matter, the usefulness of a perfect conductivity is well established in a variety of applications involving high field magnets (that necessitate high currents) and low loss power lines and each step towards an increase of the critical temperature can disclose new applications and scale up the usage of superconductor-based technologies. In the perspective of an ultrafast switch, a fast transition process between an ohmic and a superconducting behavior is of high interest and intense experimental efforts have been already devoted towards its control on short timescales and the search for a route to increase T_c [21, 46, 48, 50, 54].

High-temperature superconducting cuprates have been a natural candidate for the attempts to induce and stabilize superconductivity with strong light pulses, since they already offer high equilibrium critical temperatures. In this case, the technique used to stimulate superconductivity and try to enhance T_c has been the one of resonant-phonon excitation: light pulses resonantly tuned to relevant Cu-O modes of the cuprate lattice (in compounds like $YBa_2Cu_3O_{7-\delta}$ [48, 50, 54] and $La_{1.8-x}Eu_{0.2}Sr_xCuO_4$ [46]) in order to modulate the relative orientation of the oxygen octahedra, led to the observation of a transient behavior compatible with a superconductor above the equilibrium T_c. The mechanism associated to these experimental observations is still under investigation. While for $La_{1.8-x}Eu_{0.2}Sr_xCuO_4$, it has been first assumed that the crucial role of the light pulse was to melt and remove a competing order (stripe order in this case) detrimental to the onset of superconductivity, see the phase diagram in Fig. 3, the observation of a similar phenomenon in underdoped $YBa_2Cu_3O_{7-\delta}$ compounds, where the superconducting dome is already quite robust, suggests perhaps a different interpretation based on light-induced redistribution of interlayer Josephson coupling [48, 50].

In this thesis work, we try to deepen our understanding on this light-matter interaction by driving lattice vibrations in a more conventional superconductor, the organic molecular solid K_3C_{60}, where lattice vibrations of the C_{60} molecules are known to be important for the onset of the superconducting state. We find that under resonant excitation conditions, the normal state of K_3C_{60} develops superconducting-like features in the optical spectrum for temperatures as high as

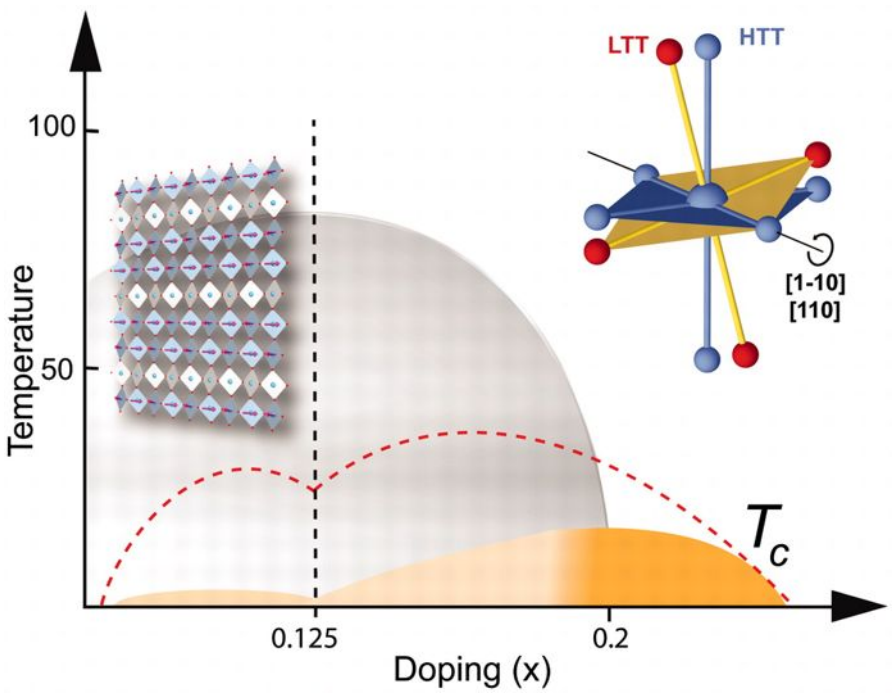

FIGURE 3: **Photoinduced superconducting behavior in $\mathbf{La_{1.8-x}Eu_{0.2}Sr_xCuO_4}$.** In the equilibrium state of $La_{1.8-x}Eu_{0.2}Sr_xCuO_4$, superconductivity (yellow dome) is quenched for doping levels below 0.2 (gray region). At the investigated 0.125 doping, the copper-oxygen planes are in a charge-ordered state, the stripe phase (left inset), that is associated with a low temperature tetragonal (LTT) distortion with tilted oxygen octahedra (right inset). The red dashed curve is profile of the superconducting dome in compounds of the type $La_{2-x}Sr_xCuO_4$ with a less pronounced LTT distortion. From Ref. [46]. Reprinted with permission from AAAS.

100 K and we discuss the possible role of large amplitude molecular distortions in determining these observations. These findings may be relevant for both the achievement of switching capabilities of the superconducting phase and for possible engineering of improved molecular superconductors at equilibrium.

Structure of the Thesis

The first chapter provides a short introduction to the physics of organic molecular solids and their correlated behavior. Chapter 2 and 3 introduce the materials investigated, (ET-F_2TCNQ and K_3C_{60}), their equilibrium and non-equilibrium physics, in order to define concepts and problems studied in this work. Chapters 4 and 5 represent the main results of this thesis and can be read independently. Experimental methods and protocols are reported in Appendix A.

Chapter 1

Organics as model systems for strongly correlated materials

This chapter briefly introduces organic molecular solids and their experimental phase diagrams with a particular emphasis on the presence of strong correlations. The experimentally observed phase transitions are, therefore, discussed in terms of a simple Hubbard Hamiltonian and for different dimensionality. The ending of the chapter is, instead, devoted to a short overview of photoinduced phase transitions in some well studies organic systems and their connection to the relevant interactions in these solids.

1.1 Organic molecular crystals and their phase diagrams

An important class of materials for contemporary condensed matter research is the one of *organic molecular solids*. Among the reasons that attracted increasing efforts in this research field is the fact that the physics of organics spans from Mott-Hubbard transitions [64–71], to low dimensionality [66, 72–79], several low-temperature broken symmetry states [66, 73, 80], like antiferromagnetism, charge and spin density waves [81–87], possible spin liquids [88–90] and, last but not least, superconductivity [65, 73, 82, 91, 92], sometimes with unconventional symmetries and properties [93–96].

Unlike normal solids, these crystals are constituted by a periodic arrangement of

organic *molecules* sitting at each lattice position and this translates into a coexistence of long-range crystalline order coupled to a local order at each site.

In Fig. 1.1 we show a schematic structure of a molecular crystal (the quasi-1D

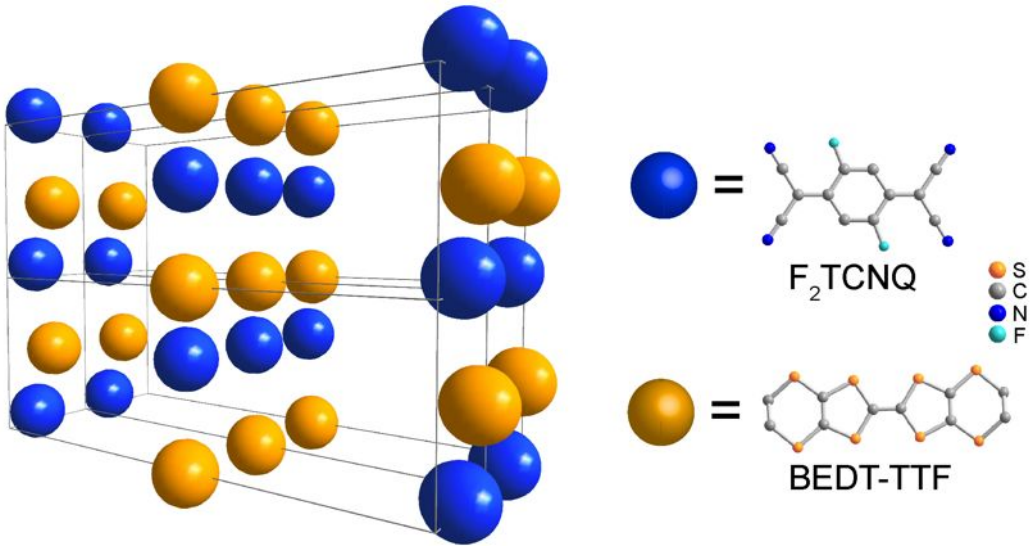

FIGURE 1.1: **Sample structure of an organic molecular solid**. Structure of an organic molecular solid (the quasi-1D compound (BEDT-TTF)-F_2TCNQ) over multiple unit cells. Each large sphere represents a molecule while the small spheres on the right are the atoms present in each molecular arrangement. H atoms and bonds are omitted for clarity.

compound (BEDT-TTF)-F_2TCNQ) over 4 unit cells in order to show the molecular arrangement in the crystalline structure.

The first and most important consequence of this structural character is that while in normal solids the atomic bonds along the *whole* crystal structure are usually covalent, ionic or metallic, in molecular solids the local molecular structure often involves covalent bonds but long range order is, instead, achieved through weaker bonds of van der Waals, or hydrogenic type [97].

From this difference, unlike most solids, molecular crystals manifest a clear hierarchy of energy scales both in the electronic excitations and in the vibrational ones. A higher energy scale is the one related to *intra*molecular excitations (electronic molecular transitions and molecular vibrations), while at lower energy *inter*molecular excitations (intermolecular hopping and phonons) are found.

Two scales are also present in the nearest-neighbor atomic separation, with atom-atom distances between different molecules being larger than the average atom-atom distance in the molecule.

This means that the bandwidth W, roughly proportional to the reciprocal of the intermolecular distance d, will be generally narrower than in normal solids and

the electrons of the highest occupied molecular orbitals (HOMO) will be prone to develop correlated states [64–71, 98].

A large fraction of organic molecular solids belongs to the class of charge-transfer complexes, namely molecular crystals constituted by at least two different molecular units where one is an electron donor and the other one an electron acceptor [82, 99]. When electron transfer occurs between the donor and the acceptor molecule, provided that the crystal symmetry and the degree of electron transfer are appropriate in equilibrium conditions, the resulting solid has an unfilled band. In some cases, this leads to a conducting or semiconducting state [1], but in a number of systems [2] the electronic correlations, combined to the very narrow bandwidths, give rise to a Mott insulating state. Many members of the organics family thus represent a physical realization of strongly correlated systems and, because of their tunability, they can be used as an ideal playground for the experimental investigation of Mott-Hubbard physics and of a number of phase transitions.

This entire class of materials is, indeed, highly tunable both in dimensionality and in interaction strength. The dimensionality D of the electrodynamics is mainly defined by the relative ratios between hopping amplitudes along different structural directions, while the relative interaction strength U/W is simultaneously defined by both the molecular orbital details (through the onsite Coulomb repulsion U) and the intermolecular bandwidth W. These parameters can be varied either by chemical substitution in the structure or by applying an external pressure. In both cases, these materials are extremely flexible because of the great variety of base molecules available for their synthesis (see for examples Refs. [82, 91]) and the large compressibility (and hence tunability) deriving from their weak intermolecular bonds. In order to better appreciate the variety of ground states offered by these solids, we report in Fig. 1.2 the (p, T) phase diagrams of some of the most important and investigated families of organics: the alkali fullerides A_3C_{60} [87], the kappa salts κ-(BEDT-TTF)$_2$X [100], and the Bechgaard salts (TMTTF)$_2$X (or (TMTSF)$_2$X) [78].

The choice of this kind of phase diagram is motivated by the fact that pressure (as well as chemical doping) is a powerful tuning knob for the degree of correlation of materials, by acting on the effective interaction U/W, while temperature acts on the systems through their fluctuations.

[1] Like in κ-(BEDT-TTF)$_2$I$_3$, κ-(BEDT-TTF)$_2$Cu(NCS)$_2$, (TMTSF)$_2$ClO$_4$, (TMTSF)$_2$PF$_6$, K_3C_{60}, Rb_3C_{60}.

[2] Examples are κ-(BEDT-TTF)$_2$Cu[N(CN)$_2$]Cl, (TMTTF)$_2$SbF$_6$, (TMTTF)$_2$AsF$_6$, and Cs_3C_{60}.

These three families exhibit different effective dimensionality [3] thanks to their diverse lattice symmetry and molecular structures (that in turn define the hopping integrals along the crystalline axes) and a direct comparison of these phase diagrams can reveal interesting features.

The first important observation to be made is that, independent of dimensionality,

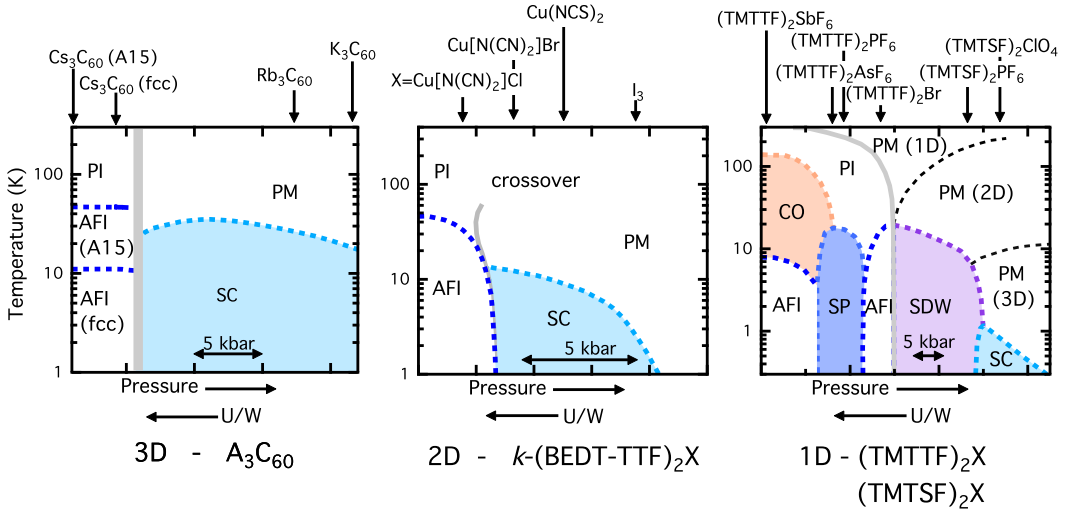

FIGURE 1.2: **Phase diagrams of different organics families** Pressure-Temperature (p, T) phase diagrams for three different families of organic molecular solids with different dimensionality: the alkali fullerides A_3C_{60} (adapted from Ref. [87]), the kappa salts κ-(BEDT-TTF)$_2$X (adapted from Ref. [100]), and the Bechgaard salts (TMTTF)$_2$X (or (TMTSF)$_2$X) (adapted from Ref. [78]). in this picture we use the following abbreviations: (PI)-paramagnetic insulator, (PM)-paramagnetic Metal, (AFI)-Antiferromagnetic insulator, (SC)-superconductor, (CO)-charge order, (SP)-Spin Peierls insulator, (SDW)-spin density wave.

at high temperature (higher energies) all the compounds exhibit a paramagnetic insulating (PI) and a paramagnetic metallic (PM) phase upon variation of mechanical or chemical pressure (or, equivalently, of the effective correlation U/W). The transition between these two states occurs either through a crossover or through a first-order insulator-to-metal transition, depending on the temperature. Since these compounds are all half filled, the material is expected to remain metallic and the relatively high temperature of the transition (approximately up to 100 K) suggests a role of purely electronic degrees of freedom. As we will see in the following, this insulator-to-metal transition is one of the most spectacular manifestations of strong correlations in solids and constitutes a first common pattern linking these very different material families.

[3] A_3C_{60} are three-dimensional systems, the kappa salts κ-(BEDT-TTF)$_2$X have a two-dimensional structure, while the Bechgaard salts (TMTTF)$_2$X (or (TMTSF)$_2$X) have effectively one-dimensional ground states in part of their phase diagram.

A second important common feature is that at lower temperatures and for all the different dimensionality one can find an antiferromagnetic instability on the insulating side of the phase diagram, while at higher pressures (or different chemical doping) a superconducting dome is found in its proximity.
This latter finding is also suggestive of the importance of strong correlations and triggered an intensive research activity because of its similarity with the cuprate phase diagrams (see Refs. [67, 101, 102] and references therein). Most importantly, the study of the interplay between electron-electron correlations and superconductivity is a fundamental theme in this field [25, 101–103] (and references therein).
As the dimensionality is reduced, the superconductive instability occurs at lower temperatures and in the one dimensional compounds (TMTTF)/$(TMTSF)_2X$ it is just one among additional competing ground states. In particular, the spin degrees of freedom play an important role, ultimately leading to spin ordered states like the spin-Peierls one or the spin density wave [76, 84].
Moreover, in these compounds pressure acts also as a symmetrizing parameter that increases the effective dimensionality of the quasi 1D solid (by reducing the difference between different axial hopping elements) and pushes the material across a progressive crossover towards a tridimensional conductor [84].
Based on these observations, we can conclude that organic molecular crystals exhibit a wide variety of ground states with common trends among families based on very different molecular constituents and/or dimensionality. The phase diagrams in Fig. 1.2 highlight a strong dependence of the crystalline ground states upon the ratio U/W and definitely give an impression about the degree of tunability of these compounds. It is sufficient to mention that the relevant pressure scales in Fig. 1.2 are measured in kbars, i.e. on average much lower than the corresponding pressure scales of transition metal oxides (e.g. VO_2 [104, 105], or V_2O_3 [106]) or cuprates (e.g. Ref. [107]). This implies that by reaching a certain maximum experimental pressure, the surface of phase diagram (and the corresponding U/W value) that can be covered in the average organic solid is far higher than in the aforementioned inorganic compounds.

1.2 Understanding the phase diagrams of strongly correlated electron systems

Strongly correlated materials are both fascinating and difficult to study because the electrons are interacting through their Coulomb repulsion and the behavior of each particle is at some degree determined by the dynamics of the surrounding electronic distribution.

The simplest model Hamiltonian that can be used to understand correlations in solids is the one introduced by Hubbard for spin 1/2 fermions in a single band on a cubic lattice [108]

$$H = -t \sum_{i\sigma} \left(c^{\dagger}_{i\sigma} c_{i+1\sigma} + H.c. \right) + U \sum_{i} n_{i\uparrow} n_{i\downarrow} \tag{1.1}$$

where $c^{\dagger}_{i\sigma}$ and $c_{i\sigma}$ are the electron creation and annihilation operators and $n_{i\sigma} = c^{\dagger}_{i\sigma} c_{i\sigma}$ is the usual number operator. The index i runs over the lattice sites, σ is the spin index. The first term describes the electronic hopping between nearest-neighboring lattice sites with an energy scale t, while the second term approximates the Coulomb repulsion integral with a fully screened interaction that retains only the *onsite* term U, i.e. two electrons feel each other only when sitting on the very same lattice site with a different spin configuration and U is the characteristic energy scale of this electronic repulsion[4]. The hopping term promotes, indeed, electron delocalization within the lattice, while the Coulomb repulsion makes the hopping on filled neighboring sites energetically unfavorable.

The bandwidth, often used as a reference scale for the relevant interaction energies, is defined as $W = 2zt$, where z is the number of nearest neighbors [23]. In order to keep the analysis simple, we will always refer to an hypercubic bipartite lattice at

[4] In some cases the onsite approximation for the Coulomb interaction is too crude, e.g. when the screening is less effective, and it is necessary to include additional interaction terms that take into account the electronic repulsion among particles sitting on nearest-neighboring sites (V_1), on next-nearest-neighboring sites (V_2) and so on.
In this case, one talks about extended Hubbard models and they can be cast into the following form

$$H = -t \sum_{i\sigma} \left(c^{\dagger}_{i\sigma} c_{i+1\sigma} + H.c. \right) + U \sum_{i} n_{i\uparrow} n_{i\downarrow} + V_1 \sum_{i} n_i n_{i+1} + V_2 \sum_{i} n_i n_{i+2} + \ldots, \tag{1.2}$$

with $n_i = n_{i\uparrow} + n_{i\downarrow}$. Normally the magnitude of the V_i integrals decreases with the increasing distance among charges and quite often only the first term is retained.

half-filling[5] and we consider a dimensionality $D > 2$. The cases $D = 2$ and $D = 1$ are discussed separately at the end of the section.
Despite its apparent simplicity, the Hubbard model is not easily solvable because it is constituted of a hopping term diagonal in reciprocal space and an interaction term diagonal in real space and has been solved, so far, only in dimensionality $D = 1$ [109] and $D = \infty$ [110, 111].
The main tuning parameters for this simple model are:

- *filling*, i.e. number of electrons per site;
- *interaction strength* (or *Mottness*) U/W, where W is the bandwidth.

Two interesting exact limiting cases of the Hubbard model at half filling are the Fermi-gas limit ($U = 0$) and the atomic limit ($t = 0$). In the limit of $U = 0$ the model reduces to the usual tight binding picture where electrons are delocalized and a conventional band is formed. Since the band is half-filled, the resulting ground state is metallic.
In the atomic limit $t = 0$ the electrons are completely localized and transport between sites no longer occurs. The obtained ground state is insulating and it is commonly referred as Mott insulating state. Between the two limits there is a metal-to-insulator transition (MIT) driven by the competition between hopping transport and Coulomb repulsion that represents the core transition in the electronic phase diagram (for a short introduction see Appendix E while a detailed review can be found in Refs. [111, 112]). The MIT occurs at finite U/W ratio, i.e. the insulating state is stabilized by the Coulomb repulsion U for increasing t despite the increased mobility of the carriers, and the transition is first-order at finite temperatures below the critical point. At the critical temperature T_c, it becomes second-order while, for higher temperatures, it becomes a smooth crossover.
In case of higher dimensionality ($D > 2$), the Hubbard model is unstable against antiferromagnetic ordering; as a result the temperature-effective interaction phase diagram (see Fig. 1.3) exhibits an antiferromagnetic insulating region that covers the metal-insulator transition, so that the only trace left is the crossover observed in the paramagnetic region. In real materials, the antiferromagnetic dome is strongly suppressed by frustration, but for the purpose of our qualitative arguments we can neglect frustration effects. In the weak coupling region ($U \to 0$) the

[5] When the integer filling condition $n = 0, 2$ is realized, we fall in the case of a trivial band insulator

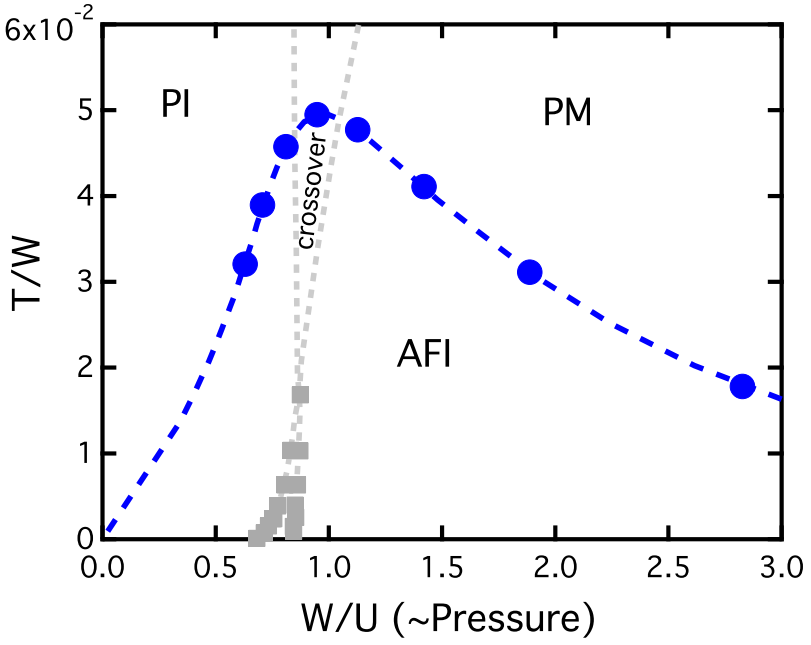

FIGURE 1.3: **Temperature vs effective interaction W/U (pressure) phase diagram of the Hubbard model for a bipartite lattice with $D > 2$.** In this diagram, based on dynamical mean field theory (DMFT) calculations, we can observe three distinct phases, namely a paramagnetic metal (PM), a paramagnetic insulator (PI), and an antiferromagnetic insulator (AFI). The blue circles and the blue dashed lines mark the Neél transition temperature. The grey squares mark, instead the metal to insulator transition while the grey dashed lines enclose the crossover region associated to this latter instability. All the temperatures are normalized to the overall bandwidth W. This phase diagram has been adapted from Ref. [113].

antiferromagnet appears at a Neél temperature $T_N \propto e^{-W/U}$, while in the strong coupling limit $U \to \infty$ the Neél temperature goes roughly as the superexchange interaction $T_N \propto J = 4t^2/U \sim W/U$. By inspecting the temperature-effective interaction phase diagram we can notice that the maximum Neél temperature occurs for intermediate couplings, close to the MIT and the associated energy scale is about twice the MIT critical point.

At lower dimensionalities ($D = 1, 2$) the scenario is modified because the antiferromagnetic transition is no longer allowed for finite temperatures (Mermin-Wagner theorem [114]) since infinitesimal thermal fluctuations are sufficient to destroy the magnetic ordering. This implies that in low dimensionality the MIT is completely exposed for any finite temperature. In addition, the case $D = 1$ presents a MIT transition pushed at $U/W = 0$, hence an arbitrarily small U is sufficient to turn the ground state into an insulating one [109]. Before summarizing the main physical features captured by the Hubbard model, it is useful to recall the connection

between Hubbard parameters and external pressure. When applying an external pressure to a solid its lattice constant d will shrink according to a corresponding equation of state and this will affect the Hubbard parameters U, V, and t in a different fashion.
In particular, U is an onsite property determined by the orbital details and can be regarded as pressure-independent for low pressure regimes. The hopping amplitude is instead expected to increase as the overlap between wavefunctions sitting at different lattice sites is increased by the lattice parameter reduction. As a consequence, also the bandwidth $W \propto t$ will increase; external pressure can thus be regarded as roughly proportional to W/U.
The similarity between the experimental (Fig. 1.2, especially (a) and (b)) and the theoretical phase (Fig. 1.3) diagrams is clear: the Hubbard model can reproduce a correlation driven MIT and with it both the PM and the PI phases. It also correctly captures the antiferromagnetic instability, but other ground states clearly require to go beyond this simple model, e.g. a BCS superconducting instability requires the inclusion of electron-phonon interactions that have been neglected in this discussion.

1.3 Ultrafast dynamics in organic molecular solids

Owing to their high degree of tunability and the rich physics reflected by their phase diagrams, organic molecular compounds opened new research perspectives in the field of ultrafast optics and nonlinear control of correlated solids,
In this section, we try to give a short (not exhaustive) introduction to the rapidly evolving field of photoinduced phase transitions in organics. The key concept of a majority of these experiments is to inject carriers through direct optical excitation and, possibly, trigger collective responses [9, 99, 115].
Three typical examples for this kind of photoinduced phase transitions in quasi-1D molecular solids, shown in Fig. 1.4, are the ones occurring in halogen-bridged nickel-chain compound, $[Ni(chxn)_2Br]Br_2$ (chxn=cyclohexanediamine), in K-TCNQ (K-tetracyanoquinodimethane), and in tetrathiafulvalene-*p*-chloranil, TTF-CA [9].
We are going to discuss how, starting with the same excitation protocol (excitation with short pulses centered at 1.55 eV) different systems can undergo different transient phase transitions depending on the dominant interactions in the electronic and lattice subsystems.

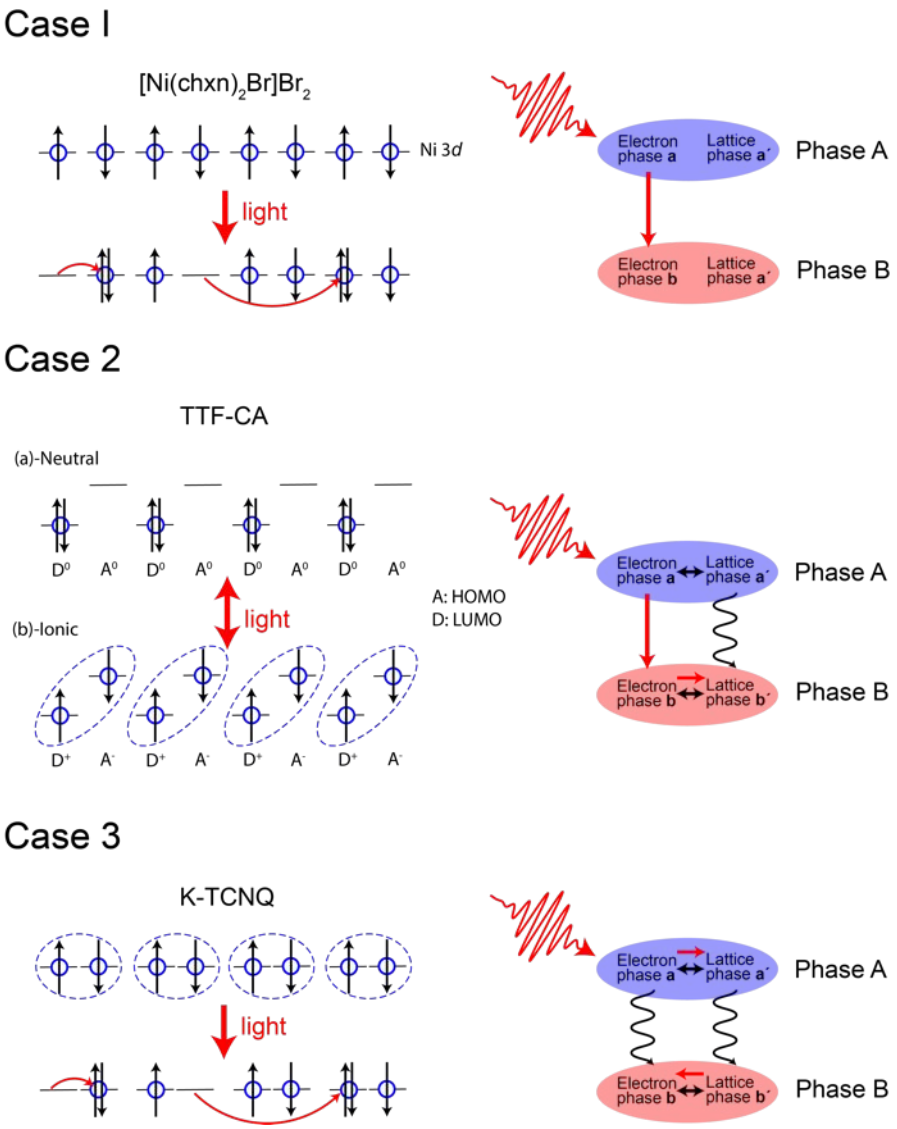

FIGURE 1.4: **Examples of photoinduced phase transition in organic molecular solids**. On the left are reported schematic electronic structures before and after photoexcitation for three examples of quasi-1D organic compounds. Electrons are pictured like black arrows, while red lines represent light-induced transitions. (Adapted from Ref. [9]). On the right are instead represented transition schemes from the initial phase A to the induced phase B after irradiation with a short laser pulse. Red lines represent electronic (or electron induced) changes, while wiggled lines represent lattice-induced changes. Case I represent a photoinduced phase transition dominated by electron-electron interactions, Case 2 one where electron-electron interactions are as important as electron(spin)-lattice interactions, while Case 3 pictures a transition dominated by electron(spin)-lattice interactions. (Adapted from Ref. [9]).

In the case of halogen-bridged nickel-chain compound, the starting ground state is constituted by an half-filled 1D chain of Ni sites that is insulating due to the large Coulomb repulsion among the Ni $3d$ electrons[6] [9, 115]. The excitation with high energy (1.55 eV) photons allows hopping processes to overcome the Coulomb repulsion and transiently generates electron and hole carriers (see Fig. 1.4). When the photoexcitation density exceeds 0.1 photons/Ni site, a Drude-like feature appears in the infrared optical spectrum, signaling the formation of a transient metallic state that decays with a time constant of approximately 3 picoseconds [115]. The transition, in this case, is mainly driven by electronic degrees of freedom and represents an example of ultrafast insulator-to-metal transition.

The second example of photoinduced transition, shown in Fig. 1.4, is the one of the TTF-CA compound, where one finds 1D chains of donor (D) TTF and acceptor (A) CA molecules. The overlap between π molecular orbital (between adiacent D and A units) is small compared to the Coulomb repulsion (both onsite and between nearest-neighboring sites), in a way similar to other previously mentioned compounds [9]. This material is found to be in a so called "neutral" (N) phase at room temperature (where singlets are formed in the D orbitals, while the A orbitals are empty), while below a T_c=81 K [116–119] it undergoes a phase transition towards an "ionic" phase (I) where both A and D orbitals are half-filled and dimerized (SP distorted). The neutral and ionic phases are almost degenerate and it has been found that light excitation at 1.55 eV can induce a transition between these two phases [120–126] by allowing electron hopping from the donor to the acceptor sites (and the opposite). The transition can be, in this case, bidirectional [9] and involves a massive structural rearrangement of approximately 100 DA pairs per photon [120]. In this transition, electron-lattice interactions are playing a role as important as the one of electron-electron ones, and, differently from the first example, here a structural change associated with the excitation of electronic hopping processes is observed.

The third system, K-TCNQ, Fig. 1.4, also forms 1D chains made of $TCNQ^-$ molecules with spin 1/2. The ground state of this system is a Mott insulator and exhibits a Spin-Peierls (SP) transition that leads to a dimerization of the $TCNQ^-$ molecules [9, 127–129]. When pumping the system with 1.55 eV photons, intermolecular hopping processes are promoted and the spin-singlet states present in the SP phase are perturbed. Since the magnetic gain associated to the singlet state is essential in stabilizing the the SP phase, the photoexcitation leads to a melting

[6] The ions in this compound are in the oxidation states Ni^{3+} and Br^-

of the SP state, i.e. a removal of the dimerization with a structural rearrangement (with ∼20 $TCNQ^-$ molecules displaced per photon) [9] and induces a transition from the diamagnetic SP phase to a paramagnetic nondistorted phase [9, 128, 129]. This transition is not an insulator-to-metal one, since carriers are localized in polaronic absorptions [9, 128, 129], but is instead a clear-cut example of collective transition induced by the coupling between spin and lattice degrees of freedom. To summarize we presented three cases of photoinduced phase transitions that can be classified according to the following scheme [9]:

(1) Electronic interactions are more important than electron-lattice and spin-lattice ones. The transition from phase A to phase B is purely electronic: the electronic subsystem evolves from a state a to a state b without structural changes.

(2) Electron-electron interactions are as relevant as electron-lattice (or spin-lattice interactions). The transition from phase A to phase B occurs first in the electronic subsystem, that goes from the state a to b, and, after the electronic transition, also the lattice evolves from a state a' to a state b' due to electron-lattice (or spin-lattice) interactions.

(3) Electron-lattice (or spin-lattice) interactions are dominant over electron-electron interactions. The transition from phase A to phase B occurs first in the lattice subsystem (going from a' to b'), then the electrons are driven by electron-lattice (or spin-lattice interaction) into the transition from a to b.

As visible in Fig. 1.4, the transition in halogen-bridged nickel-chain compound belongs to the first case of this list, while the one in TTF-CA to the second and the K-TCNQ to the third case. This classification allows to appreciate how important is the role of effective interactions in defining the nature of the photoinduced phase transitions and how organic materials can provide a flexible environment for the study of these dynamical phenomena.
We now focus on further implications of electron-lattice interactions (i.e. electron-phonon coupling or electron-molecular vibration coupling) in the photoinduced phase transitions. The crucial observation to be made is that in many charge-transfer complexes the molecular structure is strongly coupled to the degree of charge-transfer; from an intuitive point of view, if the charge density in a certain region of a molecule is larger, the bonds in that region will be stiffer (if not distorted) due to the presence of the electronic cloud. This can in turn translate in a

significant change of the vibrational mode energies and intensities. When dealing with a material where electron-lattice interactions are important, the excitation of electrons at the charge-transfer energy can modulate the electronic density in the molecular orbitals (i.e. the charge-transfer) and trigger a response of the lattice, that can evolve into transient states with different properties with respect to the equilibrium phases, i.e. hidden phases.

A clear example of hidden phase resulting from the photoexcitation of the molecular charge-transfer is found in the (EDO-TTF)$_2$PF$_6$ compound. This organic molecular solid is a quasi-1D system that undergoes an equilibrium metal-to-insulator transition when cooled below 280 K [7, 99, 130]. At the transition the charge-transfer is varied from a charge of +0.5 per EDO-TTF molecule in the metallic state to alternate dimers with charge 0 and +1 in the low temperature phase. In the two phases, due to the electron-lattice interaction the shape of the molecules is strongly affected by their charge: bent (0 charge), nearly flat (charge $+0.5e$), and flat (charge $+1e$). When pumping the low temperature insulating state with 1.55 eV photons, this compound first (after 40 fs) accesses a transient state a new charge-ordered state, shown in Fig. 1.5, that melts after approximately 100 ps towards the high temperature phase. The differences between the molecular arrangements in the equilibrium transition and in the photoinduced phase transition are shown in Fig. 1.5.

A second, subtle implication of the coupling between charge-transfer and vibrational degrees of freedom is instead associated to the possibility of manipulating the effective interactions, the correlations of these solids. An experiment in this direction has been performed by Iwai and coworkers [131] on the well known class of two dimensional κ-(BEDT-TTF)$_2$Cu[N(CN)$_2$]X (X=Br, Cl) (see phase diagram in Fig. 1.2) and proved the possibility to induce an insulator-to-metal transition in the Br compound due to an effective modulation of the correlation energy U [131]. The compound κ-(BEDT-TTF)$_2$Cu[N(CN)$_2$]Br in equilibrium conditions shows an insulator-to-metal transition upon substitution of hydrogen (metal) with deuterium (insulator) and for a T$\leq$50 K. The (BEDT-TTF) molecules in the unit cell are dimerized (see Fig. 1.6a) and one needs to distinguish between *intra*dimer and *inter*dimer energy scales. The effective correlation that drives the Mott transition is the onsite correlation energy of the dimer, that can be expressed as [131, 132]

$$U_{\mathrm{dimer}} = \frac{U}{2}\left[1 - \sqrt{1 + \left(\frac{4t_{\mathrm{dimer}}}{U}\right)^2}\right] + 2t_{\mathrm{dimer}} \simeq 2t_{\mathrm{dimer}}, \tag{1.3}$$

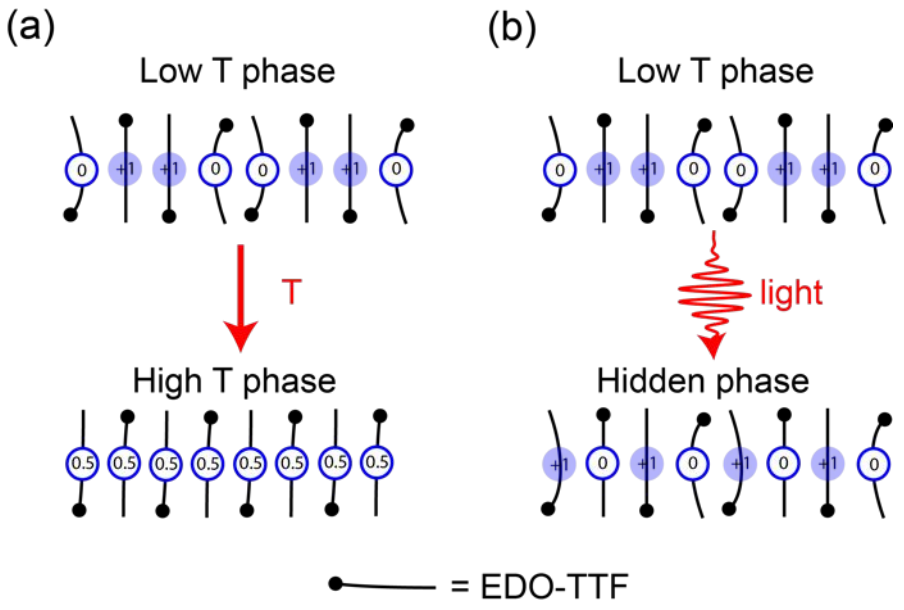

FIGURE 1.5: **Photoinduced hidden phase in the quasi-1D insulator (EDO-TTF)$_2$PF$_6$.** Schematic diagram of the thermal (a) and photoinduced (b) phase transition in the quasi-1D insulator (EDO-TTF)$_2$PF$_6$. Black lines stand for the EDO-TTF units while the numbers indicate the charge transfer state of each molecule. The relaxation of (b) towards the high-temperature phase is not shown. (Adapted from Ref. [130]).

when U (onsite BEDT-TTF correlation energy) is significantly larger than the *intra*dimer hopping integral (t_{dimer}). In this experiment the photoinduced phase transition (optical spectra compared to the equilibrium transition are shown in Fig. 1.6b) is obtained by exciting the intradimer transitions at 0.89 eV and, thus, inducing a displacement of the BEDT-TTF molecules due to electron-molecular vibration coupling. This displacement decreases the intradimer hopping and, due to the relation (1.3), the effective dimer correlation energy by approximately 0.4-0.7%, that corresponds to roughly the same change in U_{dimer} needed for the equilibrium transition [131]. This experiment is conceptually very different from the former examples and pushes the experimental investigation towards a direct control of the effective interactions strength (e.g. U/W, V/W) in strongly correlated electron systems, that is the underlying research line of this thesis work.

An additional way to investigate the relationship between electronic interactions and photoinduced phase transitions is to tune both the equilibrium and the photoexcited state by means of external pressure. This approach, due to the softness of most of these organic structures, can be effective in inducing large bandwidth changes and structural rearrangements, but so far only a limited number of nonequilibrium experiments has been carried out (especially when compared to

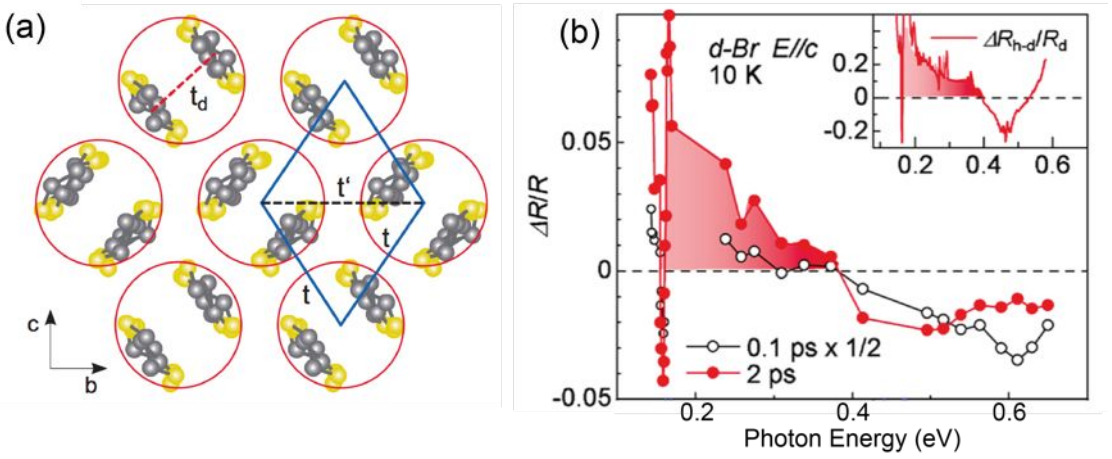

FIGURE 1.6: **Insulator-to-metal transition and optical modulation of the onsite correlation energy in κ-(BEDT-TTF)$_2$Cu[N(CN)$_2$]Br**. Panel (a) shows the structural arrangement of the BEDT-TTF molecules in the κ-(BEDT-TTF)$_2$X lattice (bc planes). Red circles mark the BEDT-TTF dimers, t_d represents the intradimer hopping amplitude while t and t' are two interdimer hopping integrals. Reprinted figure with permission from [89]. Copyright © 2012 by the American Physical Society. Panel (b) shows instead the photoinduced reflectivity change $\Delta R/R$ for a pump pulse centered at 0.89 eV used to modulate the intradimer hopping and correlation energy. The inset shows the equilibrium reflectivity change $\Delta R/R$ between the hydrogen compound (metal) and the deuterated one (insulator). Reprinted figure with permission from [131]. Copyright © 2009 by the American Physical Society.

equiilbrium solid state physics where pressure is routinely employed as a tuning parameter). Among previous pump-probe studies under pressure, we mention pioneering studies on bismuth (that does not belong to this section and will not be discussed) [133], on the charge ordered compound α-(BEDT-TTF)$_2$I$_3$ [134], and on polydiacetylenes (PDA) like PDA-4BCMU [135]. In the α-(BEDT-TTF)$_2$I$_3$ a prompt photoexcitation in the near infrared (0.89 eV) can melt the charge ordered state by forming microscopic metallic domains (with a size of less than 10 nm). For strong enough excitations, these domains tend to condense in larger patches that accomodate the photoinduced molecular rearrangements. Since the domain size is connected to relative molecular positions, pressure has a strong effect on the condensation of these microscopic domains into macroscopic ones and, ultimately, on the lifetime of the photoexcited state [134]. Pressure effects on the lifetime of the transient states have been measured also in the PDA-4BCMU compound, where, thanks to the different behavior of the lifetimes in a double exponential decay, it has been possible to discriminate between in-chain and out of chain relaxation processes [135].

Chapter 2

The ET-F_2TCNQ as a prototypical Mott insulator

This chapter, connected to Chapter 4, reviews the structural and electronic properties of the first material investigated in this thesis work, the quasi-1D Mott insulator ET-F_2TCNQ, that constitutes a neat example of almost ideal Mott insulator in half-filling conditions and with low electron-phonon coupling. Several non-equilibrium experiments focused on the photo-induced insulator-to-metal transition and on vibrational control are reviewed. The next section describes the physics of holon-doublon excitations in Mott insulators and the current knowledge about their generation and decay. At the end of the chapter, we summarize its content and define the experimental goal within the framework of this thesis.

2.1 The ET-F_2TCNQ Mott Insulator

2.1.1 Crystal structure

The bis-(ethylendithyo)-tetrathiafulvalene-difluorotetracyano-quinodimethane (also named ET–F_2TCNQ) is an organic salt synthetized in 1997 [136] and belonging to a broader class of compounds based on the BEDT-TTF molecule as a building block (e.g. the family of κ-(BEDT-TTF)$_2$X superconductors). This molecular crystal is made of stacked BEDT-TTF and F_2TCNQ (shown in Fig. 2.1b) molecules that crystallize in a monoclinic cell with space group $P2/n$ and the

following cell parameters [137, 138]

$$a = 5.8024(14)\ \text{Å} \quad b = 8.2032(18)\ \text{Å} \quad c = 25.104(6)\ \text{Å} \quad \beta = 95.66°.$$

The crystal is strongly anisotropic along the elongated c-axis but ET (and F_2TCNQ)

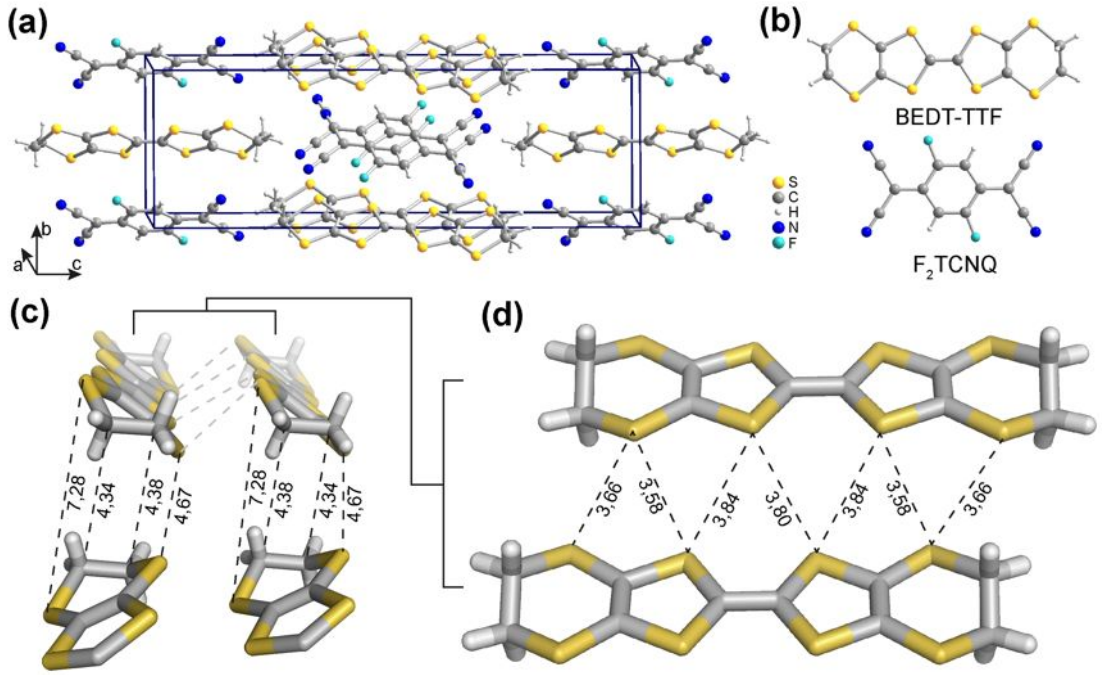

FIGURE 2.1: **Crystal structure of the organic salt ET-F_2TCNQ**. Panel (a) depicts the monoclinic unit cell of the organic salt ET-F_2TCNQ [138]. Panel (b) reports the structure of the constituent molecules BEDT-TTF (ET) and F_2TCNQ [138]. Panel (c) and (d) report instead the main intermolecular distances between nearest neighboring ET molecules in the *ab* and *ac* plane respectively [138].

molecules form chains along the a-axis with a *side-by-side* disposition [137]. The molecular arrangement in this solid is referred to as mixed-stack because the molecular chains are alternated along each cell axis normal to them. If we consider a chain made of molecules of A kind and another of molecules of the B kind, the stacking configurations seen in the cross-sectional plane are like [139]

$$\text{Mixed Stack} = \begin{pmatrix} A & B & A & B \\ B & A & B & A \\ A & B & A & B \\ B & A & B & A \\ A & B & A & B \end{pmatrix} \qquad \text{Segregated Stack} = \begin{pmatrix} A & B & A & B \\ A & B & A & B \\ A & B & A & B \\ A & B & A & B \\ A & B & A & B \end{pmatrix}$$

Unlike other mixed-stack compounds [140], the ET-F_2TCNQ has some relevant structural differences, namely [137]

(1) The intermolecular distance between ET and F_2TCNQ is 4.13 Å, significantly larger than the one observed in other similar mixed stack compounds (3.3-3.7 Å);

(2) The intermolecular S-S separation along the *a*-axis (in-chain) is on average 3.59 Å, i.e. shorter than the twice the van der Waals radius (3.7 Å) (see Fig. 2.1d).

In addition, it has to be stressed that ET-molecules lying in different chains are separated more than 4.3 Å (see Fig. 2.1d).
These structural features are crucial in determining the peculiar electronic properties of this compound, as we will see in the next section.

2.1.2 Electronic properties

The ET-F_2TCNQ is defined as a *charge-transfer (CT) complex*, i.e. a compound where the ET molecules act as acceptors and the F_2TCNQ ones as donors. The orbitals involved in the charge transfer are π molecular orbitals arising from the hybridization of carbon $2p$ orbitals on the aromatic rings [82]. Being weaker bound with respect to in-plane σ bonds on the rings, they constitute the highest occupied molecular orbital (HOMO) and the lowest occupied molecular orbitals (LUMO) and therefore define the low energy electrodynamics of this solid. In Fig. 2.2 we show the real space charge density in the HOMO and LUMO states over the ET molecule as determined with the Gaussian code [141] for quantum chemistry calculations. As visible from the green HOMO orbitals in the figure, the charges reside mainly in the central bonds of the molecule.

Being a CT complex, an important parameter to be determined is the ionization state of the acceptor molecule, i.e. what is the effective charge residing in the ET π HOMO orbital.
Since a correlation exist between the central C-C double bond lengths and the ionic state of the ET molecule [142], it can be estimated that the ET is completely ionized in the ET-F_2TCNQ[1], i.e. the CT is complete.

[1]Following [142] we determined a $\delta = 0.7124$ corresponding to a charge $+1$

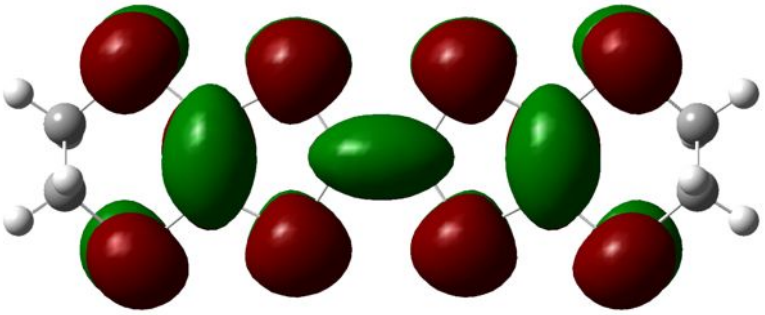

FIGURE 2.2: **ET-F_2TCNQ HOMO-LUMO orbitals**. Calculated HOMO (green) and LUMO (brown) orbitals of the ET molecule. Image kindly provided by Dr. S. Kaiser.

An important point to be considered is then the effective dimensionality of the charge transport in this crystal. The structure is strongly anisotropic and, as we have seen in section 2.1.1, the molecules lying in a same chain have overlapping van der Waals orbitals, while the overlap between molecules located on different chains is reduced by the enhanced spatial separation and by the mixed stack arrangement. This translates into a quasi-1D effective electrodynamics. From transport measurement, it exhibits a d.c. conductivity of less than $10^{-5}\,\Omega^{-1}\mathrm{cm}^{-1}$ at room temperature and shows a temperature behavior also consistent with an insulator [137]. These features allow us to position the ET-F_2TCNQ in the family of the quasi-1D organic insulators. Additional support to the one-dimensional electrodynamics picture of this compound comes from infrared spectroscopy (see Fig. 2.3a). The optical properties between 62 and 3720 meV have been measured by Hasegawa *et al.* [137], finding a strong CT feature only along the a-axis (in-chain cirection). No CT feature has been detected along the mixed stack column (b-axis). The experimental observation is consistent with a complete ionization of the molecules, and thus negligible hybridization between donor and acceptor. The feature observed in the optical spectra along the a-axis are instead due to the charge hopping between neighboring in-chain ET molecules [137].
The optical properties show a typical insulating behavior with a gap of roughly 600 meV in the $\sigma_1(\omega)$ and the insulating state is attributed to a Mott-Hubbard mechanism [137]. A detailed analysis of the optical properties and of their relation to the material parameters will be presented in Chap. 4. One final remark has to be made about the electron-phonon coupling. It has been, indeed, verified that this compound does not undergo a Peierls or spin-Peierls transition at low temperature [137]. Being a quasi-1D compound, this result points to a low electron-phonon coupling between HOMO electrons and long range lattice modes. Different is

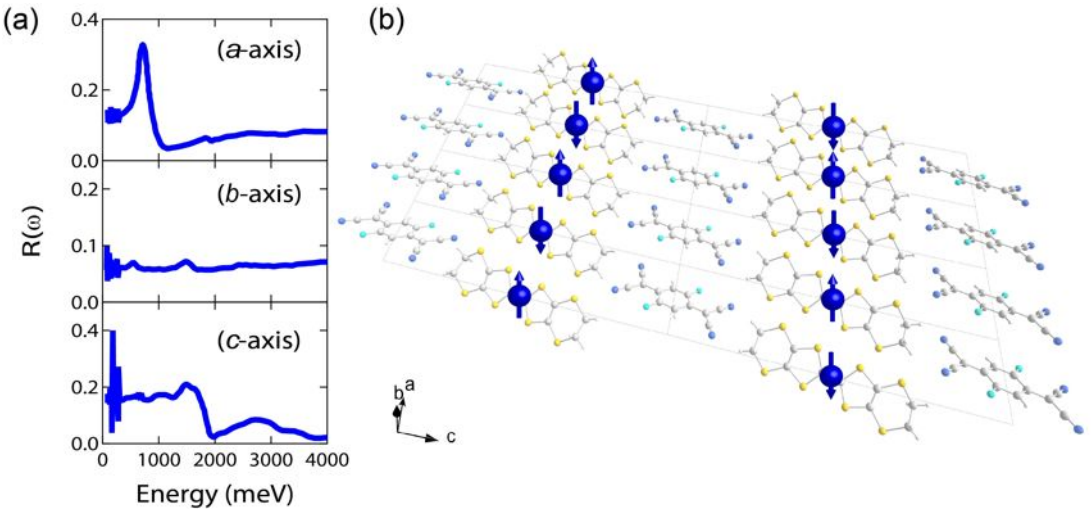

FIGURE 2.3: **One dimensional electrodynamics in the ET-F_2TCNQ Mott insulator**. Panel (a) shows broadband reflectivity measurements of the Mott insulator ET-F_2TCNQ along its different crystalline axes (adapted from Ref. [137]). The sharp CT feature at 700 meV is entirely polarized along the *a*-axis. Panel (b) shows instead a sketch of the *ac*-plane that highlights the half-filled ET-chains along which hopping transport can take place. The molecules are represented with the same color coding as in Fig. 2.1.

the case of the coupling between electrons and *intra*molecular vibration (referred as Electron-Molecular Vibration or EMV coupling), that is known to be present and important for the explanation of vibrational lineshapes in the equilibrium optical data, as well as non-equilibrium dynamical effects [49, 51, 143]. From these observations, we can conclude that the ET-F_2TCNQ can be regarded as a model quasi-one dimensional Mott insulator, with low electron-phonon coupling and negligible interchain interactions.

2.2 Nonequilibrium states and dynamical control of the ET-F_2TCNQ Mott insulator

One-dimensional systems are particularly attractive from both an experimental and theoretical point of view, because they can display physical phenomena peculiar to their low dimensionality and they can often be theoretically treated with analytical methods [76, 82, 84, 144] and powerful numerical methods like Density-Matrix Renormalization Group (DMRG) [145–147].

The ET-F_2TCNQ, as we have seen in the previous section, provides an almost

ideal realization of quasi one-dimensional Mott insulator and represents an important laboratory for the investigation of the nonequilibrium dynamics of strongly correlated electrons in real materials. Nonequilibrium experiments carried so far on the ET-F_2TCNQ can be grouped into two different classes. A first class is focused on the investigation of the melting and recovery of its Mott gap, while a second class of pump-probe studies is aimed to the control of its many-body dynamics through a direct action on electronic parameters like onsite correlations.

2.2.1 Mott gap dynamics and transient insulator-to-metal transition

The experiments performed by Okamoto and coworkers on this compound belong to the first class and found the gap melting in the ET-F_2TCNQ significantly and qualitatively different from other quasi-1D organics [38, 129]. When a half-filled Mott insulator is irradiated with photons having energies of the order of (or higher than) the onsite correlation U, their absorption can transiently induce hopping between neighboring sites, thus creating quasiparticles and possibly inducing a transient insulator-to-metal (IMT) transition. Empty and doubly occupied sites resulting from this excitation process are, respectively, called holons and doublons. In [38] the ET-F_2TCNQ is pumped along the 1D ET chains (a-axis) using 1.55 eV photons[2] (130 fs, 1kHz) and its optical properties are probed with tunable light spanning the 0.08-2.5 eV region.

The core results of this work are reported in Fig. 2.4. Immediately after photoexcitation[3], the reflectivity of the Mott gap is depleted and simultaneously increased roughly below 200 meV (see Fig. 2.4). The decay of the transient reflectivity change $\Delta R = R(t) - R_{eq}$ follows a double exponential behavior and the decay dynamics is so fast that after 2 ps the system is almost completely relaxed back to equilibrium. The analysis of the transient optical properties reveals a photoinduced insulator-to-metal phase transition and the corresponding manifestation of a Drude-like behavior at low energy (Fig. 2.4b) irrespective of the incident pump fluence. This behavior is interpreted as a signature of spin-charge separation [148, 149].

Other quasi-1D systems excited with a similar scheme, like Sr_2CuO_3 [150] or the

[2]Compared to a 700 meV gap value.

[3]Wiithin the pulse duration accuracy.

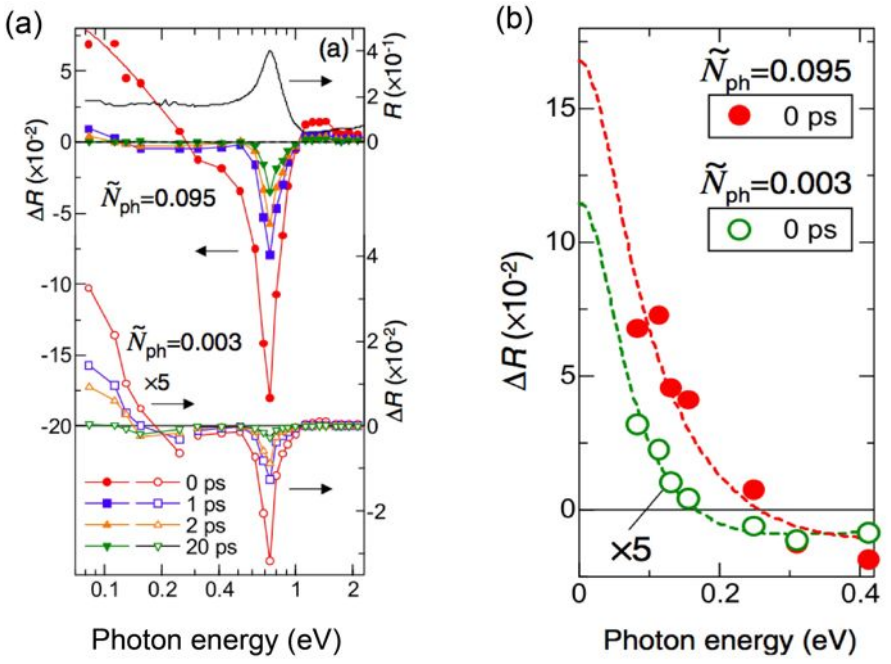

FIGURE 2.4: **Mott gap melting and spin charge separation in the ET-F_2TCNQ**. Panel (a) shows the transient reflectivity changes $\Delta R = R(t) - R_{eq}$ of the ET-F_2TCNQ (along its a-axis) after the photoexcitation with 1.55 eV photons for two different excitation regimes, 0.095 photons/ET molecule (above) and 0.003 photons/ET molecule. Panel (b) shows a zoom of the experimental ΔR (circles) in the low energy region together with an analytical Drude model calculation (dashed lines). Reprinted figures with permission from [38]. Copyright © 2007 by the American Physical Society.

parent compound K-TCNQ [128], exhibited, instead, a different nonequilibrium state with midgap absorptions related to a polaronic behavior, thus confirming the uniqueness of the ET-F_2TCNQ as a model one-dimensional system.

Another relevant experiment on the ET-F_2TCNQ focused on the nature of the photoinduced metallic state and on its formation and transient dynamics within the coherence time of the system. Wall *et al.*, performed pump-probe measurements with short (∼10 fs) pulses at 700 meV energy and polarized along the in-chain CT axis (a-axis) [10].

As we have seen, after photoexcitation this half-filled system undergoes an IMT [38] and in real space this results in the creation of a number of holons and doublons. If a nonlocal part of the Coulomb repulsion energy is present (see eq. (1.2)), these quasiparticles can form excitonic bound states and this will affect the initial dynamics of the photoexcited carriers. In their experiment, Wall *et al.* were able to resolve the delocalization dynamics at timescales shorter than the hopping time ($\tau_{\text{hopp}} \sim \hbar/t \approx 100$ fs) and found that the formation of the transient metallic state is characterized by an interference between bound and ionized holon-doublon pairs

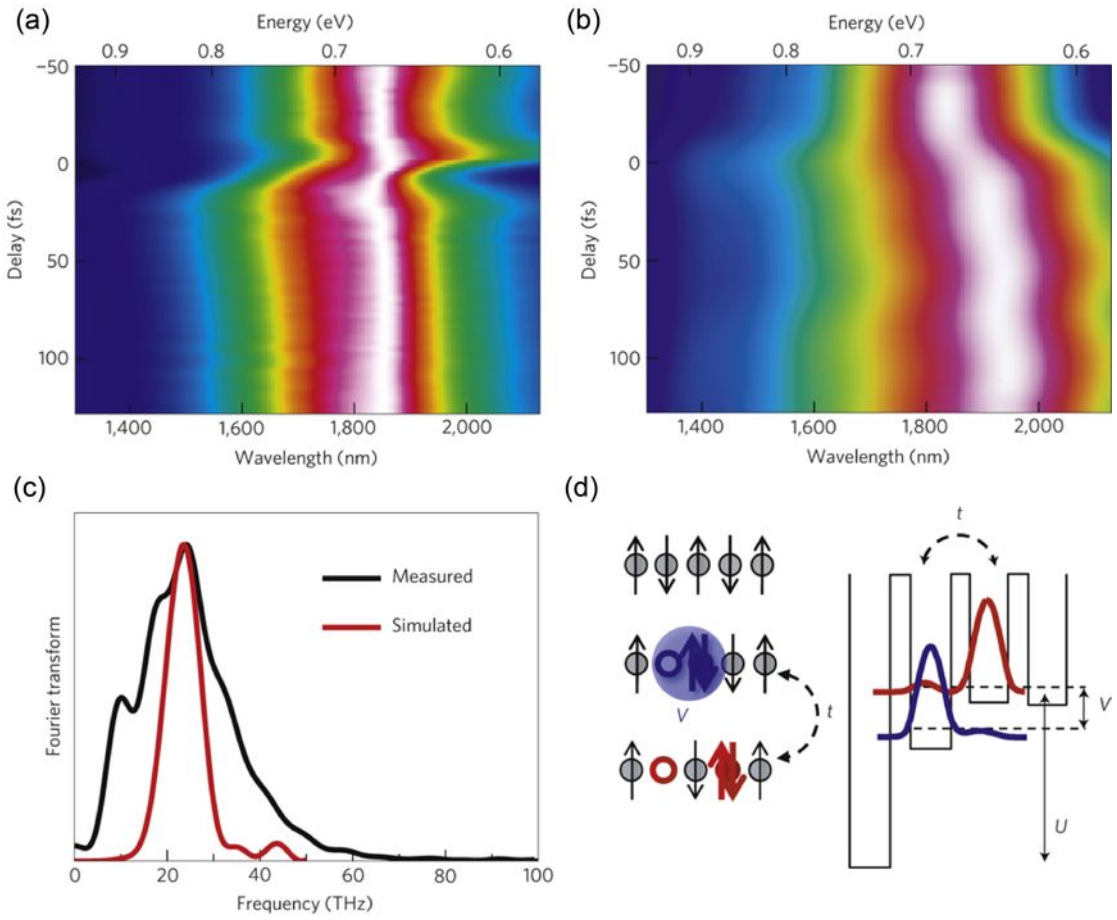

FIGURE 2.5: **Holon-Doublon interference in the ET-F_2TCNQ**. Panel (a) and (b) show respectively the measured and simulated transient $\sigma_1(\omega)$ of the ET-F_2TCNQ right after gap-resonant photoecitation. Its spectral weigth oscillates with a period of approximately 40 fs. Panel (c) shows the Fourier transform of the $\sigma_1(\omega)$ oscillations. Panel (d) shows instead the two interfering holon-doublon configurations (bound and unbound). Reprinted by permission from Macmillan Publishers Ltd: *Nature Physics* [10], copyright © 2010.

because of the presence of an intersite correlation energy scale V (see Fig. 2.5) [10].

The transient optical conductivity in the gap region shows a modulation at a frequency of 25 THz, in a way reminiscent of single-particle excitations in quantum wells (see Fig. 2.5) [10]. This result demonstrated, in this particular compound, the possibility of accessing high-energy many-body dynamics that, so far, has been almost exclusively investigated in cold atoms experiments [10].

2.2.2 Vibrational control of the electronic interactions

We now briefly summarize the main results connected to vibrational control experiments in this material. The core idea of these family of experiments is to modulate the Coulomb interactions (mainly the onsite U) by deforming the local molecular orbitals through selective vibrational excitation and electron-molecular vibration coupling.

In a first experiment by Kaiser *et al.* the ET-F_2TCNQ is strongly driven with light resonant to a 124 meV vibrational mode and probed between 223 and 868 meV. After the pump pulse arrival the material shows a redshift of the Mott gap (consistent with a gap melting) but remarkably sidebands appear at twice the pump photon energy [49].

This behavior is interpreted as a pump-induced vibrational modulation of the onsite correlation U due to unfolded higher order terms in the normal mode coordinate displacements $q(t)$. More specifically, the experimental findings are consistent with a second order modulation of the $q(t)$ coordinate

$$U(t) \sim q(t)^2 \propto Q^2(1 + \cos(2\Omega t)) \tag{2.1}$$

when assuming an oscillatory displacement $q(t) = Q\cos(\Omega t)$, with Q being the oscillation amplitude and Ω the vibrational mode frequency [49]. Importantly, the sidebands appearance is not symmetrical around the gap energy and this is compatible with a strong holon-doublon asymmetry towards their coupling to molecular vibrations [49]. A second experiment by Singla *et al.* performed on a 10 fs timescale and with phase stable pulses directly showed Mott gap oscillations at 2Ω, thus corroborating the scenario outlined above [51].

2.3 Excitations of a 1D Mott insulator

In Chapter 4 we focus on the IMT and its relaxation back to equilibrium. We will merge the two concepts outlined in the previous section by following the holon-doublon dynamics while tuning the parameters of the electronic ground state with pressure. In this section we briefly summarize some relevant properties of the holon-doublon excitations, with a particular focus on the 1D case.

2.3.1 Systematics of the excitations

Since the relevant model for the description of the ET-F_2TCNQ electronic properties is the extended Hubbard model at half filling, we restrict to it the discussion of the possible optical excitations. Unless additional energy is injected into the system by an external driving, all these excitations can be regarded as virtual states, i.e. zero-point fluctuations of the ground state around its half-filled configuration. The topic has been already theoretically investigated with Density Matrix Renormalization Group (DMRG) and field theoretic techniques [145, 147], and two key findings emerged.

The first finding is that the nature (and the phase diagram itself) of the optical excitation closely follows the ground state phase diagram that presents two distinct phases: a charge density wave state (CDW) and a Mott insulating one, the former dominating at low U (high V) values, the latter in the high U, (low V) region [146].

The second finding is that four different types of optical excitations are allowed, their nature being determined by the relative strength of U and V [147]. In Fig. 2.6a, we show the optical excitations' phase diagram, that are pictorially visualized in Fig. 2.6b.

Optical excitations must preserve the total charge, therefore they have to contain an equal number of holons and doublons, but what discriminates the different phase diagram regions is the degree of correlation (or binding energy) between holons and doublons.

If we start from the free charge carriers region, namely where holons and doublons are free to move with respect to each other, and we keep U constant, an increase in V will translate in an increasing binding between holons and doublons.

When $V = 2t$ a sharp transition occurs and holons and doublons start to form excitonic states (holon-doublon pairs), while for higher V values the pairs start to form excitonic strings (with 2 or more pairs), and eventually clusters of pairs that are essentially CDW droplets.

Eventually, if U is low enough (lower than $2V$) there will be a transition to a real CDW state.

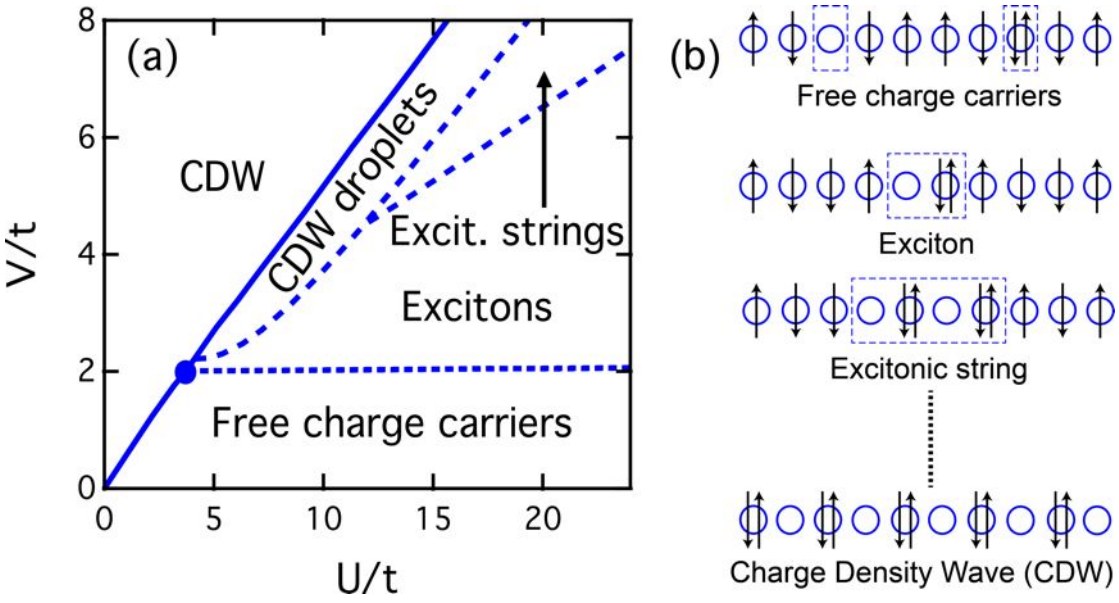

FIGURE 2.6: **(U,V) phase diagram for the optical excitations of a 1D extended Hubbard model.**Panel (a) shows the optical excitations phase diagram in the (U/t,V/t) plane for the extended Hubbard model as derived in Ref. [147]. The solid line indicates the transition between a Mott and a CDW ground state. Panel (b) represents instead these excitations in real space (adapted from Ref. [147]). Bounds states are highlighted by dashed lines.

2.3.2 Relevance of holon-doublon excitations in describing a metal-to-insulator transition

Holon-doublon excitations are not only relevant to the determination of the optical spectrum of a Mott insulating system, but also deeply involved in the definition of Mott MIT itself.

It has been recently shown [151, 152] that in frustrated and unfrustrated lattices the MIT can be also interpreted as a transition between ground states with a different number of holon-doublon excitations and a different binding strength between them.

These authors consider an half-filled system on a square lattice described by a simple Hubbard Hamiltonian[4] with and without diagonal hopping. The core idea of this approach is that in the metallic side of the transition holon and doublon excitations can form quite easily and be spread over several lattice sites (see Fig. 2.7a). On the insulating side, correlations are larger than hopping amplitudes therefore the holon-doublon density will be lower and their binding will be strong enough to prevent a separation larger than their decay distance (see Fig. 2.7b).

[4]Where only the onsite correlation U is considered.

In this view, the difference between a metal and an insulator is that in the former holon-doublon pairs can profilerate and freely propagate, while in the latter they are sparse and bound.

Variational Monte Carlo calculations [151, 152] pointed out that in such a system correlations tend to increase the binding between holon and doublons and to reduce their density but, importantly, these quantities show a neat discontinuity close to the U/t transition value and they can be regarded as a sort of order parameter for this phase transition (Fig, 2.7c-d). This behavior reflects a dramatic change

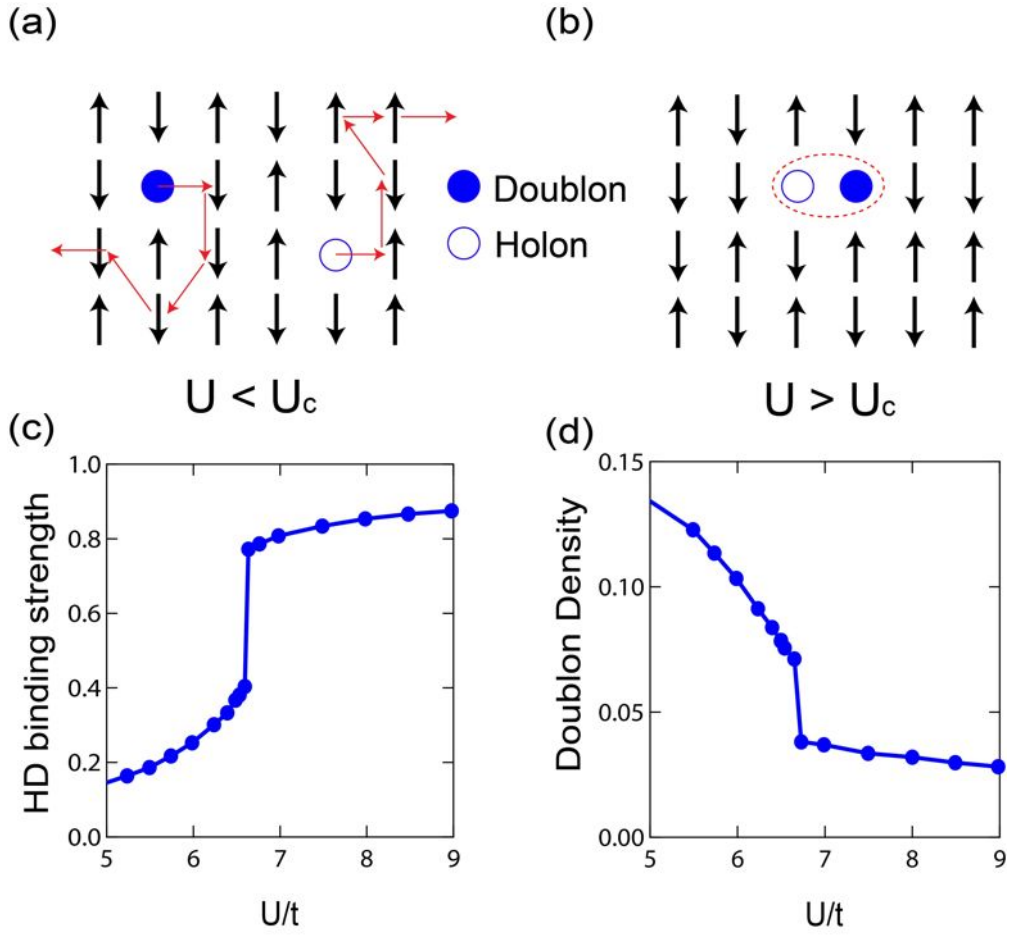

FIGURE 2.7: **Mott MIT as a Holon-Doublon binding transition**.Panels (a)-(b) show the behavior of holon and doublon excitation in a 2D antiferromagnetic background for a metallic and Mott insulating state, respectively (from Ref. [151]). Panels (c)-(d) show instead the HD binding strength (from the variational parameter μ in Ref. [152]) and the doublon density as a function of U/t across the Mott transition (adapted from Ref. [152]). In these panels, the data correspond to $L \times L$ models with $L = 14$ and zero diagonal hopping amplitude.

in the nearest-neighbor correlation of holons and doublons and points out the potential role of holon-doublon excitations as both equilibrium and nonequilibrium

indicators of the Mott MIT. As we will see in the next section and in Chapter 4, not only the binding strength of holon-doublon pairs but also their decay is intimately related to the degree of correlation of the ground state and, therefore, holon-doublon excitations can be used as a dynamical, experimental probe for nonequilbrium, as well as equilibrium, Mott transitions.

2.3.3 Holon-Doublon decay

The experiments presented in section 2.2.1 mainly focused on the formation of the metallic state in the ET-F_2TCNQ and on its peculiar 1D nature, but the recombination dynamics of the photoexcited state has been only marginally investigated. The holon-doublon recombination in condensed matter is an extremely important problem and a precise and predictive knowledge in this topic would open a different perspective of control in photoinduced phase transitions. In particular, and to the best of our knowledge, a crucial missing detail is the connection between the ground state properties of the equilibrium insulator and the photo-induced relaxation dynamics.

A photoexcited holon-doublon pair involves an energy fluctuation of order $U - V$ (in an extended Hubbard model [145]) with respect to the ground state. In order to decay back, this excitation must dissipate the excess energy by coupling to its surrounding environment acting as a dissipative bath (see Fig. 2.8a). The characteristic energy scales of the bath dictate the number of primary scatterers needed for the decay and thus the relaxation rate by which the holon-doublon pairs recombine into singly occupied sites. The bath can further thermalize through secondary scattering processes that are beyond the scope of this study. Due to the mismatch of energy scales between the initial and final states, the holon-doublon decay can in principle involve a great number of particles per decay event and be very slow.

Experimental work has been performed with fermionic cold gases in optical lattices that followed, in absence of correlation terms other than the onsite U, the doublon decay as a function of the Mottness U/W in a 3D half-filled lattice [62, 63]. In that context, the holon-doublon pair can dissipate energy only via spin excitations with characteristic energy $J = 4t^2/U$, or through kinetic energy transfer, that involves the creation of particle-hole pairs with a characteristic energy scale t [62, 63]. In both cases the scatterer energy scale is much smaller than the energy associated to the holon-doublon pair, therefore a large number of scattering

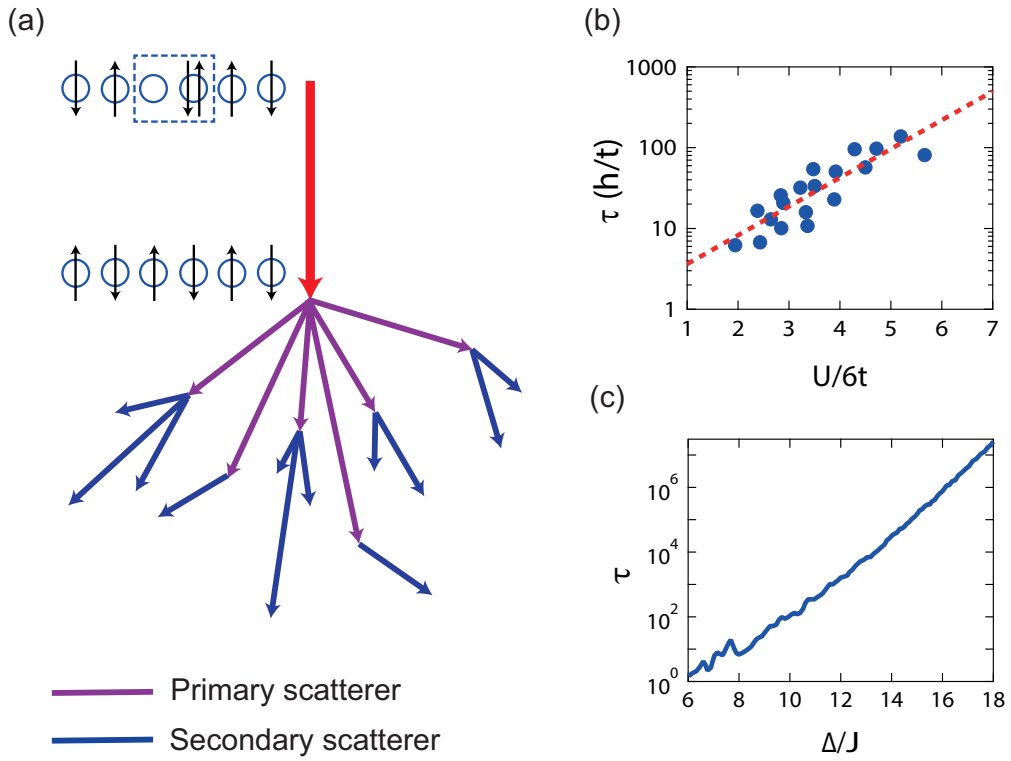

FIGURE 2.8: **Holon-Doublon decay dynamics.** Panel (a) sketches a generic holon-doublon (red) recombination chain through a primary scattering channel (purple), like phonons, magnons or particle-hole excitations., that can possibly dissipate energy into a secondary dissipative channel (blue), e.g. acoustic phonons. Panel (b) shows the experimental lifetimes of double occupancies as measured with cold atoms in optical lattices (blue circles) as a function of $U/6t$, or $2U/W$ (data from Ref. [62]). Panel (c) shows instead the theoretical holon-doublon lifetimes as a function of the ratio Δ/J for a two dimensional Mott-Hubbard insulator and with multimagnon emission as primary decay channel (data from Ref. [153] and with $J = 0.6t$).

events is needed. In both cases, the relaxation rate Γ is found to scale exponentially with the U/t ratio (see Fig. 2.8b). In more detail, dissipation by spin excitation goes as $\Gamma = 1/\tau \sim t \exp[-\alpha U^2/t^2 \ln(U/t)]$, while relaxation by creation of particle-hole pairs is more efficient in compressible systems and leads to a rate $\Gamma = 1/\tau \sim t \exp[-\alpha U/t \ln(U/t)]$ [63].

The tendency towards an exponential behavior of the holon-doublon recombination rate has been found also in theoretical studies of the decay through coupling to magnons in 2D Mott insulators with antiferromagnetic background [61, 153]. In that case the relaxation rate found from exact diagonalization of the Hubbard hamiltonian follows an exponential behavior in the ratio between the Mott-Hubbard gap Δ (defined with respect to the antiferromagnetic ground state) and

the exchange energy scale J, i.e. $\Gamma = 1/\tau \sim \exp[-\alpha\Delta/J\ln(\Delta/et)]$ [5] (see Fig. 2.8c) [61, 153]. This study is particularly relevant to the physics of cuprates and their photoinduced phase-transitions [154], where a viable dissipation mechanism for nonradiative holon-doublon recombination can be found in multimagnon emission events [61, 153]. Before closing we remark that the presence of exponential or power-law trends for the holon-doublon decay is ubiquitous in a number of different models and relaxation scenarios [34, 155–158], but direct experimental studies of this complex many-body problem in solid state systems are still lacking.

2.4 Summary

In this chapter we reviewed the properties of the organic Mott insulator ET-F_2TCNQ, a quasi one-dimensional Mott insulator with a weak electron-phonon coupling [137] that can be described in terms of an extended Hubbard model and provides an almost unique testbed for the investigation of pure Hubbard physics in a real solid state material.

Following the experimental observation of characteristic fingerprints of well-defined holon-doublon excitations [10] and of spin-charge separation [38], we described possible types of charge excitations and outlined their phase diagram in terms of the onsite and intersite correlation energy scales U and V of an extended Hubbard model. Holon-doublon excitations are not only relevant for a complete description of the photoinduced IMT observed in this specific compound, but are proposed to be also intimately connected to the equilibrium IMT for Mott-Hubbard systems.

We then introduced the problem of the decay of holon-doublon excitations that involve the dissipation of a large amount of energy and can involve many surrounding electrons. Because of these properties, the decay can be both very slow and extremely complex from a many-body point of view. The knowledge of its relation with the ground state interactions could be of obvious importance for a quantitative and predictive understanding of the relaxation timescales of photoinduced phase transitions in correlated materials and for a systematic stabilization of transient photoinduced states in these systems.

Organics are usually quite compressible, thus offering a wide tuning range of their electronic interactions even with moderate pressures and can allow to map in a real solid state material physical processes that have been so far investigated only with

[5] e being here the Euler's number and t the hopping amplitude.

theoretical methods or cold atoms experiments. Importantly, ultrafast relaxation in solids is often dictated by electron-phonon interactions (to both long-range and local vibrational degrees of freedom) that can profoundly affect the relaxation rate of holon-doublon excitations and that, so far, have not been reproduced with cold gases quantum simulations.

Our experimental goal is to elucidate the relation between the holon-doublon recombination lifetimes in the ET-F_2TCNQ, as a representative solid state Mott insulator, and its ground state interactions (U, V and t) by measuring the lifetimes associated to the reflectivity changes occurring at the Mott gap and by simultaneously tuning the ground state parameters V and t with the application of external pressure. The results of these optical measurements, reported in Chap. 4 are expected to extend our knowledge about the relaxation of a deep Mott insulating state and, thus, to help defining new protocols for the control of photoinduced electronic phase transitions in these systems

Chapter 3

The K_3C_{60} molecular superconductor

In this chapter, connected to Chapter 5, we introduce the second system investigated in this thesis, the alkali fulleride superconductor K_3C_{60}. While focusing our attention on this very compound, we will stress common features and differences with other members of the broader A_3C_{60} (A=K, Rb, Cs) family. In the following, the crystal structure and the main electronic properties are described. The focus is then shifted on one intriguing aspect of the A_3C_{60} system, namely the coexistence of superconductivity and strong electronic correlations, and we conclude by reviewing nonequilibrium optical studies on A_3C_{60} compounds. The last part of the chapter summarizes its content, with a particular attention to the superconducting transition of K_3C_{60}, and introduces the experimental goal of the research work reported in Chapter 5.

3.1 Structure of K_3C_{60}

The fundamental building blocks of A_3C_{60} are the fullerene molecules, one of the most intriguing carbon allotropes, first synthesized in 1985 by Kroto *et al.* [159]. Free fullerene molecules consists of 60 C atoms arranged in truncated icosahedron, with a surface tiling formed by 12 pentagons and 60 hexagons (see Fig. 3.1b). Pentagon-hexagon edges (p) are single C-C bonds, while hexagon-hexagon edges

(h) are made of double C=C bonds [160]. The bond lengths are, respectively, [161]

$$b_p = 1.455 \text{ Å} \qquad b_h = 1.391 \text{ Å}.$$

In many, but not all, compounds C_{60} molecules are arranged in an face-centered

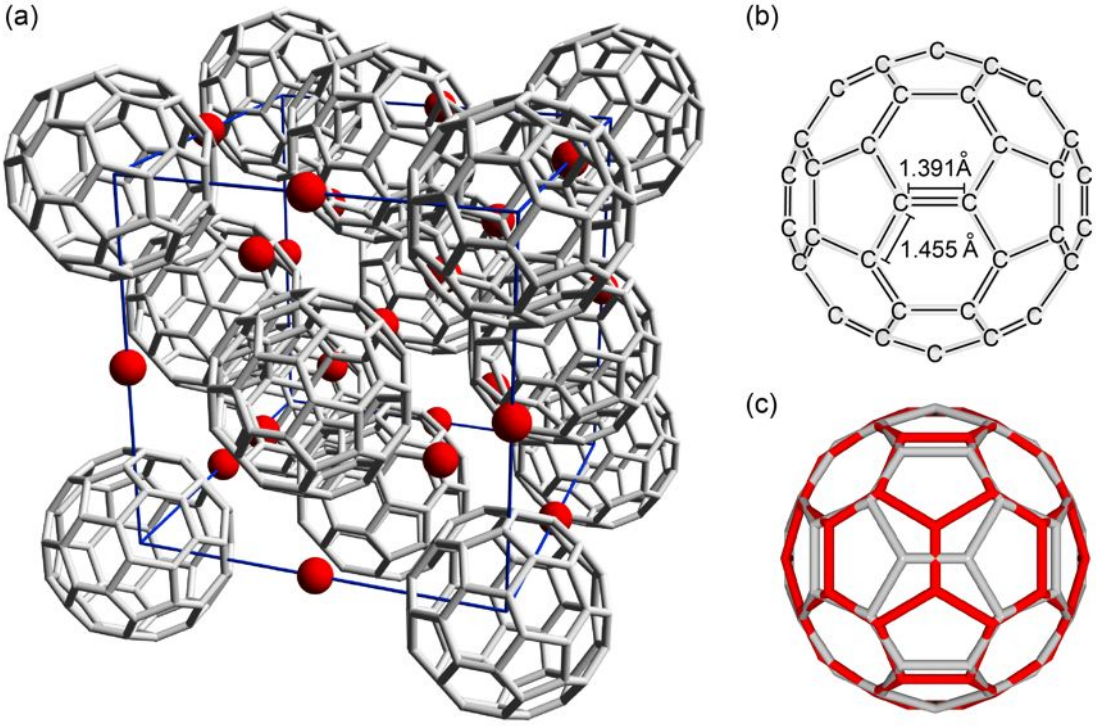

FIGURE 3.1: **Crystal structure of K_3C_{60}.** Panel (a) shows the unit cell of K_3C_{60} Grey lines represent C atoms and bonds, while K atoms are represented in red. Panel (b) shows the bond structure of the single C_{60} molecule (only front hemisphere). Panel (c) shows the two possible orientation states (in different color) of C_{60} molecules in the orientationally disordered fcc structure. The two states are rotated by 90°. The structural parameters are given in [162].

cubic lattice and this is the case of K_3C_{60}. The full structure of K_3C_{60}, illustrated in Fig. 3.1a, belongs thus to the $Fm\bar{3}m$ space-group with a lattice constant of 14.24 Å and the atomic positions listed in Table 3.1. In this structure, there is room for three alkali atoms per C_{60} molecule that occupy interstitial positions in a tetrahedral and octahedral arrangement [160]. As we will see in the following, thanks to their atomic radii, the alkali atoms effectively act as spacers between neighboring C_{60} molecules and this has deep consequences for the determination of the overall electronic properties.

From the experimental diffraction data (e.g. Stephens *et al.* [162] or Allen *et al.* [163]) it has been found that C_{60} molecules arrange themselves with two equivalent orientations with respect to the neighboring alkali atoms and they seem to be

Atom	Wyckoff	x/a	y/b	z/b	Occupancy
K1	8c	0.25	0.25	0.25	1.0
K2	4b	0.50	0.50	0.50	1.0
C1	96j	0	0.046	0.245	0.5
C2	192l	0.213	0.084	0.096	0.5
C3	192l	0.184	0.160	0.051	0.5

TABLE 3.1: **Atomic positions in the K_3C_{60} unit cell**. Atomic positions obtained from Rietveld refinements of single crystal X-ray diffraction data [162].

randomly oriented, i.e. the structure is orientationally disordered.[1]
On the other hand, there is evidence (at least in Rb_3C_{60}) of some degree of "antiferromagnetic" correlation between molecular orientations, i.e. neighboring C_{60} molecules tend to have opposite orientation [164, 165]. Other crystalline structures also found in C_{60}-based solids are body-centered-cubic, orthorhombic and the important A15 expanded cubic system (relevant to the high-temperature superconductor Cs_3C_{60}) [69–71, 160].

3.2 Phonons and molecular vibrations of K_3C_{60}

The K_3C_{60} structural complexity and the high number of atoms per unit cell translate into a rich vibrational spectrum that has an important role in determining the superconducting properties of A_3C_{60} compounds.
The isolated C_{60} molecule belongs to the icosahedral point group I_h and it has $(3 \times 60) - 6 = 174$ *intra*molecular modes falling into 46 different vibrational levels [166]. Among them, 14 modes are optical (10 Raman and 4 infrared active), while 32 are silent.
When considering the fcc lattice of K_3C_{60}, the vibrational spectrum gains three additional types of modes, namely A^+-C_{60}^{3-} phonons, optical C_{60}-C_{60} phonons and C_{60} librations [160, 167, 168]. In addition to these supplementary modes, the whole spectrum is found to soften with respect to the free C_{60} energies because of a C-C bond weakening due to the charge transfer between K ions and C_{60} units [166].
These modes have been extensively investigated both in pristine C_{60} and in A_3C_{60}

[1] If the C_{60} orientation were completely ordered, the structure would belong to the $Fm\bar{3}$ space group.

compounds with Raman scattering [169–173], infrared absorption [169], photoemission spectroscopy [174] and neutron scattering [175–177]. In Fig. 3.2a-b we show the vibrational spectrum of both pristine C_{60} and K_3C_{60} as measured from inelastic neutron scattering [175].

From both these measurements and theoretical calculations [166, 178], it emerges

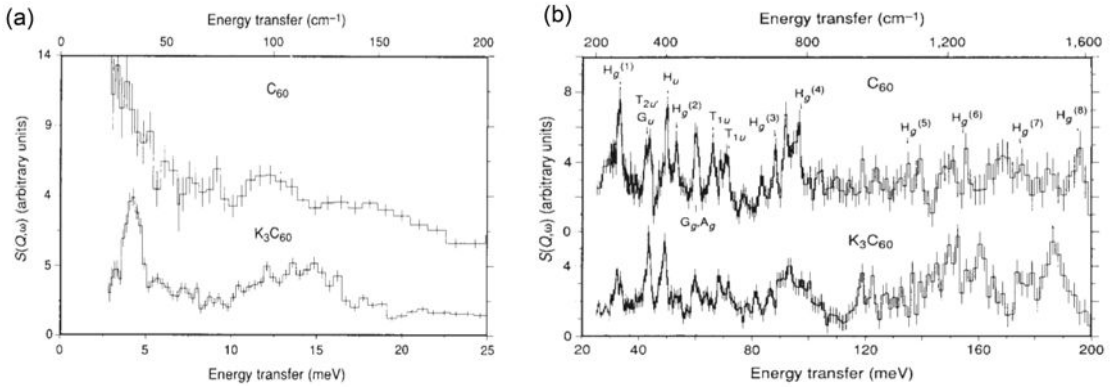

FIGURE 3.2: **Vibrational spectrum of K_3C_{60} and of pure C_{60}.** Panel (a)-(b) show the dynamic structure factor S(q,ω) measured with inelastic neutron scattering for C_{60} at 20 K and for K_3C_{60} at 5 and 30 K (these latter data have been summed). Panel (a) is restricted to low energy transfer (0-25 meV), while panel (b) covers all the vibrational spectrum between 20 and 200 meV. Some assignments within the icosahedral point group I_h are also shown. Reprinted by permission from Macmillan Publishers Ltd: *Nature* [175], copyright © 1991.

a clear separation of energy scales associated to the different vibrational modes: *inter*molecular modes, such as C_{60}-C_{60} phonons, A^+-C_{60}^{3-} phonons and librations, are typically located below 150 cm^{-1} ($\sim$ 20 meV), while *intra*molecular vibrations span from 200 to 1600 cm^{-1} ($\sim$25-200 meV) [166, 175, 178]. The *intra*molecular modes can have either a prevalent radial or tangential character. The latter type has higher energy than the radial modes because of the higher C_{60} molecule stiffness along its tangential directions.

The relevance of these modes to superconductivity has also been extensively investigated. In particular, it has been shown through lack of isotope effect (with alkali substitution) in Rb_3C_{60} that A^+-C_{60}^{3-} phonons do not contribute to the determination of T_c [179] and this has been explained in term of efficient metallic screening that reduces the net charge coupling to these modes [180].

C_{60}-C_{60} phonons are also weakly coupled to electrons [181] and the librations do not show linewidth changes above and below T_c [182], thus suggesting also weak coupling to the electronic subsystem [183].

It follows that the main players in mediating the superconducting pairing, in a BCS-like scenario, are the high energy *intra*molecular modes of each C_{60} molecule

[160, 168, 178, 184–191].

Among these modes, the A_g symmetry ones are expected to be screened out in A_3C_{60} [192, 193], while the five-fold degenerate Jahn-Teller H_g modes are less screened and are found to be coupled to the electronic subsystem. In Table 3.2 are reported the partial electron-phonon coupling constants $\lambda_\nu/N(\epsilon_F)$ (normalized to the density of states at the Fermi level) for the H_g modes as determined with different experimental techniques [160].

Mode	Energy	$\lambda_\nu/N(\epsilon_F)$ (eV)			
	meV (cm^{-1})	Raman [170, 171]	Raman [172]	Neutron [176]	Photoemission [174]
$H_g(1)$	33.85 (273)		0.048	0.019	0.019
$H_g(2)$	54.18 (437)	0.032	0.020	0.033	0.040
$H_g(3)$	88.03 (710)		0.003	0.001	0.013
$H_g(4)$	95.96 (774)		0.003	0.007	0.018
$H_g(5)$	136.26 (1099)		0.001		0.012
$H_g(6)$	154.98 (1250)		0.001		0.005
$H_g(7)$	177.05 (1428)		0.004		0.017
$H_g(8)$	195.28 (1575)		0.003		0.023

TABLE 3.2: **Partial electron-phonon coupling constants $\lambda_\nu/N(\epsilon_F)$ for solid C_{60} H_g modes.** Raman and neutron data are collected from solid C_{60} and A_3C_{60}, while photoemission data are relative to free C_{60} molecules. λ_ν is the electron-phonon coupling constant for the ν-th mode [160].

3.3 Electronic properties of K_3C_{60}

3.3.1 Band structure

The band structure of K_3C_{60} has been calculated through Density-Functional Theory (DFT) within the Local-Density Approximation (LDA) [194, 195].

The calculations were carried out by Erwin *et al.* for an *ordered* structure with the structural parameters reported in Ref. [162] and some fine details of the actual bands may not be captured. Nevertheless, by considering that the two different C_{60} orientations do not change the intermolecular nearest neighbor C_{60}-C_{60} distances and angles, it can be easily concluded that disorder does not affect intermolecular hopping that is the main player in determining the actual band structure [194, 195].

The resulting band structure and the associated density of states are shown in Fig. 3.3. A first inspection of the band structure is sufficient to appreciate the typical

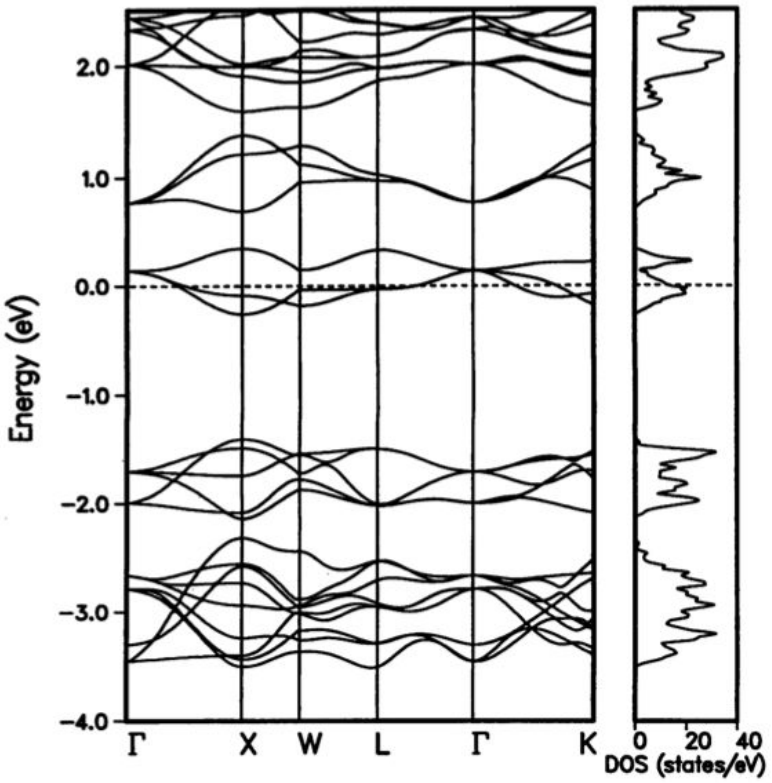

FIGURE 3.3: **Self-consistent electronic band structure and density of states (DOS) of $\mathbf{K_3C_{60}}$.** On the left panel is reported the self-consistent band structure for fcc K_3C_{60} in a ordered configuration (space group $Fm\bar{3}$). The Fermi energy is set as zero and crosses the t_{1u} orbitals. On the right panel is instead shown the corresponding DOS. From [194]. Reprinted with permission from AAAS.

signatures of the low energy electronic states of molecular solids, i.e. the bands are narrow (due to the large intermolecular separation) and slightly dispersing along the different reciprocal space direction (larger localization of the electronic states). The three bands at the Fermi energy (marked as zero) have t_{1u} symmetry and are half-filled by three electrons coming from the three surrounding K atoms, therefore the system is predicted to be metallic with a bandwidth $W = 0.5 - 0.6$ eV [194, 195]. This bandwidth corresponds to an hopping amplitude $t \sim 50$ meV[2] compatible with the large inter-cage C_{60}-C_{60} distance of 3.12 Å[3] and implies a substantial residence time of charge carriers on each C_{60} molecules.

A fundamental quantity that is obtained from this band structure is the density

[2]From the tight-binding expression $W = 2zt$, with z being the number of nearest neighbors.

[3]This distance is defined as the minimum C-C distance between carbon atoms belonging to two different molecules.

of states (DOS) at the Fermi level $N(\epsilon_F)$ and, as can be seen from the right panel of Fig. 3.3, it is found to be $N(\epsilon_F) = 13.2$ states/eV·cell (or equivalently 6.6 states/eV·spin). Other theoretical estimates are collected and compared in Ref. [160]. This value is in agreement with experimental data coming from Pauli paramagnetic susceptibility, NMR, and specific heat measurements (also on the parent compound Rb_3C_{60}) [196–201].
An important experimental proof of this band structure picture would be angle-resolved photoemission spectroscopy (ARPES), but the presence of orientational disorder and the small size of the Brillouin zone constitutes a serious obstacle to such measurements on A_3C_{60} compounds. Angle-integrated photoemission measurements on K_3C_{60} [202] showed an anomalously large bandwidth ($\sim$ 1.3 eV), and this has been explained in terms of combined many-body effects [160], while angle-resolved measurements on monolayer C_{60} on Ag(111) surfaces provided partial support to the validity of band structure calculations [160, 203]. Further support for the picture illustrated in this section comes from the implications of band structural details in the manifestation of the superconducting state, that will be analyzed in the following sections.

3.3.2 Correlation and metal-insulator transition in A_3C_{60}

In addition to the evaluation of the electronic bandwidth W, the estimate of Coulomb interactions in A_3C_{60} is essential for an accurate description and understanding of their experimentally observed behavior. In particular, the insulating nature of Cs_3C_{60} in presence of half filled t_{1u} bands [69] can be understood in terms of strong correlations, as introduced in Chapter 1.
We describe in this section an A_3C_{60} fcc lattice where each lattice site is occupied by a C_{60} molecule in terms of a three-band, 3D Hubbard model with effective interactions for the entire C_{60} molecule (U-onsite Coulomb repulsion, V-intersite Coulomb repulsion and W-bandwidth).
The onsite correlation U thus represents the repulsion associated to the addition of an electron on each C_{60} molecule and it has been evaluated both theoretically and experimentally. The U_0 energy scale of a free C_{60} molecule has been experimentally evaluated through the relation [204–206]

$$U_0 = I(C_{60}) - A(C_{60}) - E_g = (7.6 - 2.7 - 1.6)\,\text{eV} = 3.3\,\text{eV} \qquad (3.1)$$

where $I(C_{60})$ is the ionization potential of the C_{60} molecule, $A(C_{60})$ is its electronic affinity and E_g is the electronic band gap. Theoretical estimates gave instead values comprised between 2.7 and 3.0 eV [207–210].
When C_{60} molecules form a solid, U becomes strongly screened by the polarization of the surrounding molecules [160] and the effective U will be given with the screen contribution δU subtracted, i.e. $U = U_0 - \delta U$ [160]. Typical theoretical values obtained for the screened U range from 0.8 to 1.27 eV [160, 207, 209], while experiments of Auger spectroscopy on solid C_{60} and on K_6C_{60} gave respectively $U = (1.6 \pm 0.2)$ eV [211] and $U = (1.4 \pm 0.2)$ eV [212].
In addition to U, also the intersite Coulomb repulsion V can be estimated using the very same approach and theoretical values for V are estimated to be approximately 0.3 eV [207, 209].
It is worth to mention that recent theoretical work (based on maximally localized Wannier orbitals and constrained-random-phase approximation) on A_3C_{60} gave results in agreement with the aforementioned estimates [213].
When comparing these values to the bandwidth W, one gets an effective correlation strength $U/W \sim 1.5 - 3.0$, that positions these compounds on the verge of a Mott transition (see Fig. 1.2), with the K_3C_{60} and Rb_3C_{60} on the metallic side of the phase diagram and the Cs_3C_{60} on the insulating one[4] [70, 160, 191].

3.4 Strongly correlated superconductivity in K_3C_{60}

3.4.1 Phenomenology of the superconducting state in K_3C_{60}

One of the most relevant features of the A_3C_{60} family, perhaps the one that has attracted over the years the most of the scientific interest, is the presence of superconductivity (SC) to fairly high temperatures (between 20 and 40 K) [214–216].
In this thesis, we deal exclusively with K_3C_{60}, but we will often compare its properties with the other alkali-doped fullerides belonging to the A_3C_{60} class.
The main experimental results regarding the K_3C_{60} superconducting state are summarized in Fig. 3.4. In Fig. 3.4a we show the K_3C_{60} resistivity curve as a function of temperature as measured on a single crystal by Xiang *et al.* [217] and normalized to its value at 280 K. The superconducting temperature is 19.8 K

[4] At ambient pressure conditions.

and the superconducting transition appears very sharp with a width of less than 200 mK. The normal state resistivity is instead typical of a metal and shows a continuous increase up to 800 K without signs of saturation [218], in violation of the Ioffe-Regel-Mott criterion [160].

The zero resistivity state is an actual superconducting state and the second experimental fingerprint came from the magnetic susceptibility measurements shown in Fig. 3.4b [162]. Below 10 K the sample exhibits diamagnetism with a 100% diamagnetic fraction[5], thus signaling the perfect magnetic field expulsion typical of the Meissner-Ochsenfeld effect [219, 220].

As we will see, the mechanism of superconductivity in these compounds is not entirely clear and is still debated especially because of its proximity to the Mott-insulating ground state (present in Cs_3C_{60}), that closely resembles the cuprate phase diagram.

Experiments hitherto performed in order to clarify the microscopic mechanism for the A_3C_{60} pointed out the presence of isotope effect with respect to C substitution ($^{12}C \leftrightarrow ^{13}C$). In a conventional superconductor (described by the Bardeen-Cooper-Schrieffer theory) with a single ion type with mass M, the critical temperature is expected to scale as $T_c \sim M^{-\alpha}$ with $\alpha = 0.5$ [220]. The exponents found for an almost complete isotope substitution in K_3C_{60} and Rb_3C_{60} gave $\alpha = (0.30 \pm 0.06)$ and $\alpha = (0.30 \pm 0.05)$ respectively [224, 225], while incomplete substitution experiments have led to contradicting results (see Ref. [168] for a more detailed review). Alkali dopant substitution showed instead a lack of isotope effect within the experimental uncertainty [226–228].

These results suggest that A_3C_{60} compounds, including K_3C_{60}, belong to the broader class of BCS superconductors with a coupling mediated by intramolecular carbon modes, likely the H_g modes described in the previous section.

An essential measurement for a superconductor is the determination of the gap associated to the superconducting transition Δ, that can be accessed with several experimental techniques, like optical spectroscopy, NMR, tunneling spectroscopy or ARPES.

The reduced gap $2\Delta/k_BT_c$, as well as the temperature dependence of the gap itself $\Delta(T)$, can assess the strength of the coupling to the pairing modes. While in the BCS theory (weak coupling) $2\Delta/k_BT_c \approx 3.53$, in case of intermediate couplings this ratio can be larger than the BCS value and a logarithmic correction has to be

[5]Diamagnetic fraction expressed in terms of a niobium standard [162].

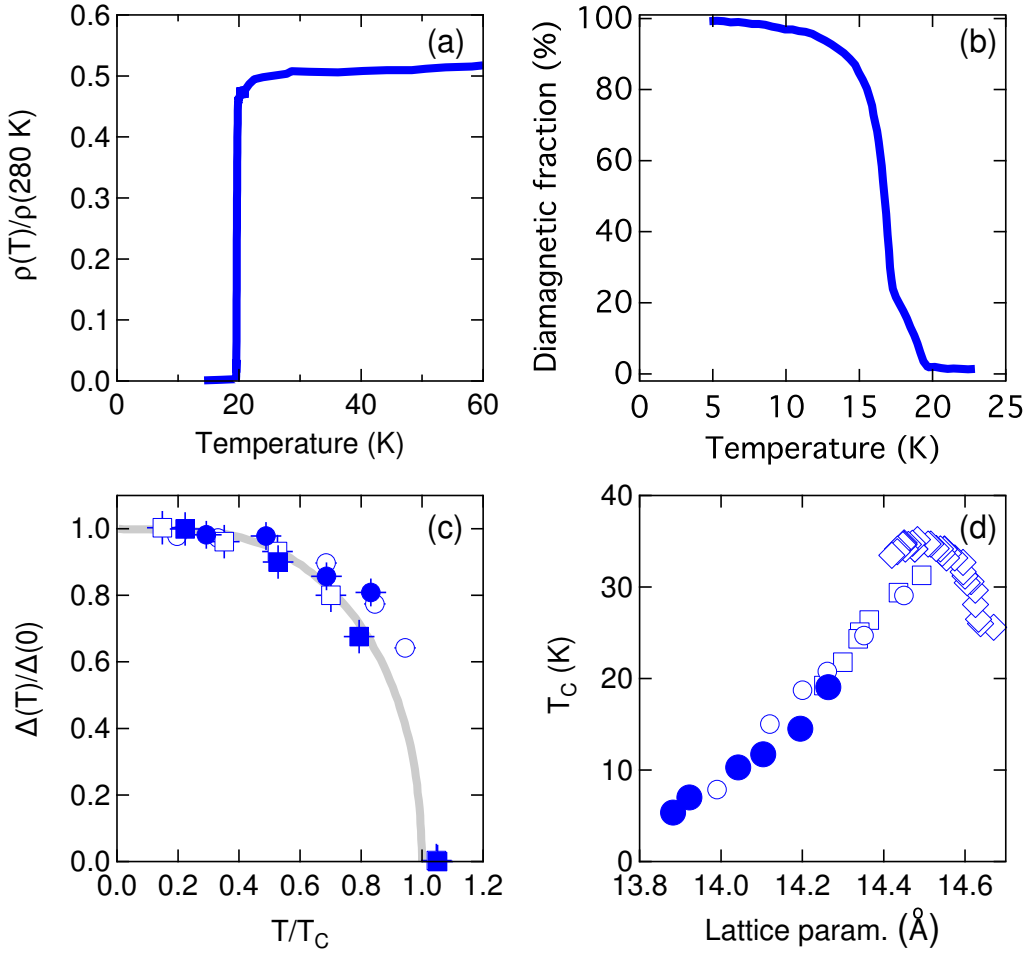

FIGURE 3.4: **Experimental hallmarks of the superconducting state in $\mathbf{K_3C_{60}}$.** Panel (a) shows the normalized DC resistivity for a single crystal of K_3C_{60} as a function of temperature (adapted from Ref. [217]). $\rho(280K) = 5$ mΩ cm. Panel (b) reports the diamagnetic shielding fraction against temperature for a powder sample of K_3C_{60} (adapted from Ref. [162]). Panel (c) shows the temperature dependent normalized superconducting gap $\Delta(T)/\Delta(0)$ for K_3C_{60} (filled symbols) and Rb_3C_{60} (empty symbols) as measured in optical spectroscopy (circles) and in tunneling experiments (squares) (data from Refs. [185, 221]). Panel (d) shows instead the T_c against the lattice parameter for K_3C_{60} (filled symbols), Rb_3C_{60} (empty circles), fcc Cs_3C_{60} (empty diamonds) and other A_3C_{60} compounds (empty squares) (data from Refs. [71, 222, 223]).

added [229]

$$\frac{2\Delta}{k_B T_c} = 3.53\left[1 + 12.5\left(\frac{k_B T_c}{\hbar\omega_{\ln}}\right)^2 \ln\left(\frac{\hbar\omega_{\ln}}{2k_B T_c}\right)\right] \tag{3.2}$$

where $\omega_{\ln}$ is the logarithmic average phonon frequency. Values for the reduced gap of K_3C_{60} and Rb_3C_{60} obtained with different techniques show different results ranging from the BCS value [185–187, 230] to substantially higher values like 4.2

(e.g. Ref. [188]) or even 5.3 [221], thus leading to a debated coupling strength to the carbon modes[6].

The second relevant information comes from the gap temperature behavior $\Delta(T)$, that in a pure BCS approach is determined by the relation [220]

$$\int_0^{\hbar\omega_D} \frac{\tanh \frac{1}{2}\beta\sqrt{\xi^2+\Delta(T)^2}}{\sqrt{\xi^2+\Delta(T)^2}} d\xi = \frac{1}{N(\epsilon_F)\mathcal{V}} \tag{3.3}$$

where $\hbar\omega_D$ is the Debye energy, $\mathcal{V}$ is the pairing interaction, $N(\epsilon_F)$ is the density of states at the Fermi level, $\beta = 1/k_BT$ and ξ is the electron energy with respect to the Fermi level.

This mean-field relation can be numerically evaluated and a comparison with the experimental values for Δ can tell whether a BCS-like description of the SC state applies or not. As visible in Fig. 3.4c, the measured gap (normalized to its $\Delta(0)$ value) as a function of temperature closely follows a mean-field (BCS) behavior where for low temperatures it shows a rather insensitive behavior to temperature ($\Delta(T) \sim \exp(-\Delta(0)/k_BT)$ [220]) while close to T_c it drops as $(1-T/T_c)^{1/2}$. This experimental trend has been reported both in tunneling [221] and optical spectroscopy [185–187, 230], despite their different observations for the reduced gap value, and represents a serious constraint for any theoretical model of the superconducting state in these compounds.

A last important fact concerns the behavior of T_c (and thus of the gap) as a function of the lattice parameter. The lattice parameter can be varied by chemical substitution of the alkali atoms or by applying external pressure.

The findings for several compounds belonging to the class A_3C_{60} (A=K, Rb, Cs) and only for fcc lattice arrangements are compared in Fig. 3.4d. The first important observation is that there is a strong correlation between the lattice parameter and the T_c, with a maximum and a dome feature at 14.5 Å [71, 222, 223]. Different compounds show a universal linear behavior below the maximum (with a slope of 50 K/Å), suggesting that the lattice parameter is a key player in the determination of the SC state and not the chemical species of the alkali dopant [222, 223]. Under the assumption that the pairing interaction is not affected by the lattice parameter d, one could partially explain the experimental findings in view of a simple BCS scenario, where $k_BT_c = 1.13\hbar\omega_D e^{-1/N(\epsilon_F)\mathcal{V}}$ [220]. The density of states should increase with d, let us say $N(\epsilon_F) \approx d$, and therefore T_c would be

[6]By carbon modes, we mean vibrational modes, both inter- and intra-molecular, that involve the vibration of C atoms only.

also bound to increase as $e^{-1/d\mathcal{V}}$. Eventually, this trend breaks and some other physical effect becomes dominant for very narrow bandwidths (expanded lattice constants). This consideration plays an important role in the debate about the microscopic explanation of the superconducting pairing in A_3C_{60} compounds.
Before closing this short review of the main properties of the K_3C_{60} superconductor we recall that this material belongs to type II superconductors ([168] and references therein) and we summarize its main properties in the following table together with the ones of Rb_3C_{60} for comparison [168]

Property	K_3C_{60}	Rb_3C_{60}
T_c	**19.5 K**	29.5 K
λ (μSR)	**4800 ± 200** Å	4200 Å
λ (optical)	**8000 ± 500** Å	8000 ± 500 Å
λ (NMR)	**6000** Å	4600 Å
ξ_0	**29 − 35** Å	30 Å
$\Delta C/T_c$	**64 ± 14** mJ/mol-K^2	75 ± 14 mJ/mol-K^2
$2\Delta/k_BT_c$ (NMR)	**3.0**	4.1
$2\Delta/k_BT_c$ (optical)	**3.44**	3.45, 4.1
$2\Delta/k_BT_c$ (μSR)		3.6 ± 0.3
$2\Delta/k_BT_c$ (tunneling)	**5.3 ± 0.2**	5.2 ± 0.3
$2\Delta/k_BT_c$ (tunneling)	4.3	

TABLE 3.3: **Superconducting parameters for K_3C_{60} and Rb_3C_{60}.** Superconducting parameters for K_3C_{60} and Rb_3C_{60}, as determined from tunneling, NMR, optical spectroscopy, specific heat and muon spin resonance (μSR) measurements [168]. λ indicates here the penetration depth, while ξ_0 stands for the coherence length parameter.

3.4.2 Optical signatures of the superconducting state in K_3C_{60}

In Chap. 5 we will study the nonequilibrium dynamics of K_3C_{60} by means of time-resolved THz spectroscopy, therefore we devote a special attention to the optical signatures of superconductivity in this compound. Optical studies on A_3C_{60} have been performed both on single crystals and on pressed powder pellets [185–187, 230–232], leading to similar results in the midinfrared and far-infrared range. Reflectivity measurements provided by Prof. L. Degiorgi for K_3C_{60} single crystals above and below T_c are shown in Fig. 3.5. The normal state curve (red) has a clear metallic shape with a plasma edge located at approximately 700 meV (Fig. 3.5a), while below T_c the reflectivity is enhanced below a threshold energy of 6 meV (Fig.

3.5b) [185–187, 230]. Below this energy the reflectivity reaches unity, as expected in the case of a BCS superconductor well below its transition temperature [220].

From a Kramers-Kronig analysis of the reflectivity data the full optical response

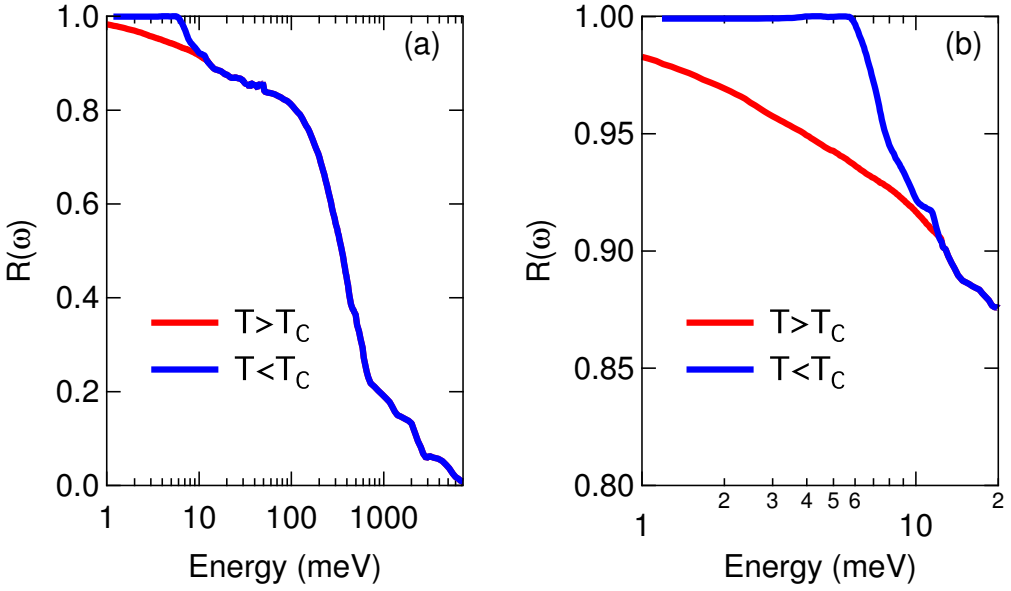

FIGURE 3.5: **K_3C_{60} equilibrium reflectivity in normal and superconducting state**. Panel (a) shows the broadband absolute reflectivity of K_3C_{60} above and below T_c (red and blue curves respectively). Panel (b) shows instead a zoom of Panel (a) in the far-infrared region. Data below T_c are at a temperature between 5 and 10 K while the others are measured a few degrees above T_c (between 20 and 25 K). These data have been kindly provided by Prof. L. Degiorgi and are in agreement with Refs. [185–187, 230].

has been determined and the obtained complex optical conductivity $\hat{\sigma}(\omega)$ is reported in Fig. 3.6 (data kindly provided by Prof. L. Degiorgi). The real part of the conductivity $\sigma_1(\omega)$ in the normal state (3.6a, red curve) exhibits a Drude peak that at zero frequency extrapolates to a value compatible with resistivity measurements discussed in the previous section. Additional absorptions are observed at approximately 496 meV, 2230 meV and 4340 meV and are attributed to interband transitions involving s and p carbon orbitals and s, p, and d alkali orbitals [185, 187]. The Drude contribution has not a simple Lorentzian shape and presents an additional absorption located at approximately 60-100 meV, whose origin is not well understood, that has been ascribed to electron-electron interactions, polaronic effects, pseudogap or charged phonon effects (for a detailed discussion see [185] and references therein).

The far-infrared part of this optical conductivity has been analyzed through a simple Drude-Lorentz approach where the complex dielectric constant is determined

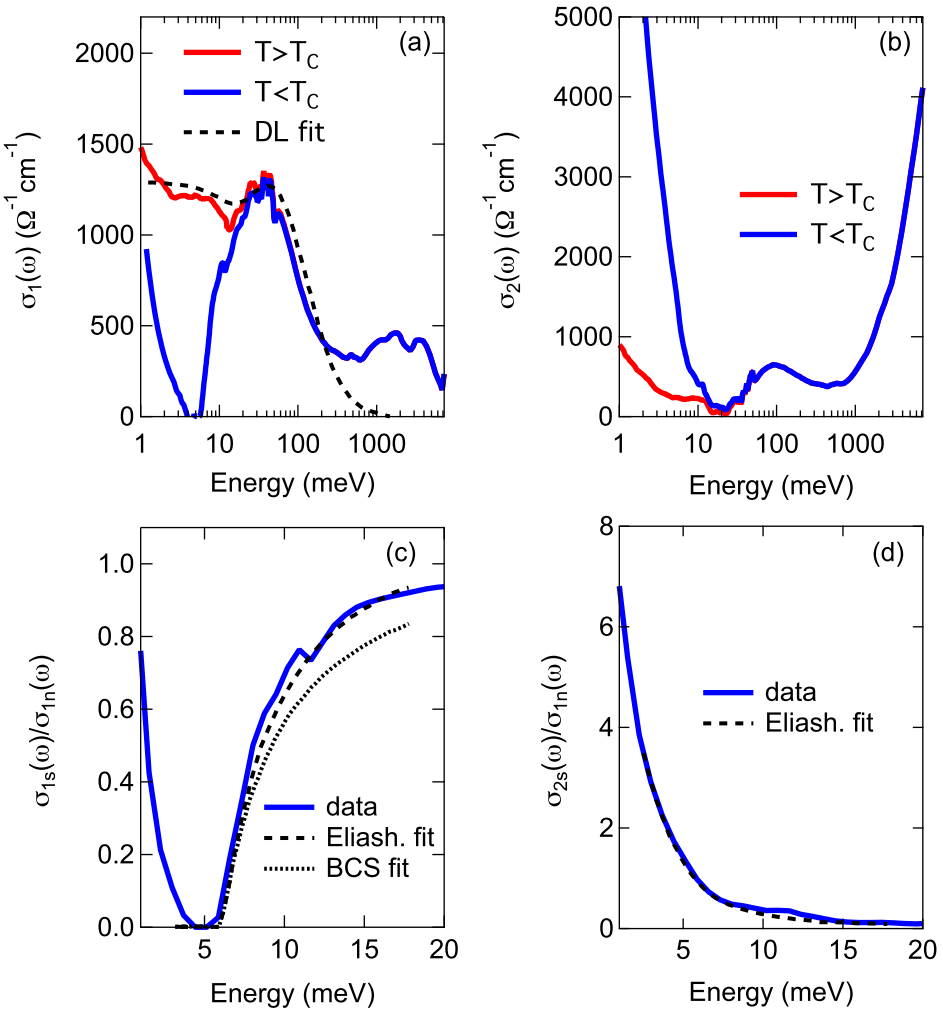

FIGURE 3.6: **K_3C_{60} equilibrium optical conductivity in normal and superconducting state**. Panel (a) and Panel (b) show, respectively, the real and imaginary part of the optical conductivity of K_3C_{60} above (red curve) and below (blue curve) the superconducting transition temperature T_c. A fit to the normal state $\sigma_1(\omega)$ with a Drude-Lorentz (DL) model is shown. Panel (c) and (d) show the ratios σ_{1s}/σ_{1n} and σ_{2s}/σ_{1n} respectively. Data below T_c are at a temperature between 5 and 10 K while the others are measured a few degrees above T_c (between 20 and 25 K). Fits to the ratio with a Mattis-Bardeen (BCS) approach and an Eliashberg response are shown for comparison. These data and the fits have been kindly provided by Prof. L. Degiorgi and are in agreement with Refs. [185–187, 230].

by free electrons belonging to the Drude and a fraction f_G of electrons associated to low-energy absorption [185]

$$\epsilon(\omega) = \epsilon_\infty + \omega_p^2 \left[\frac{f_G}{\omega_G^2 - \omega^2 - i\omega\gamma_G} - \frac{1 - f_G}{\omega(\omega + i\gamma_D)} \right]. \tag{3.4}$$

In this expression, ϵ_∞ describes the high-frequency contributions to the dielectric function, while the first and second term in brackets describe, respectively, the midinfrared absorption and the Drude part of the optical response [185]. From a simple counting, the number of carriers for K_3C_{60} is $4 \cdot 10^{21}$ carriers/cm^3 and a fraction of 87.8% of them contributes to the midinfrared oscillator. Only the remnant 12.2 % responds as Drude free carriers [185]. From a fit to the data, it was estimated that $\epsilon_\infty = 5$ and the midinfrared band has a plasma frequency ω_G of 55 meV and a damping Γ_G of 150 meV [185]. The Drude peak has instead a damping Γ_D of 18.23 meV and the overall plasma frequency associated to these low energy electrons is 1177 meV.

Below T_c, already at temperatures below 10 K, the gap fully opens and the sample becomes superconducting. All the spectral weight associated to the Drude electrons collapses in a δ function associated to the supercurrents, as expected in a BCS superconductor [220], but for finite temperatures there is still trace of thermally activated transport that contributes to $\sigma_1(\omega)$ as an in-gap absorption below 6 meV [185–187, 230]. Importantly, the imaginary part of the optical conductivity, $\sigma_2(\omega)$ also shows dramatic changes when crossing the transition temperature.

In Fig. 3.6b, we show $\sigma_2(\omega)$ in the normal and superconducting state. Below the transition temperature, $\sigma_2(\omega)$ becomes divergent in the DC limit, i.e. the electrodynamical response of the superconductor is entirely inductive, while negligible changes occurs for energies much higher than the gap energy.

The electrodynamic response of K_3C_{60} closely follow the behavior predicted by Mattis and Bardeen for a BCS superconductor [233] and this behavior becomes evident when looking at the ratios σ_{1s}/σ_{1n} and σ_{2s}/σ_{1n}. In a pure BCS system these ratio are determined by the coherence factors and by the non-local relationship between the vector potential of the external field and the induced supercurrents. The ratio of σ_{1s}/σ_{1n} (Fig. 3.6) is suppressed below twice the gap value, because there is no absorption until the incident photons have enough energy to break the Cooper pairs. Nevertheless, at very low energy (below 6 meV) one can observe spectral content associated to thermally excited quasiparticles that partially recover the Drude structure of the normal state (with a narrower linewidth). Above

the threshold value 2Δ, it smoothly increases to unity but in a steeper way than what predicted in the BCS case where $\sigma_{1s}(\omega)/\sigma_{1n} \propto 1-(\hbar\omega/k_BT_c)^{-1.65}$ [233, 234]. This discrepancy led to the conclusion that an Eliashberg description of the pairing interaction with the intramolecular modes [235] may be more appropriate for K_3C_{60} and other members of the A_3C_{60} family [185, 187]. On the other hand, the ratio σ_{2s}/σ_{1n} nicely follows the limiting trend for $T \ll T_c$ of the Mattis-Bardeen relation $\sigma_{2s}/\sigma_{1n} \propto \pi\Delta/\hbar\omega$ [233].
These optical spectroscopy observations strongly support the view that K_3C_{60} is a BCS-like singlet superconductor, probably in the weak coupling limit, where the pairing mechanism involves high-energy intramolecular vibrations but with a normal state different from a conventional metal [185].

3.4.3 Relevance of correlations in the superconducting dynamics

In conventional superconductors the pairing between electrons forming a Cooper pair stems from a weakly attractive interaction involving electron-phonon coupling (BCS) [160, 236].
An electron propagating through the lattice attracts the surrounding nuclei and, since the nuclear motion is typically much slower than the electronic one, a second electron passing across the same path will find the lattice distorted by the first electron polarization. This second electron will transit when the first will be already far away, but on a timescale shorter than the time needed to the atoms to return at their equilibrium positions. The resulting interaction between the two electrons is weakly attractive and retarded [160].
The retardation of the weak interaction is crucial for the establishment of a superconducting state because it makes possible for the phonon-induced attraction to win over the much stronger Coulomb repulsion by allowing interaction while the electrons are well separated in space. An indicator of retardation effects relevance is the ratio between the Debye temperature Θ_D, quantifying the lattice motion time scale, and the Fermi energy ϵ_F, related to the time scale of the electronic motion [160]. In a conventional metal $\Theta_D/\epsilon_F \sim 10^{-3}-10^{-2}$ [160], thus indicating that the electronic motion is several orders of magnitude faster than the lattice one and the retardation mechanism is efficient. In alkali fullerides, we have seen that the Jahn-Teller H_g *intra*molecular modes, associated to the superconducting

pairing, have a $\Theta_D = 200$ meV, while ϵ_F (from the bottom of the band) is approximately $\epsilon_F = 300$ meV [160], therefore $\Theta_D/\epsilon_F = 0.7$ and retardation effects are expected to be much smaller than in conventional superconductors [160]. In addition, due to the narrowband molecular nature of these solids, the electrons often sit onto the very same molecule, and they cannot easily avoid each other even with retardation [160].

Since electronic correlations in these compounds are rather large $U \approx 1.0 - 1.5$ eV, a very important question arose on how superconducting pairing is possible when conditions of negligible retardation and strong onsite repulsion are present. More generally, A_3C_{60} compounds represent a fundamental benchmark for the investigation of the coexistence and interplay of superconductivity and strong correlations, and during the last two decades a number of theoretical works focused on this physics [180, 184, 189–193, 237–239].

While in a conventional superconductor electronic correlations are believed to be detrimental to the onset of a superconducting state, the presence of high transition temperatures in A_3C_{60} testifies that there has to be either a mechanism other than retardation that allows the pairing interaction to screen correlations [160, 190, 240] or electron-electron interactions acting directly on the superconductivity in a different fashion than in BCS systems [189, 191].

It has been recognized that a complete description of the A_3C_{60} needed a simultaneous treatment of both electron-phonon and electron-electron interactions [160, 190].

Han and coworkers [190] investigated this problem with DMFT and they explained the existence of high temperature superconductivity in A_3C_{60} thanks to a local pairing mechanism mediated by the onsite Jahn-Teller H_g modes. They calculated the transition temperature for the case of a nondegenerate electronic state (a) coupled to a nondegenerate non-Jahn-Teller phonon (A) and in the case of the threefold degenerate t_{1u} orbitals strongly coupled to Jahn-Teller H_g modes. Their findings are summarized in Fig. 3.7 and it is found that t_{1u} electron coupled by H_g modes are substantially more resilient to an increase of the effective correlation than in a conventional BCS scenario. The conclusion reached in Ref. [190] is that superconductivity in A_3C_{60} is possible thanks to an alternative coupling mechanism, the so called local pairing, that reduces the effects of the Coulomb repulsion and can overcome the lack of retardation effects. As an experimental corroboration of the local pairing picture, these authors indicate the relatively short coherence length $\xi_0 \sim 30$ Å that spans only a couple unit cells and up to

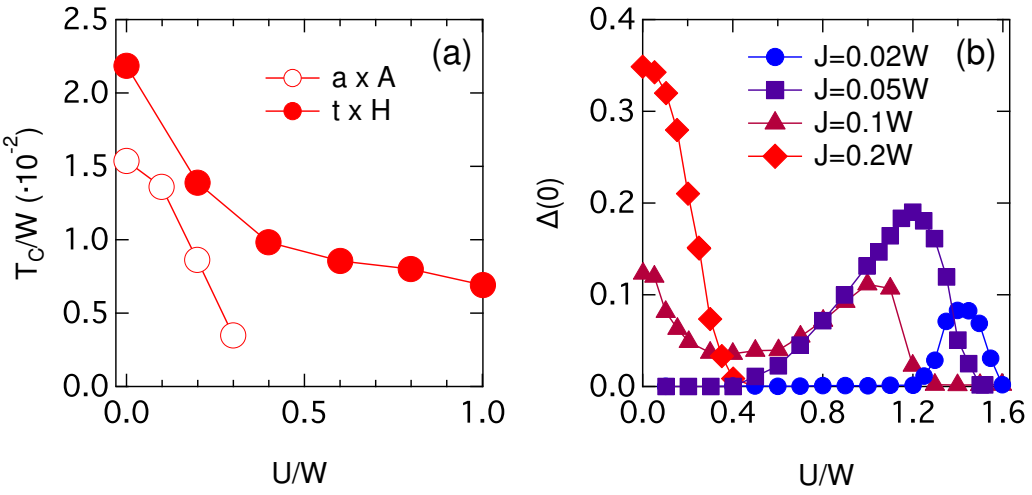

FIGURE 3.7: **DMFT investigation of the superconducting pairing in $\mathbf{A_3C_{60}}$.** Panel (a) shows T_c as a function of U/W for $t \times H$ and $a \times A$ models at half filling from DMFT calculations. The el-ph coupling is $\lambda = 0.6$ and $\hbar\omega_{ph}/W = 0.25$ (data from Ref. [190]). Panel (b) shows instead the anomalous part of the quasiparticle self-energy $\Delta(0)$ (proportional to the SC gap through a factor Z^{-1}) for different effective Jahn Teller couplings (data from Ref. [191]).

three neighboring C_{60} molecules [190].

A novel, alternative view on this problem is instead the one proposed by Capone and coworkers, that led to a scenario referred as "strongly correlated superconductivity" [189, 191].

In this framework, correlations are not necessarily depleting the superconducting state but can, instead, enhance it under certain conditions, especially in proximity of a Mott transition.

The core phenomenon at the basis of this view is the renormalization with U/W of the effective bandwidth and of the effective mass, both controlled by the quasiparticle weight Z (see Appendix E) [191]. If we consider the well know BCS relation $k_BT_c = 1.13\hbar\omega_D e^{-1/N(\epsilon_F)V}$, in proximity of the Mott transition the bandwidth W is renormalized as $W^* = ZW$ and $N(\epsilon_F)$ gets enhanced as $N^*(\epsilon_F) = N(\epsilon_F)/Z$ with $Z \ll 1$ [189, 191]. The enhancement of T_c is then possible because the Jahn-Teller phonon interaction of the fullerides preserves the pairing interaction $\mathcal{V}$ unaffected by U/W and therefore $k_BT_c \sim e^{-Z(U/W)/N(\epsilon_F)\mathcal{V}}$[7].

Importantly, it has been pointed out that a correct description of the superconducting state in A_3C_{60} has to take into account also a partial cancellation of the

[7] In a Migdal-Eliashberg framework, the decrease of Z does not translate into an increase of T_c because the pairing interaction $\mathcal{V}$ is also renormalized as $\mathcal{V}^* = Z^2\mathcal{V}$. T_c goes, then, as $k_BT_c \sim e^{-1/Z(U/W)N(\epsilon_F)\mathcal{V}}$ and is suppressed by the increased degree of correlation [189].

Jahn-Teller electron-phonon coupling due to exchange interaction associated to the Hund's rule.

The Jahn-Teller interaction (J_{JT}) splits the t_{1u} orbital degeneracy and favors low spin states, while Hund's exchange term (J_H) stabilizes molecular states with the highest total spin state and the highest total angular momentum [191]. Estimates for these energy scales give $J_H = 0.03 - 0.1$ eV [210, 241], while $J_{JT} = 0.06 - 0.12$ eV [174, 237, 241–243], therefore the Jahn-Teller coupling is almost completely cancelled and only narrowly prevails over the Hund's exchange [191]. The net effect of this cancellation is that electron-phonon coupling through the Jahn-Teller modes is effectively reduced and the overall JT energy scale is $J = J_{JT} - J_H$.

In Fig. 3.7b are reported the anomalous quasiparticle self-energies $\Delta(0)$ (related to the superconducting gap by a factor Z^{-1}) calculated in Ref. [191] for several values of the screened JT coupling. For incomplete cancellation ($J = 0.1$ and 0.2 W) the superconducting state behave consistent with Ref. [190] at low U/W. The superconducting state is BCS and at low U/W is suppressed by correlations. As the Jahn-Teller cancellation increases (thus leading to a smaller el-ph coupling) and at higher effective correlations, there is a second superconducting pocket appearing, the strongly correlated superconductor. The BCS state at $U = 0$ vanishes instead [191]. According to Refs. [189, 191], this is the state that best describes the phenomenology of the superconducting state in A_3C_{60}.

3.5 Nonequilibrium states and photoinduced dynamics in K_3C_{60}

As seen in the previous sections, the ground state of A_3C_{60} is governed by a balance of diverse electronic interactions and the proximity of the superconducting state to a Mott transition makes them a unique system for the study of possible new physics arising from this overlap. Nonequilibrium studies, like pump-probe spectroscopy, can naturally contribute to the elucidation of the superconductivity mechanism in alkali-fullerides, because of their particular sensitivity to electron-phonon coupling, but more importantly strong excitations can help accessing highly nonlinear regimes or hidden phases that cannot be studied within normal equilibrium spectroscopy.

To the best of our knowledge, there is a limited number of optical studies concerning the dynamics of photoexcited states in A_3C_{60} and all associated to moderate

excitation regimes (with pump fluences of the order of a few μJ/cm^2). in this paragraph we briefly review the main results obtained from nonequilibrium optical studies of K_3C_{60} and connect them to the equilibrium observation reported earlier in the chapter.

Among the different members of the A_3C_{60} family, only K_3C_{60} and Rb_3C_{60} have been characterized by means of ultrafast optical studies [244, 245]. The more recently synthetized compound Cs_3C_{60}, instead, still lacks investigations of its electrodynamics on ultrafast timescales.

A first work by Fleischer *et al.* [246] focused on the transient response of K_3C_{60} and Rb_3C_{60} films when compared to pure C_{60} films. It has been found that after photoexcitation with 1.98 eV light (50 fs, 100 MHz) and for moderate fluences up to 20 μJ/cm^2 the transient reflectivity ΔR/R at the same energy of K_3C_{60} and Rb_3C_{60} has an exponential decay with a constant of 0.14 ps, while pure C_{60} films decay with a non-exponential decay law and a characteristic lifetime of 30 to 40 ps [246]. This important difference in the electronic response is attributed to the band-like, metallic character of K_3C_{60} and Rb_3C_{60} that relaxes the selection rules associated to the optical absorption between HOMO and LUMO states of pure C_{60} and allows a more efficient recombination of the photoinjected quasiparticles.

A second extended work mapped instead the temperature dependence of the photoinduced nonequilibrium state in the two metallic compounds [245]. The experimental differential reflectivity curves for K_3C_{60} at different temperatures are shown in Fig. 3.8a. In this case the pump and probe energies were 1.60 eV and 0.62 eV, respectively, while the pump fluence was kept below 1 μJ/cm^2 [8][245]. The observed transient reflectivity changes follow a double exponential decay, with a fast time constant τ_1 of approximately 1 ps associated to electron-phonon mediated relaxation and a slow decay time τ_2 of the order of several ps, present only below the critical temperature and thus related to the Cooper pair recombination from the excited quasiparticles [245]. The key finding of this work is related to the latter time constant that increases as the temperature is decreased while in a conventional BCS scenario it should go as $\tau_2 \approx \Delta(0)/\Delta(T)$, with Δ being the superconducting gap [245]. According to this relation, the time constant should diverge at the transition temperature and approach a finite value at very low temperatures, while Fleischer and coworkers find instead an opposite monotonic trend, thus suggesting a non-trivial BCS ground state in these compounds.

An additional, different experiment by Fleischer *et al.* [244] observed coher-

[8] Also in this case the repeetition rate was 83 MHz [245].

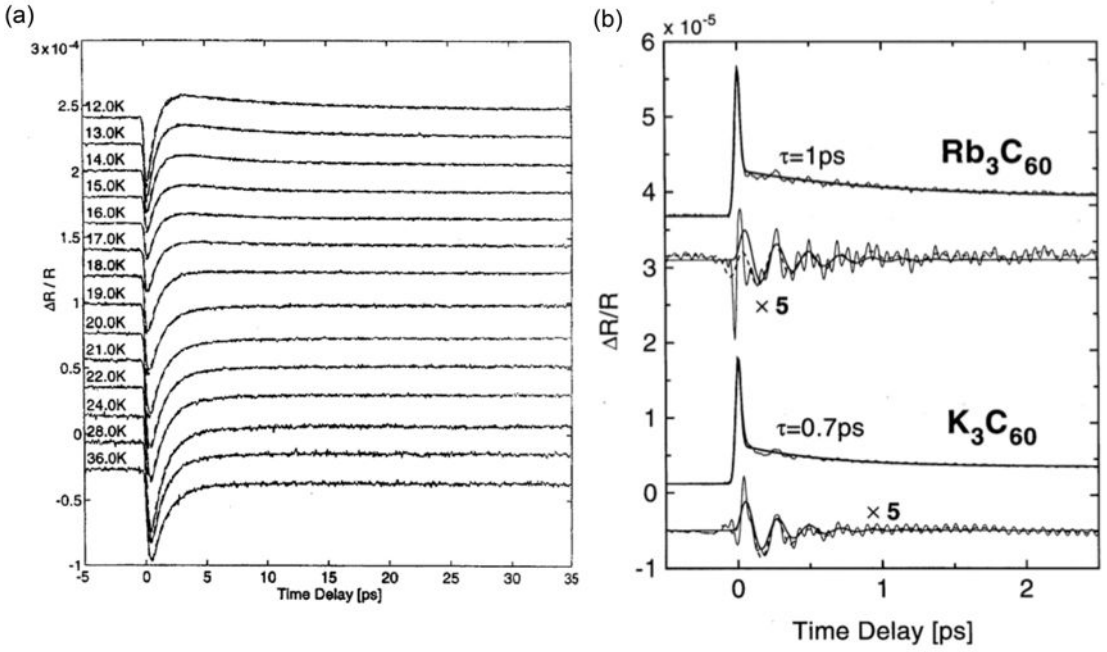

FIGURE 3.8: **Nonequilibrium reflectivity changes and coherent phonon generation in K_3C_{60}.** Panel (a) reports transient reflectivity changes $\Delta R(t)/R$ in K_3C_{60} for temperatures above and below T_c. Reprinted figure with permission from [245]. Copyright © 2000 by the American Physical Society. Panel (b) shows instead room temperature coherent phonon oscillations on top of the transient reflectivity change of K_3C_{60} and Rb_3C_{60} after excitation with 10 fs pump pulses. Below each curve is reported the oscillatory contribution once subtracted the exponential decay. Reprinted with permission from [244]. Copyright © 1997, AIP Publishing LLC.

ent phonons generation following the pump beam arrival. By photoexciting both K_3C_{60} and Rb_3C_{60} at ambient conditions with 10 fs pulses (1.55 eV energy, 38 MHz rep. rate) it was possible to coherently generate Raman phonons that can be observed as periodic modulations on top of the transient reflectivity change. The data associated to this experiment are reported in Fig. 3.8b and it was possible to detect two Raman modes, one $A_g(1)$ molecular vibration ($\hbar\omega_{A_g(1)}$=61.062±0.031 meV) and a second mode at 18 (±4) meV with a dephasing time of 0.25 ps [244]. This second mode has not been detected in previous Raman experiments, probably because of its broad linewidth, and could possibly be related to C_{60}-alkali ion motion [244].

Up to now little is known about the electronic dynamics of these compounds in conditions of strong excitation (mJ/cm^2 regime) and for energies closer to the mid-infrared and THz region where the most of the relevant electrodynamics changes take place. Time-resolved studies either with far-infrared or Raman spectroscopy could therefore prove extremely relevant for the understanding and the control of

these fascinating superconductors.

3.6 Summary

In this chapter we introduced the organic superconductor K_3C_{60}, a three dimensional metal belonging to the well studied family of the alkali fullerides, that in equilibrium conditions shows a sharp BCS-like superconducting transition with a T_c ≈20 K. We first described the fcc lattice of C_{60} molecules where alkali atom intercalation plays an essential role in both doping the fullerene molecules and in acting as intermolecular spacers that contribute to a band narrowing at the Fermi level.

After the structure, we discussed the vibrational properties in connection to the superconducting state, with a particular attention to the Raman active intramolecular vibrations with H_g symmetry that are believed to be relevant for the pairing interaction in these systems. Band structure calculations from literature [194] have been discussed in connection with the determination of the onsite correlation energy on each C_{60} molecule. From both experimental and theoretical work it emerged that A_3C_{60} (A=K, Rb, Cs) are strongly correlated compounds at the verge of a Mott transition.

The core of the chapter has been instead devoted to the discussion of the superconducting transition, that attracted a great attention in the scientific community in the last years. If on one hand, the magnitude of the gap, the diamagnetic response of the superconducting phase, and the isotope effect with C atom substitution point towards a BCS-like scenario for the superconducting pairing, the presence of correlations and the high energy molecular vibrations that should mediate the pairing point toward a non-conventional nature of the superconducting state [189, 190], either locally paired or even correlation-assisted. We discussed in detail the optical signatures of the superconducting transition that is extremely clear in the THz region and that surprisingly follows a rather conventional behavior.

All these features (high-energy molecular vibrations, clear spectroscopic signatures of the superconducting transition, a correlated ground state) make K_3C_{60} an appealing system for the manipulation of the superconducting transition with light, through the resonant phonon excitation technique. Our experimental goal is to control the superconducting state, possibly leading to an enhancement of

the coupling and therefore of T_c, by selectively exciting with strong midinfrared fields the IR active T_{1u} intramolecular vibrations that can potentially couple to the H_g modes involved in the pairing. We will then monitor with delayed THz pulses the low energy electrodynamic response of the photoexcited state in order to assess the transient changes induced by the pump pulse both in the normal and superconducting state.

Chapter 4

Nonequilibrium dynamics of the ET-F_2TCNQ under pressure

In this chapter, we describe an experiment of pressure tuning of the holon-doublon lifetimes in a one-dimensional organic Mott insulator after a photoexcitation of the Mott gap. In the first part, the measured equilibrium optical properties of the ET-F_2TCNQ, both in ambient and high pressure conditions, are presented and fitted with the analytical optical response of an extended Hubbard model to obtain the relevant effective interactions energies (onsite Coulomb repulsion U, intersite Coulomb repulsion V, hopping amplitude t) and determine their pressure dependence. The second part of the chapter, reports the measurement of holon-doublon recombination times by means of a pump-probe experiment with variable external pressure. The last part compares, finally, the experimental pressure-dependence of the relaxation times (mapped onto the absolute changes of the effective correlation $(U-V)/t$ with a numerical simulation that unveils the relevance of tunneling between bound and unbound holon-doublon configurations in determining the observed dynamics.
This chapter is based on original experimental work reported in [247].

4.1 Nonequilibrium quasiparticle recombination in metals and semiconductors

A well established framework for the rationalization of hot carrier dynamics in solids, and more appropriately for metals, with a negligible degree of correlation is the so called "Two-Temperature" model for the electronic thermal relaxation [248, 249].
The core concept of this powerful theoretical model is that with respect to an ultrafast stimulus the electrons and the lattice of a metal can be treated as separate subsystems with their own heat capacity C and only coupled by the electron-phonon interaction in the spirit of a pure Born-Oppenheimer approximation [250]. After the absorption of a femtosecond pulse the electrons are instantaneously thermalized at a temperature T_e much higher than the lattice one T_L[1]. They can subsequently dissipate energy into the lattice itself thanks to the electron-phonon coupling and thus through phonon emission. If the lattice heat capacity C_L is much higher than the electronic heat capacity C_e, it will represent an efficient dissipative bath and the electronic temperature will equilibrate according to the following rate equation [249, 251]

$$\frac{dT_e}{d\tau} = -\frac{g}{C_e}(T_e - T_L) \tag{4.1}$$

where τ is the time delay after the light pulse arrival and g is the coupling constant between the electrons and the lattice.
The coupling constant can be explicitly written in terms of basic quantities where the material dependence enters only through the electron phonon coupling constant $\lambda\langle\omega^2\rangle$ [249]

$$\gamma = \frac{g}{C_e} = \frac{3\hbar\lambda\langle\omega^2\rangle}{\pi k_B T_e} \tag{4.2}$$

thus, a measurement of the relaxation rate can be used as a precise measurement of the electron-phonon coupling in a metal [251–253].
We now propose a different and complementary view of the relaxation rate description since we are interested in determining how the electronic dynamics is controlled by *purely electronic* properties like the bandwidth W. In a one-dimensional chain with lattice spacing a and hopping amplitude t, within the tight binding approximation the electronic dispersion $\epsilon(k)$ is given by $\epsilon(k) = -2t\cos(ka)$ and has

[1] We assume to be at temperatures much lower than the Debye one.

a bandwidth $W = 4t$. Since the heat capacity of an electron gas is proportional to the density of states at the Fermi level ϵ_F [97] and the density of states of this linear chain is given by [97, 254]

$$N(\epsilon) = \frac{1}{2\pi}\frac{4}{|d\epsilon(k)/dk|} = \frac{1}{2\pi}\frac{4}{|2t\sin(ka)|} \tag{4.3}$$

At half filling condition the Fermi level will be located at $k = \pi/2a$, therefore the heat capacity will go as

$$C_e \sim N(\epsilon_F) = \frac{1}{\pi}\frac{1}{t} \tag{4.4}$$

and the relaxation rate (or the decay time $\tau_d = 1/\gamma$) as

$$\gamma = \frac{1}{\tau_d} \sim \frac{1}{C_e} \sim t. \tag{4.5}$$

This relation tells us that a larger bandwidth W allows for a more efficient and faster thermalization of the photoexcited electrons and the decay time is expected to go as the reciprocal of the electronic hopping amplitude.

In the case of semiconductors, the recombination dynamics of electron and holes is different than in metals and can occur through diverse paths, each characterized by its own transition rate. Excited states can indeed decay by emitting a photon, a phonon or by exciting another electron (hole) in the band. The first case is commonly referred to as *radiative recombination*, while the other cases belong to the broader class of *nonradiative transitions* [255, 256].

For simplicity, we consider the case of an intrinsic semiconductor (with equal number of electrons and holes) where electrons can recombine with any hole, thus implying that the k-selection rule does not strictly hold [255].

In the case of radiative recombination it can be shown that the recombination rate R goes with the density of electrons (n) and holes (p) [255, 256]

$$R = Anp \simeq An^2, \tag{4.6}$$

where A is a constant. Since the rate R is also defined as $dn/d\tau = -R$, one can define a radiative lifetime τ_r such that the rate equation reduces to the one associated to an exponential process [255, 256]

$$\frac{dn}{d\tau} = -\frac{n}{\tau_r}, \tag{4.7}$$

with $\tau_r = (An)^{-1}$.
The density of carriers is proportional to the density of states of each band [97], and in the case of the electrons in conduction band (c) the temperature dependent density can be written as

$$n(T) = \int_{\epsilon_c}^{\infty} d\epsilon N_c(\epsilon) \frac{1}{e^{(\epsilon-\mu)/k_B T} + 1}, \tag{4.8}$$

and, as seen in the case of metals, in 1D $N_c(\epsilon) \propto 1/t$. This implies that in a one-dimensional semiconductor the radiative recombination is expected to slow down with increasing t like $\tau_r \propto t$. If the recombination occurs through a nonradiative mechanism (like trap-assisted or Auger recombination) the rate equation has to be adapted to the dominant relaxation mechanism. In the important case of the Auger recombination, where electron and hole recombine by transferring the energy to another electron (hole) in the band, the rate equation describes this three-body interaction as $dn/d\tau = -R = -Bnpn = -Bn^3$ (B is a suitable constant) [255]. Having defined the nonradiative lifetime associated to the Auger decay in the same fashion as for the radiative case, one gets a lifetime $\tau_{nr} = (Bn^2)^{-1}$ and therefore a $\tau_{nr} \propto t^2$ [255].
Also in the nonradiative case, a one-dimensional semiconductor is expected to have a slower decay with increased bandwidth but with a quadratic dependence in the hopping parameter.
The dynamics of quasiparticle recombination in Mott insulators is, instead, expected to depend also on the correlation strength among electrons and, so far, direct measurements in solid state materials are, to the best of our knowledge, lacking. In this chapter we try to address the problem of hot carriers recombination in Mott insulators driven across an ultrafast insulator-to-metal transition and elucidate the connection between the experimentally observed lifetimes of photoexcited state and the effective correlations of the ground state.

4.2 Equilibrium optical properties at ambient conditions

In Chap. 2, we already introduced the one-dimensional electronic character of the ET-F_2TCNQ and a crucial aspect of our experiments is the accurate knowledge of the degree of correlation of its ground state, needed to gauge the nonequilibrium

dynamics experiments. Optical spectroscopy is an ideal tool for the measurement of correlation in solids (see Appendix E) and here we exploit equilibrium infrared spectroscopy to quantitatively assess the correlated nature of this compound.

In Fig. 4.1 we report the optical properties of the ET-F_2TCNQ along the a-axis, corresponding to the in-chain direction. The optical properties are measured with the same instrumentation described in Appendix A.3, but in this case the sample is in contact with air and the reference for the infrared measurement has been taken with a gold mirror. The optical conductivity has been extracted through standard Kramers-Kronig transformations (see Appendix B) by following the high energy extrapolations suggested in Ref. [257]. Our ambient pressure results are overall consistent with previous optical studies reported in literature [10, 38, 49, 137]. Both the reflectivity $R(\omega)$ (Fig. 4.1a) and the optical conductivity $\sigma_1(\omega)$ (Fig. 4.1b) are showing a typical insulating behavior. The reflectivity goes as a constant (approximately 0.15) at low energy and the optical conductivity is gapped with a prominent sharp peak at 700 meV. The gap energy, in this case is dictated by the energy scale of the charge transfer between neighboring π orbitals [82], while the in-gap conductivity follows approximately an ω^2 behavior and extrapolates to a negligible DC value consistent with transport measurements [137].

At higher energies (around 3-4 eV) the infrared spectra show instead resonances associated with intramolecular excitations that introduce a marginal tail in the sub-eV spectra [10, 49]. The detailed analysis of intramolecular dynamics is beyond the scope of our work and these contributions are subtracted from the $\sigma_1(\omega)$ for the purpose of our analyses.

The peak in $\sigma_1(\omega)$ is associated with the electronic hopping between nearest neighboring ET molecules (ET^+,ET^+ $\rightarrow$$ET^{2+}ET^0$), that, due to the correlated nature of this compound, represents a proper transition from the lower to upper Hubbard band [137] and can be also referred as charge transfer (CT) resonance [10, 49].

Interestingly, this resonance is both very sharp ($\sim$ 100 meV) and not simply described by a single Lorentzian oscillator (in agreement with previous findings [10, 49]). These features point towards a non trivial nature of the Mott gap of the ET-F_2TCNQ and we therefore employed a different analysis protocol (with respect to a conventional Lorentz oscillator model approach [234]) to better understand the properties of this ground state.

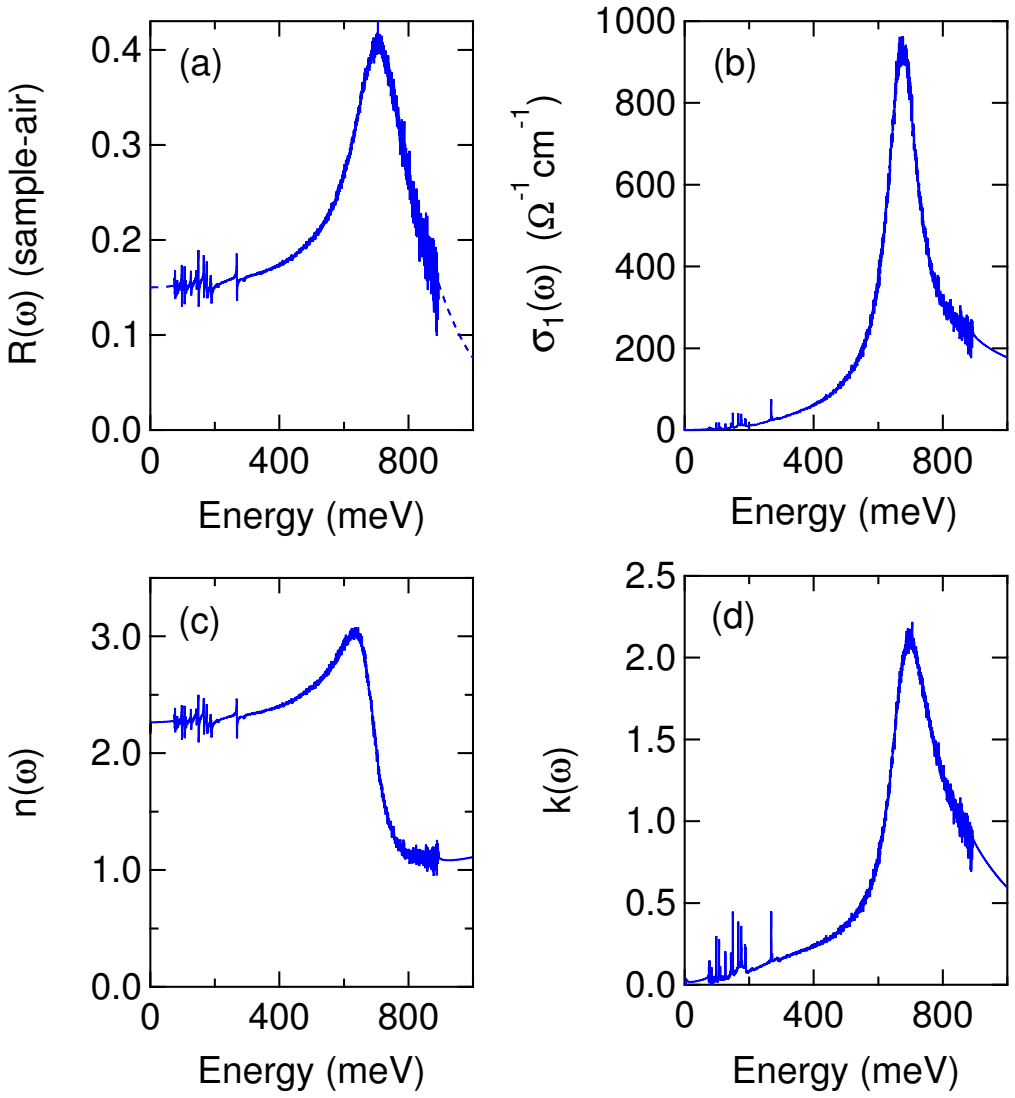

FIGURE 4.1: **ET-F_2TCNQ ambient pressure optical properties along the a-axis**. Panel (a) shows the ET-F_2TCNQ reflectivity along the a-axis. Measured data are shown with solid lines, while dashed lines are extrapolations based on Ref. [10]. Panel (b) shows the corresponding optical conductivity, while panels (c) and (d) show the real and imaginary part of the complex refractive index, $n(\omega)$ and $k(\omega)$ respectively.

4.2.1 Extraction of the Hubbard parameters from the optical conductivity

We discussed earlier that the ET-F_2TCNQ has an almost ideal quasi one-dimensional electrodynamics that can be captured within the framework of a simple extended Hubbard model

$$H = -t \sum_{i\sigma} \left(c^{\dagger}_{i\sigma} c_{i+1\sigma} + H.c. \right) + U \sum_{i} n_{i\uparrow} n_{i\downarrow} + V \sum_{i} n_i n_{i+1} \qquad (4.9)$$

where the $c^{\dagger}_{i\sigma}$, $c_{i\sigma}$ are the usual fermion creation and annihilation operators (i denoting the lattice site and σ the spin) and $n_{i\sigma} = c^{\dagger}_{i\sigma}c_{i\sigma}$ the number operators[2]. In this model t is the hopping amplitude, U the onsite correlation energy and V the intersite correlation (between nearest neighboring sites).

In the limit of large Mott gaps ($U >> V, t$) this model can be analyzed in terms of a $1/U$ expansion in which the hopping events are allowed only when preserving the total number of doubly occupied sites and the ground state configuration has all singly occupied sites [145].

In this regime spin and charge are separated and the spin degrees of freedom can be integrated away as scalar form factors g_q at quasi-q momentum. For the calculation of the optical conductivity, the relevant form factors are the ones arising from transitions at $q = 0$ and $q = \pi/a$ and the form factors reduce to $g_0 = 2.65$ and $g_\pi = 0.05$ [145].

Once the spin is integrated out, the charge will dictate the optical response of this Hubbard model through the current-current correlation function $\chi_{jj}(\omega)$ that is related to the reduced optical conductivity $\omega\sigma_1(\omega)$ by the following constitutive relation [145]

$$\omega\sigma_1(\omega) = \mathrm{Im}\{\chi_{jj}(\omega)\} \tag{4.10}$$

and the full optical response for the model Hamiltonian (4.9) will be described by the reduced optical conductivity

$$\begin{aligned}\omega\sigma_1(\omega) =& \pi g_\pi t^2 e^2 \delta(\omega - \omega_2) \\ &+ g_0 t^2 e^2 \Bigg\{ \Theta(V - 2t)\pi\left(1 - \frac{4t^2}{V^2}\right)\delta(\omega - \omega_1) + \\ &+ \Theta(4t - |\omega - U|)\frac{2t\sqrt{1 - (\omega - U/4t)^2}}{V(\omega - \omega_1)} \Bigg\}.\end{aligned} \tag{4.11}$$

Here $\Theta(x)$ stands for the Heaviside function, while $\omega_1 = U - V - 4t^2/V$ and $\omega_2 = U - V$. The two delta peaks at ω_1 and ω_2 represent two different Mott-Hubbard excitons, the former existing only for $V > 2t$ and accounting for bound holon-doublon pairs. As a consequence of the small value of g_π, the excitonic contribution at $\omega = \omega_2$ is neglected in our analysis.

The third and last term of (4.11) is a semielliptic contribution coming from a continuum of unbound holons and doublons (particle-hole continuum) that spans an energy range defined by the condition $|\omega - U| \leq 4t$.

[2] n_i is defined as $n_i = n_{i\uparrow} + n_{i\downarrow}$.

This reduced optical conductivity can be actually used as a fitting function for our equilibrium optical data to extract the model Hubbard parameters U, V, and t with a constrained procedure. In order to directly fit our data, we convolved the function with a Lorentzian broadening $\eta \sim 2t$ that allows a physical smearing of the sharp functions present in (4.11) and consistent with broadening induced by couplings to other degrees of freedom not contained in the Hubbard model.
All our experimental reduced optical conductivities, in the following, have been normalized to the peak value of the ambient pressure $\omega\sigma_1(\omega)$ to avoid the introduction of an additional amplitude parameter in the fit function. Moreover, we subtracted the *intra*molecular electronic contributions discussed in [10, 49], since they are not related to the low energy *inter*molecular electrodynamics of the sample. The best fit curve on $\omega\sigma_1(\omega)$ is reported in Fig. 4.2a with the corresponding holon-doublon pair (HD) and particle-hole continuum contributions (PH). Fig. 4.2b shows the real space representation of the holon-doublon exciton and of a typical particle-hole continuum excitation.

The best fit parameters obtained in this case are $U = 845$ meV, $V = 120$ meV and

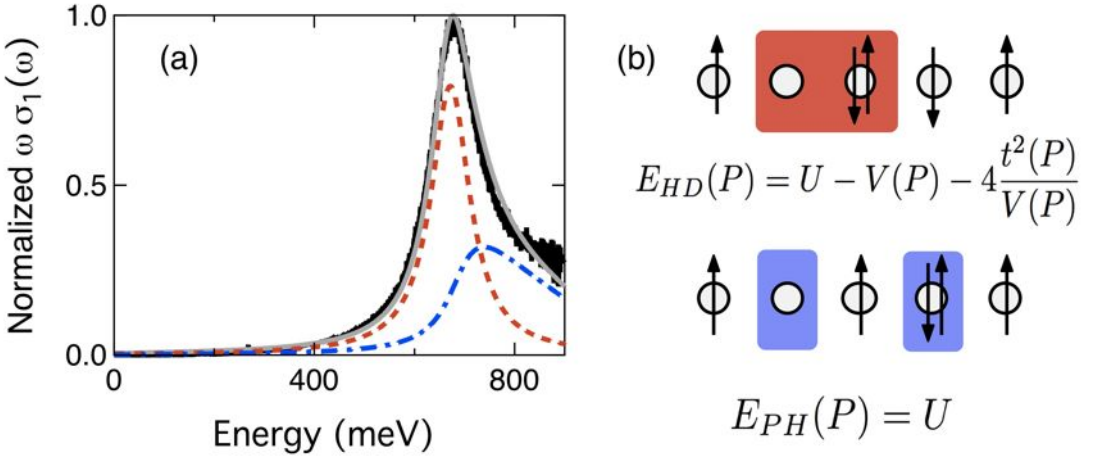

FIGURE 4.2: **ET-F_2TCNQ optical conductivity contributions**. Panel (a) shows the fit (grey solid line) of the experimental ambient pressure $\omega\sigma_1(\omega)$ (black solid line). Below the two curves are shown the separate contributions for the holon-doublon exciton (red dashed line) and for the particle-hole continuum (blue dashed-dotted line). Panel (b) sketches a holon-doublon pair (top) and a typical particle-hole continuum excitation (bottom) as seen in real space. Note that only the holon-doublon pair energy is expected to change with pressure.

$t = 40$ meV with a broadening $\eta = 95$ meV. These value confirm the ET-F_2TCNQ to be a strongly correlated solid with a $U/t = 21.1$ (or alternatively $U/W = 5.3$), well into the Mott insulating sector of its phase diagram.
We remark that the peculiar shape of this optical conductivity, with respect to

other Mott insulators, is given by the importance of a nonlocal correlation interaction (modeled here with V) that gives rise to sharp excitonic bound states of optical excitations. If V were $V \leq 2t$ we would just have PH continuum components and an optical conductivity similar to the ones of a conventional Mott insulator (e.g. Fig. E.2f).

4.3 Equilibrium optical properties under pressure

We now describe the pressure evolution of the correlated state of the ET-F_2TCNQ by adopting the same protocol outlined in the previous paragraphs.
The starting point has been a measurement of its optical properties for pressures up to 2.0 GPa. Technical details about the measurements are discussed in section A.3. The data presented in this section have been measured with Synchrotron radiation based Fourier Transform Infrared (FTIR) spectroscopy with a Diamond Anvil cell pressure device. A second experimental dataset up to 1.1 GPa has been measured with laboratory-based FTIR spectroscopy and is reported in Appendix C.
A first important observation is that in the midinfrared region (below 400 meV) the refractive index of the ET-F_2TCNQ (see Fig. 4.1c) is strikingly similar to the one of the diamond ($n_d = 2.37$), thus the expected reflectivity on average will be very close to zero. The measured sample (s)-diamond (d) reflectivity is defined as

$$R_{sd} = \left| \frac{\hat{n}_d - \hat{n}_s(\omega)}{\hat{n}_d + \hat{n}_s(\omega)} \right|^2 \tag{4.12}$$

Moreover, due to multiphonon absorption in the diamond anvils, no reliable spectroscopic information can be extracted in the interval between 240 and 550 meV. In order to determine the optical properties we therefore employed a combined reflectivity and transmittivity measurement of infrared light polarized along the a-axis. The reflectivity measurement well captures the electronic changes above 400 meV, while the transmission measurement gives superior information at energies below 250 meV.
The resulting data have been then simultaneously fitted for each pressure point with a Drude-Lorentz model [234], where the complex dielectric constant $\hat{\epsilon}(\omega)$ reads as

$$\hat{\epsilon}(\omega) = \epsilon_\infty + \sum_n \frac{\omega_{p,n}^2}{(\omega_n^2 - \omega^2) - i\omega/\tau_n} \tag{4.13}$$

The oscillators used to model the electronic features at the gap are described by the following parameters used for the ambient pressure data and they are smoothly varying for increasing pressure. The Drude Lorentz fit is constrained to the 0-300

ω_n (meV)	$\omega_{p,n}$ (meV)	$1/\tau_n$ (meV)
663	964	160
806	575	338
3479	4405	3771

TABLE 4.1: **Example of Lorentz-fit parameters for the pressure dependent reflectivity and transmittivity fitting of the ET-F_2TCNQ crystal along the a-axis**. Lorentz fit parameter for ET-F_2TCNQ crystal along its a-axis at 0.2 GPa. $\epsilon_\infty = 2.46$ is kept as a pressure independent parameter.

meV region for the transmittivities $T(\omega)$, while the reflectivities $R_{sd}(\omega)$ are fitted from 400 meV to 1000 meV. An example of the Drude-Lorentz fitting is shown in Fig. 4.3. From the Drude-Lorentz fit of the transmittance data, the low frequency

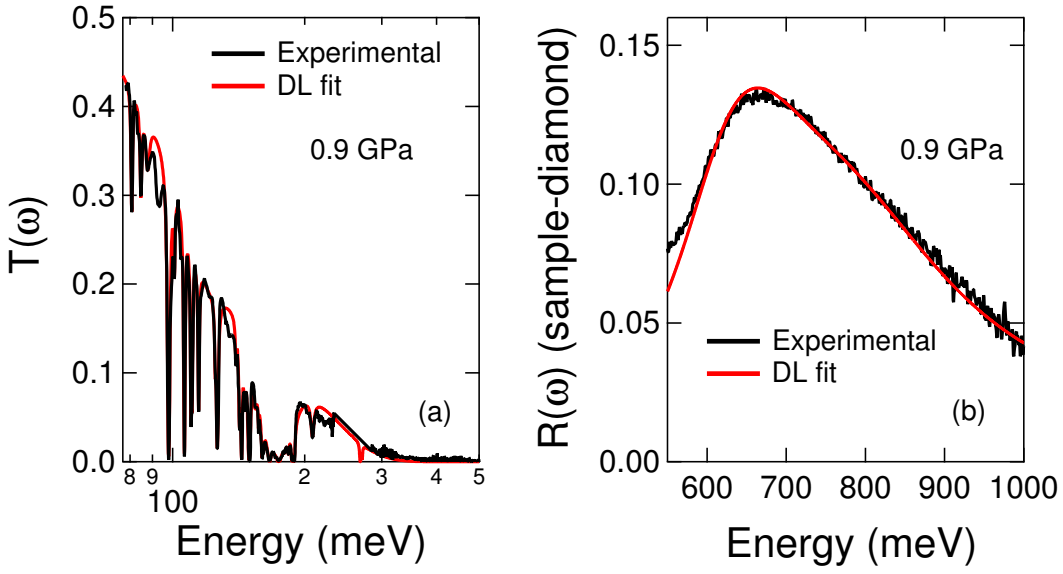

FIGURE 4.3: **Drude-Lorentz fit of the ET-F_2TCNQ optical properties under pressure**. Example of simultaneous Drude-Lorentz fit of the transmittivity $T(\omega)$ (a) and reflectivity $R(\omega)$ at the sample-diamond interface (b) for the ET-F_2TCNQ along the a-axis at a selected pressure. Reprinted figure with permission from [247]. Copyright © 2014 by the American Physical Society.

part of the reflectivity is recalculated at the sample-diamond interface and merged with the experimental data above the diamond absorptions (namely above 550 meV).

The obtained reflectivity at the sample diamond interface spanning the whole range of interest is then used to calculate the optical conductivity $\sigma_1(\omega)$ through a standard Kramers-Kronig algorithm for samples in contact with a transmitting window (see Appendix B). The β parameter for the Kramers-Kronig transformation is kept fixed at 471 meV by evaluating the consistency of the output $\sigma_1(\omega)$ with the corresponding ambient pressure curve that is independent from this parameter. The complete optical properties for selected pressures are shown in Fig. 4.4. The most important fact emerging from these data is the presence of a large

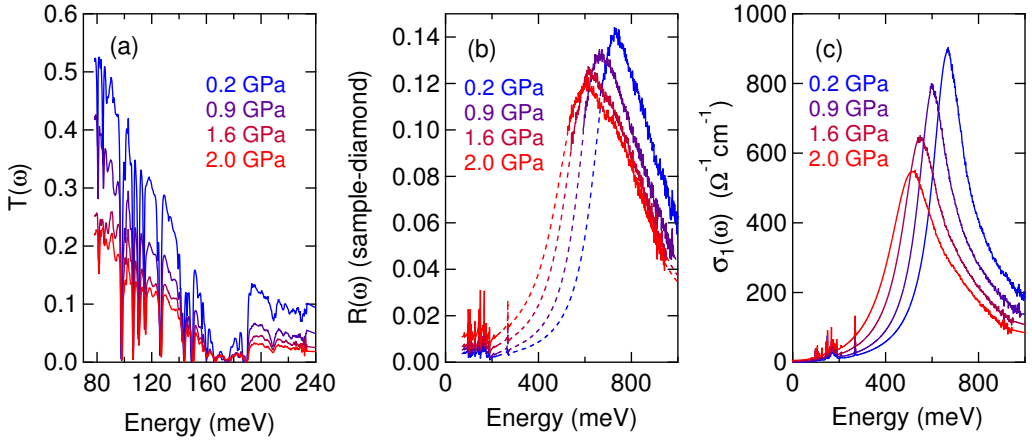

FIGURE 4.4: **ET-F_2TCNQ optical properties under pressure**. Broadband ET-F_2TCNQ optical properties along the a-axis for selected pressure. Panel (a) shows the sample transmittivity $T(\omega)$, panel (b) the reflectivity at the sample-diamond interface, and panel (c) the real part of the optical conductivity $\sigma_1(\omega)$ obtained via a Kramers-Kronig transformation of the data shown in panel (b). Dashed lines of panel (b) are reflectivities reconstructed from the Drude Lorentz fit in the region where diamond absorptions prevent a reliable reflectivity measurement.

redshift of the CT resonance upon increasing pressure (see Fig. 4.4 (b) and (c)). The shifting rate is of about 70 meV/GPa, qualitatively consistent with analogous observations on other quasi-1D organic compounds [77, 79], but significantly larger in magnitude. In addition, the resonance exhibits an evident broadening towards higher frequencies, becoming less and less symmetric in its line shape. In Fig. 4.4a, the transmittivity $T(\omega)$ shows a clear decrease due to the redshifting electronic weight from the CT band, but it remains too high to be compatible with a pure Drude response. The extrapolated σ_{DC} grows from zero to less than 10 Ω^{-1} cm^{-1}, a value still compatible with an insulating state and the Mott gap is

still widely open. Bearing in mind that our measurement interval covers energies above 75 meV and does not access the single meV region, we can state that our data give no indication for an incipient metallization within the investigated pressure range. The transmittivity shows very clearly the entire spectrum of molecular vibrations in the region between 75 and 220 meV. As can be seen in Fig. 4.5, the whole spectrum of molecular vibrations undergoes only slight changes, at most 1 meV in frequency shift ($\Delta\omega/\omega \sim 1\%$) due to bond compression and no significant reshaping is detected in our measured data. From this observation, we can infer that the molecular structure is not significantly changed in our pressure range. To the best of our knowledge, structural studies (such as X-ray or neutron diffraction experiments) on this very compound are lacking but in other ET-based solids (e.g. the κ-(BEDT-TTF)$_2$Cu(NCS)$_2$) the molecules have been found to be only slightly affected by the application of pressures comparable with ours [258], thus supporting the observations of this study.

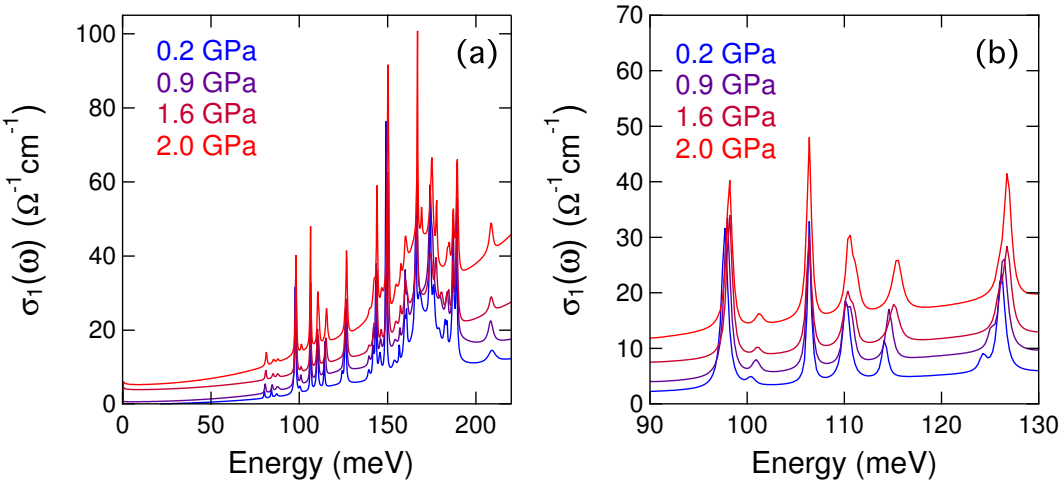

FIGURE 4.5: **Pressure dependence of the ET-F_2TCNQ molecular vibrations**. Panel (a) shows an expanded view of the ET-F_2TCNQ molecular vibration spectrum in the midinfrared region of the $\sigma_1(\omega)$. Panel (b) shows instead a zoom of the energy interval 90-130 meV to better show the magnitude of the frequency shifts of selected molecular vibrations.

4.4 Hubbard parameters of the ET-F_2TCNQ under pressure

The determination of the parameters of the Hubbard Hamiltonian (4.9) is carried out with the same fitting procedure described in section 4.2.1. The fitting results for selected pressures are shown in Fig. 4.6. Upon increasing pressure, both the HD exciton and the PH continuum undergo a broadening and the relative weight between the two contributions evolves in favor of a more prominent continuum. The main responsible for the shift of the CT resonance is the redshifting HD peak;

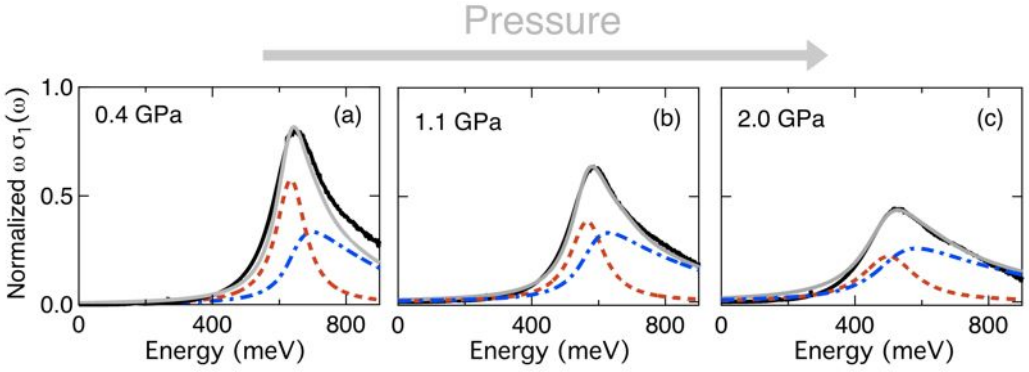

FIGURE 4.6: **Extraction of the Hubbard model parameters under pressure**. Panel (a)-(c) show the theoretical fit curve (grey solid line) of the experimental $\omega\sigma_1(\omega)$ (black solid line) for selected pressures in the range 0.0-2.0 GPa. Below the two curves are shown the separate contributions for the holon-doublon exciton (red dashed line) and for the particle-hole continuum (blue dashed-dotted line).

the PH continuum remains instead at the same energy with a redshifting onset (at $U - 4t$) due to the increasing bandwidth. The changes translate in a growing overlap of the two spectral features, reflecting a fading boundary between these two classes of excitations.

As mentioned in the previous sections, the experimental $\omega\sigma_1(\omega)$ curves have been normalized to the ambient pressure curve and subtracted of the high energy *intra*molecular contributions prior to the fitting routine.

During the fit we assume U to remain constant at 845 meV while the broadening factor η changes from 95 meV to 193 meV. The resulting fit parameters are plotted as a function of pressure in Fig. 4.7a. The most important observations here is that the hopping t is found to increase from 40 to 85 meV, but also the correlation energy V increases from 120 to 203 meV.

We can compare these values against the predictions for a realistic tight-binding

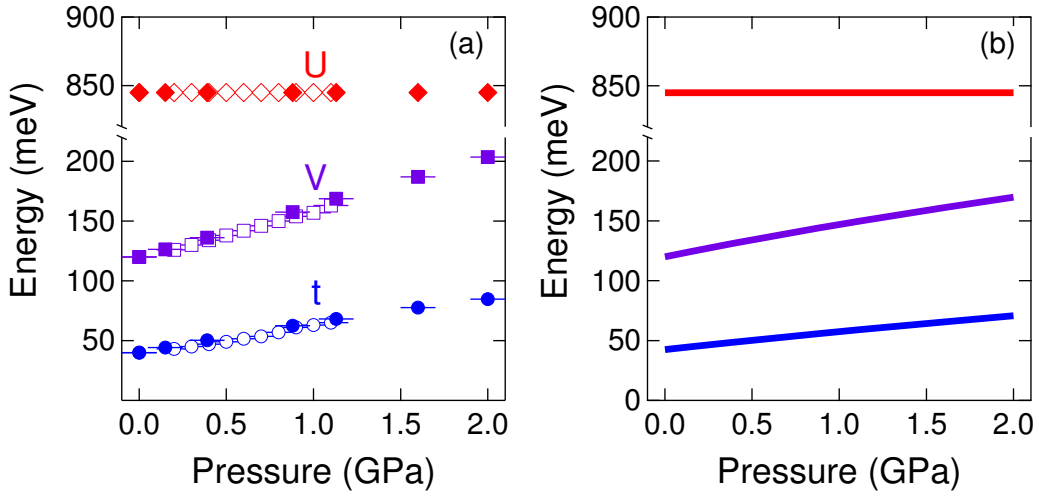

FIGURE 4.7: **ET-F_2TCNQ extended Hubbard model parameters under pressure**. Panel (a) shows the extended Hubbard model parameters obtained form a fitting of the reduced optical conductivity $\omega\sigma_1(\omega)$ as a function of pressure. Filled and empty symbols identify distinct experimental runs. Panel (b) shows instead the theoretical prediction for a model tight binding calculation with realistic parameters discussed in the text.

chain with hydrogenic wavefunctions with a lattice spacing given by a. It can be shown that the extended Hubbard parameters in this case can be parametrized as [23, 24, 259]

$$U(a) = \text{constant} \tag{4.14}$$

$$t(a) = A(1+a)e^{-a} \tag{4.15}$$

$$V(a) = \frac{B}{a^6} \tag{4.16}$$

These equations are representing the fact that the onsite Coulomb repulsion U is expected not to be affected by changes in the lattice spacing, that the hopping increases exponentially thanks to the increased overlap between neighboring electronic wavefunctions and that the intersite correlation V effectively reduces to a simple van der Waals potential[3] under s-wave symmetry assumption [24]. We now consider a realistic pressure dependence for the lattice spacing $a(P)$ through an

[3]In [24] the actual expression for V is a purely Coulomb potential e^2/a, but, due to the nature of the molecular bonding in these materials, a van der Waals potential is more appropriate [97, 260].

invertible equation of state [261]

$$a(P) = a_0 \left(1 + \frac{B_0'}{B_0} P\right)^{-\frac{1}{3B_0'}} \tag{4.17}$$

where B_0 is the material bulk modulus and B_0' is its pressure derivative. By inserting $a_0 = 10$ Å, $B_0 = 8$ GPa and $B_0' = 4$[4] and recasting the parameters as functions of their starting values U_0, V_0 and t_0

$$U(a) = U_0 \tag{4.18}$$

$$t(a) = \frac{t_0}{1 + a_0}(1 + a)e^{-(a - a_0)} \tag{4.19}$$

$$V(a) = V_0 \left(\frac{a_0}{a}\right)^6 \tag{4.20}$$

we can calculate the expected variation for the Hubbard parameter as a function of pressure. As we can see by directly comparing panels (a) and (b) of Fig. 4.7, this simple model captures the correct order of magnitude of the observed experimental trends. Especially important is the growth of V, since the observed increase could not be accounted for in case of a purely Coulombic potential and is deeply connected to the molecular nature of this organic solid.

The change in the interaction parameters has, obviously, relevant consequences on the correlation between holons and doublons and as we will see on their dynamics. In Fig. 4.8a, we can see that, as pressure is applied, the simultaneous reduction of the U/t and V/t ratios leads to a general reduction of the correlation among holons and doublons. The V/t ratio in particular is reduced from $V/t \sim 3$ to $V/t \sim 2.4$ close to the critical ratio $V/t \sim 2$ for which the excitonic state cannot be isolated from the continuum. Excitonic states are still possible in our pressure regime, but they are on average less bound than in the ambient pressure condition. The binding energy, defined as $V + \frac{4t^2}{V} - 4t$ in the limit of large Mott gaps [145], is halved (see Fig. 4.8). As a consequence the average exciton size (defined as $\zeta_{hd} = \frac{1}{1-(2t/V)^2}$ [145]) increases, also reflecting a weaker correlation between the holons and the doublons.

[4]These values represent realistic estimates for the equation-of-state parameters of ET-based molecular compounds.

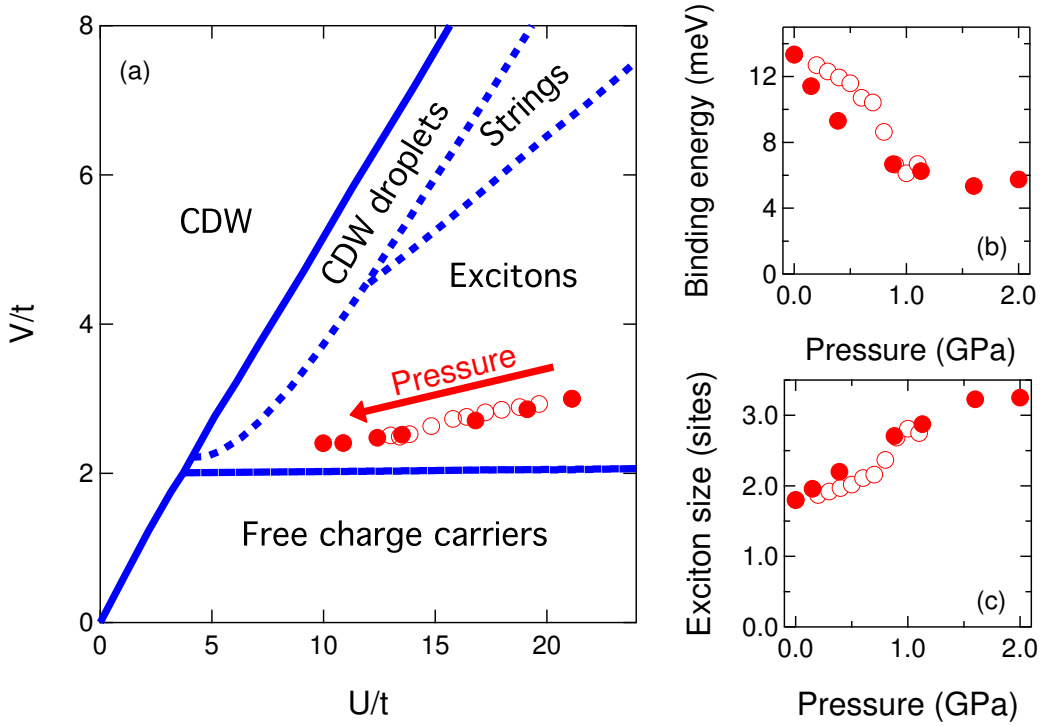

FIGURE 4.8: **ET-F_2TCNQ Holon-Doublon parameters under pressure**. Panel (a) shows the experimental pressure runs in the V/t-U/t phase diagram of the extended Hubbard model optical excitations (adapted from Ref. [147]). Panel (b) shows the binding energy calculated from the interaction parameters as a function of pressure. Panel (c) reports the calculated exciton size as a function of pressure. Empty and filled symbols identify distinct experimental runs.

4.5 Pump-probe measurements under pressure

The ultrafast recombination of photoinjected holon-doublons has been measured by means of an optical pump-probe experiment under variable pressure conditions. An optical pump pulse resonantly tuned with the Mott gap (∼700 meV) and polarized along the a-axis excites holon-doublon pairs and causes a drop in the reflectivity. A second delayed pulse, polarized as the pump and with the same energy, probes the transient change in the reflectivity and follows its recovery back to the equilibrium. Further details about the experimental protocol and methods are given in A.4.

As shown in previous experiments [10, 38, 129], the transient change in the reflectivity is directly connected to the amount of photoexcited holon-doublon pairs and therefore constitutes a good experimental observable to assess the holon-doublon recombination dynamics. In Fig. 4.9 we show a typical time-resolved reflectivity measurement of the CT peak as a function of the time delay between the pump

and the probe pulses. The recovery dynamics of the ET-F_2TCNQ is quite fast compared to other quasi-1D solids like K-TCNQ [129]. The transient change of the reflectivity at the pump arrival is essentially istantaneous and limited by the pump pulse duration [10]. It has a negative sign, namely the reflectivity is reduced as a result of the optical excitation, and its relaxation is almost complete in less than 2 ps (aside from a metastable, small amplitude component). The relaxation

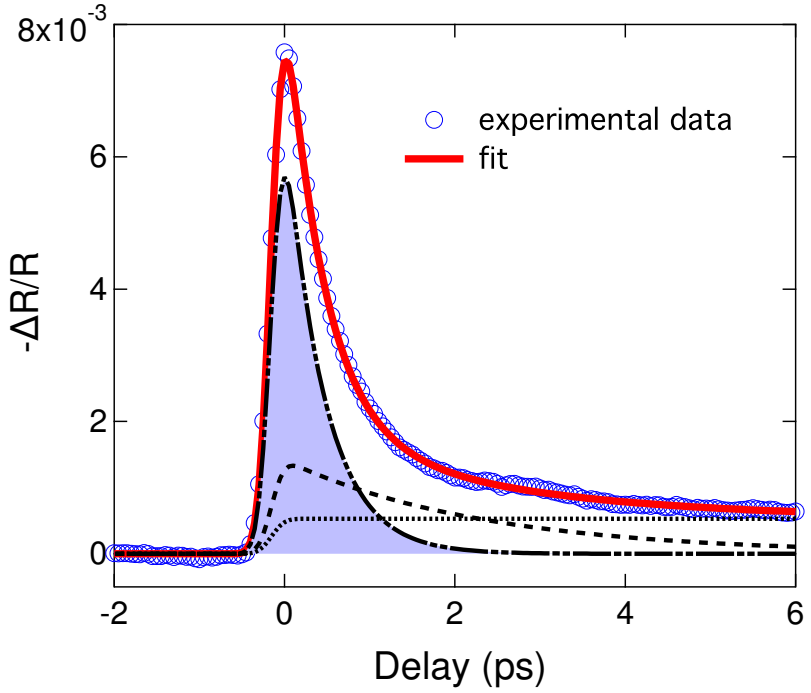

FIGURE 4.9: **Pump probe measurement of the ET-F_2TCNQ and the Holon-Doublon recombination**. Example of transient reflectivity change (in the diamond anvil cell) for degenerate pump and probe pulses polarized along the ET-F_2TCNQ *a*-axis as a function of the time delay between the pump and probe pulses. Empty symbols are experimental data, the red line is the overall fit to the data, while the black curves below are the single fitting components. The shaded area marks the electronic part of the recombination dynamics associated with the holon-doublon recombination.

of this excited state follows a double exponential decay and therefore we fitted our data with a double exponential function convoluted with a gaussian pulse [38, 129]

$$\frac{\Delta R(t_d)}{R} = \frac{R(t_d) - R(t_d < 0)}{R(t_d < 0)} = \\ = \int_{-\infty}^{t_d} \left[A_0 + \sum_{i=1,2} A_i \exp\Big(- \frac{t_d - t'}{\tau_i} \Big) \right] \exp\Big(\frac{t'^2}{\tau_c^2} \Big) dt' \qquad (4.21)$$

where t_d stands for the time delay between pump and probe pulses, A_i and τ_i are respectively the amplitudes and the lifetimes of the exponential decays, A_0 stands

for a metastable component[5], and τ_c is the cross-correlation time between pump and probe pulses. The different component of the fit function are also reported in Fig. 4.9.

For completeness, we need to mention that we checked the possibility of a fit involving a three-body recombination like the one described in Downer *et al.* [36], but it fails in reproducing the experimental data. This suggests a nature of the recombination process different from an Auger recombination, observed in conventional semiconductors [36].

Our pump-probe experiments under high pressure conditions have been performed at a moderate fluence of 300 μJ/cm^2, in a regime where the excitation of holon-doublon pairs is sparse and the signal scales linearly with the number of absorbed photons. The measured differential reflectivity change under these conditions and for all the pressures measured is approximately on a level of $\Delta R/R \sim 1\%$.

The pump probe experiment has been performed with two different protocols: in one case both the pump and the probe are kept fixed at an energy of 740 meV (mainly resonant to the PH continuum), while in other series of experimental runs both the pump and the probe energies have been tuned at each pressure point to track the redshift of the HD exciton resonance. The measured data for selected pressures, together with the fitted lifetimes of the exponential decay, are shown for these two experimental conditions in Figg. 4.10 and 4.11.

The most important observation emerging from these data is that upon pressure increase the fast decay constant associated with electronic recombination exhibits a clear decrease with a rate of 85 fs/GPa for PH continuum excitations and 116 fs/GPa for bound HD pairs. The second, longer decay constant, interpreted here as associated to the thermalization of high-energy intramolecular modes heated by the quasiparticle recombination does not show a clear pressure dependence within the systematic error associated with the experimental conditions.

From here, we will consider only the purely electronic, pressure dependent part of the transient response (the one decaying with the τ_1 lifetime) that accounts for the recombination of the photoinjected holons and doublons. As a final comment, the data emerging from these two different experiments show a rather similar behavior: holon-doublon and particle-hole excitations decay with a similar pressure dependence and similar recombination times. We explain this observation in terms of increasing intermixing between the two types of excitations, due to the increased

[5]Likely a thermalization component with a lifetime that is too long to be determined within our experimental parameters

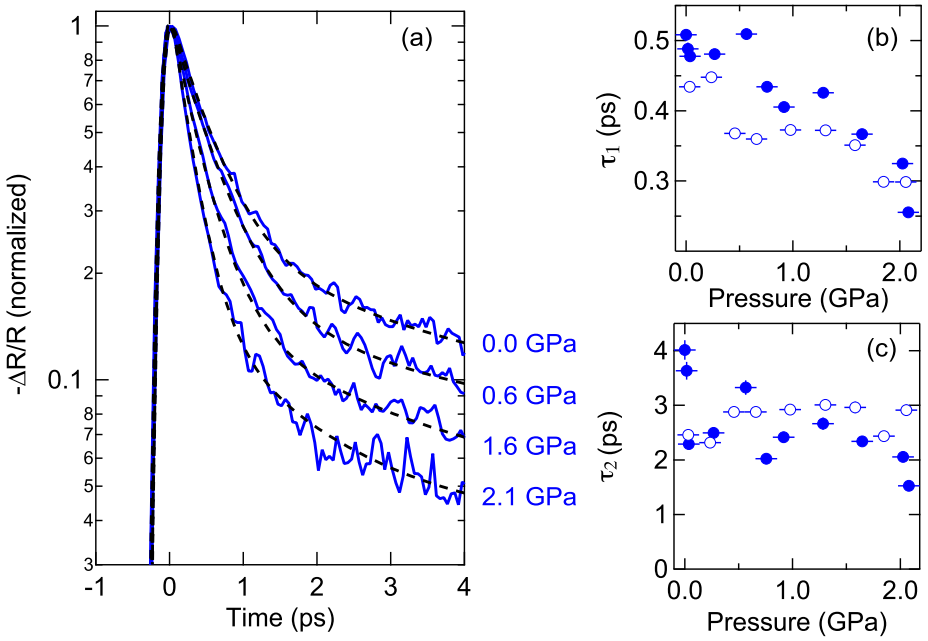

FIGURE 4.10: **Pump-probe experiment resonant to the Particle-Hole continuum**. Panel (a) shows the normalized $\Delta R/R$ time-domain curves on the PH continuum peak for selected pressures. Black dashed lines are fits to the data. Panel (b) and (c) show instead the two lifetimes of the exponential decays involved in the photoexcited state relaxation vs applied pressure. Filled and empty symbols identify distinct experimental runs.

hopping amplitude. The higher the pressure, the more difficult is the spectral separation of the two spectral features.

4.6 Modeling holon-doublon dynamics

A quantitative analysis of the pressure dependence of τ_1 requires the development of an adequate theoretical framework to deal with the problem of holon-doublon recombination. The recombination of bound holon-doublon pairs (or disassociated pairs in the PH continuum) involves the dissipation of a quite high energy (of order $U - V$) per event and the dissipation has to occur through a dissipative bath coupled to the electronic subsystem.

In absence of such a bath the only possible decay channels involve either kinetic energy transfer (i.e. creation of particle-hole pairs) or spin excitations. The energy scales for these two dissipation mechanisms are respectively the hopping t and the exchange coupling $t^2/(U - V)$ [63]. Since we consider a case where the strong

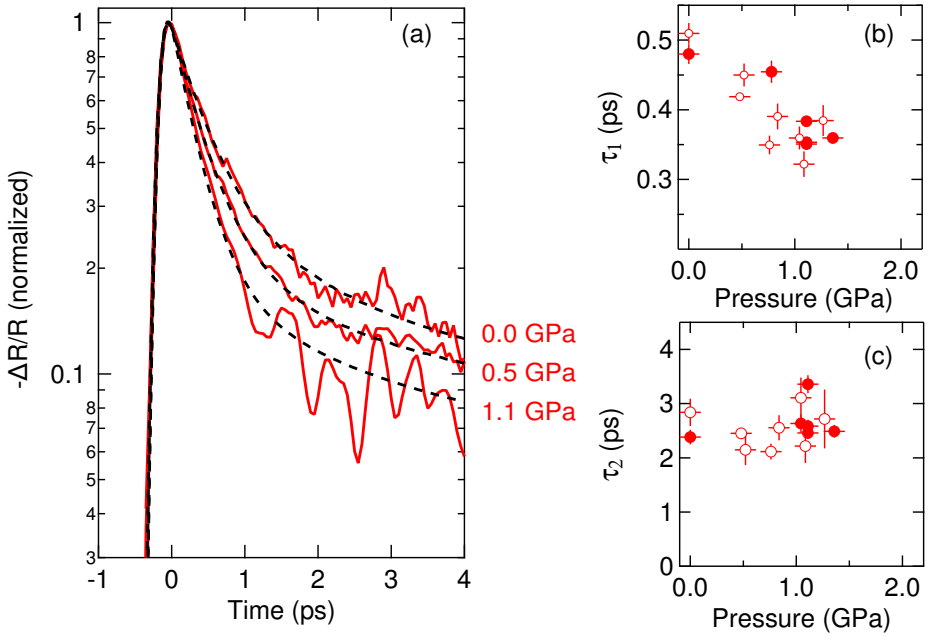

FIGURE 4.11: **Pump-probe experiment resonant to the Holon-Doublon exciton**. Panel (a) shows the normalized $\Delta R/R$ time-domain curves on the HD exciton peak for selected pressures. Black dashed lines are fits to the data. Panel (b) and (c) show instead the two lifetimes of the exponential decays involved in the photoexcited state relaxation vs applied pressure. Filled and empty symbols identify distinct experimental runs.

coupling regime holds ($U \gg V, t$), dissipation through these paths requires a large number of scattering events, leading to an exponentially small decay rate with the U/t ratio [62, 63, 153]. In Fig. 4.12, that constitutes the main result of this work, we plot the experimental lifetimes for both the HD pairs and the PH continuum as a function of the effective Mottness $(U-V)/t$ of the system. Here the interactions U, V and t are the experimental values determined from the equilibrium optical data.

The lifetimes of the photoexcited state are found to increase as the overall degree of correlation is increased but the lifetime enhancement is weaker than the aforementioned exponential behavior (given the same Mottness variation) and, as we propose in the following, this phenomenon has a deeper physical interpretation. In the ET-F_2TCNQ, since electron-phonon coupling is small [137] and efficient radiative emission is lacking, we assume as a working hypothesis that the high frequency molecular modes (see Fig. 4.5) are the primary scattering partners for the rapid decay observed in our experiment.

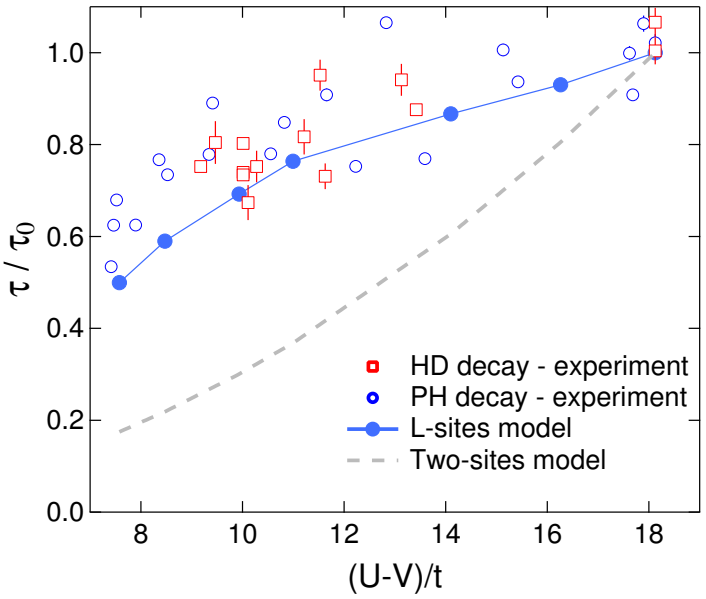

FIGURE 4.12: **Holon-Doublon decay as a function of the effective correlation**. Experimental relaxation times (empty symbols) for HD and PH resonant excitation normalized to their ambient pressure value τ_0 and shown as function of $(U-V)/t$. The calculated holon-doublon lifetimes (filled circles) found from solving an L-site effective model (discussed in the text) with spin-boson scaling for the bare decay rate. For comparison the spin-boson dimer result is shown (dashed line). Reprinted figure with permission from [247]. Copyright © 2014 by the American Physical Society.

These modes are intrinsically localized[6] and the holon-doublon recombination has to occur via a single hopping event from the doubly occupied to the empty site, thus we describe the recombination process as local.

The density of injected doublons for the fluences investigated is 0.06/site, i.e. low enough to consider the holon-doublon pairs mutually non-interacting. The simplest possible model for the HD recombination process involves a dimer of ET molecules coupled to a continuum of bosonic modes, a typical ansatz for dissipative electron transfer models [262, 263]. The holon-doublon pair and a pair of singly occupied states can be viewed as the excited and ground state (respectively) of a two level system with energy gap $U-V$ and tunneling amplitude equal to t, therefore this dissipative system can be described as an effective spin-boson model [264]. The dissipative bath is modeled by an appropriate super-Ohmic spectral function [265]

$$\mathcal{J}(\omega) = \alpha \frac{\omega^3}{\omega_0^2} e^{-\omega/\omega_c} \tag{4.22}$$

[6]Being *intra*molecular vibrations.

where α is a dimensionless coupling constant for the system-bath interaction, ω_0 is a typical bath energy scale while ω_c is a cutoff energy.
We consider a physical situation where $U - V \gg t$ (large-bias limit), therefore the tunneling mediating the HD decay and the energy dissipation into the bath is far off-resonant. The decay rate in this regime is found to be [264]

$$\Gamma = \frac{1}{\tau} = \frac{t^2}{(U-V)^2}\mathcal{J}(U-V). \tag{4.23}$$

The main contribution to the spectral function $\mathcal{J}(U-V)$ comes, within our model, from the high-energy *intra*molecular modes and it is assumed to be pressure independent. As a consequence the pressure dependence of the decay rate comes exclusively from the ratio $t^2/(U-V)^2$ and entails an increased (decreased) decay with t (with $U-V$).
The theoretical decay rate derived from this spin boson calculation is reported in Fig. 4.12 as "Two sites model" and it predicts a more than fivefold increase of the decay rate at the largest pressure (minimum $(U-V)/t$) investigated, not at all reproducing the experimental trend.
Previous time-resolved measurements proved that the transient response of the insulating state involves at least three different sites with the possibility of tunneling between HD pairs and PH states [10]. A bound holon-doublon pair next to singly occupied sites $|\cdots \_0 \Updownarrow \_\_ \cdots\rangle$ can tunnel into a state $|\cdots \_0\_ \Updownarrow \_ \cdots\rangle$ belonging to the class of PH continuum excitations through a single hopping event. In this formalism we indicate a holon as $|\cdots 0 \cdots\rangle$, a doublon as $|\cdots \Updownarrow \cdots\rangle$, and the singly occupied sites as $|\cdots \_ \cdots\rangle$.
This process occurs with a rate dictated by t and the barrier between the two configurations is given by V, both increasing with pressure. It has to be remarked that the PH state $|\cdots \_0\_ \Updownarrow \_ \cdots\rangle$ has a lower probability to recombine with respect to a bound HD pair $|\cdots \_0 \Updownarrow \_\_ \cdots\rangle$, since it needs two hopping events to recombine (instead of one). In order to describe the observed dynamics we therefore employed an effective model derived form the strong coupling limit and sketched in Fig. 4.13. The key idea is that in a realistic physical situation the photoinjected holons and doublons will be able to hop over several sites and the recombination will occur after different intermediate steps (over different spatial separations) that are decay-forbidden[7] and that will therefore slow down the global decay of the photoexcited state. We try to model this picture by allowing coherent

[7] In the framework of an exclusively local recombination.

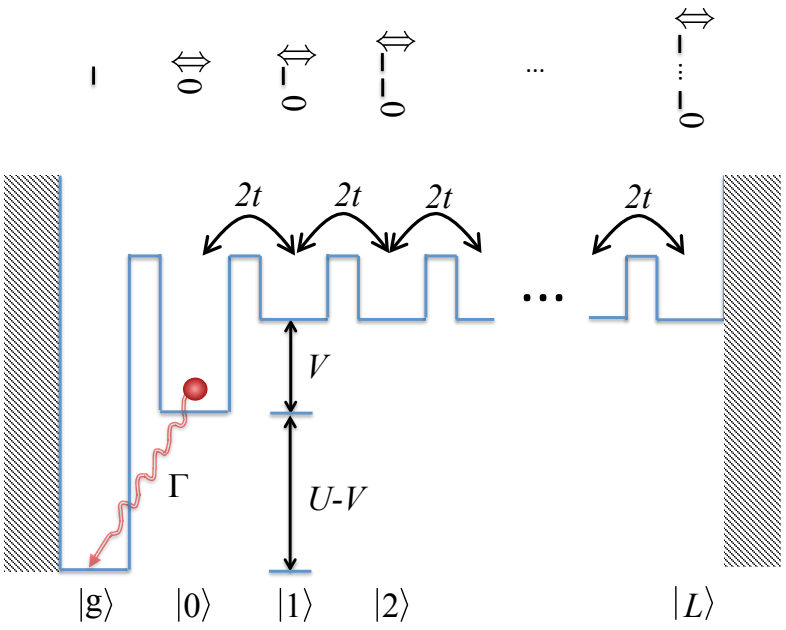

FIGURE 4.13: **Holon-Doublon decay model**. Scheme of the effective model used to describe the holon-doublon dynamics in the strong coupling limit. The state $|g\rangle$ indicates the ground state containing no holons or doublons, the state $|0\rangle$ indicates an adiacent (zero separation) holon-doublon pair, while the other $|l\rangle$ states stand for configurations where the holon and doublon are separated by l sites. In the limit $L \to \infty$ the unbound states ($|1\rangle$, $|2\rangle$,...) form the particle-hole continuum. The relaxation to $|g\rangle$ is only allowed from the $|0\rangle$ state with a bare spin-boson rate Γ. Reprinted figure with permission from [247]. Copyright © 2014 by the American Physical Society.

hopping events on a L-sites chain and we define $|g\rangle$ a singly occupied configuration, $|0\rangle$ a bound HD pair, and $|l\rangle$ states where the holon and the doublon are separated by l singly occupied sites (up to a maximum distance L). The potential energy of the model mimicks the equivalent many-body configurations in the full extended Hubbard model, while its optical conductivity reproduces the full extended Hubbard model one (4.11) in the limit $L \to \infty$.

The recombination has been added to this model via a Markovian quantum dissipation process, suitable for modeling in the super-Ohmic large-bias limit [265]. The Markovian dissipation incoherently drives only the transition $|0\rangle \to |g\rangle$ at the bare "two sites" rate.

This effective model shows that separation of holons and doublons suppresses the decay rate and already adding a single site of separation renormalizes the bare rate Γ to

$$\Gamma_{eff} = \frac{\Gamma}{2}\left(1 + \frac{V}{\sqrt{V^2 + 16t^2}}\right). \tag{4.24}$$

We applied this effective model by first fitting the bare rate Γ to the value that reproduces the observed zero pressure decay rate.
This bare rate is calculated at each pressure point through (4.23) without free parameters, since U, V and t come from the equilibrium optical properties.
The effective rate Γ_{eff} has been instead numerically calculated from this model for different L values.
The increase of the system size L increases the suppression of Γ_{eff}, in agreement with the intuitive picture outlined above and with a chain size of $L = 20$ sites this model fully reproduces the experimental observations (see filled circles in Fig. 4.12).
The important physical conclusion that emerges from this comparison is that coherent tunneling dynamics between bound and unbound holon-doublon pairs competes with and slows the recombination of quasiparticles in a real half-filled Mott insulator.

4.7 Summary

In this work we investigated the problem of quasiparticle recombination in a Mott-insulator system and the role of effective interactions (correlations and hopping amplitude) in determining the relaxation of a photoinduced state towards equilibrium. The experiments have been focused on a particular class of excitations, holon-doublon pairs, that are of fundamental relevance for the Mott metal-to-insulator transition and can be injected in the insulating ground state by exciting carriers at the Mott gap in the optical spectrum. While in conventional metals the decay rate of photoexcited carriers is expected to scale with the hopping amplitude t and in band semiconductors like $1/t$ or $1/t^2$ depending on the specific decay mechanism, in Mott insulator the decay dynamics is still poorly understood. Previous work, both theoretical, and experimental, but with cold atoms in optical lattices, pointed towards a strong role of the correlation energy (onsite Coulomb repulsion U) in defining the doublon relaxation rate by imparting an exponential dependence in the ratio U/t.
In order to study this phenomenon in a real solid state material, we chose a quasi-1D half-filled Mott insulator, the ET-F_2TCNQ, that has a strong degree of correlation $U/t \sim 21$, a low electron phonon-coupling and exhibits a well characterized

insulator-to-metal transition upon photoexcitation of the Mott gap. Importantly, we used pressure, and therefore the lattice spacing, as a tuning parameter for the effective correlations existing in the system. We measured the equilibrium optical properties of the ET- F_2TCNQ, both in ambient and high pressure conditions and determined, through a fit with the analytical optical response of an extended Hubbard model, the relevant effective interactions energies (onsite Coulomb repulsion U, intersite Coulomb repulsion V, hopping amplitude t). Due to the presence of an important intersite correlation energy V ($\sim U/6$), in this material holons and doublons can either be independent (and thus constitute a particle-hole continuum in the optical spectrum) or form an excitonic bound state (holon-doublon pair) with a binding energy dependent on to both t and V.

We, then, measured the holon-doublon recombination times by means of a pump-probe reflectivity measurement under variable external pressure conditions. The holon-doublon quasiparticles (either bound or unbound) are injected by a pump beam resonantly tuned to the Mott gap and their recombination is measured by observing the recovery of the sample-reflectivity at the Mott gap, that coincides with the reconstruction of the half-filled insulating state.

The extracted relaxation times are finally mapped onto the correlation strength parameter $(U - V)/t$ based on the values measured in equilibrium. In modeling the recombination dynamics of bound and unbound holon-doublon quasiparticles we assume the decay occurring through coupling to *intra*molecuar vibrations, that have high energies ($\hbar\omega \sim U/6$) and localized character, thus representing efficient scattering partners for the excited state. We experimentally observe a clear increase of the recombination time with growing correlations, but the slope of this dependence is not compatible with the prediction of a simple spin-boson model, predicting a relaxation time roughly proportional to $(U - V)^2/t^2$. A comparison of the experimental data with a Markovian simulation of the decay dynamics revealed that coherent tunneling between bound and unbound holon-doublon pairs (in systems where V is a relevant energy scale) competes with and slows the recombination of quasiparticles in solid state half-filled Mott insulators and is an essential process for a quantitative assessment of photoinduced phase transition timescales in these systems.

Chapter 5

An optically stimulated superconducting-like phase in K_3C_{60} far above T_c

In this chapter we describe the midinfrared pump-THz probe experiments performed on the molecular superconductor K_3C_{60} with the aim to control its superconducting properties through resonant vibrational excitation. We first describe the measurement and analysis of the equilibrium optical properties for the very samples investigated in this work. Time- and frequency-resolved measurements of the gap spectral region above and below the critical temperature, and their dependence upon variation of temperature, pump fluence and pump energy are reported. We subsequently discuss the relevance of our findings to the manipulation of the superconducting state in correlated superconductors and propose further extensions of this work to other compounds. The results described in this chapter, unlike the ones of Chapter 4, are currently under review.

5.1 Light control of the superconducting state

A crucial problem in superconductivity is to find a route to increase the transition temperatures and thus to boost the development of cheap and scalable superconductivity-based technologies.
One approach to the problem is to create a crystal structure that can sustain a

more robust Cooper pairing interaction and thus a higher T_c. Starting from the empirical Matthias rules for conventional superconductors [266], this path, guided by a thorough synthesis work, led to the breakthrough of cuprates [267–269] and pnictides [270, 271] superconducting families that raised the critical temperatures at ambient conditions (up to 93 and 43 K respectively) by producing radically different structures with respect to conventional superconductors.

Another approach is instead to apply external stimuli that can tune important structural or electronic paramters and possibly lead to a higher T_c. Within a given structure, important tuning parameters for the superconducting T_c are both chemical doping (e.g. Ref. [102] and references therein) and pressure [272–276], that represented so far the unique tools to increase T_c in equilibrium conditions. Especially the application of pressure up to 45 GPa led to the current record T_c of 164 K in a bulk Hg-cuprate [274].

In the last decade, thanks to substantial technological advancements in light sources and measurement protocols, nonequilibrium studies of superconductivity have acquired a special role in the quest for a higher T_c. Ultrafast pump-probe experiments allowed not only to gain new insights on the relevant couplings in high-T_c superconductors [277] but also opened new perspectives for actually controlling their electronic states and thus pave the way towards a higher T_c.

A class of recent experiments on several cuprate compounds showed that strong midinfrared and THz excitations resonant with structural phonons [46, 48, 49, 54, 278, 279] or with particular interlayer resonances (also named Josephson plasmons) [21, 55] can actually induce a highly coherent state above the equilibrium transition temperature or even gate the Cooper pair transport among different planes.

A natural extension is to resonantly excite phonons in conventional superconductors where lattice degrees of freedom are not only able to perturb or distort the equilibrium structure, but are the main players in defining the pairing interaction. Since pairing phonon modes have even symmetry, they cannot be excited with linear dipole interaction and thus simple infrared absorption of the pump pulse. An alternative excitation mechanism relies on nonlinear phonon coupling, where higher order terms in the atomic displacement along an IR normal mode coordinate (Q_{IR}) can couple to Raman active mode displacements (Q_{R}), e.g. through a $Q_{\mathrm{IR}}^2 Q_{\mathrm{R}}$ in the interaction potential [44, 45, 52, 54, 280]. This kind of excitation requires intense midinfrared fields that can unfold the anharmonicity of the infrared active mode and, since we aim to follow this path, the experiments presented in

this chapter are mainly in the mJ/cm^2 excitation regime.

In the case of A_3C_{60}, the relatively high transition temperatures, the peculiar nature of both the normal and superconducting states outlined in Chapter 3, and the simultaneous relevance of high energy molecular vibrations and electronic correlations offer an ideal testbed for vibrational excitation studies of a BCS-like superconductor.

The core idea of these experiments is sketched in Fig. 5.1. A strong midinfrared

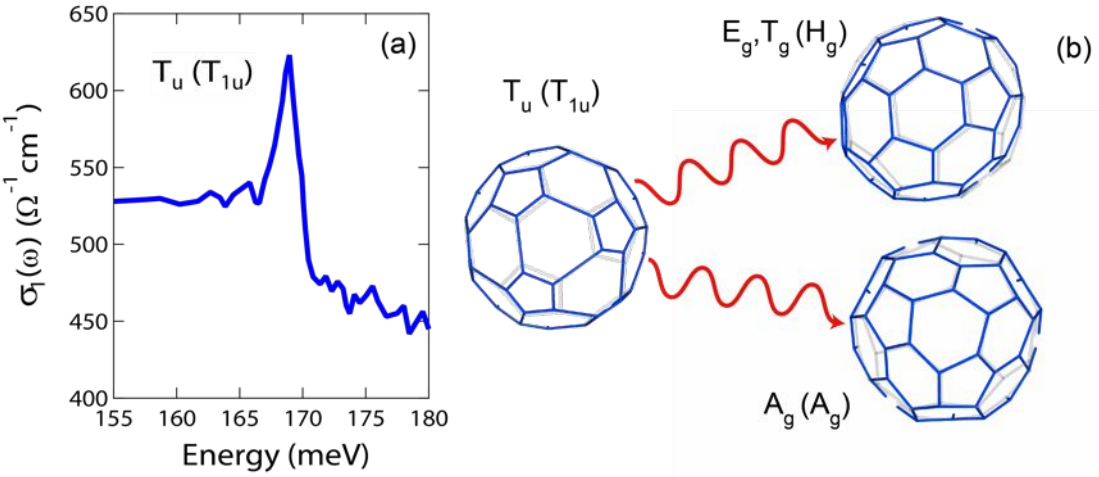

FIGURE 5.1: **K_3C_{60} T_u ($T_{1u}(4)$) phonon and possible Raman mode couplings**. Panel (a) shows the T_u mode in the infrared spectrum of K_3C_{60} measured by Iwasa *et al.* [232]. Panel (b) shows instead possible couplings between the T_u ($T_{1u}(4)$) mode and Raman vibrations of the C_{60}^{3-} molecules. The distorted structure associated with each mode and for a 9% change of the C-C bond length are shown as blue lines while the equilibrium structure is depicted in light grey. Distorted structures have been kindly provided by Dr. Alaska Subedi.

pulse centered at the IR active T_{1u} molecular vibration, having a tangential character and a 170 meV energy, drives the mode enough to rectify it and displaces the C atoms on each C_{60} molecule along a Raman-active vibration coordinate symmetry-compatible with a T_{1u}^2 coupling term. In the icosahedral point group I_h describing the C_{60} molecule, the rectification of the IR mode can occur along an A_g Raman coordinate (mainly radial direction), an H_g one (Jahn-Teller modes relevant to the SC pairing), or a T_{1g} mode. The coupling between the rectified T_{1u} mode and these Raman modes is not yet known, but a possible coupling to A_g or H_g modes could lead to some interesting scenarios (T_{1g} modes are not coupled because of symmetry reasons [160, 242]). In case a displacement is induced along the A_g coordinate, the C_{60} molecules would transiently expand along their radial

direction. While the molecular orbitals would be certainly affected by this expansion, also the intermolecular hopping, and thus the bandwidth at the Fermi level, could be changed with obvious consequences on the superconducting properties.
A second scenario is the one where the largest effect comes from the coupling to H_g modes. They govern the balancing between Hund's correlation and Jahn-Teller interaction, but they are also believed to be the main coupling modes in the Cooper channel (see Chapter 3). A change in the population of these modes induced by the pump would probably lead to sizable changes in the superconducting transition.
In both cases, the delicate interplay between electronic and vibrational degrees of freedom suggests the possibility of inducing changes in both the normal and superconducting state and, thus, to control the superconducting transition boundary in a completely different fashion than what has been done in the past in other conventional superconductors [12, 56, 281–284] or with cuprates [21, 46, 48, 49, 54, 55, 278, 279].

5.2 Characterization of the K_3C_{60} powders equilibrium optical properties

5.2.1 Normal state optical properties

Prior to the analysis of the time-resolved experiments, we discuss the equilibrium optical properties of the K_3C_{60} samples used in this work. These powders are compacted in an inert Ar atmosphere and enclosed in a sealed sample holder (similar to the one sketched in Fig. A.16) that provides optical access through an infrared grade diamond window (IIac, 1.5 mm thickness, 2 mm culet diameter), with the same protocol discussed in section A.5.4. The sample has been then placed inside a He flow cryostat (Helitran) with thin (50 μm thickness) polypropilene windows for the entire measurement.
Broadband infrared reflectivity data in the normal state have been measured between 4 and 1000 meV and for a temperature of approximately 25 K, therefore above the critical temperature of this sample (T_c=19.8 K). The measurement has been carried out with synchrotron radiation-based FITR spectroscopy (SISSI

beamline, Elettra Synchrotron, Trieste, Italy), as described in section A.3 [1].
The minimum temperature achieved in that experiment was 25 K, therefore all the broadband reflectivity curves are measured above T_c. Each spectrum has been referenced against the diamond-vacuum interface, and at the end of the measurement run the curves have been referenced against the reflectivity of a gold mirror placed at the sample position. Being relative to the normal state, our data have been extrapolated below 3-4 meV with an Hagen-Rubens type behavior, $R(\omega) = 1 - (2\omega/\pi\sigma_{DC})^{0.385}$, with the exponent and the σ_{DC} calibrated to allow a smooth connection between the experimental data and the low frequency extrapolation. High frequency extrapolations have been instead performed by recalculating the sample-diamond reflectivity from single crystal data provided by Prof. L. Degiorgi up to 6 eV.
The obtained full-range reflectivity at the sample-diamond interface is then used to calculate the optical conductivity $\sigma_1(\omega)$ through a standard Kramers-Kronig algorithm for samples in contact with a transparent window (see Appendix B). The β parameter for the Kramers-Kronig transformation is kept fixed at 217 meV by optimizing the center frequency and the weight of the FIR absorption band with respect to reference data on single crystal K_3C_{60} measured by Degiorgi *et al.* and reported in Fig. 3.6.
In order to quantitatively compare our data with previous studies (e.g. Ref. [185–187, 230–232]), we modeled the low energy ($\hbar\omega < 200$ meV) part of the dielectric function in the normal state with a Drude term (D) and a Lorentz oscillator (G) accounting for the 55 meV absorption with the same model used in [185]

$$\epsilon(\omega) = \epsilon_\infty + \left[\frac{\omega_{PG}^2}{\omega_G^2 - \omega^2 - i\omega\gamma_G} - \frac{\omega_{PD}^2}{\omega(\omega + i\gamma_D)} \right]. \tag{5.1}$$

where ϵ_∞ is the high frequency contribution to the dielectric constant, ω_{PG} and ω_{PD} are the plasma frequencies of the 55 meV absorption band and of the Drude respectively, while γ_{G} and γ_D are their relaxation rates and ω_{G} the band center frequency. A sample fit is shown in Fig. 5.2, together with the optical properties measured at different temperatures.
The corresponding fit parameters are listed in Table 5.1.
Our data present a lower far-infrared spectral weight (quantified by the plasma frequencies of both the Drude and the FIR band) with respect to the one reported

[1] In this case no pressure is applied

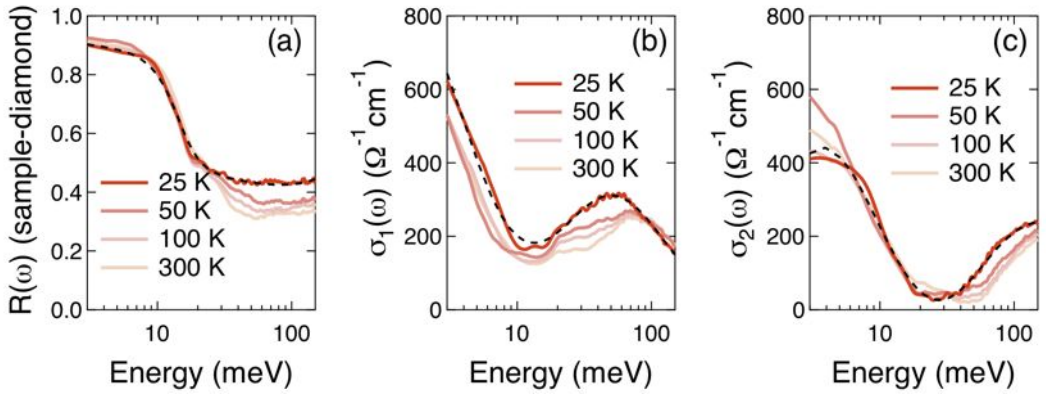

FIGURE 5.2: **Temperature dependence of K_3C_{60} optical properties in the normal state**. Panels (a)-(c) show respectively the normal state reflectivity (sample-diamond interface), real and imaginary part of the optical conductivity for selected temperatures (solid lines). A sample fit in the low energy region of the optical response ($\hbar\omega < 200$ meV) is shown for the 25 K data with a black dashed line.

in Ref. [185]. Both the Drude and the G oscillator have a plasma frequency approximately halved with respect to the values in Ref. [185] (411 and 1102 meV), but their relative ratio is compatible with the finding that roughly 92% of the carriers is localized in the G band, instead of contributing to the metallic transport. This low spectral weight can be attributed to the granularity of the powders that contributes to lower the carrier density and that is certainly relevant in this case. Moreover, the scattering rate of the Drude carriers is strongly reduced from a single crystal value of 17 meV [185] to our value of 3-4 meV. Under the assumption that the scattering rate is affected by the carrier density [285], we can interpret this reduction as originating from the lower electronic density. Intuitively, a lower carrier density can translate into a lower electron-electron scattering and therefore a longer scattering time. A second possible explanation for this phenomenon is related to the influence of powder grain boundaries that tend to localize the charges and can also play a role in determining the global carrier scattering rate.

Our samples present a weak temperature dependence of the Drude feature (compatible with observations on thin film samples [286]), while the G band shows a gradual evolution from a single Lorentzian shape to a double peak structure with a blue-shifted center frequency. The investigation of the origin and the changes of this FIR band is beyond the scope of our work and, in the rest of this chapter, we will focus on the Drude part of the conductivity spectrum.

We do not detect higher energy oscillators and also the ϵ_∞ is reduced from the single crystal value of 5 [185], but in this case the light scattering on the irregular

T (K)	ϵ_∞	ω_{PG} (meV)	ω_G (meV)	γ_G (meV)	ω_{PD} (meV)	γ_D (meV)
25	2.021	542.17	51.811	129.57	172.80	4.046
	±0.016	±0.40	±0.058	±0.24	±0.13	±0.090
50	1.123	613.9	57.16	197.8	152.25	2.2064
	±0.044	±1.7	±0.22	±1.4	±0.21	±0.0083
100	1.251	615.7	65.91	205.5	155.50	3.234
	±0.037	±1.6	±0.20	±1.3	±0.22	±0.012
200	1.253	591.0	57.29	172.9	163.52	2.6430
	±0.042	±1.4	±0.18	±1.0	±0.22	±0.0094
300	1.442	609.4	70.96	214.0	155.45	2.880
	±0.050	±2.3	±0.29	±1.9	±0.26	±0.013

TABLE 5.1: **K_3C_{60} normal state low energy parameters at various temperatures**. Fit parameter for the low energy infrared spectrum of the K_3C_{60} powders used in this experiment. The parameters are defined in the text.

powder facets is the expected to be the main player.

We compare in Fig. 5.3a the reflectivity spectrum at the sample-vacuum interface (in our case, recalculated from the complex refractive index) of single crystal data provided by Prof. L. Degiorgi and for our very sample.

Even if our data are in qualitative agreement with the single crystal curve, we can notice an increasing difference between the two curves for increasing photon energy. This effect can be partly due to surface scattering that is important for near infrared and visible wavelengths [287] but in the far-infrared region (<200 meV) the difference seems to be related to an intrinsic, quantitative difference of the powder transport properties with respect to the single crystal specimens.

An important quantity for the analysis of the time-resolved data[2] that is also affected by the granularity of our samples is the penetration depth ($l_p(\omega) = c/2\kappa\omega$) and in our powder pellets is larger than in single crystal data (see Fig. 5.3). In the pump energy region (between 100 and 200 meV), the penetration depth is quite featureless and about a factor two larger than in single crystal data.

[2]In order to determine the pump-probe penetration mismatch, as summarized in section A.5.3

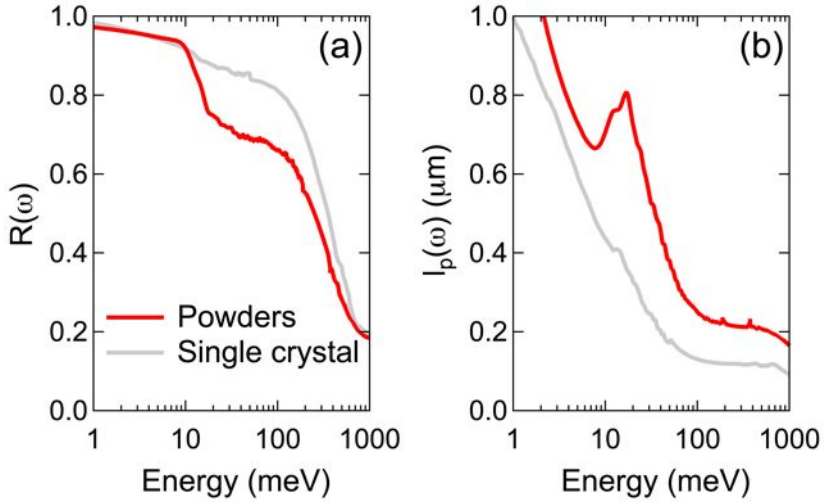

FIGURE 5.3: **Comparison between reflectivity and penetration depth for single crystal and powder K_3C_{60}.** Panel (a) shows the comparison between reference single crystal reflectivity data provided by Prof. L. Degiorgi (gray) and our powder reflectivity recalculated at the sample-vacuum interface (red). Panel (b) shows instead the corresponding penetration depth $l_p(\omega) = c/2\kappa\omega$.

5.2.2 Temperature dependence of the optical properties in the superconducting state

The reflectivity measurement of our K_3C_{60} powders below T_c is necessary for a correct referencing of the transient reflectivity data discussed later in this chapter, but also for testing the quality of our samples. Importantly, if the sample is damaged or contaminated it is not expected to show superconductivity.

Reflectivity data below the superconducting transition temperature have been measured with the same THz-time domain spectrometer used in the time-resolved experiment. In this case the reflected THz field is referenced against the reflected field at 25 K (normal state) and the ratio between the reflectivity in the superconducting (S) and normal (N) state is simply given by $R_S/R_N = |E_S(\omega)/E_N(\omega)|^2$. This ratio is then multiplied by the measured normal state reflectivity, thus giving the absolute reflectivity of the superconducting K_3C_{60}. In Fig. 5.4a, we show the ratio between reflectivities $R(T)$ at temperatures below and above T_c and the reflectivity just above T_c, $R(20\,\mathrm{K})$ as measured with our THz-time domain spectrometer, while in Fig. 5.4b-c we report the recalculated reflectivity. From previous spectroscopic measurements (e.g. Refs. [185–187, 230]), it is known that across the transition the main spectral changes occur at photon energies below

$3\Delta(T)$ and higher energy portions of the K_3C_{60} spectrum are unaffected, therefore our measurements are sufficient for the determination of the optical response below T_c.

Due to limitations of our THz time-domain spectrometer, we cannot reliably

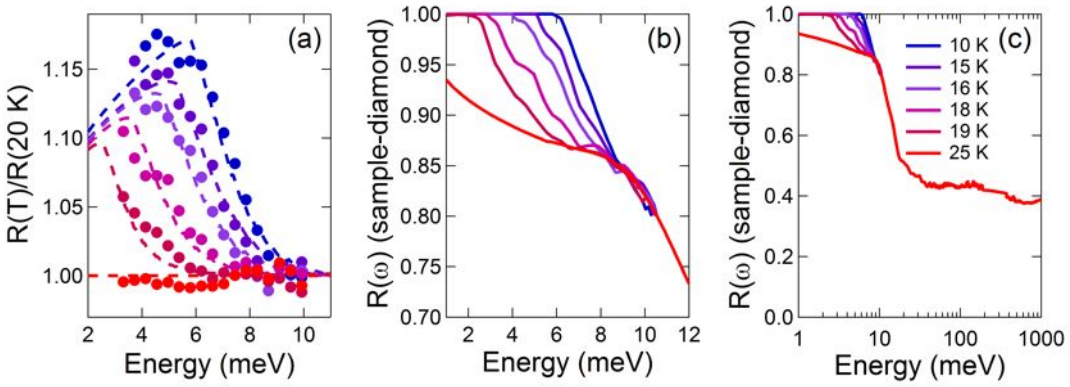

FIGURE 5.4: **Equilibrium reflectivity of K_3C_{60} powders below the superconducting transition temperature**. Panel (a) shows THz time-domain measurements of the reflectivity ratio between superconducting and normal state for several temperatures. Filled circles represent the experimental data, while the dashed lines are fits to the data with Zimmermann formulas. Panel (b) shows the recalculated absolute reflectivity of K_3C_{60} in the THz region, while panel (c) shows the resulting broadband reflectivity.

measure below 3 meV and we need to extrapolate the data through a fitting of the $R(T)/R(20\,\mathrm{K})$ data. The fit function is constituted by a reflectivity ratio where the normal state dielectric function is modeled as in eq. (5.1) and its changes across the transition are determined with a modification of the Mattis-Bardeen formulas for BCS superconductors with a Drude scattering rate γ_D comparable with the gap energy Δ[3] due to Zimmermann *et al.* [288]. The starting parameters for this fits are the one for the 25 K optical response listed in Table 5.1, while the only two free parameters are the ratio T/T_c and the gap parameter $\Delta(T)$. The fit function for the optical conductivity in the superconducting state is reported in Ref. [288] and takes into account the contributions to the conductivity of Cooper pairs, but also thermally and photon excited quasiparticles. The experimental data, extrapolated with the fit, are then multiplied by the equilibrium reflectivity at 25 K (normal state) and we, thus, obtain the absolute reflectivity of the samples below T_c. When the reflectivity approaches the 100% line, we extrapolate to 1.0 down to zero energy in order to avoid unphysical artifacts in the optical conductivity (as reported in other references, e.g. Ref. [185]). Due to the relative

[3]In our case $\gamma_D \simeq \Delta$.

noise of the THz time-domain measurement (approx. 1.0%), we are not sensitive to the small deviations from a perfect reflectivity that signal the recovery of the Drude component of the optical spectrum and our data can just capture the gap closure but not its filling. These reflectivity data are then used to obtain the full optical conductivity through Kramers-Kronig relations with the same $\beta = 217$ meV parameter used for the normal state. The resulting optical conductivity is shown in Fig. 5.5 As visible in Fig. 5.5a, upon crossing the superconducting tran-

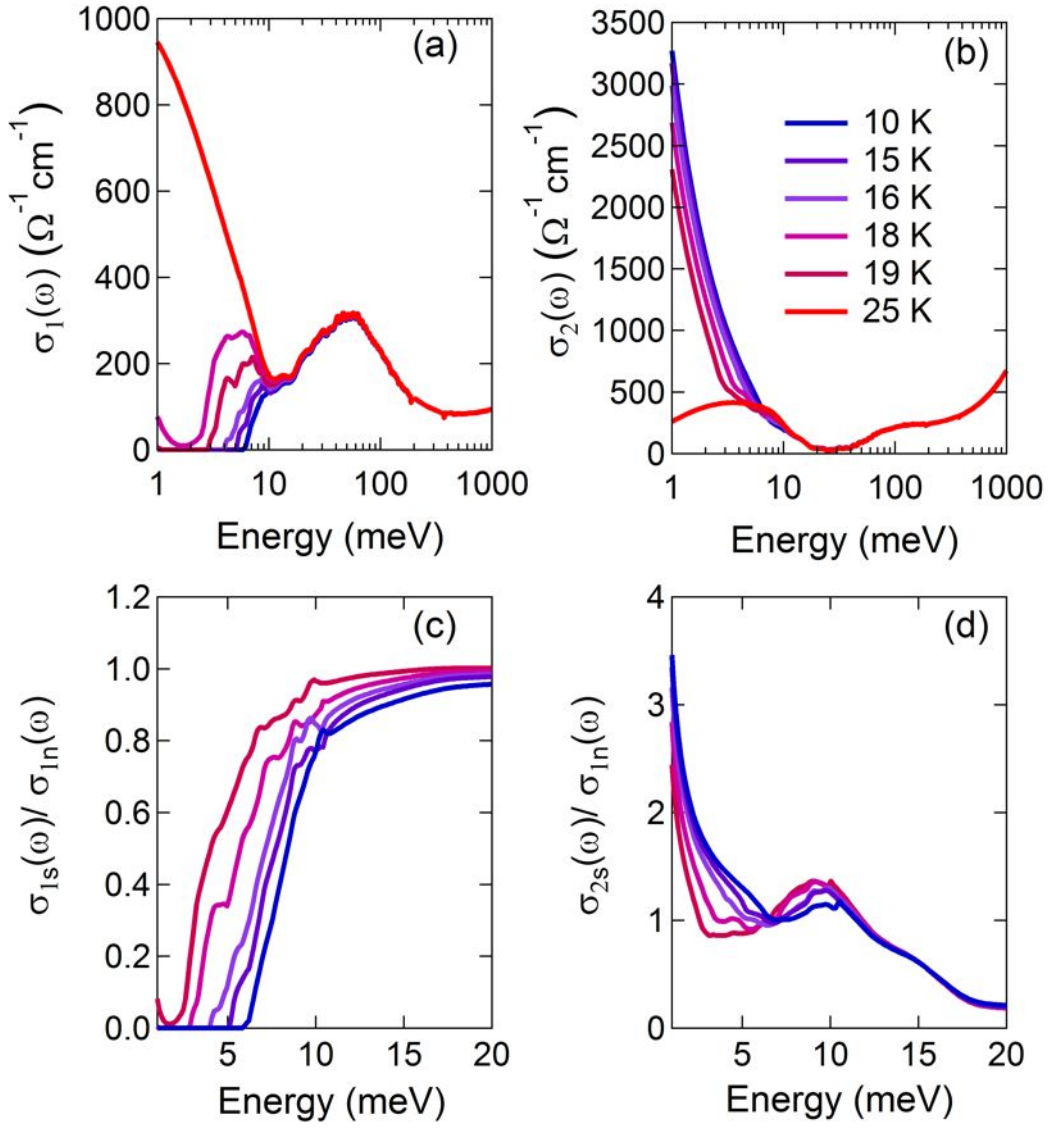

FIGURE 5.5: **Equilibrium optical conductivity of K_3C_{60} powders below the superconducting transition temperature**. Panels (a) and (b) show the real and imaginary part of the optical conductivity for the K_3C_{60} powders used in the pump-probe experiment for several temperatures. Panels (c) and (d) show instead the ratios σ_{1s}/σ_{1n} and σ_{2s}/σ_{1n}.

sition boundary the real part of the optical conductivity, $\sigma_1(\omega)$, develops a fully

opened gap and the spectral weight of the Drude is collapsed into the δ function at zero energy, while the imaginary part $\sigma_2(\omega)$ becomes divergent, as described in section 3.4.2. As the temperature is raised the gap closes, reducing its value from 6 meV at 10 K to 3 meV at 19 K and the Drude is partially reconstructed. The ratios $\sigma_{1s}(\omega)/\sigma_{1n}(\omega)$ and $\sigma_{2s}(\omega)/\sigma_{1n}(\omega)$ (shown in Fig. 5.5c-d) follow instead the characteristic Mattis-Bardeen behavior exhibited by single crystal data reported in Fig. 3.6, showing the gradual gap closure in $\sigma_1(\omega)$ and the suppression of the divergence in $\sigma_2(\omega)$.

As a last element to this picture, we compare the temperature dependent value of the gap with previous observations in order to evaluate the consistency of this trend with the know behavior of K_3C_{60}. Values of the gap parameter coming from the Zimmermann fit of the reflectivity ratio in Fig. 5.4 normalized to the literature value of 6 meV [185] are shown in Fig. 5.6. Our data follow quite closely the expected mean field behavior predicted for BCS superconductors in weak coupling [220, 236, 289]

$$\frac{\Delta(T)}{\Delta(0)} = \tanh\left(\frac{\pi}{\Delta(0}\sqrt{\frac{T_c}{T}-1}\right) \tag{5.2}$$

and are consistent with previous data coming from both optical and tunneling studies. From these measurements, we can conclude that our samples present

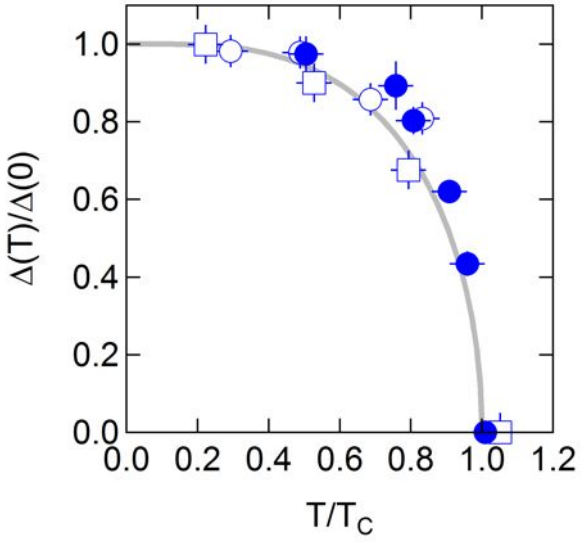

FIGURE 5.6: **Temperature dependence of the K_3C_{60} equilibrium gap**. Superconducting gap of the K_3C_{60} powders used in this experiment as a function of the reduced temperature T/T_C. Empty symbols are data from previous optical (circles) and tunneling experiments (squares) [185, 221]. Filled symbols are the gap extracted from the fit of the reflectivity ratios in Fig. 5.4a.

a clear superconducting transition in their optical spectrum and we are able to quantitatively assess changes of the transport properties in the THz region.

5.3 Nonequilibrium dynamics below T_c

The nonequilibrium response of K_3C_{60} under resonant phonon excitation has been measured with a MIR pump-THz probe experiment at several temperatures above and below T_c. The experimental details are extensively discussed in Appendix A, but, following the idea outlined at the beginning of this chapter, we excited the sample with strong s-polarized MIR pulses (170 meV) and probed the pump-induced changes in the optical response close the equilibrium gap region with delayed p-polarized THz pulses ranging from 2 to 11 meV. With our pulses we can achieve a time resolution of approximately 300 fs, while our frequency resolution is typically 0.1 THz. The optical response of K_3C_{60} for equilibrium temperatures below T_c recalls the ones previously observed in other superconductors [41, 290] in the case of photoinduced pair breaking and relaxation. When looking to the pump-induced changes at the peak of the reflected field in the time-domain (see Fig. 5.7), we observe a response with a slow buildup (compared to the pulse duration) and a single exponential relaxation towards equilibrium. The sign of the reflectivity change is negative, therefore the pump induces a decrease of the reflectivity. This response can be interpreted as a pump-induced pair breaking and described in terms of a Rothwarf-Taylor model [41, 290–292].
The hot electrons excited by the pump are initially releasing energy through emission of optical phonons that induce Cooper pair breaking. Assuming a change of reflectivity directly proportional to the number of quasiparticles $n(t_d)$ (t_d is the pump-probe time delay), we can model the response buildup as [41, 290]

$$\Delta E \propto n(t_d) = \frac{\beta}{R}\left[-\frac{1}{4} - \frac{1}{2\tau} + \frac{1}{\tau}\frac{1}{1 - K\exp(-t_d\beta/\tau)}\right] \tag{5.3}$$

In this expression β is the transition probability for the breaking of pairs by high frequency phonons, R is the bare quasiparticle recombination rate, while τ and K are dimensionless parameters related to the initial quasiparticle (n_0) and phonon

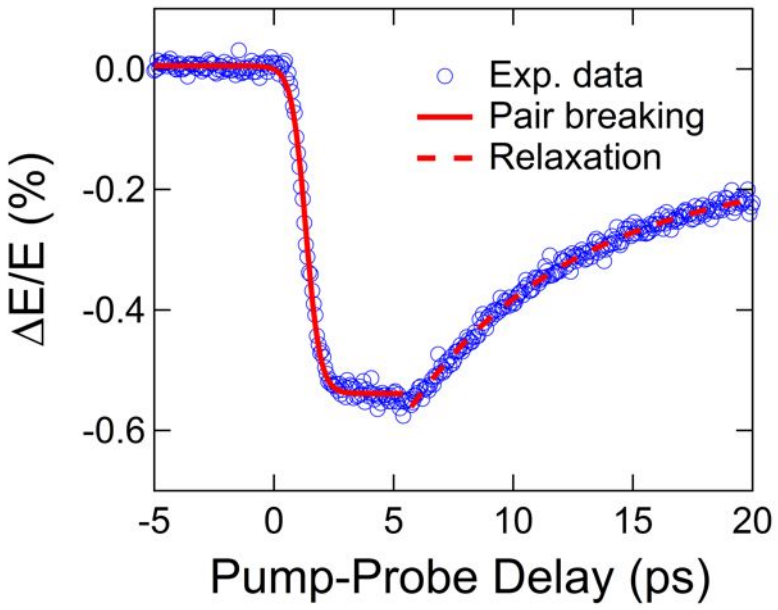

FIGURE 5.7: **Relaxation of the K_3C_{60} photoexcited state at 10 K under resonant MIR excitation**. Example of scan along the pump-probe delay axis (at the top of the reflected EOS in time domain) for K_3C_{60} at 10 K under a MIR pump excitation with 170 meV energy and 0.4 mJ/cm^2 incident fluence. The pump induced changes ΔE are normalized to the equilibrium reflected field E. The data (blue circles) are fitted with a Rothwarf-Taylor profile (red solid line) and a subsequent exponential decay (red dashed line).

(N_0) populations

$$\frac{1}{\tau} = \sqrt{\frac{1}{4} + \frac{2R}{\beta}(n_0 + 2N_0)} \tag{5.4}$$

$$K = \frac{\frac{\tau}{2}(\frac{4Rn_0}{\beta} + 1) - 1}{\frac{\tau}{2}(\frac{4Rn_0}{\beta} + 1) + 1}. \tag{5.5}$$

When fitting the pump-induces response up to 5 ps after the pump arrival, we get a characteristic time $\tau/\beta = (0.2958 \pm 0.0074)$ ps and a dimensionless K parameter $K = (-0.986 \pm 0.020)$.

An extraction of the microscopic parameters R and β would require a study of the response for variable excitation density [290] that goes beyond the purpose of our study, but we can notice that the obtained K parameter positions the sample response in a regime ($-1 \leq K < 0$) where the initial temperature of the optical phonons is higher than the quasi-equilibrium one reached at the top of the response.

The recovery of the superconducting state happens instead with a single expo-

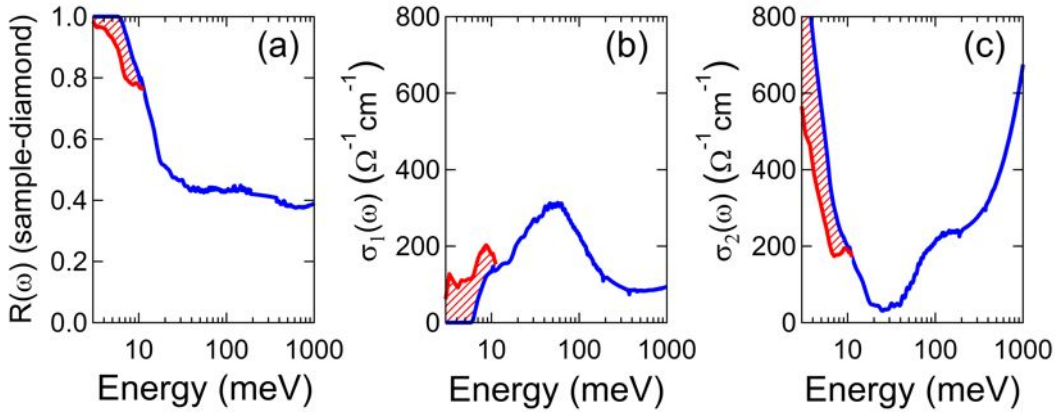

FIGURE 5.8: **Nonequilibrium optical properties of K_3C_{60} at 10 K under resonant MIR excitation**. Panel (a), (b), (c) show respectively the reflectivity at the sample-diamond interface, the real and the imaginary part of the optical conductivity K_3C_{60} in the THz region under excitation with 170 meV light pulses (0.4 mJ/cm^2 fluence) at 3 ps from the pump arrival. Blue curves are the equilibrium optical properties, red curves are the ones in the photoexcited state. Shaded areas mark the main differences between the equilibrium and the photoinduced optical properties.

nential decay and an almost metastable component. The characteristic timescale for this decay is $\tau_R = (7.11 \pm 0.19)$ ps, i.e. an order of magnitude smaller than in other BCS superconductors [41, 290].

The spectrally resolved measurements (at 3 ps after the pump arrival) are validating the picture of a pump-induced pair breaking (see Fig. 5.8). After photoexcitation, the reflectivity is decreasing in all the probed range, while the gap in $\sigma_1(\omega)$ is partially filled and the divergent $\sigma_2(\omega)$ (quantifying the superfluid density) is depleted. These changes are consistent with a partial light-induced superconductor-to-metal transition. The time-dependent optical properties appear to have a monotonic dependence, but the observed gap filling is different from a thermally-driven transition. In the equilibrium superconductior-to-metal transition, the gap in the real part of the optical conductivity closes with a redshift of the gap edge and a reconstruction of the Drude peak [234]. In our case, the light-driven gap closure (Fig. 5.9b) occurs without a significant shift of the gap edge (always located at 6 meV), but rather with a sudden increase of in-gap spectral weight.

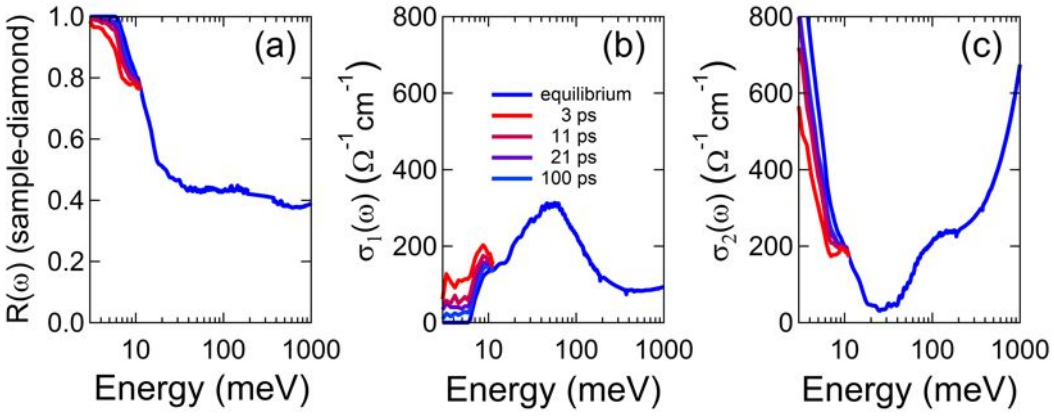

FIGURE 5.9: **Time dependent optical properties of the K_3C_{60} photoexcited state at 10 K under resonant MIR excitation**. Panel (a), (b), (c) show respectively the reflectivity at the sample-diamond interface, the real and the imaginary part of the optical conductivity K_3C_{60} in the THz region under excitation with 170 meV light pulses (0.4 mJ/cm^2 fluence) and at several pump-probe time delays.

5.4 Nonequilibrium dynamics above T_c

The electronic response of K_3C_{60} at 25 K, as visible by looking to the pump-induced changes at the peak of the reflected field in the time-domain (see Fig. 5.10), is prompt: it follows the pump pulse profile (risetime 0.3269±0.0098 ps) and decays back with a double exponential process towards a nearly metastable state, in a way qualitatively similar to what observed in [244, 245]. A direct comparison with the dynamics observed below T_c, shown in Fig. 5.10a, reveals a faster response both in the buildup and in the decay. By fitting this curve with a function of the type (4.21), we can obtain a characteristic decay time of 0.650±0.034 ps for the first decay process (shaded area), while the second exponential decay has a time constant of 9.6±1.8 ps. A third decay component, much longer lived, is also present and is modeled in our analysis as a metastable state.

The sign of the pump induced changes is positive, therefore corresponds to an increase in the sample reflectivity. The sign of the reflectivity change (opposite with respect to the one observed below T_c), the faster dynamics and the double exponential decay, as opposed to the single exponential decay observed below T_c, indicate a different photoinduced process above and below the critical temperature and, with the THz-time resolved technique, we can spectrally resolve this light induced changes to determine the nature of the increased reflectivity state.

The spectrally resolved measurement at the peak of the pump induced response

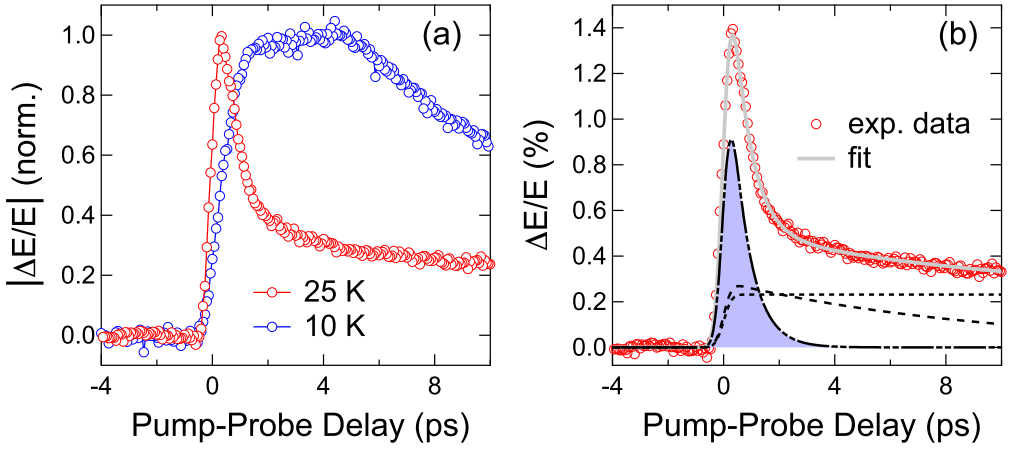

FIGURE 5.10: **Relaxation of the K_3C_{60} photoexcited state at 25 K under resonant MIR excitation**. Panel (a) shows a direct comparison between scans along the pump-probe delay axis (at the top of the reflected EOS in time domain) for K_3C_{60} at 25 K (red) and 10 K (blue) under a MIR pump excitation with 170 meV energy and 1.0 mJ/cm^2 and 0.4 mJ/cm^2 incident fluence, respectively. The pump-probe changes are normalized to their peak value. Panel (b) shows the pump induced changes ΔE at 25 K reported in panel (a) and normalized to the equilibrium reflected field E. The data (red circles) are fitted with a double exponential profile (gray), while below are represented the various components of the relaxation process (black lines). The fast decay process is indicated with a shaded area.

(approximately 1.0 ps after the pump arrival) reveals a quite surprising effect in the complex optical properties and represents, perhaps, the most relevant observation of the present study. As shown in Fig. 5.11, at the peak of the sample response the reflectivity is saturated to 1, while there is a robust loss of spectral weight in $\sigma_1(\omega)$ and an increase in $\sigma_2(\omega)$. These changes are qualitatively similar to the ones observed in the equilibrium superconducting transition shown earlier in the chapter, but are occurring at 5 K above the equilibrium transition temperature. The spectral weight loss in $\sigma_1(\omega)$ is compatible with a gap opening and a weight transfer to the δ peak at zero energy associated with supercurrents. Importantly, in all our measurements we get a characteristic conductivity increase towards zero energy. While in equilibrium measurements, this spectral feature is usually associated with thermally activated transport [220, 234], in our experiments the attribution is not so straightforward. In our view, this low energy behavior of $\sigma_1(\omega)$ is instead connected to the finite response and decay times of the effects we observe and to the more fundamental question related to the time needed for a gap to open.

In a quite intuitive way, the gap opening (and a zero conductivity) below 4 meV is

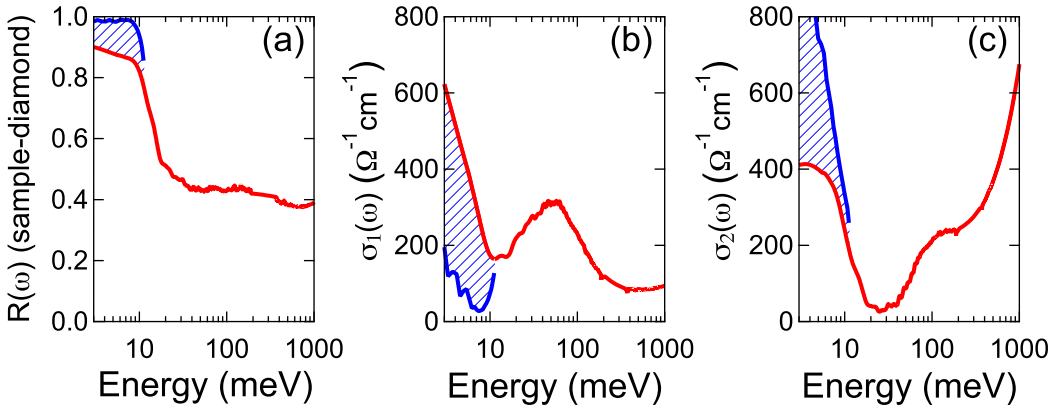

FIGURE 5.11: **Nonequilibrium optical properties of K_3C_{60} at 25 K under resonant MIR excitation**. Panel (a), (b), (c) show respectively the reflectivity at the sample-diamond interface, the real and the imaginary part of the optical conductivity K_3C_{60} in the THz region under excitation with 170 meV light pulses (1.0 mJ/cm^2 fluence) at 1 ps from the pump arrival. Red curves are the equilibrium optical properties, blue curves are the ones in the photoexcited state. Shaded areas mark the main differences between the equilibrium and the photoinduced optical properties.

associated with a characteristic timescale approximately larger than 1 ps, therefore a snapshot of the collective electronic motion taken at 1 ps (or less) will likely capture a state where the lower energy response is still building up. The gap opening will be not complete and this will lead to an in gap content as the one observed in Fig. 5.11.

In addition to the finite response time to the photoexcitation, this transient state has also a finite lifetime, as shown in Fig. 5.12. By inspecting the complete optical response of this state, we can trace two distinct regimes: at very short pump-probe delays (less than 2 ps) the material exhibits a saturated, flat reflectivity, a gap opening, and a strongly enhanced $\sigma_2(\omega)$ in a fashion similar to a superconducting transition. At longer delays, the gap is completely filled and the material responds as a more conventional Drude-like system. The finite lifetime of the gapped state is likely contributing in defining the shape of the gap (as previously discussed). Since the excited state decays with an extremely short timescale (less than 1.0 ps), the spectral response below 4 meV ($\sim$ 1 ps oscillation period) is convolved with the relaxation process and does not react as strongly as higher energy part of the THz spectrum (i.e. from 6 to 10 meV). The presence of two distinct decay regimes in the spectrally resolved optical response mirrors the two decay processes observed already in the pump-probe scan reported in Fig. 5.10 and in the following of the chapter we will mainly devote our attention to the short

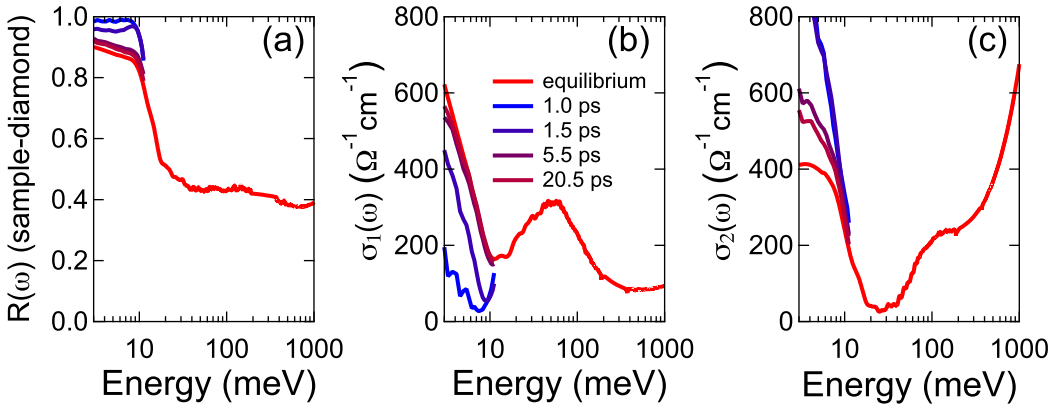

FIGURE 5.12: **Time dependent optical properties of the K_3C_{60} photoexcited state at 25 K under resonant MIR excitation**. Panel (a), (b), (c) show respectively the reflectivity at the sample-diamond interface, the real and the imaginary part of the optical conductivity K_3C_{60} in the THz region under excitation with 170 meV light pulses (1.0 mJ/cm^2 fluence) and at several pump-probe time delays.

lived component of the light-induced response.

5.5 Characterization of the photoinduced response above T_c

In this section, we describe the dependence of the photoinduced response above T_c upon several parameters with the aim to elucidate the nature of the photoinduced transition.

In order to quantify the behavior of the excited state, we perform a global fit of the optical properties (in the temperature dependence section) but we also rely on spectral weight arguments. The quantity we are going to discuss the most is the spectral weight change in $\sigma_1(\omega)$ defined as

$$\Delta\sigma_1 = \int_{3\text{ meV}}^{11\text{ meV}} \left[\sigma_1(\omega)\Big|_{\text{eq}} - \sigma_1(\omega)\Big|_{1\text{ ps}} \right] d\omega. \tag{5.6}$$

where we limit the integration to the usable spectral bandwidth of our THz probe. This quantity is model independent and can efficiently capture spectral changes across the superconducting transition. In equilibrium superconductivity, the spectral weight change can be shown to be directly proportional to the superfluid

density n_s [185, 220]

$$\Delta\sigma_1 = \int_0^\infty \Big[\sigma_{1n}(\omega) - \sigma_{1s}(\omega)\Big] d\omega = \frac{c^2}{8\lambda^2} = \frac{\pi}{2}\frac{n_s e^2}{m} \tag{5.7}$$

where c is the speed of light in vacuum, e and m are the bare electron charge and mass.

This last relation is exact with an integration spanning from zero to infinite energy, but a common practical approach is to introduce a cutoff that is a multiple of the gap value, since for $\hbar\omega \leq 6\Delta$ the difference between σ_{1s} and σ_{1n} becomes negligible. Remarkably, the spectral weight is also proportional to the the quantity $\omega\sigma_2(\omega)$ that is also often used as an estimate for the superfluid density. More specifically, $\Delta\sigma_1 = \frac{\pi}{2}\lim_{\hbar\omega\to 0}\omega\sigma_2(\omega)$.

5.5.1 Temperature dependence of the transient response above T_c

The behavior of the photoinduced state for different equilibrium temperatures and under the same excitation fluence of 1.0 mJ/cm^2 shows two qualitatively different regimes. For a base temperature of 25 K and 100 K, as shown in Fig. 5.13, the resonant MIR excitation induces a complete gap opening in $\sigma_1(\omega)$ and a strong divergence in $\sigma_2(\omega)$. The optical properties of the photoexcited state can be fitted according to a Zimmermann optical conductivity [288] and from the fit one can obtain in both cases a gap value of approximately $2\Delta = 11$ meV, almost twice the equilibrium gap $2\Delta(0) = 6$ meV, that would be suggestive of an enhanced superconducting response.

At higher temperatures, reported in Fig. 5.14, the reduction of spectral weight is less prominent than in the 25 K and 100 K datasets. At 200 K, the optical properties are still consistent with a partial gap opening, but there is already a substantial recovery of the Drude at low energy. The photoinduced response at 300 K is, instead, reduced and more similar to a Drude metal with a decreased scattering rate than to a superconductor close to its T_c. We compare for the 200 K datasets the best fit with a Zimmermann (BCS superconductor) or a Drude-Lorentz (metal) profile, by keeping most of the parameters fixed to the values reported in Table 5.1 and allowing only the Drude parameters (scattering rate and plasma frequency) to change. In the 200 K the two best fits curve are quite close (with the Zimmermann curve giving a $T/T_c \sim 0.9$). In the 300 K datasets

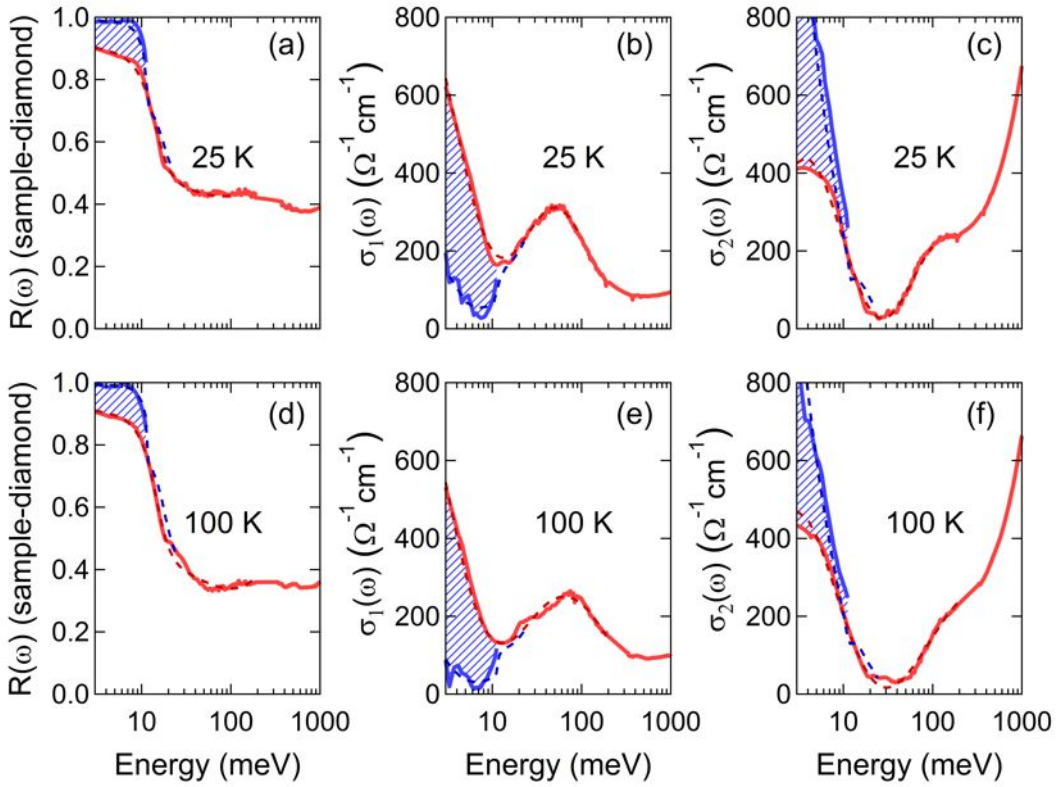

FIGURE 5.13: **Optical properties of the K_3C_{60} photoexcited state under resonant MIR excitation at 25 K and 100 K**. Reflectivity at the sample-diamond interface, real and the imaginary part of the optical conductivity K_3C_{60} in the THz region under excitation with 170 meV light pulses (1.0 mJ/cm^2 fluence) for a equilibrium temperature of 25 K (Panels (a)-(c)) and 100 K (Panels (d)-(f)). Equilibrium data are described with red solid lines, while the photoexcited state at 1.0 ps time delay is represented with blue solid lines. Fits to the normal state data (red dashed line) are carried out with the model described in section 5.2.1, while nonequilibrium data are described with a Zimmermann model (blue dashed line) [288] with a gap of approximately 11 meV and a $T/T_c \sim 0.5$. Shaded areas mark the main differences between the equilibrium and the photoinduced optical properties.

only a Drude-Lorentz description is possible.

An important observation is that the gap feature in the optical spectrum of the photoexcited state does not redshift with temperature as expected within a BCS superconducting state, it stays constant at approximately 11 meV and the only effect of temperature is to increase the thermal quasiparticles below twice the gap value. This observation is compatible with previous studies on the recovery of the superconducting state after a nonequilibrium perturbation in other conventional superconductors and can be possibly explained in terms of coexistence of superconducting and normal regions in the probed material volume [12].

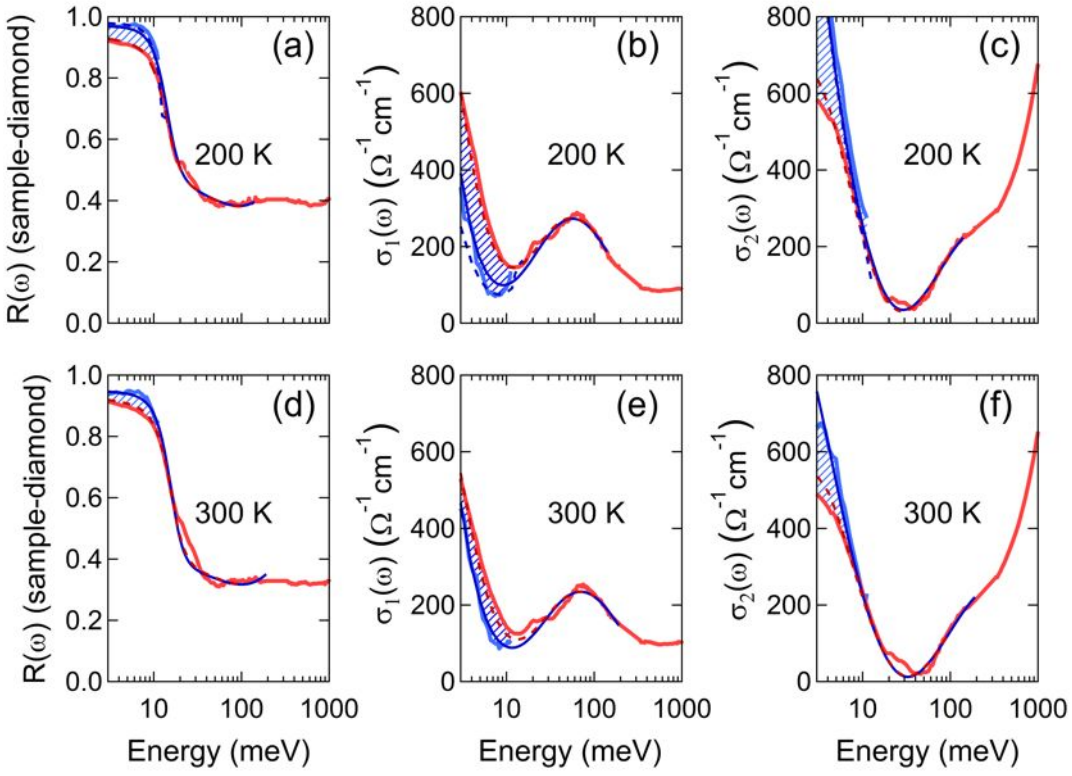

FIGURE 5.14: **Optical properties of the K_3C_{60} photoexcited state under resonant MIR excitation at 200 K and 300 K**. Reflectivity at the sample-diamond interface, real and imaginary part of the optical conductivity of K_3C_{60} in the THz region under excitation with 170 meV light pulses (1.0 mJ/cm^2 fluence) for a equilibrium temperature of 200 K (Panels (a)-(c)) and 300 K (Panels (d)-(f)). Equilibrium data are described with red solid lines, while the photoexcited state at 1.0 ps time delay is represented with blue solid lines. Fits to the normal state data (red dashed line) are carried out with the model described in section 5.2.1, while nonequilibrium data are described with a Zimmermann model (blue dashed line) [288] with a gap of approximately 11 meV and a $T/T_c \sim 0.9$ or with a Drude-Lorentz model (thin blue solid line). Shaded areas mark the main differences between the equilibrium and the photoinduced optical properties.

This analysis suggests that the MIR excitation is able to induce a state with optical properties similar to the ones of a superconductor (with a spectral weight reduction in the Drude part of the spectrum and a gap $2\Delta = 11$ meV), but, as the temperature is raised above 200 K, this effect is smoothly reduced and the resulting state is more consistent with a metal with a reduced scattering rate ($\gamma_D = 1.0$ meV at 200 K and 1.74 meV at 300 K). These findings are well captured by the temperature dependence of the spectral weight change, shown in Fig. 5.15.

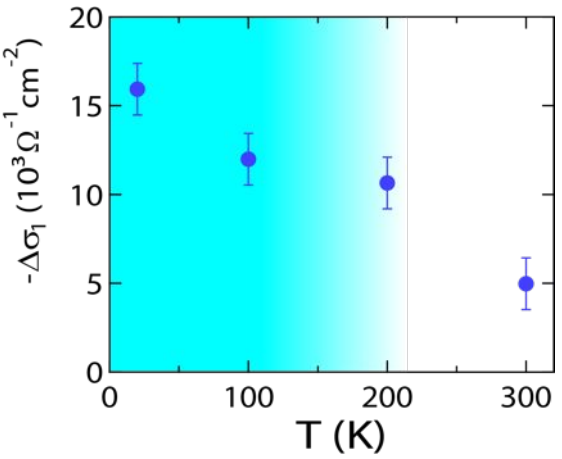

FIGURE 5.15: **Spectral weight change $\Delta\sigma_1$ at 170 meV pump energy as a function of the equilibrium temperature**. Spectral weight change in $\sigma_1(\omega)$ for variable temperature conditions and a pump energy of 170 meV. Error bars on the spectral weights are the standard deviations of repeated independent measurements. The shaded blue area corresponds to temperatures where it was possible to fit the transient response with the optical properties of a superconductor.

5.5.2 Fluence and pump energy dependence of the transient response above T_c

The transient response of K_3C_{60} at 25 K and under resonant MIR excitation at 170 meV has been studied in conditions of variable incident fluence. The results, summarized through the spectral weight change (5.6), are reported in Fig. 5.16 The fluence dependent spectral weights do not show saturation or a clear threshold in the investigated range. Saturation is, nevertheless, expected to occur at higher fluences since the entire spectral weight of the equilibrium Drude in the THz range investigated is approximately $2.2{\cdot}10^4\ \Omega^{-1}\ \mathrm{cm}^{-2}$ and the response is gradually approaching a complete depletion of the equilibrium spectral weight. A study of the response as a function of pump energy at constant fluence is also performed at 25 K for two different fluences. This dependence has been extended up to 600 meV, but, due to multiphonon absorption in the diamond window, it has not been possible to measure in the region between 220 and 500 meV.

The first important point is that the effect is not observed at 600 meV, therefore photoinduced redistribution of quasiparticles [281, 293, 294], involved in the enhancement of superconductivity at microwave [295, 296] or optical frequencies [297, 298] cannot explain our observations. The second relevant finding, especially visible in the low fluence data (far from a possible saturation regime of this

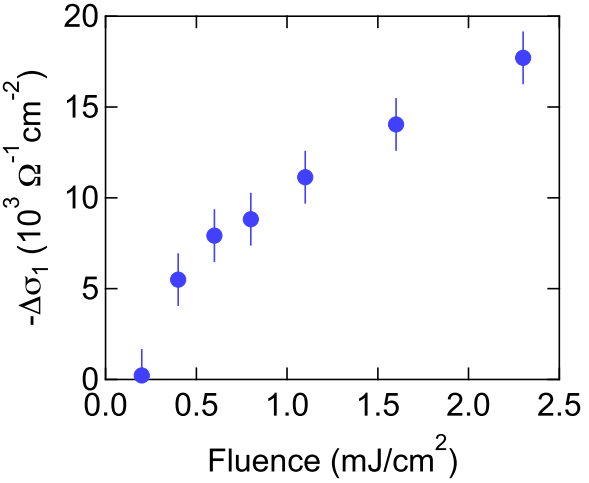

FIGURE 5.16: **Spectral weight change $\Delta\sigma_1$ at 25 K as a function of the incident fluence**. Spectral weight change in $\sigma_1(\omega)$ for variable fluence conditions for an equilibrium temperature of 25 K and a pump energy of 170 meV. Error bars on the spectral weights are the standard deviations of repeated independent measurements.

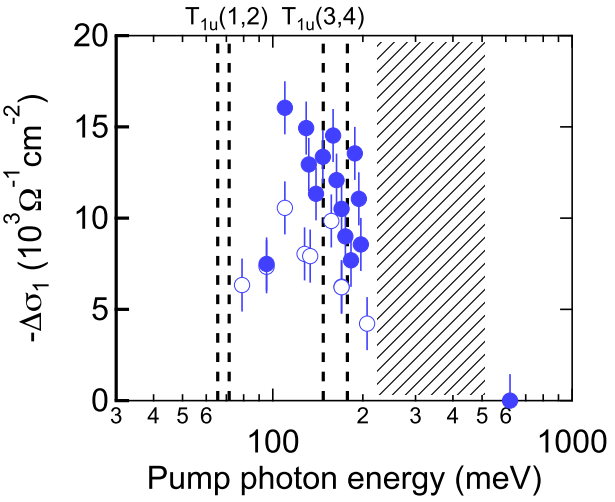

FIGURE 5.17: **Spectral weight change $\Delta\sigma_1$ at 25 K as a function of the pump photon energy**. Spectral weight change in $\sigma_1(\omega)$ for variable pump energy conditions. The equilibrium temperature is 25 K and the pump fluence is kept constant at 0.4 mJ/cm^2 (empty circles) and 1.1 mJ/cm^2. Error bars on the spectral weights are the standard deviations of repeated independent measurements.

phenomenon), is that the spectral weight change is more pronounced for energies resonant to both the highest T_{1u} phonons present in this system ($T_{1u}(3) = 138$ meV and $T_{1u}(4) = 168$ meV) and tends to decrease for lower pump energies. This resonant behavior is consistent with a picture where photoexcitation of intramolecular vibrational modes plays a key role in the observed gapping of $\sigma_1(\omega)$.

5.6 Considerations on the origin of the excited state above T_c

The characterization of the transient state above T_c, especially the pump-energy dependence, supports a picture where molecular degrees of freedom, like the intramolecular vibrations $T_{1u}(3)$ and $T_{1u}(4)$, play a role in dictating the electronic response of the nonequilibrium state. Theoretical work on the problem is still in progress, but here we can elaborate some initial considerations that may be helpful for a further understanding of the observed dynamics.

Before describing possible scenarios, it is useful to quantify the pump-induced excitation by estimating the light-induced displacements in the C_{60} molecules. The peak electric field E_0 used in these experiments is of the order of 800 kV/cm[4], while the polarization associated with one of these IR intramolecular modes[5] is given by

$$P = \frac{\sigma_1(\omega_0)}{\omega_0} E_0 \tag{5.8}$$

with $\sigma_1(\omega_0)$ indicating the peak optical conductivity of the mode (subtracted by possible electronic backgrounds) and ω_0 is the center frequency of the mode. This polarization arises from a light-induced dipole moment $P = d \cdot n \cdot Z_{eff}$, where n is the number of dipoles per unit volume, d is the dipole moment and Z_{eff} is the effective charge defined as in Ref. [299]. From literature data [232], we can estimate the polarizability to be $P = 2.35 \cdot 10^{-6} C/\mathrm{cm}^2$ and a total displacement of 0.24 Å, i.e. approximately 17% of the C-C bond amplitude[6]. Such a large atomic displacement of the C atoms on each C_{60} molecule can give rise to a number of

[4]In SI units, the relation between peak field E_0 and fluence F is

$$E_0 = \sqrt{\frac{F}{2c\epsilon_0 \Delta t}},$$

where c is the speed of light in vacuum, ϵ_0 is the vacuum permittivity and Δt is the pulse duration. In practical units, we can write

$$E\Big[\frac{MV}{\mathrm{cm}}\Big] = 0.434\sqrt{\frac{F\Big[mJ/\mathrm{cm}^2\Big]}{\Delta t[\mathrm{ps}]}}$$

.

[5]We consider here just the $T_{1u}(4)$ that is well characterized with optical spectroscopy (e.g. Ref. [232])

[6]In this calculation, we used the t_{1u} phonon parameters $\omega_p(t_{1u}) = 10.63$ meV (plasma frequency), $\omega_0(t_{1u}) = 168.62$ meV (center frequency), $\gamma(t_{1u}) = 1.95$ meV (phonon linewidth), while the $\sigma_1(\omega_0(t_{1u})) = (630 - 510) = 120\,\Omega^{-1}\,\mathrm{cm}^{-1}$ [232]. The effective charge factor Z_{eff}, estimated as in Ref. [299], is in this case $Z_{eff} = 0.147$.

nonlinear effects that can alter the electronic interactions, but also induce transient changes in the band structure.
Among the possible scenarios, we distinguish the following two possibilities and we try to estimate their relevance towards the Cooper pairing:

(1) Modulation of the onsite correlation energy, through a change of the local electronic wavefunction induced by the T_{1u} vibrational mode displacement;

(2) Nonlinear phonon coupling between T_{1u} and H_g modes (that are known to be relevant for the electron pairing) which causes the latter to be indirectly displaced by driving the former.

We focus on the first mechanism, by calculating the magnitude of the changes to the inter- and intra-molecular Coulomb repulsion of the t_{1u} orbitals on a single C_{60} molecule when the $T_{1u}(4)$ mode is driven. The model used for this description is a nearest-neighbour Hückel tight-binding, that captures the orbital hybridisation on the single molecule and the formation of the π orbitals. The hopping parameters between C atoms are assumed to vary with the C-C distance d as [300]

$$V(d) = \frac{\Lambda}{d^2}, \qquad \Lambda = 5.63 \text{ eV Å}^2. \tag{5.9}$$

The onsite C-C distance is assumed to be $d_S = 1.45$ Å, while the C=C one is $d_D = 1.37$ Å, and the resulting hopping integrals are $V_S = 2.69$ eV and $V_D = 3.00$ eV. The important orbitals for our discussion are the three t_{1u} (x, y, z) orbitals, that are degenerate single electron eigenstates of the Hückel model and constitute the lowest unoccupied molecular orbitals (LUMO) in the free C_{60} molecule [301]. We calculated the t_{1u} molecular orbitals for a distortion of 5 pm (∼3.4% of the C-C bond length) along the $T_{1u}(4)$ normal mode coordinate and for which the atomic motions have been taken from complete nearest-neighbor force field model calculation previously reported in literature [302][7]. The onsite correlation energy U is evaluated through the direct Coulomb integral

$$F^0 = \int d^3r_1 \int d^3r_2 \frac{\rho(\mathbf{r}_1)\rho(\mathbf{r}_2)}{4\pi\epsilon_{eff}\epsilon_0|\mathbf{r}_1 - \mathbf{r}_2|} \tag{5.10}$$

[7]This calculation is based on a "frozen phonon" approach that assumes the validity of the Born-Oppenheimer approximation and that the molecular orbitals follow the atomic distortions adiabatically. This is obviously not appropriate for such high-energy molecular vibrations and for the derivation of low energy electronic properties. We are nevertheless interested in a rough order-of-magnitude estimate of the changes induced by such an atomic displacement and this motivates the present discussion.

where $\rho(\mathbf{r})$ is the charge density corresponding to a t_{1u} orbital, ϵ_0 is the vacuum permittivity, and ϵ_{eff} is the dielectric constant of the system. We approximate the charges on each C atom as point charges and recast the integral as

$$F^0 = \sum_{i \neq j} \frac{p_i p_j e^2}{4\pi\epsilon_{eff}\epsilon_0 |\mathbf{r}_1 - \mathbf{r}_2|} + \sum_i p_i^2 F_C^0 \tag{5.11}$$

where p_i indicates the probability given by a t_{1u} orbital of an electron being on the i-th C atom, and $F_C^0 = 12$ eV is the atomic onsite repulsion [209]. The variation of U with the vibrational excitation is obtained by using the p_i's of the driven t_{1u} orbitals.

The results of this calculation are shown in Fig. 5.18, where we report both the single particle energies for the t_{1u} orbitals and the Coulomb repulsion U over one oscillation period. The vibration, in this case, is polarized along the x axis and we

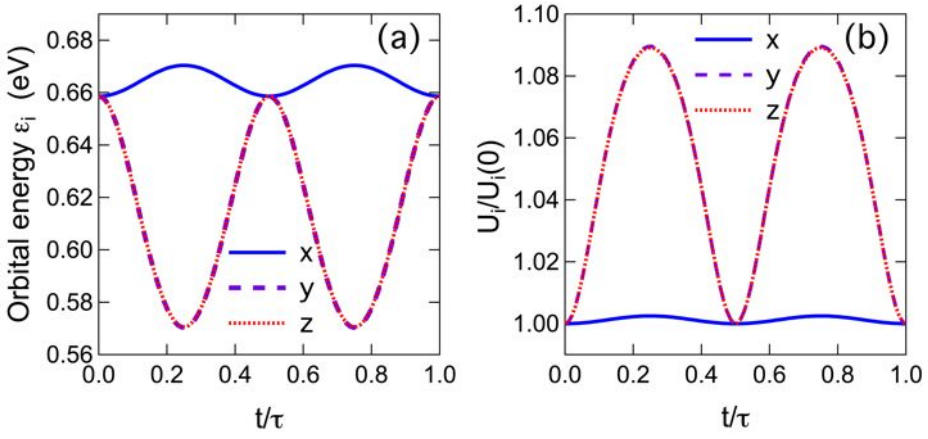

FIGURE 5.18: **Pump-induced modulation of the orbital energy and of the onsite correlation in K_3C_{60}.** Panel (a) shows the changes in the single-particle energies of the t_{1u} orbitals over one period of the $T_{1u}(4)$ vibration with an amplitude $A = 5$ pm. Panel (b) shows the relative changes in the *intra*orbital Coulomb repulsions. These data have been kindly provided by Dr. Stephen R. Clark.

find a change of roughly 10% in both the quantities on the y and z orbitals with twice the period of the vibrational mode, in a fashion similar to the observation reported in Ref. [51]. The change of U is asymmetric in the three orbitals (y and z change more than x) and electron-pairing in the x orbital could be favored in order to avoid the enhanced repulsion (in a way reminiscent of the Jahn-Teller distortions in the equilibrium state).

The second mechanism, involving coupling between infrared active and Raman active vibrations, is instead more in line with the ideas illustrated in the opening

of this chapter. In equilibrium, the coupling between the t_{1u} electrons and the pumped T_{1u} phonon is zero for symmetry reasons, however a large displacement along this mode coordinate can unfold interaction terms proportional to $Q_{IR}^2 Q_R$, that can lead to a nonzero electron-phonon coupling via a Raman mode, like the important H_g vibrations. In order to quantitatively assess this scenario, we performed density functional theory calculations with a plane-wave basis set and a projector augmented wave pseudopotentials (VASP software package) [303–305]. The calculations have been performed within the local density approximation with a cutoff of 900 eV for the plane wave basis set, while a $6 \times 6 \times 6$ k-point grid and a Gaussian smearing (0.1 eV width) have been used for the Brillouin-zone integration during the self-consistency.

The lattice parameters and atomic positions, for a disorder-free structure, have been obtained by energy minimization and the obtained lattice constant is 13.888 Å, against an experimental value of 14.240 Å. Vibrational energies and eigenvectors have been, instead, determined through a frozen-phonon approach (PHONOPY software package) [306, 307]. The determination of the nonlinear phonon-coupling is performed by calculating the total energy curve for variable Raman mode amplitude Q_R and keeping the the amplitude of the pumped T_{1u} mode finite. The signature of the coupling between these two modes is, then, a shift of the total energy curve minimum in the Q_R coordinate due to the finite amplitude of the T_{1u} mode, as shown in Fig. 5.19a.

The electron-phonon calculations have been performed using density functional perturbation theory within local density approximation as implemented in the Quantum ESPRESSO software package [308] with 42 and 420 Ry cutoff for the plane-wave basis set and the charge-density expansions. The Brillouin zone integration during the self-consistency involved a $6 \times 6 \times 6$ k-point grid and a Gaussian smearing with a 0.020 Ry width.

The results of these calculations are summarized in Fig. 5.19. The majority of the Raman modes couples to the photoexcited T_{1u} mode. In Fig. 5.19a we show as an example the energy curve for the $H_g(16)$ mode that exhibits a clear shift of the energy minimum for a T_{1u} amplitude of 2.0 Å$\sqrt{\text{amu}}$ [8]. The shifted minimum implies the presence of a displacement along the Raman mode coordinate, due to the excitation of the IR mode. This nonlinear phonon coupling has, in turn, important consequences on the band structure and the electron-phonon coupling.

The first finding (see Fig. 5.19b) is that a 1.5 Å$\sqrt{\text{amu}}$ displacement along the

[8] The atomic displacements are here indicated in practical units used in the dynamical matrix diagonalisation that leads to the phonon eigenvalues ($\omega(\mathbf{k}, s)$) and eigenvectors $\mathbf{w}((\mathbf{k}, s))$, where

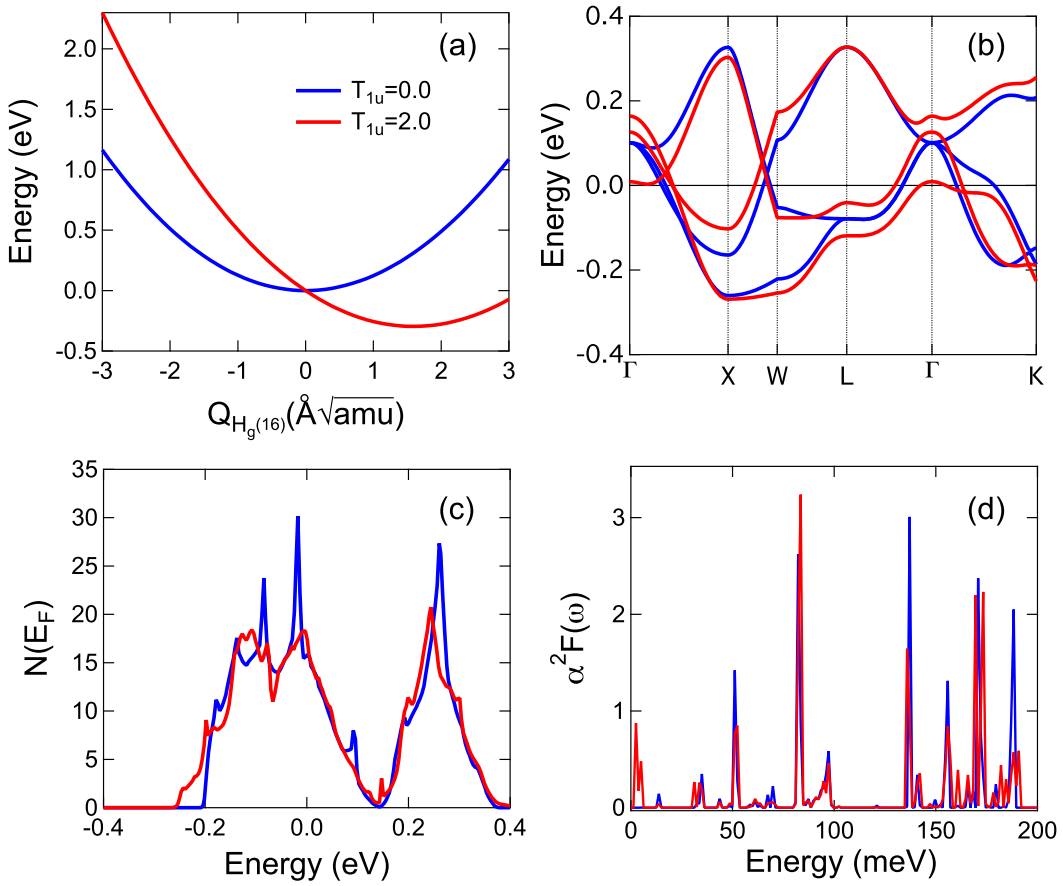

FIGURE 5.19: **Implications of nonlinear phonon coupling between T_{1u} and H_g molecular vibrations**. Panel (a) shows the calculated total energy curves as a function of the $H_g(16)$ mode amplitude when the amplitude of the $T_{1u}(166)$ mode is 0.0 (blue) and 2.0 Å$\sqrt{\text{amu}}$ (red).Panel (b) shows the calculated band structure of K_3C_{60} at equilibrium (blue) and for a displaced structure along the $H_g(16)$ coordinate with an amplitude of 1.5 Å$\sqrt{\text{amu}}$ (red). Panel (c) shows the corresponding density of states for the two cases, while Panel (d) reports the electron-phonon coupling function $\alpha^2F(\omega)$ as a function of energy for K_3C_{60} in both the equilibrium (blue) and the displaced (red) structure. These data have been kindly provided by Dr. Alaska Subedi.

$\mathbf{k}$ is the momentum and s is the band index. The eigenvector components $\mathbf{w}(\mathbf{k}, s)$ are linked to the actual atomic displacements $\mathbf{U}(i, \mathbf{k}, s)$ (i stands for the atom index)through the relation

$$\mathbf{w}(\mathbf{k}, s) = \begin{pmatrix} \sqrt{M_1}U_x(1, \mathbf{k}, s) \\ \sqrt{M_1}U_y(1, \mathbf{k}, s) \\ \sqrt{M_1}U_z(1, \mathbf{k}, s) \\ \sqrt{M_2}U_x(2, \mathbf{k}, s) \\ \sqrt{M_2}U_y(2, \mathbf{k}, s) \\ \sqrt{M_2}U_z(2, \mathbf{k}, s) \\ \vdots \end{pmatrix},$$

where M_i are the atomic masses. In order to obtain the actual displacement, one has to divide this number by the mass of the moved atom.

$H_g(16)$ coordinate slightly lifts the band degeneracy at the Γ point [9]. Secondly, we also find a modest change of the density of states at the Fermi level, that is a crucial parameter for the occurrence of superconductivity (Fig. 5.19c). This variation is caused by the shift in a van Hove singularity near Γ as the bands are moved by the $H_g(16)$ mode displacement. The density of states first increases and then decreases as a function of the $H_g(16)$ mode amplitude, since the van Hove singularity near Γ first approaches and then moves away from the Fermi level, but the bandwidth monotonically increases with the mode amplitude. Intuitively, the displacement along the H_g mode elongates the C_{60} molecule and thus decreases the intermolecular distance (and increases the intermolecular hopping amplitude). Eventually, we find a dramatic increase of the electron-phonon coupling for the displaced structure (along the Raman coordinate). In the equilibrium structure, the three intermolecular modes with 5 meV [10] energy are not coupled to the t_{1u} electrons, however two of them develop a strong coupling under the $H_g(16)$ distortion (see Fig. 5.19d). The electron-phonon coupling constant λ is evaluated through the integration of the function $\alpha\mathrm{F}^2(\omega)$ shown in Fig. 5.19d, for both the equilibrium and displaced structure [309]

$$\lambda = 2\int_0^\infty \frac{\alpha\mathrm{F}^2(\omega)}{\omega}d\omega, \tag{5.12}$$

and the result is that, while the equilibrium structure is coupled with a constant $\lambda_{eq} = 0.52$, the distortion along the Raman coordinate induces an increase up to $\lambda_{eq} = 1.44$. This increase in the electron-phonon coupling could translate into a stronger pairing and lead to the observed superconducting-like state.

5.7 Summary

In this work, we devoted our attention to the dynamical control of the superconducting transition in a BCS-like superconductor through resonant vibrational excitations. The fundamental question associated to this experiment is whether superconductivity can be enhanced by coherently driving the degrees of freedom that mediate Cooper pairing at equilibrium. Since in a pure BCS scenario the transition temperature depends exponentially on the density of states at the Fermi level

[9] However the three t_{1u} bands are still part of the same manifold since they cross at other high-symmetry points of the Brillouin zone

[10] Notice that this energy is quite close to the equilibrium gap value $2\Delta(0) = 6$ meV.

and on the pairing interaction, even small perturbations are expected to result in strong effects on the macroscopic scale.

In order to investigate this problem, we focused on the organic molecular superconductor K_3C_{60}, a compound that exhibits a sharp superconducting transition at a T_c=19.8 K in equilibrium conditions. The spectroscopic signatures of this phase transition are extremely clear, with a saturation of the reflectivity to 1, the opening of an optical gap energy $2\Delta(T = 0) = 6$ meV in the real part of the optical conductivity $\sigma_1(\omega)$ and a divergent imaginary part $\sigma_2(\omega)$ towards zero energy. Despite the apparent simplicity of this transition, where high-energy *intra*molecular modes are likely mediating the pairing, the physics of this compound is the result of a delicate interplay of diverse interactions like the onsite Coulomb correlation U, the Jahn-Teller and Hund interactions. All these quantities are of relevance in this class of materials (A_3C_{60} with A=K, Rb, Cs) and make them an ideal testbed for the investigation of superconductivity in strongly correlated materials.

We first performed a careful characterization of the samples used for the experiments, that are in the form of powders and are strongly reactive to air. Equilibrium optical measurements above T_c allowed to confirm previous observations of a non-trivial Drude conductivity. Below T_c, the superconducting transition occurs in agreement with the literature and we have been able to measure the gap for temperatures between $T_c/2$ and T_c. Both the size of the gap and its temperature dependent behavior are suggestive of a weak coupling limit.

Time- and frequency-resolved measurements of the optical properties in the THz region under resonant vibrational excitation of the $T_{1u}(4)$ *intra*molecular mode have been carried out both above and below T_c. Below T_c, the resonant vibration excitation induces a gap filling consistent with a depletion of the superconducting state. The timescale associated to the Cooper pair breaking is a few ps, i.e. slow when compared to the pump-pulse duration, and the relaxation of the photoinduced state occurs with a single exponential relaxation process. Above T_c, we observe instead a striking superconducting-like behavior, namely the reflectivity of the normal state is saturated to 1, a 11 meV gap opens in $\sigma_1(\omega)$ and a divergent $\sigma_2(\omega)$ towards zero energy is observed up to 100 K, that evolves in as smooth crossover towards a Drude with reduced scattering rate for base temperatures of 200 and 300 K. This effect is fast when compared to the dynamics below T_c, it has a characteristic lifetime of approximately 1 ps and is maximum when the pump pulse is tuned resonantly to the highest frequency T_{1u} (3,4) molecular vibrations. The fluence dependence shows that the gap opening is complete for fluences of 1.0

mJ/cm^2 and points towards a crossover from a high mobility metallic state to a gapped, superconducting-like state.

We discuss the present findings by analyzing the consequences of the pump-induced molecular distortion on the pairing in terms of two scenarios, where modulation of the onsite correlation U or anharmonic coupling between T_{1u} and H_g modes are the primary causes for the experimental observations above T_c. In the first case, "frozen phonon" calculations show that a distortion of the molecule along the T_{1u} coordinate leads to a change in the energy ϵ and in the onsite correlation U that lifts the degeneracy of the t_{1u} electronic states at the Fermi level. This effect could help electronic pairing in a fashion similar to the dynamical Jahn-Teller at equilibrium. In the second case, in line with the general ideas reported in the introduction to the chapter, a strong distortion along the T_{1u} vibrational coordinate can unfold anharmonic vibrational coupling terms and lead to a sizable displacement along the Raman coordinates H_g, that are relevant to the coupling at equilibrium. A displacement along this coordinate would have several effects on the band, structure, the density of states at the Fermi level, but, also, on the electron phonon coupling, that according to our calculations undergoes a threefold increase in such a distorted structure.

Chapter 6

Conclusions and outlook

6.1 Conclusions

In this work, we investigated the connection between structural and electronic parameters in complex solids and the properties of their light-induced transient states on ultrafast timescales. Strong electron-electron and electron-phonon interactions can induce phase transitions and broken symmetry states in equilibrium conditions and their role is expected to be relevant when these materials are driven far from equilibrium. Understanding this connection at the microscopic level is of importance for the realization of ultrafast devices and technologies and, since systems offering interesting ground state properties are often presenting strong electronic correlations, this task is not trivial.

Organic molecular materials have been chosen as an ideal testbed for the study of this relation between structure, correlation and nonequilibrium states due to a number of appealing features and to their high interest for technological applications. These materials can be grown in different arrangements and dimensionality and the richness of their ground state phase diagrams reveals the presence of different energy scales and interactions at work. The molecular arrangement is suited for the development of correlated states and the soft van der Waals intermolecular bonds allow a strong tunability of the ground state with moderate external stimuli (e.g. pressure) and, possibly, with ultrafast vibrational excitation.

The first achievement of this thesis work (reported in Chapter 4) is concerned with the investigation of the role of correlations in dictating the relaxation rate of holes (holons) and double occupancies (doublons) in a solid state Mott insulator. This

problem has been previously investigated with theoretical methods or experiments with cold atoms in optical lattices, pointing towards an exponential dependence of the relaxation rate from the Mottness parameter U/t, but measurements in the solid state were still lacking. In solids, this dynamics can deviate from cold atoms observations because of different energy dissipation mechanisms (e.g. by electron-phonon coupling) and different range of the correlations (that can be longer ranged with the respect to the onsite term only) and direct experimental observations are essential to the understanding of this connection.

For this purpose, we measured the dependence of holon-doublon lifetimes in a prototypical quasi-1D Mott insulator, the ET-F_2TCNQ, while varying the ground state effective correlation by means of external pressures. The equilibrium correlation energies (the onsite Coulomb repulsion U and the intersite one V) and the hopping amplitude have been determined by analyzing the equilibrium optical properties with the optical response of an extended Hubbard model. The holon-doublon lifetimes, determined in a spectrally integrated pump-probe reflectivity measurement of the Mott gap, have been mapped onto the effective correlation $(U - V)/t$ (that has been varied by roughly 50% of its ambient pressure value). We found that in such solid state materials the decay rate of photoinjected holon-doublon excitations depends on the degree of correlations between carriers[1] and, furthermore, the presence of a competition between local recombination and delocalization of holon-doublon pairs is also relevant to the efficiency of the recombination. This knowledge about hot carrier relaxation in a Mott insulating background is crucial for the estimate of operational timescales in the design of devices based on the Mott transition and operating at femtosecond timescales. A future perspective for this field would be to tailor the photoinduced dynamics of correlated electron systems by pulse shaping and by coherent optical control techniques and, thus, lead to more sophisticated technological applications.

The second achievement of this thesis shifts, instead, the focus on the use of this connection between structural and electronic degrees of freedom to control the superconducting phase transition. The underlying question in a broad sense is whether it is possible to drive the superconducting phase transition (possibly in a bidirectional fashion) by exciting on ultrafast timescale those degrees of freedom that mediate the pairing interaction.

[1] In a way reminiscent of the cold gases experiments.

We selected a well characterized molecular superconductor, the K_3C_{60}, which exhibits an equilibrium superconducting phase transition at relatively high temperatures (T_c=19.8 K) and where high-energy intramolecular vibrations are regarded as the relevant bosons for the Cooper pairing. We excited the sample with strong midinfrared fields resonantly tuned to infrared active *intra*molecular vibrations and measured with a delayed THz pulse the low energy electronic response of the sample. We observed a short lived transient state with striking superconducting-like optical properties above the equilibrium T_c with a photoinduced optical gap of approximately 11 meV and up to 100 K, five times the equilibrium T_c (progressively disappearing when approaching room temperature). A pump energy dependence of the effect showed a peaked response at resonance with the vibrational modes, thus suggesting the relevance of vibrational degrees of freedom in determining this surprising response. Calculations of the light induced changes in the orbital wavefunctions and of the anharmonic coupling between infrared- and Raman-active IR vibrations, based on a "frozen phonon" approach, estimated that a light-induced distortion of a few percents in the C-C distance can induce significant changes in the onsite correlation energy of the orbitals at the Fermi level and increase the electron-phonon coupling, thus affecting the superconducting transition. The results of this work reveal novel emergent physics out of equilibrium and represent a step further in the field of light-control of strongly correlated materials, pointing towards an on-demand switching of the superconducting transition on ultrashort timescales. Moreover, these measurement may help in designing quantum materials with more robust superconducting states at equilibrium.

As a side observation with respect to the scientific conclusions discussed so far, this thesis work involved important technical and methodological developments towards a quantitative ultrafast spectroscopy under high pressure conditions, that is of extreme interest for the study of the interplay of structural and electronic degrees of freedom far from equilibrium. The first experiment constituted one of the few ultrafast pump-probe optical measurements under high pressure (up to 2.0 GPa) in the contemporary research landscape and explicitly connected pressure induced changes in the ground state to the ones imparted on the out-of-equilibrium state. The second experiment, even though performed at ambient pressure, has been engineered with the purpose of a ready implementation of high external pressures. In this case, the MIR pump-THz probe experiment requires samples large at least as the wavelength (1 THz is approximately 300 μm), but the application of high pressures usually requires samples not larger than 100-200 μm. This

implies that a THz-time resolved experiment is bound to work close to the diffraction limit[2]. Our sample holder has the same design of an ordinary diamond anvil cell and we successfully managed to measure the transient changes in the optical properties down to 3 meV, a number that represents a challenging low energy limit already in conventional Fourier Transform Infrared spectroscopy with synchrotron radiation. These achievement pave the way for the realization of MIR pump-THz probe studies in which pressure represents an additional tuning parameter on the same footing as temperature and that, to the best of our knowledge, have not yet been performed.

6.2 Outlook

The work presented in this thesis can be naturally extended along many different directions. On one hand, the experiments of pump-probe under pressure in the ET-F_2TCNQ Mott insulator can be extended to a variety of other systems, not only organics, where lattice interactions are relevant for the emergence of different ground states (like Peierls distorted phases or superconductivity). Pressure could lead to the observation of novel states of matter also out of equilibrium and, when properly connected to a research program in material design, like in the case of strained heterostructures [310–315], would represent a powerful tool for the realization of functional materials for ultrafast applications.
On the other hand, the experiments of vibrational control in K_3C_{60} can be applied to other conventional superconductors or represent a starting point for the investigation of dynamical effects and control of superconductivity in carbon-based materials [316, 317]. The application of pressure in the nonequilbrium state above T_c, even though not as definitive as the Meissner measurement, could help clarifying the nature of this photoexcited state. In analogy with equilibrium physics and under the assumption of the absence of structural transitions, a metallic state would become more metallic under application of high pressures, while a superconducting state (in K_3C_{60}) would be weakened by the increase of bandwidth and the consequent reduction of the density of states. Further experiments of this kind could be also performed in cuprates where structural parameters are relevant for the onset of superconducting states with very high transition temperatures [318].

[2] $\lambda \sim d$, where d is the characteristic dimension of the sample.

In a more general perspective, tuning the effective interactions in solid state materials with the application of pressures or through vibrational excitation represents a suitable ground for establishing a cooperative research efforts between the area of nonequilibrium control of solid state materials and quantum simulations with cold atoms in optical lattices [319–329]. In the area of quantum simulation, correlations are tuned with clean and well controllable protocols, e.g by modifying the onsite correlations by means of Feshbach resonances [321]. In solid state materials, this level of control has not yet been reached, and it is often limited to the electronics bandwidth (that enters the Mottness ratio U/W). The establishment of parallel research programs with the area of cold atoms could, therefore, lead to new physical insights and to the discovery of new emergent physics in strongly correlated materials out of equilibrium.

Appendix A

Experimental Methods

In this appendix, we summarize relevant experimental details and methods for the measurements presented in this thesis. In the opening, the working principles and the structure of the optical parametric amplifiers (OPAs), that represent a common element for the experiments described in Chapters 4 and 5, are presented. After the introduction to OPAs, we discuss methods of equilibrium and non-equilibrium spectroscopy under high pressure conditions, that pertain to the investigation of holon-doublon dynamics in the quasi-1D Mott insulator ET-F_2TCNQ under pressure (Chapter 4). The last part describes, instead, the experimental techniques involved in the optical control of the electronic dynamic in K_3C_{60} (Chapter 5), with a particular focus on THz-time resolved spectroscopy and on the specific protocols required by this class of samples.

A.1 Ultrafast NIR and MIR light generation

A.1.1 Difference frequency generation and optical parametric amplification

The light used as pump pulse in our experiments always covers regions that are not accessed by the fundamental line of the Ti:sapphire laser, like near- (400-700 meV) and midinfrared (70-200 meV), and it needs to be easily tunable according to experimental requirements. Near-infrared light is used for pump and probe beams in the experiments on the quasi-1D Mott insulator ET-F_2TCNQ, while midinfrared

light is used for vibrational pumping experiments on K_3C_{60}.

The ideal techniques to meet these requirements are optical parametric amplification (OPA) for the generation of short near-infrared (NIR) pulses and difference frequency generation (DFG) of two NIR pulses to achieve short midinfrared (MIR) pulses.

The unifying working principle of these two generation methods is quite simple and relies on the nonlinear polarization response of a suitable medium. If we expand the polarization of a material in terms of the field strength, we get terms of the type

$$\widetilde{P}(t) = \epsilon_0 \left[\chi^{(1)} \widetilde{E}(t) + \chi^{(2)} \widetilde{E}^2(t) + \chi^{(3)} \widetilde{E}^3(t) + \dots \right] \tag{A.1}$$

where $\chi^{(n)}$ denotes the n-th order susceptibility [330]. When a material is illuminated with strong enough fields one can unfold higher order terms in this series and thus access nonlinear optical responses.

Optical parametric amplification is a phenomenon connected to the second order contribution in the polarizability and, from symmetry considerations, it requires the medium to be noncentrosymmetric (otherwise the $\chi^{(2)}$ tensor would identically vanish). If we consider an incident optical field composed by two distinct spectral components

$$\widetilde{E}(t) = \widetilde{E}_1 e^{-i\omega_1 t} + \widetilde{E}_2 e^{-i\omega_2 t} + c.c. \tag{A.2}$$

the second order polarization will in general contain several contributions at frequencies $2\omega_1$ (second harmonic generation-SHG), $2\omega_2$ (second harmonic generation-SHG), $\omega_1 + \omega_2$ (sum frequency generation-SFG), $\omega_1 - \omega_2$ (Difference frequency generation-DFG) and at zero frequency (optical rectification-OR). All these processes are defined as parametric since their initial and final quantum states are identical and they involve transitions to virtual levels. We now focus on difference frequency generation that stems from a polarization term of the type

$$\widetilde{P}(t) = \epsilon_0 \left[\chi^{(2)} \widetilde{E}_1 \widetilde{E}_2^* \right] \tag{A.3}$$

In an optical parametric amplifier (OPA), the two incident fields are a high intensity light beam with frequency ω_p (pump) and a lower frequency, lower intensity beam with frequency ω_s (signal). The nonlinear medium allows then an energy transfer (amplification) from the pump beam to the signal beam and as a result a third beam (idler) with frequency ω_i is generated.

Energy conservation requires that

$$\hbar\omega_p = \hbar\omega_s + \hbar\omega_i \qquad \rightarrow \qquad \hbar\omega_i = \hbar\omega_p - \hbar\omega_s \tag{A.4}$$

therefore the OPA performs a difference frequency generation process in which both the signal and idler beam reinforce their generation with a divergent buildup during the beam propagation in the nonlinear medium [330]. The efficiency of the parametric process is maximized when there is perfect momentum conservation

$$\mathbf{k}_p = \mathbf{k}_s + \mathbf{k}_i \tag{A.5}$$

with $\mathbf{k}_p$, $\mathbf{k}_s$, $\mathbf{k}_i$ being the wavevectors of pump, signal and idler beams respectively. In this condition (also referred as *perfect phase-matching*) the atomic dipoles in the nonlinear medium are correctly phased and their emitted field can add up coherently in the forward direction [330], therefore the efficiency of the DFG process is enhanced.
In practice, this is a quite difficult condition to achieve because of normal dispersion of the medium refractive indices that reduces eq. (A.5) to

$$n_p\omega_p = n_s\omega_s + n_i\omega_i \tag{A.6}$$

A possible way to satisfy this condition is to employ birefringent (uniaxial) crystals as nonlinear optical media and tuning the angle θ between the crystalline optical axis and the propagation vector of the beams polarized in the plane defined by these two vectors. In this way, the beam will experience an effective refractive index $n(\theta)$ given by an angle-dependent mixture of the ordinary and extraordinary refractive indices.
This method, together with a broad seed spectrum from ω_s, lends the OPA a convenient tunability in the output energies that is essential for selective excitation experiments.
Before coming to the actual description of the apparatus employed in this work, we specify the initial practical distinction between OPA and DFG processes. As we have seen, optical parametric amplification *is* a difference frequency generation. Nevertheless there is an important quantitative distinction between the two and it concerns the intensity ratio between the pump and the signal beam. In a typical OPA, the pump is usually several orders of magnitude stronger than the initial faint NIR signal beam so the process is said to be in the *undepleted* pump regime,

while in the MIR generation (e.g. through the DFG of the two NIR ω_s and ω_i of the OPA output) the two beams have nearly the same intensity and the undepleted pump regime does not apply anymore. In the following we will retain this naming convention for the different parts of the optical apparatus.

A.1.2 Experimental realization of the OPA and DFG units

A typical OPA used for the experiments described in this thesis work is structured as in Fig. A.1.

An intense (mJ pulse energy) p-polarized 800 nm (1.55 eV) beam enters the

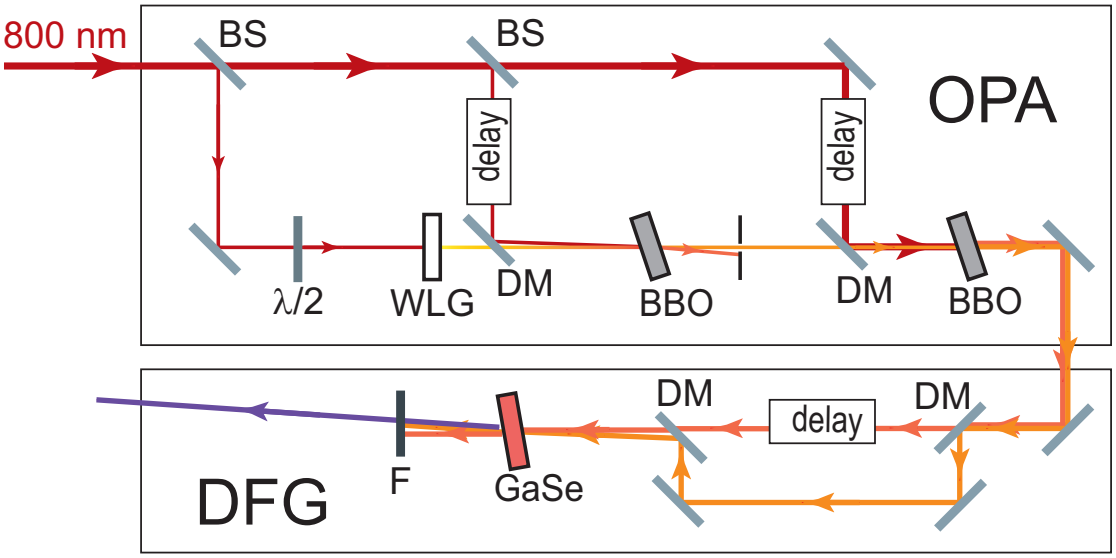

FIGURE A.1: **Simplified scheme of the OPA and DFG setups**. Top view scheme of a double stage OPA combined with a DFG setup for MIR light generation. Red lines represent light at 1.55 eV (800 nm), orange lines the output NIR beams (light orange-signal, dark orange-idler), while MIR is violet. Line thickness is roughly indicative of the beam intensity. For representation purposes the MIR setup is represented with a phase matching rotation axis normal to the page plane, while in the actual setup this axis is parallel to the page. We use the following abbreviations: BS-Beamsplitter, $\lambda/2$-Half waveplate, WLG-white light generation, DM-Dichroic mirror, BBO-Beta barium borate, F-filter.

optical setup and immediately a negligible fraction of the beam is sampled by a first beamsplitter in order to feed the white light generation (WLG). This light, s-polarized after passing through a half-waveplate, is focused on a thick (3 mm) sapphire crystal and the white light continuum obtained is then used to provide a tunable seed beam ω_s for the parametric amplification. The copropagating 800 nm beam after the continuum generation is filtered out before entering the amplification process.

The remaining 800 nm beam is then used as a pump for the parametric amplification that this setup achieves in a two stage configuration, both using 5 mm thick β-barium borate (BBO) crystals as nonlinear media and with a type II phase matching condition [330]. This beam is split in two with a ratio 15:85 in order to provide the pump for each stage of the OPA.

In the first stage the WLG seed (ω_s) and the pump beam (ω_p) are focused and recombined on a dichroic mirror (DM) before being mixed in a non-collinear geometry with a narrow angle ($\sim 1°$), that allows an easier spatial filtering of the beams after the amplification. The two beams are overlapped both spatially and temporally (by means of the delay line) on the BBO crystal and through the process described in the previous section the pump field transfers energy to the signal ω_s field and to the generated difference frequency ω_i. The output energy of these last two beams can be tuned by varying the BBO crystal angle, allowing an almost complete coverage of the NIR spectral region (signal energy routinely spanning from 0.8 to 1.1 eV, idler energy from 0.4 to 0.7 eV).

After the optical amplification in the first stage, the μJ energy NIR beams are spatially filtered and the signal is sent as input for the second stage amplification that scales the NIR output pulse energy in the mJ region. The optical amplification in the second stage shares the same first stage characteristics except for the relative propagation of the signal and pump beams that in this case are *collinear* to maximize the amplification efficiency. Moreover, due to the high pulse energies employed in this stage, the beams are collimated before interacting on the BBO crystal.

After the crystal, a longpass filter with an edge at 1.24 eV (1 μm) cuts the unconverted pump beam and only the copropagating NIR beams are left for extraction from the OPA. In Fig. A.2 we show a typical spectrum of the two NIR signal and idler beams and a typical pulse autocorrelation with a duration of approximately 100 fs.

As a final stage, in order to obtain MIR light from the two NIR beams, the copropagating signal and idler are separated and recombined on a suitable nonlinear crystal in order to extract the DFG light between these two colors. The beams are separated and recombined under a narrow angle ($\sim 1°$) on dichroic mirrors, with the idler being delayed on a translation stage. The crystal of choice for MIR light generation is a 2 mm thick z-cut GaSe crystal that offers high damage thresholds and wide DFG tunability from 70 to approximately 300 meV. With respect to the OPA geometry, where all the relevant angles are on the p-plane, here the angle

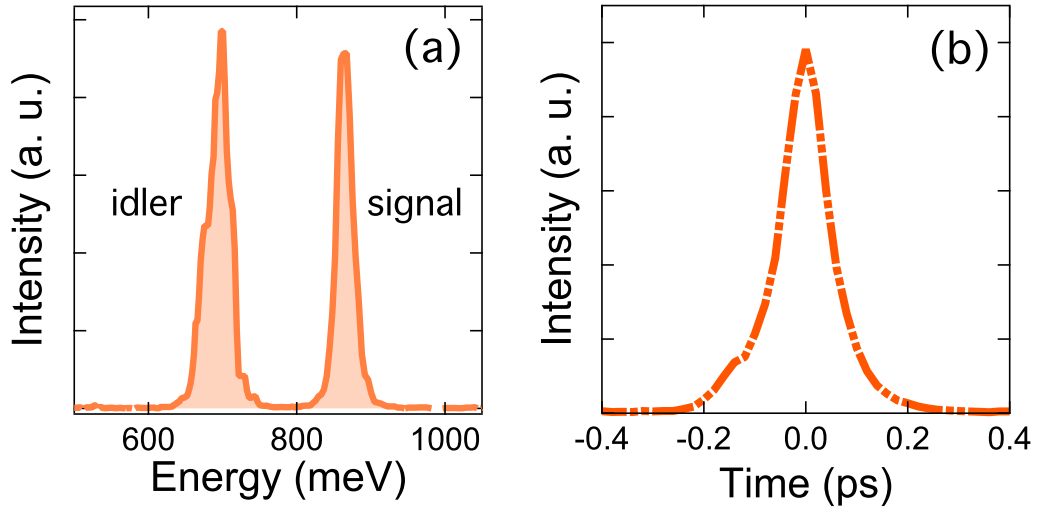

FIGURE A.2: **Spectral and temporal structure of a typical OPA output**. Panel (a) shows a typical spectrum for the NIR beams after the second amplification OPA stage. Panel (b) shows instead a pulse autocorrelation for an idler beam centered at 700 meV.

between the two NIR and the phase matching angle are on the s-plane. In our case the resulting DFG light is first spatially separated by the two depleted signal and idler beams through an iris and an additional Ge-based longpass filter cutting at 250 meV. After this filtering, the output of the DFG is a clean MIR beam like the one shown in Fig. A.3 NIR pulses are measured with a commercial spectrom-

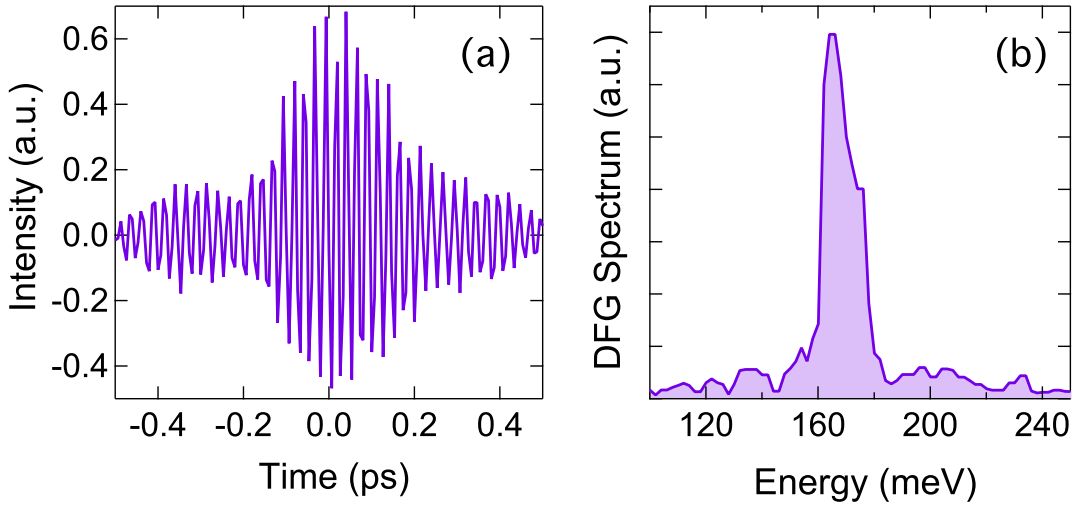

FIGURE A.3: **DFG Spectrum**. Panel (a) shows a raw interferogram used to measure the MIR light used as a pump in our experiments. Panel (b) shows the corresponding spectrum after Fourier transform of Panel (a)

eter unit (Ocean Optics NIRQuest256, 1100-2100 nm range, resolution below 8

nm) to tune their center energies and their pulse duration is instead monitored through the intensity autocorrelation method [331]. MIR pulse spectra after the DFG stage are instead measured with a home-built Michelson interferometer and a MCT detector.

A.2 High pressure techniques

A part of the experiments reported in this thesis makes use of external pressures as a tuning tool for materials' ground states, as we have introduced in Chap. 1. The relevant pressure scale for each solid is deeply connected to details of the chemical bonds and of the lattice structure, but a useful parameter for an unambiguous determination of this scale is the so called *bulk modulus* [97]. The bulk modulus is defined as

$$B_0 = \frac{1}{\kappa_T} = -V\frac{\partial P}{\partial V}\bigg|_T \tag{A.7}$$

where P and V are respectively pressure and volume and κ_T is the isothermal compressibility. This parameter has the dimension of a pressure (often quantified in units of GPa) and quantifies the atomic/molecular cohesion in solids [97].
When dealing with molecular solids where the intermolecular interaction is weak, of a van der Waals type, we expect to have a weaker cohesion and a larger compressibility, therefore the bulk moduli are expected to be lower than in conventional solids [260]. From an experimental point of view, this means that relatively low pressures are capable of inducing relevant changes in the ground state of the investigated compounds, and, as we are going to explain in this section, this in turn relaxes the technological constraints to spectroscopy investigations.

A.2.1 The Diamond Anvil Cell as a tool for high pressure generation

The Diamond Anvil Cell (DAC) is a versatile and compact tool for high pressure generation that is nowadays routinely used in a great variety of condensed matter investigations. Its success relies mainly in its intrinsic simplicity, wide spectrum of applications (from X-ray and neutron diffraction to optical spectroscopy, to NMR and high magnetic fields to name just some examples) and the unique range of attainable static pressures (up to 300 GPa and more) [261, 332–334]. Other devices

are also used to reach high pressures (in the GPa range), e.g. hydraulic presses in the case of static pressures [332] or shock-waves in case of dynamics pressures [335, 336], but we will specifically focus on the DAC.

As mentioned the working principle of the DAC is fairly simple and a DAC can be basically represented as in Fig. A.4: the investigated sample is placed between two diamond anvil tips, closed in a metallic sample chamber and a strong external force is applied on the diamonds that will in turn compress the sample.

The diamond anvils are a key element of the DAC and they are typically high-

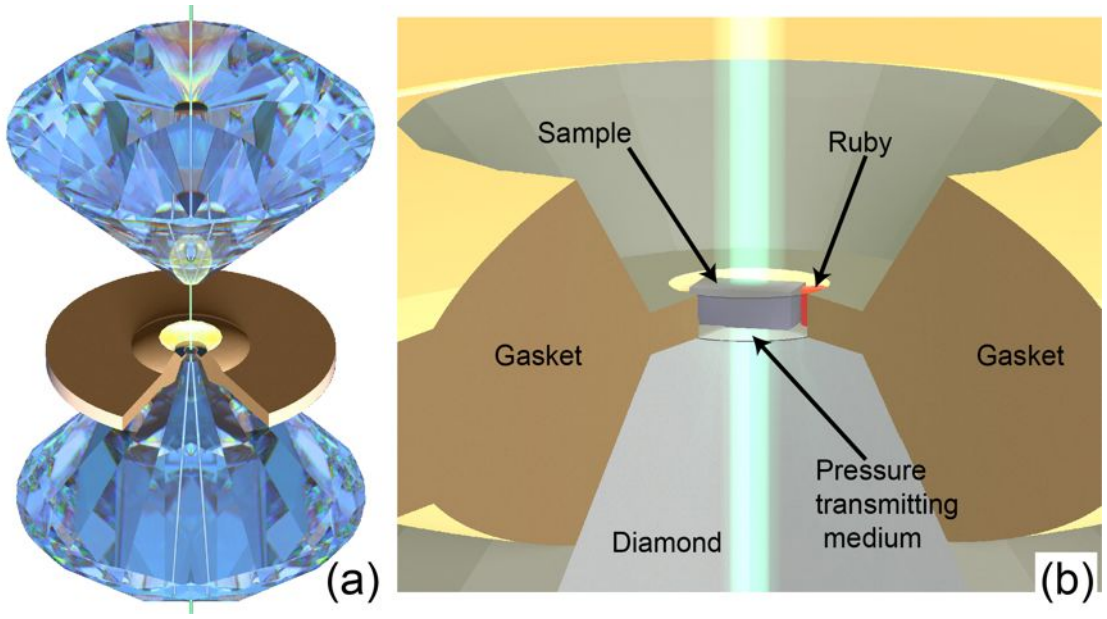

FIGURE A.4: **Sketch of a Diamond anvil cell**. Panel (a)illustrates the core of a Diamond Anvil Cell assembly, Two opposed gem quality diamonds squeeze a sample (black) located in a sample chamber drilled in a pre-indented metallic gasket. Panel (b) shows a zoom of the sample region where a ruby chip (red) is used as a pressure gauge and together with the sample is immersed in a suitable pressure-transmitting medium (transparent) to reach quasi-hydrostatic pressurization conditions. A green light beam exemplifies the typical light access through the diamond anvils in an optical experiment.

quality single crystal gems (cut in different ways according to the DAC structure). Diamond is widely exploited as an anvil material because of its outstanding material strength ($B_0 \sim 450$ GPa [332]) and because of its transparency over a large frequency range [261, 332], but also other materials can be used depending on the specific experimental requirements. Suitable alternative anvil materials are for example moissanite, sapphire and cubic zirconia [337, 338].

The role of the diamond in a DAC is both that of an anvil and of a window for a variety of experiments. Diamonds are normally mounted on plates or seats with a diameter of 1-2 cm in contact with their largest facet called *table* (typically of 2-3

mm diameter) while the facet in contact with the sample is called *culet* and has normally a diameter well below 1 mm.

By recalling the definition of pressure (P) as applied force (F) per unit area (A), it becomes trivial to understand how high pressures are generated. A moderate pressure P_{ext} is applied on the anvil seat/plate (with area A_t), but the pressure exerted on the sample at the culet facet (with area A_c) will be given by $P = (A_t/A_c)P_{ext}$. In routine experimental conditions, the effective pressure amplification factor is around 10^3 (or higher) and pressures up to a few hundreds GPa can be safely obtained in normal laboratory conditions.

As a window material, diamond is also quite remarkable thanks to its optical properties. Diamond refractive index is slowly varying over an extremely broad frequency range in the optical and infrared region [261, 332, 336]. Pure diamond is not transparent only in the region between 200 meV and 500 meV due to multiphonon absorption, while the presence of impurities could introduce additional vibrational lines in the infrared. A relevant impurity atom is N [339] and diamonds are classified according to their nitrogen content. In the N case, we refer to type IA diamonds when the impurity content is about 10^3 ppm while purer gems with an impurity level close or below 1 ppm are commonly referred to as IIA diamonds. In midinfrared and far-infrared spectroscopy IIA type diamonds are required, while for NIR and optical applications the difference between the two types can be neglected[1]. In our experiments we make use of both the diamond types and we will specify the type in the different circumstances.

Another key component of the DAC assembly is the metallic gasket between the anvils. The gasket is crucial for a high pressure experiment because it works as a mechanical support for the anvils and as an experimental chamber for the sample. The DAC needs to be mechanically stable in order to avoid a direct contact between anvils and thus their possible failure. Typical gasket materials have to be plastic under static compression and metals like copper, molybdenum, stainless steel or rhenium (depending on the pressure range of interest) represent an obvious choice.

In most of DAC-based high pressure experiments, the gasket is formed starting from a 0.25-0.3 mm thick blank that is pre-indented with the very same diamond anvils to be used in the experiment [332]. During the indentation procedure the metal below the culet tends to flow out and as a result the blank thickness below the anvils is reduced to one third/one fifth of the original one. The thickness can

[1]Unless low fluorescence constitutes an additional requirement (e.g. in Raman spectroscopy)

be monitored either by direct measurement with a suitable micrometer, like in our experiments, or by interferometric method [332]. The metal extruded from the centre of the blank forms a lateral massive support that helps the mechanical stabilization of the DAC assembly through anvil-gasket friction [340] and through a reduction of the metal flow from the pressurized to the unpressurized region. Once the gasket has been indented and its thickness measured, the sample chamber is formed by drilling a hole in the middle of the culet footprint. The suggested hole diameter for a safe operation has to be between one-third (maximum one-half) of the culet diameter, i.e. a few hundred microns wide. A routine technique for precision drilling of gaskets made of conductive material is electro-erosion [332], that warrants high quality holes without inducing mechanical stresses to the material that will undergo subsequent pressurization. The obtained hole constitutes the sample chamber for the high pressure experiment and, once the gasket is positioned and fixed on one of the anvils, it can be filled with the sample together with a pressure transmitting medium and a pressure gauge.

The relevance of the pressure transmitting medium stands in the fact that, by geometry, the diamond anvils exert a uniaxial pressure, while in most experiment is desirable to have an hydrostatic pressure, i.e. the sample is pressurized in the same fashion in all the directions[2].

The pressure transmitting medium allows to communicate to the sample the compression coming from the chamber sides and from the culet surface that is not in contact with it, therefore reaching a quasi-hydrostatic compression.

From the practical point of view, perfect hydrostaticity is difficult to attain and often pressure gradients inside the sample chamber have to be taken into account. A good hydrostatic medium need a low viscosity and high plasticity in order to minimize pressure gradients; moreover it has to be chemically inert with respect to the sample and not interfering with the measurement with a spurious signal. Depending on the specific experimental requirements one can choose solid (e.g. cubic salts like NaCl, CsI, KBr, AgCl, KCl), liquid (e.g. ethanol-methanol mixtures) or gaseous hydrostatic media (e.g. noble gases). The medium of choice for a vast majority of experiment is He since its high hydrostaticity and chemical inertness make it the best approximation of a perfectly hydrostatic pressure transmitting medium. On the other hand, solid media are easier to handle and for low pressure (up to 10 GPa) applications are also a convenient choice.

Once placed the sample in its experimental chamber, the surrounding empty space

[2]For a more rigorous definition of hydrostatic pressure see for example Appendix 1 of [341]

is filled with the pressure transmitting medium. As a final step for the experiment preparation one or more small (micron sized) pressure gauges are immersed in the hydrostatic medium, with the care of not touching the chamber walls, and the chamber is then sealed by pushing the second diamond anvil on its top. In the next section, we are going to describe the pressure measurement in a routine high pressure experiment.

A.2.2 High pressure measurement

A major breakthrough in the field of high pressure physics has been the development of a reliable pressure scale to quantify the in situ applied pressure (Forman *et al.*, 1972 [342]).
A possible way to calibrate pressure is to measure the unit cell volume V in a standard material and obtain the pressure P through an equation of state $V = V(P, T)$, where T is the temperature. One of the intrinsic complications associated to this method is the requirement of a simultaneous X-ray diffraction measurement that in some cases can be impractical.
Forman *et al.* [342] introduced instead the use of a ruby chip as a gauge by which pressure is determined from the induced shift of its fluorescence spectrum. This measurement is quite accurate, relatively simple to perform and it is, nowadays, one of the most common and well characterized measurement protocols in high pressure applications. While other materials, such as Sm-doped YAG [343] and YASG:Cr [332], can be used as possible alternative gauges, we restrict our discussion to ruby only.

From the chemical point of view, ruby is Cr doped corundum, i.e. Cr^{3+} impurities substitute Al atoms in a Al_2O_3 host lattice. The relevant energy levels for the fluorescence process, shown in Fig. A.5a, arise from a combined cubic and trigonal crystal field splitting of the Cr^{3+} $3d^3$ orbitals [341]. By exciting the ruby chip with a continuous wave (CW) green laser (2.33 eV, 532 nm), the electrons are pumped to a so called U-band made of $^4T_2$ levels. Then, in combination to phonon-assisted relaxation, they decay into the ^2E low-spin doublet and from it back to the ground state by emitting fluorescence photons at the energies R_1 and R_2 [341]. These two lines are quite narrow, since they are spin-forbidden no-phonon emissions and their radiative lifetime is roughly 4 ms at 300 K [345], therefore they are almost ideal for a precise spectroscopic measurement. In Fig. A.5b, we show a sketch of the optical elements needed to excite and the detect

the fluorescence of a ruby gauge with a typical diameter between 10 and 50 μm. As mentioned before, we use approximately 30 mW of CW laser light, focused with a lens ($f = 100$ mm), to excite the fluorescence. The ruby emits R_1 and R_2 photons in a isotropic way and we collect the fluorescence light in a backscattering geometry by employing a broadband visible beamsplitter. The collected light is then filtered with a long-pass filter (cutting at 650 nm) to reject the reflected laser light and sent into a high-resolution spectrometer (Ocean Optics HR4000, 600-700 nm range, resolution approx. 0.055 nm) connected to a computer. By applying pressure, the ruby structure is compressed and this affects the crystal field splitting leading to a shift of the ^{2}E doublet and of the associated R_1 and R_2 lines. The pressure induced shift of the lines, in particular of R_1, is clearly resolved, as shown in Fig. A.5c, and, at room temperature conditions, pressure is connected to the line wavelength $\lambda(P)$ through the following calibration equation [344]

$$P[\text{GPa}] = 248.402\left[\left(\frac{\lambda(P)}{\lambda_0}\right)^{7.665} - 1\right] \tag{A.8}$$

in case of quasi-hydrostatic conditions. For low pressures (below 20 GPa) the line shift is almost linear [346], but for higher pressures the nonlinearity of the calibration curve becomes well evident (see Fig. A.5d). The accuracy of the pressure determination from the R_1 line shift is roughly 0.03 GPa [332] but pressure gradients inside the sample chamber can introduce an additional error in case of spatially averaged measurements, like infrared optics. Pressure gradients are more and more important as pressure is ramped up, but in the interval of interest of our work (between 0.0 and 2.0 GPa), they play a relatively negligible role. For the purpose of our experiments, we estimate a conservative absolute pressure uncertainty of 0.1 GPa on all our pressure reading.

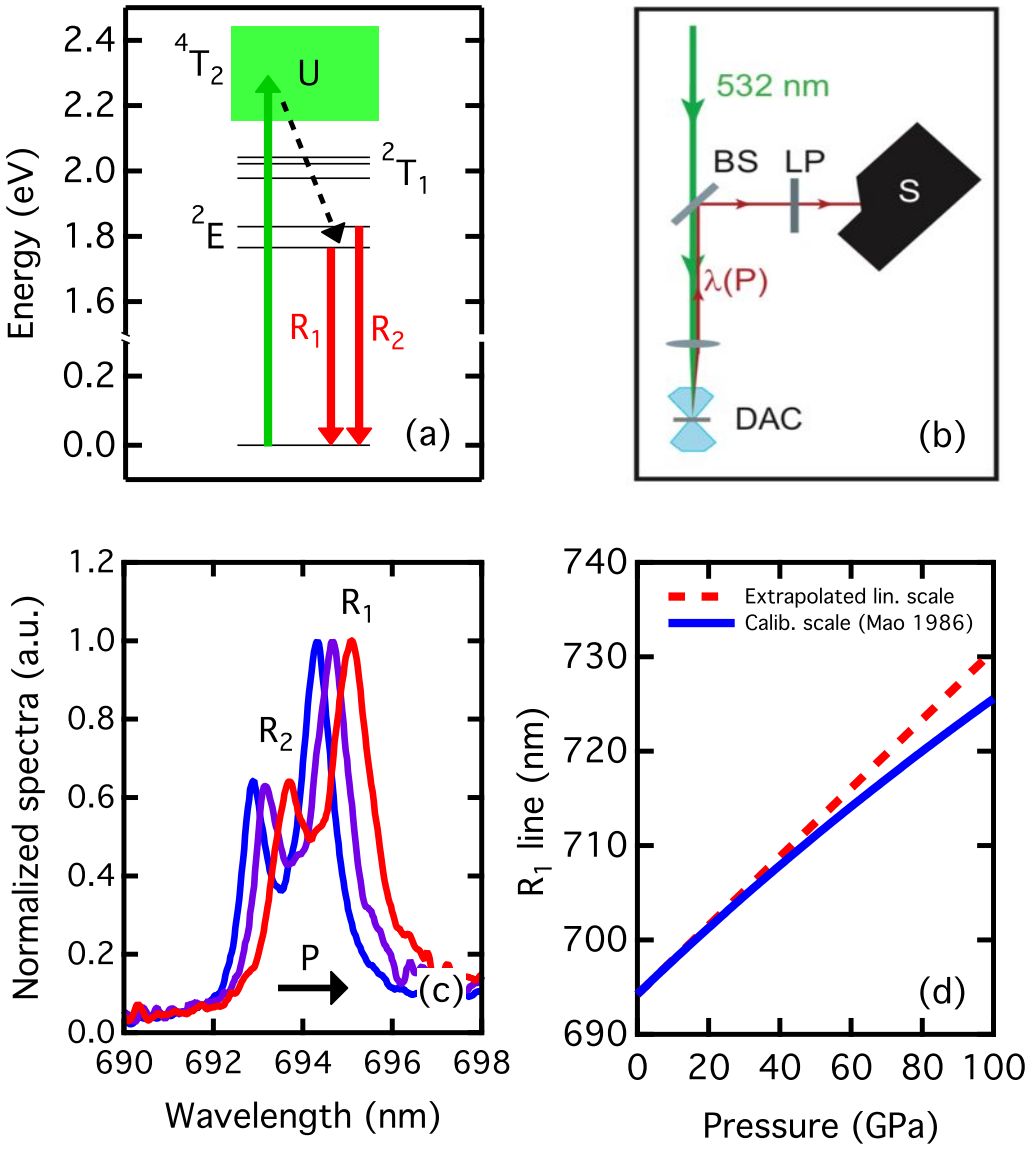

FIGURE A.5: **Pressure measurement with a ruby pressure gauge**. Panel (a) shows the electronic energy levels of ruby and the relevant transitions for pressure measurements (adapted from [341]). A 532 nm laser (green arrow) excites the electrons into a U absorption band, which decay nonradiatively into a ^2E doublet. The subsequent decay to the ground state occurs through photon emission at R_1 and R_2 energies (red arrows). Panel (b) shows a sketch of the experimental setup for ruby fluorescence measurement. BS-Beamsplitter, LP-Longpass filter, DAC-Diamond anvil cell, $\lambda(P)$-Pressure dependent ruby fluorescence. Panel (c) reports selected measured ruby fluorescence lines between 0 and 2 GPa. Panel (c) reports instead the calibration curve between the R_1 wavelength and *in situ* exerted pressure [344] and its comparison with a linear scale.

A.3 Equilibrium infrared spectroscopy under pressure

Part of the experiments presented in this thesis needed equilibrium infrared spectra measured through standard interferometric methods extensively discussed in [234].
In the case of the organic salt ET-F_2TCNQ, the acquisition of infrared optical spectra under high pressure conditions was required, therefore, in this paragraph, we discuss the most important technical aspects of this kind of measurement. Infrared measurements under pressure on the ET-F_2TCNQ have been carried out in two different setups, one located in the SISSI (Source for Imaging and Spectroscopic Studies in the Infrared) beamline of the Elettra Synchrotron Radiation Facility (Trieste, Italy), the other in the 1. Physikalisches Institut of the University of Stuttgart (Stuttgart, Germany).
The two setups are based on different pressure generation methods, the former on a opposing plate DAC as described in section A.2.1, the latter on a piston-cylinder device [332], that works approximately like a DAC where one of the diamond anvils is substituted with a metallic piston. For clarity we discuss the two systems and the associated data acquisition as separate subsections.
Equilibrium infrared spectra of K_3C_{60} have been acquired in the SISSI beamline in the same experimental conditions here described without applying external pressure.

A.3.1 Infrared optical measurements at SISSI beamline

The solid state branch of the SISSI beamline at Elettra is equipped with a Bruker Vertex70 Interferometer coupled to a Hyperion 2000 microscope equipped with gold coated Schwarzchild objectives (15x magnification, NA 0.4). Importantly, the microscope can acquire both in reflection and transmission geometry and in our work we made use of this feature to determine complete and reliable optical properties. The possibility to use brilliant and broadband synchrotron radiation together with a microscope make this experimental station extremely suited for infrared spectroscopy under high pressure conditions. More details about the facility can be found in [347–350], while here we focus on the specifications of the

experiment carried out in the framework of this thesis project.
The diamond anvil cell used in this experiment is a simple screw DAC, where the thrust is given by three screws that push the opposed plates towards each other [332]. The cell was equipped with a couple of IIA quality diamonds with a 600 μm diameter culet. Pressure has been monitored *in situ* through the ruby fluorescence technique described in section A.2.2, while the pressure transmitting medium chosen was a finely milled CsI powder. The pressure explored in this experiment was limited to the interval 0.0-2.0 GPa and a 10 μm -thick ET-F_2TCNQ single crystal has been carefully cut down to a size of 150 μm per side. After being cut, it has been fitted into a previously drilled 200 μm diameter hole together with a ruby sphere and the CsI powder. Care has been taken in orienting the sample along its crystallographic axes and in ensuring a clean contact at the sample-diamond interface, essential for a good infrared measurement. The pressure run was constituted by a continuous ramp from the lowest to the maximum pressure after which the reversibility of the pressure-induced changes during the release was checked. All the measurements were performed at room temperature and the associated pressure uncertainty is 0.1 GPa. At each pressure point, we measured the entire spectral range from 75 to 1200 meV in quasi-normal incidence conditions with polarized light, in order to select only the contribution coming from the *a*-axis. In a separate run we measured, instead, the transmission at the very same pressure points of the reflection measurements (also in this case with polarized light). In addition to these measurements, we acquired unpolarized transmittance data in the *ab*-plane and in the region between 35 and 80 meV to check for possible pressure-induced charge delocalization.
The procedure used to extract the optical properties, already reported in Refs. [348–350], is sketched in Fig. A.6. At each pressure point, by selectively optimizing the microscope focal depth, the reflected beams I_{s-d} coming from the sample-diamond interface and I_{a-d} from the air-diamond interface are separately collected. Measuring at each step the table surface, assumed to be pressure independent, allows to account any movement of the beam position or tilting of the cell. At the end of the pressure run, the cell is opened and a blind silver gasket is mounted in contact with the diamonds. Then the reflections from the air-diamond (I'_{a-d}) and from the Ag gasket-diamond (I_{Ag-d}) are measured with the same protocol without ramping up the pressure. Reflectivity at the sample-diamond interface

is then obtained through the following relation

$$R_{s-d}(\omega) = \frac{I_{s-d}(\omega)}{I_{a-d}(\omega)} \frac{I'_{a-d}(\omega)}{I_{Ag-d}(\omega)} \tag{A.9}$$

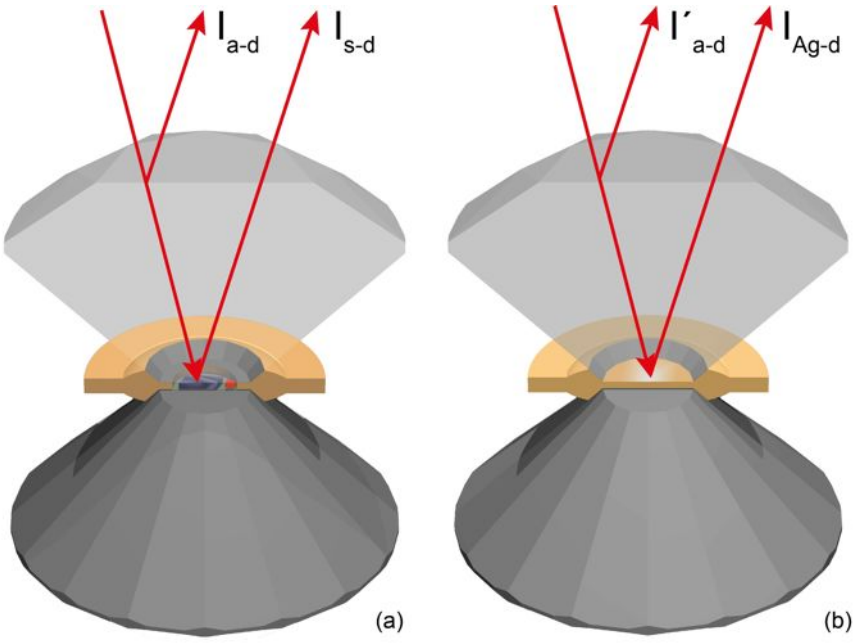

FIGURE A.6: **Absolute reflectivity retrieval in a DAC**. Panel (a) shows the reflected beams I_{a-d} from the air-diamond (*table*) and I_{s-d} from the sample-diamond (*culet*) interfaces in a typical DAC assembly. Panel (b) shows instead the I'$_{a-d}$ reflected beam and the reflection I_{Ag-d} from an Ag non-drilled gasket used as a reference for our measurement.

Equilibrium measurements on K_3C_{60} for several temperatures have been acquired in the same setup from 4 to 1000 meV, without polarizers and only in reflectivity. Since the experiment has been carried out with a compressed pellet behind a diamond window and without the application of high external pressures, the sample has been formed in a 2 mm diameter pellet without the presence of a pressure medium. The referencing of the optical spectra has been performed as described above, but placing at the end of the experimental run a gold mirror at the sample position.

The transmission measurement is in some way simpler and more intuitive since at each pressure point we measure the light transmitted through the entire gasket hole $I_s(\omega)$ and at the end of the pressure measurement the data are referenced against the intensity $I_0(\omega)$ transmitted from a pure CsI loading in the very same gasket used in pressure measurement. The transmittance is then given by

$$T_s(\omega) = \frac{I_s(\omega)}{I_0(\omega)} \tag{A.10}$$

since other absorptions are thus cancelled out.

A.3.2 Infrared optical measurements at 1. Physikalisches Institut of the University of Stuttgart

The experimental setup involved in these measurements is Bruker IFS66v interferometer with a custom cryostat for low temperature-high pressure measurements. In this case the collection optics works only in reflection geometry and does not involve a microscope. As we mentioned before, the piston-cylinder cell is slightly different from a DAC. In this case, the optical access is constituted by a cylindrical wedged diamond window (2° wedge angle, IA quality) with a diameter of 3 mm that allows a maximum internal pressure of 1.1 GPa. Pressure is monitored through the external applied pressure, together with a previously calibrated scale based on ruby fluorescence (see section A.2.2). Also in this case, the measurements are performed at room temperature and the associated pressure uncertainty is 0.1 GPa.

The hydrostatic medium of choice in this case is Daphne 7373 oil and the sample is fixed directly onto the diamond window before introducing the oil. The referencing of the absolute sample-diamond reflectivity R_{s-d} is in this case performed in a different way with respect to the protocol described in the previous subsection, but it still shares some commonalities. In this case, the wedge angle allows a *spatial* separation of the beams reflected from the sample-diamond and from the diamond-air interfaces (see Fig. A.6a). Since the diamond optical constants are well known (e.g. see Ref. [351]), the absolute sample reflectivity can be calculated by using the diamond-air reflection $I_{a-d}(\omega)$ as a reference [352]

$$R_{s-d}(\omega) = \frac{R_{a-d}(\omega)}{\left[1 - R_{a-d}(\omega)\right]^2} \frac{I_{s-d}(\omega)}{I_{a-d}.(\omega)} \tag{A.11}$$

The results of this approach are completely equivalent to the ones illustrated before, being different only the selection technique of the two reflected beams I_{a-d} and I_{s-d}. The biggest difference between the two setups stands, instead, in the

focusing optics (the focusing is less efficient than with a microscope) and in the upper pressure limit of the employed pressure generation device.

A.4 Near-infrared pump-probe measurements on ET-F_2TCNQ under pressure

In this section we discuss the experimental setup and protocols for the pump-probe experiments under pressure described in chapter 4. The light source used for these experiments is a Ti:Sapphire amplifier emitting at 800 nm (1.55 eV) and with a repetition rate of 1kHz and 30 fs pulse duration (Dragon series, KMLabs). The output light (p-polarized) is directed into a double-stage optical parametric amplifier (OPA) like the one described in section A.1.2 and one of the near infrared beams generated in the parametric process, the idler, is directly used for the experiment[3].

A typical value for the OPA input are 550 μJ, while the extracted idler pulse energy is approximately 13-15 μJ. The idler light is also p-polarized and widely tunable in the NIR region, as shown in Fig. A.7b. All idler spectra are collected with a NIRQuest spectrometer (Ocean Optics NIRQuest256, 1100-2100 nm range, resolution below 8 nm).

The idler beam propagates then to the pump-probe setup illustrated in Fig. A.7a and is split by a broadband NIR beamsplitter (splitting ratio R 55:T 45) into two beams, to be used as pump and probe. These measurements are performed with degenerate pump-probe pulses ($\lambda_{\text{pump}} = \lambda_{\text{probe}}$) having the same p-polarization, without further energy conversions. The pump pulse is tuned at the CT resonance of the ET-F_2TCNQ along the a-axis in order to excite holon-doublon pairs, while the probe, always centered resonant to this spectral feature monitors the pump-induced changes in the sample reflectivity.

The probe beam is attenuated by means of a neutral density filter to roughly 3-4% the pump beam intensity and both the beams are subsequently focused onto the sample. The beam waists in the overlap region are determined prior to the experimental run by measuring the transmitted light through a known pinhole. Typical pump beam diameters are around 600 μm, while the probe beam diameters are roughly half this value, in order to probe an homogeneously excited sample region.

[3]Without entering the midinfrared generation unit (DFG).

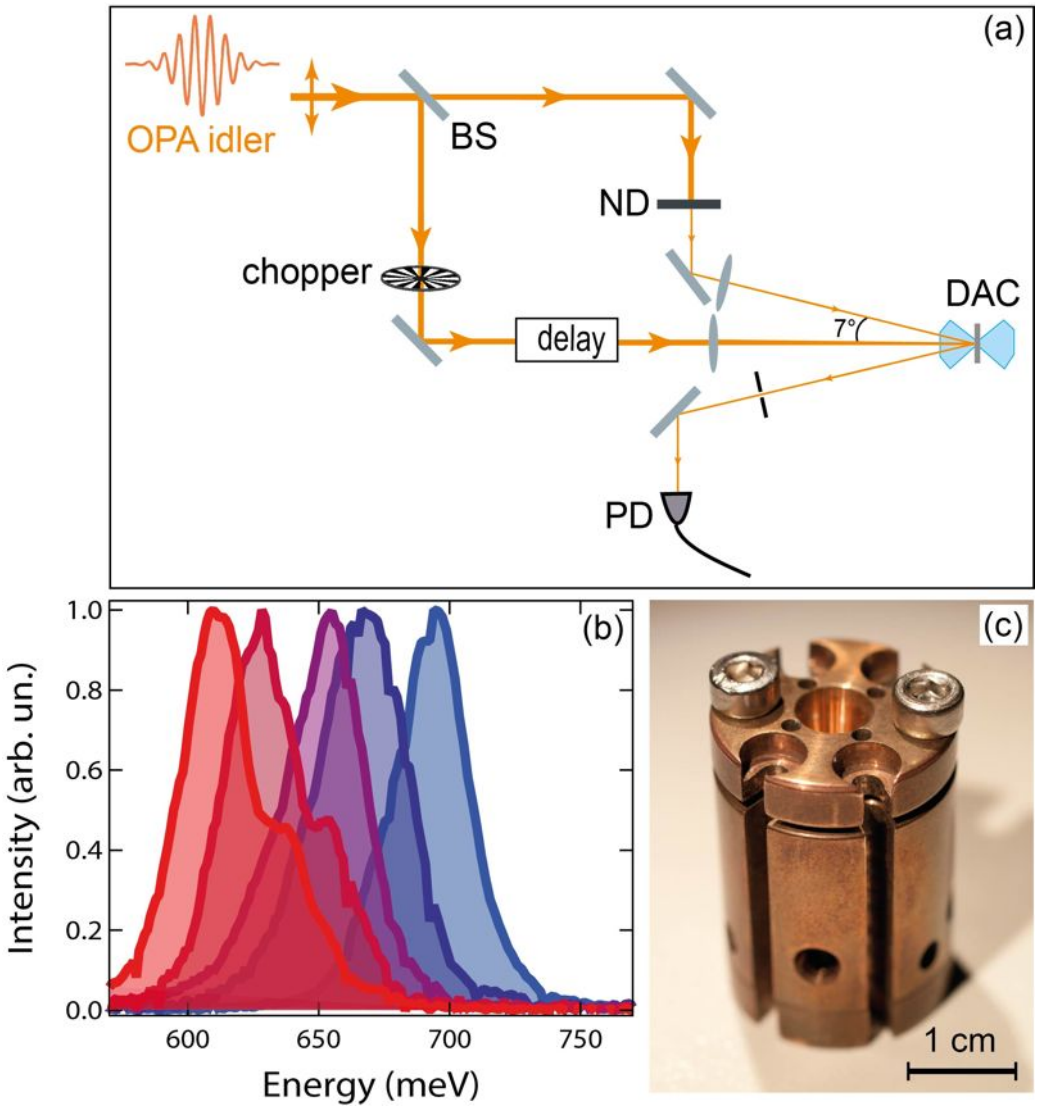

FIGURE A.7: **Experimental for pump-probe experiments under pressure**. Panel (a) shows a top view scheme of the setup employed for pump-probe reflectivity measurements under pressure. We use here the following abbreviations: BS-Beamsplitter, ND-Neutral Density filter, PD- Photodiode, DAC-Diamond anvil cell, OPA-Optical Parametric Amplifier. Line thicknesses are roughly proportional to the beam intensity. Panel (b) reports normalized Idler spectra from the two stage OPA for different tuning conditions. Panel (c) is a picture of the Dunstan-type DAC employed in these measurements.

The pump light travels on a delay stage in order to vary the relative delay with the probe beam and is sent onto the sample at normal incidence. The probe beam is instead impinging on the sample at near normal incidence conditions, with an angle of 7° with respect to the pump beam. The cross-correlation signal of the two pulses at the sample position has been measured and pulses were found to be approximately 100 fs long.

The reflected probe is subsequently detected by a photodiode (InGaAs, 800-2600

nm, 25 ns rise time) connected to a lock-in amplifier (SRS830).
Since pump and probe have same energy and polarization, the total rejection of residual pump light is achieved through the aforementioned angular separation and an iris on the reflected light path before the photodiode. In this way scattered pump light is blocked and only specularly reflected probe light is allowed on the detector.
The transient reflectivity measurement is performed by modulating the pump light with a mechanical chopper running at 433 Hz and connected to the lock-in, thus obtaining the pump-induced reflectivity change $\Delta R(\tau) = R(\tau) - R(\tau < 0)$, where τ denotes the delay between pump and probe pulses. After each measurement, the total reflected probe light is measured by blocking the pump light and chopping the probe beam, thus obtaining the reference $R(\tau < 0)$ for the normalization of the pump-induced changes. The measured quantity is thus the differential change of the sample reflectivity at the CT resonance $\Delta R(\tau)/R(\tau < 0)$ as a function of the pump-probe delay.
A peculiarity of this experiment is the use of external high-pressures to tune the sample ground state. The sample is placed inside a Diamond Anvil Cell and pump-probe reflectivity measurements are performed for variable pressure conditions, as described in chapter 4. ET-F_2TCNQ single crystals are placed in a 1 mm diameter hole drilled within a 250 μm thick Cu gasket blank pre-indented to a thickness of 100 μm. Typical crystals dimensions are 500 μm x 900 μm with a thickness of 50-70 μm. The hydrostatic medium of choice for these measurements is finely milled CsI while pressure is monitored by dispersing some ruby chips (10-50 μm diameter) in the pressure medium. Care is taken to ensure a clean sample-diamond interface. Due to geometrical constraints, unlike most of high pressure experiments, our pressure measurement setup focuses the green laser light with a $f = 100$ mm lens and a flip mirror directing the light on the sample.
The ruby fluorescence collection efficiency is still sufficient to have reliable in-situ pressure measurements but we cannot discriminate the fluorescence light coming from different ruby chips, therefore informations about pressure gradients is averaged out. As previously discussed (see section A.2.2), they do not however represent a serious issue for this very experiment.
The diamond anvil cell used in this experiment is the Dunstan-type DAC [353] shown in Fig. A.7c equipped with IA quality diamond anvils (suitable for NIR optical spectroscopy measurements). The anvils are Diacell cut with a culet diameter of 2 mm (16 sides), a table diameter of 2.5 mm and a thickness of 1.55 mm.

The optical access occurs through the bottom anvil and the cell allows for a maximum angular acceptance of roughly 40°. Our narrow angle between pump and probe beams fits this geometrical constraint without beam clipping at the table interface.

Since our measurements are performed at room-temperature the cell is used without a cryostat shielding and mounted on a high-stability xyz manual translation stage. Pressure is applied by means of an external hydraulic ram connected to metallic wires that pull the cell. In its interior this DAC is based on a piston-cilinder assembly, both elements terminated by a diamond anvil. Upon pressure application the two elements are pressed onto each other by the pulling wires and high compressions can be obtained at the sample position. Typical loads of 40-50 bars on the ram translated in pressures of 2.0-2.2 GPa (20-22 kbars) at the sample position. The pressure at the sample position has been monitored before and after each optical measurement in order to check for the presence of slow pressure drifts.

Before concluding this section, we add a few last technical details relevant to coupled ultrafast optical measurements and high pressures.

One crucial aspect of ultrafast optical measurements is the need to keep the pulses short and avoid dispersion when traveling across solid media. High pressure measurements, on the other hand, widely imply the use of a solid window material, therefore one needs to assess the extent of pulse broadening by dispersion in diamond anvils. The topic is discussed in detail in Appendix D, but we checked in this case the broadening of our pulses by means of a autocorrelation measurement with and without the anvil and found it negligible.

Moreover, given the complexity of the sample-DAC system, we checked that no spurious contributions to the pump-probe signal were coming from other elements than the ET-F_2TCNQ. We performed a measurement with the DAC loaded only with CsI and ruby chips and found no pump-probe signal under the same experimental conditions.

In addition we checked the behavior of the measured transient changes under rotation of the relative angle between the crystalline a-axis and the light polarization. The signal disappeared for fields orthogonal to the a-axis [354] and, being all the other materials of this assembly cubic in their structure, this polarization dependence corroborated the validity of our measurements. Remarkably, the diamond anvils themselves showed no detectable pump-probe reflectivity changes within our noise level and under the same experimental conditions used for the measurements reported in Chap. 4.

A.5 THz Time-Resolved Spectroscopy (THz-TRS)

The terahertz (THz) region of the electromagnetic spectrum, extending roughly from 0.1 to 10 THz (0.4-40 meV), is an extremely relevant observation range for condensed matter systems and particularly for their broken symmetry states. in that spectroscopic range can be found phonon resonances, charge collective modes and gaps associated to ordering transitions or superconductivity [234].
In part of this thesis work, we aim to observe the transient dynamics of the molecular superconductor K_3C_{60} and a direct way to probe the pump-induced changes in its electronic properties is to monitor its gap in the optical spectrum, located at approximately 1.5 THz (6 meV) as shown in Fig. 3.6.
The spectroscopic technique of choice for this study is laser-based THz Time-Domain Spectroscopy (THz-TDS), that with respect to conventional Fourier Transform Infrared (FTIR) spectroscopy offers the following advantages:

- *High brightness in the THz range* - in order to match, or beat, THz-TDS with conventional FTIR one would need to use tabletop backward-wave-oscillators [355], or synchrotron-based infrared light generation [356, 357], that imposes serious time constraints;

- *Measurement of complex fields through phase sensitive detection* - As we will see in the following THz-TD spectrometers can measure the complex reflected field from a sample and the response function can be calculated without resorting to Kramers-Kronig relations and arbitrary extrapolations outside the measured frequency range;

- *Compatibility with time-resolved studies* - Laser based THz light generation is usually achieved with pulsed light and it can be easily synchronized and controllably delayed with respect to a pump pulse, thus allowing a natural extension to time resolved studies of the electronic properties in the THz range (the so called THz-Time resolved spectroscopy or THz-TRS).

The MIR pump-THz probe experiment described in Chapter 5 required a dedicated THz-TRS setup and, after briefly recalling the basics of THz generation and detection, we will describe its realization, the measurement protocol and the associated data analysis.

A.5.1 THz light generation and detection techniques

The two most important laser-based THz light generation and detection techniques rely either on photoconductive antenna generation, where the light is emitted by accelerated carriers in a semiconductor [358–360], or on free space[4] optical rectification and electro-optic sampling, that exploits nonlinear interactions between a higher energy laser pulse and a suitable nonlinear crystal [361–363]. While photoconductive antennas need a relatively small amount of incoming laser power to operate, they are intrinsically limited in bandwidth by the carrier timescales in the semiconducting substrate and extremely sensitive to alignment. Free space generation and detection in nonlinear crystals allows higher THz bandwidths and are less sensitive to misalignments, but they usually need higher incoming laser power for ordinary operation.

In this thesis work, the latter approach is chosen for THz generation and detection and in the following the basics of free space THz generation and detection are briefly discussed. The generation of a pulsed THz field via optical rectification in a nonlinear optical medium can be described in terms of a second order component in the polarization expansion (A.1). An incoming high energy (e.g. 1.55 eV) fs laser pulse undergoes difference frequency generation (DFG) within its bandwidth and therefore between photons with relatively close energies ω_1 and ω_2 (see Fig.A.8a-b). The result of this process is a pulses field with quasi-DC components with a bandwidth limited by the bandwidth of the incoming laser pulse and by the transparency range of the nonlinear medium[5]. The time profile of the THz pulse is proportional to $\partial^2 \widetilde{P}^{(2)}/\partial t^2$, where $P^{(2)} = \epsilon_0 \chi^{(2)} \widetilde{E}(t)^2$ and its time dependence is dictated by the Gaussian time profile of the input fs laser beam [364].

The detection of the THz field, referred as electrooptic sampling (EOS) is instead performed by exploiting the Pockels effect. The THz and a short gating pulse have to co-propagate in a nonlinear detection crystal with a variable delay. The THz field (quasi-DC) induces a transient birefringence in the nonlinear detection crystal that rotates the gating pulse polarization. This polarization rotation is proportional to the instantaneous THz field and can be easily measured through a balanced detection (see Fig. A.8c-d). In our case, the gating pulse is linearly polarized (either s- or p-) and after interacting with the THz field in the detection

[4]The "free space" indication means that the beams are propagated without the use of waveguides.

[5]It naturally follows that in order to increase the bandwidth of the THz pulse, the bandwidth of the input laser pulse has to be increased and shorter pulses are needed.

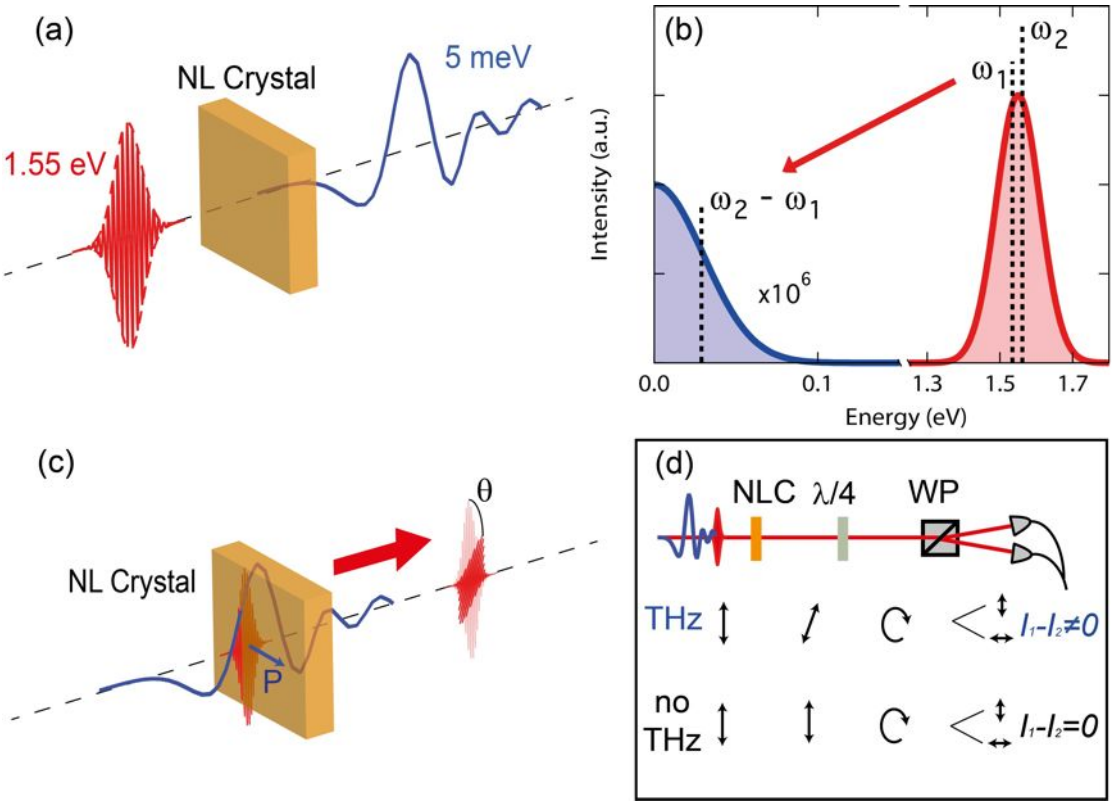

FIGURE A.8: **Free space THz light generation and detection with nonlinear crystals**. Panel (a) shows THz light generation by optical rectification of a short optical pulse in a nonlinear (NL) crystal. Panel (b) represents instead the formation of the THz spectrum as an optical rectification and DFG between photons of similar energy in the optical laser pulse. Panel (c) illustrates the THz pulse detection process through free space electrooptic sampling (EOS). P stands for the THz induced polarization in the NL crystal that rotates the gating beam polarization. Panel (d) reports a scheme of a typical THz detection path with the indication of the gating beam polarization after each optical element (panel adapted from Ref. [355]). We use the following abbreviations: NLC-Nonlinear crystal, $\lambda/4$-Quarter waveplate, WP-Wollaston prism.

crystal is still linearly polarized but with a rotated polarization vector. The gating light is then decomposed in two orthogonal polarization components by passing through a $\lambda/4$ waveplate and a Wollaston prism. The two resulting beams are detected with a couple of balanced photodiodes which measure their intensities I_1 and I_2 and, thus, the instantaneous THz field through $E_{THz} \propto I_1 - I_2$. In addition to its remarkable sensitivity (detection of THz pulses with less than a nJ energy), the EOS measures directly the THz field and this allows a straightforward extraction of the complex response function of the investigated samples. Another advantage offered by this detection technique lies in its coherent character. THz photon energies are well at and below the environmental black-body radiation of the laboratory (300 K $\sim$ 25 meV $\sim$ 6 THz) and an incoherent detection (with

absorption in a semiconductor) would need operation at cryogenic temperatures (like in bolometers for FTIR applications). The EOS is instead sensitive only to coherent, well timed THz pulses with a relatively short time duration and can be performed at room temperature.
The core element for free space THz generation and detection is the nonlinear crystal and its choice has to be tailored on the specific experimental needs. Commonly used uniaxial crystals for THz generation and detection are zincblende-type crystals ($\hat{4}3m$ point group) like ZnTe, GaP or hexagonal ones ($\hat{6}2m$ point group) like GaSe. In addition to these, other inorganic semiconductors are also used, e.g. GaAs, InP, InAs, CdTe, InSb, or ZnCdTe, or organic compounds like DAST and DSTMS (for a more comprehensive review see Ref. [364] and references therein). An important parameter that quantifies the efficiency of the THz emitter/detector is the electrooptic coefficient r_{ijk}, whose absolute value is directly proportional to the nonlinear susceptibility $\chi^{(2)}$: the higher is this parameter, the more efficient will be the THz generation/process [364]. Typical electrooptic coefficients in the visible region span from 1 pm/V in GaP [363], 4.05 pm/V in ZnTe [361] and 14.4 pm/V in GaSe [365] to extremely high values like 160 pm/V in DAST [361]. For our experiment both generation and detection crystals are $\langle 110 \rangle$ cut ZnTe with a thickness of 900 μm and 500 μm respectively.

A.5.2 Experimental realization of a MIR pump-THz probe setup

The laser source used for this experiment is a Newport Spectra Physics ACE Spitfire amplifier that delivers a 4.5 mJ laser beam at 1.55 eV (1 kHz rep. rate, 120 fs pulse duration, p-pol.). The light is initially split with a 85:15 ratio and the two outgoing beams are directed to the OPA and DFG setup for the generation of the MIR pump and to the THz-TD spectrometer. The generation of the MIR pump light has been already described in section A.1.2. Soon after the beamsplitter, the probe beam is delayed with respect to the MIR pump and split into an intense beam for THz generation (splitting ratio 99:1) and a weaker, delayed pulse is used as a gating to measure the THz probe beam reflected by the sample.
The THz-TRS setup used in this experiment, working exclusively in reflection geometry, is built as sketched in Fig. A.9. The THz spectrometer is kept under

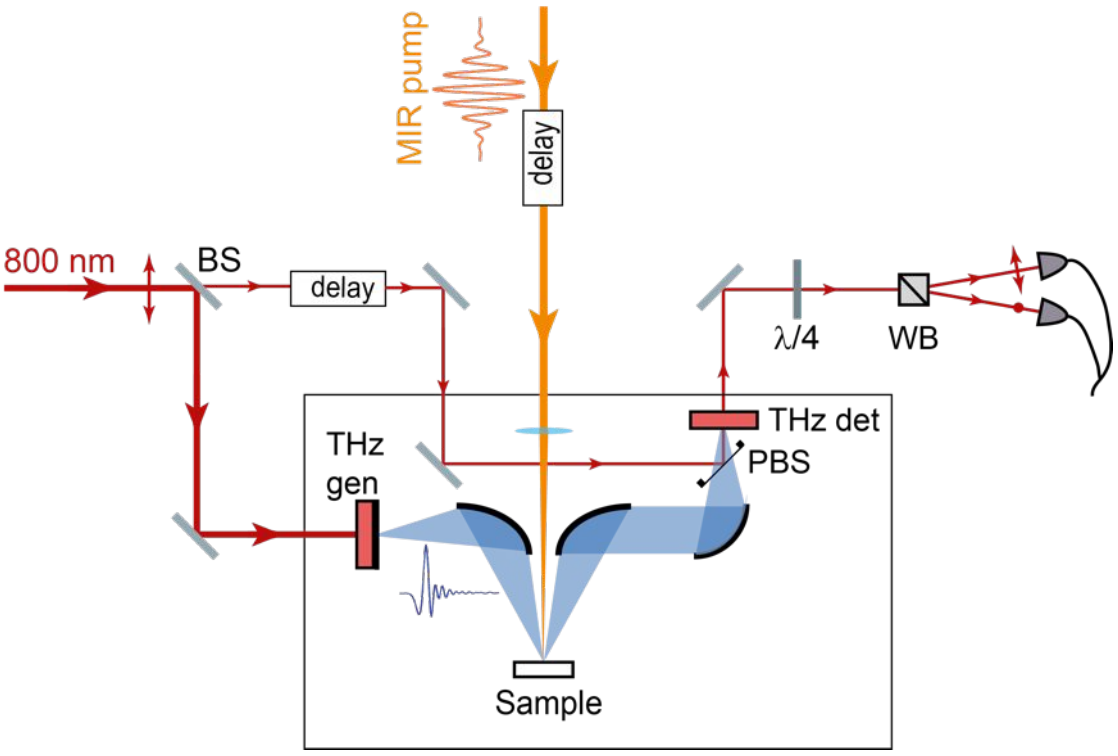

FIGURE A.9: **THz-time resolved setup optical scheme**. Top view scheme of a THz-time resolved spectrometer. Red lines represent light at 1.55 eV (800 nm), orange lines the MIR pump beam, the transparent blue lines the THz light. Line thickness is roughly indicative of the beam intensity (except for THz). Parabolic mirrors are depicted as black arcs. The black rectangle confines the portion of apparatus operated in vacuum. We use the following abbreviations: BS-Beamsplitter, $\lambda/4$-Quarter waveplate, WP-Wollaston prism, PBS-Pellicle beamsplitter.

vacuum conditions in order to:

- avoid degradation of the THz signal due to absorption lines of polar molecules in air (mainly water vapor);
- allow the sample cooling down to cryogenic temperatures (5-10 K regime);
- avoid the usage of windows that could generate replicas of the THz (and introducing modulations in frequency domain), absorb/reflect part of the field before arriving on the sample, or be not simultaneously transparent to both the pump and the probe beams;
- achieve sharper THz focusing conditions without the geometrical constraints imposed by a cryostat shielding and/or optical windows between the focusing mirror and the sample surface.

The THz setup (but not the EOS delay line) is built inside an aluminum box (size 600 x 500 x 250 mm) with a top lid and a 180 mm diameter top viewport. The optical components are mounted on an aluminum breadboard standing on three steel spheres in order to decouple the optics from the external walls of the box.
The 1.55 eV for THz generation and detection are passing through antireflection coated glass windows (28 mm diameter, 1 mm thickness), while the MIR pump beam goes through a CaF_2 (or BaF_2) window (uncoated, 28 mm diameter, 2 mm thickness). The samples are mounted on an Oxford Optistat CF-V cryostat kept in horizontal position on manual xyz translation stages with high load capacity. The cryostat is inserted without external and heat shields and is connected to the box through a highly flexible edge-welded bellow. All the components are assembled with rubber o-rings and the pressure in normal operation conditions is around $1.0\text{-}2.0 \cdot 10^{-6}$ mbar at room temperature.
As depicted in Fig. A.9, the THz beam is focused onto the sample with 90° off-axis parabolic mirrors (1" diameter, 75 mm focal length) and, after being reflected from the sample, is collected by an identical parabolic mirror that recollimates it and sends it to a third parabolic mirror that focuses it onto the detection crystal (1" diameter, 50 mm focal length). The recombination with the EOS gating beam on the detector crystal is achieved by folding the 1.55 eV with a pellicle beamsplitter, that reflects only 8% of the gating light and leaves the transmitted THz pulse unaltered. The angle of incidence of the THz light on the sample is 18° and the total aperture between incident and reflected beams is 36°, while the pump beam impinges at normal incidence.
Knife-edge measurements of the EOS peak field at the focal position on the sample revealed a beam diameter of approximately 500 μm while the pump beam is focused with a 2" diameter CaF_2 (or BaF_2) lens down to approximately 800 μm, thus allowing to probe an homogeneously excited region.
Equilibrium THz fields generated and detected with this setup, shown in Fig. A.10, have an energy spectrum spanning from approximately 2 to 11 meV, thus allowing an almost complete coverage of the gap region in the low energy spectrum of K_3C_{60}. The pulse duration of the THz light is approximately 550 fs and the resulting pulse has a few cycle structure, ideal for time-resolved investigations. As shown in the figure, the detection of the probe pulse is phase-sensitive and from a Fourier transform both the amplitude and phase of the signal can be extracted.
The main source of noise in the apparatus comes from the THz emitter and is due to laser fluctuations following a $1/f$ characteristic [366, 367]. In this spectrometer,

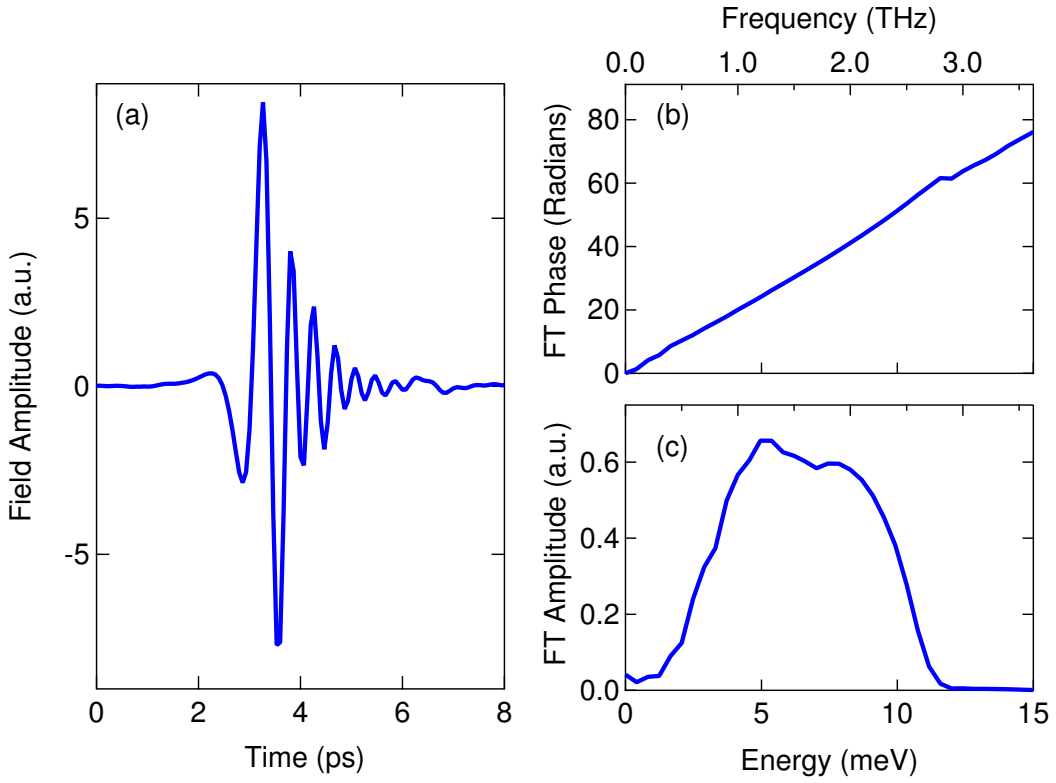

FIGURE A.10: **THz-time domain field detection**. Panel (a)shows a typical equilibrium time-domain scan of the THz field (reflected in this case from the K_3C_{60} sample at 25 K). Panel (b)-(c) report respectively its unwrapped phase and its spectrum after Fourier Transform.

we quantified the standard deviation σ_{EOS} associated to a number of consecutive EOS scans relative to the EOS maximum amplitude $\mathrm{EOS}_{\mathrm{max}}$ and we found it to be $\sigma_{\mathrm{EOS}}/\mathrm{EOS}_{\mathrm{max}} = 7 \cdot 10^{-3}$ (from a 20 scans average).

The actual time-resolved measurement follows, instead, the transient pump-induced changes on the THz probe field reflected from the sample and has an additional delay axis with respect to the equilibrium scans (like the one in Fig. A.10). A typical time-resolved measurement performed with this THz-TR spectrometer is shown in Fig. A.11. In Fig. A.11a, the measured quantity is the transient variation ΔE of the equilibrium reflected field due to the pump-induced changes in the sample complex refractive index. The outcome of the measurement is a two-dimensional grid of transient reflected fields as a function of the EOS delay and of the delay with respect to the pump pulse. Orthogonal cuts in this map can be divided in two categories: pump-probe traces at fixed EOS positions and transient EOS. In the first case the scan is performed by fixing the relative delay between THz probe and EOS gating beam and by varying the delay with respect to the MIR pump pulse (see Fig. A.11b). This scan, shown in Fig. A.11c, does not

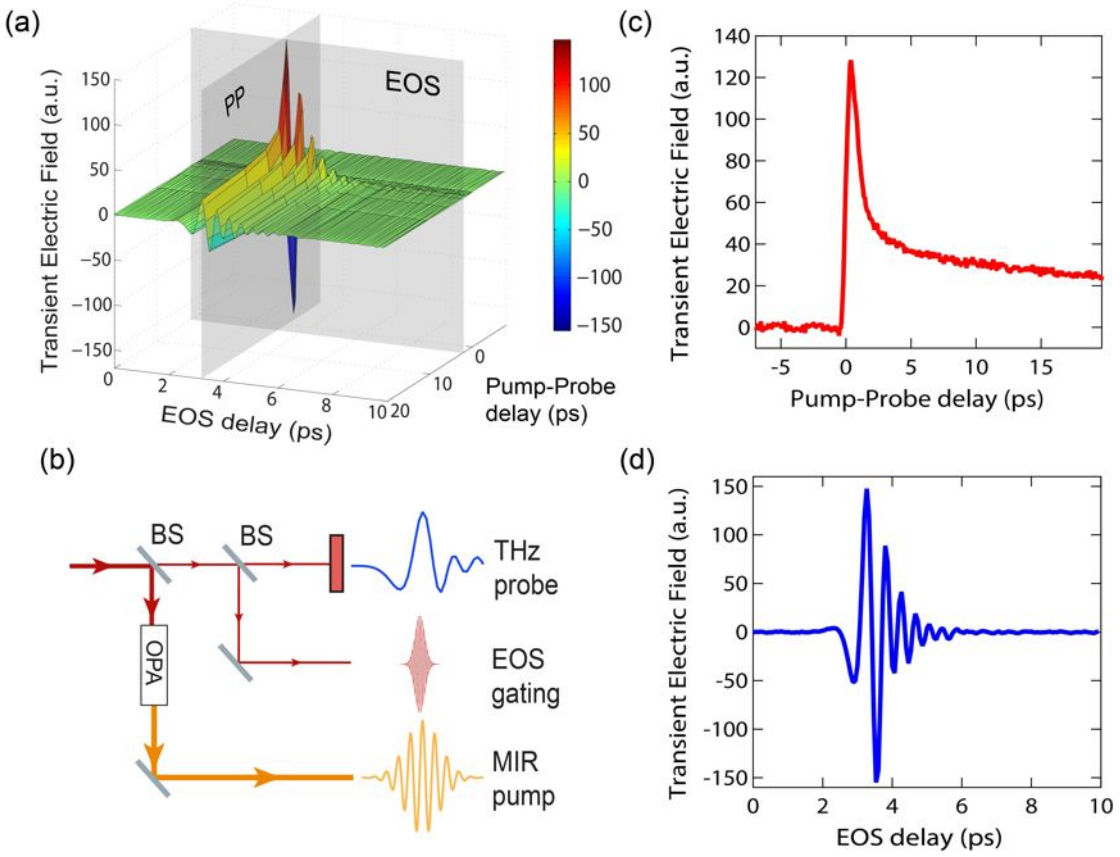

FIGURE A.11: **Example of THz time-resolved measurements.** Panel (a) shows the 2D time-resolved measurements of the MIR pump-induced changes in the electric field from a sample (in this case K_3C_{60} at 25 K). Panel (b) summarizes the arrangement of the beams involved in the measurement process. Panel (c)-(d) correspond instead to cuts of Panel (a) (respectively PP and EOS grey planes). All these data (averaged on 30 scans) are not normalized to the equilibrium reflected field.

provide spectral information and is only indicative of the timescales involved in the relaxation dynamics.

The second cut is instead realized by fixing the relative delay between EOS gating pulse and MIR pump and detecting the THz probe pulse. Since the beams are arranged like in Fig. A.11b, this condition has to be realized by synchronously moving the two delay stages used for the experiment and each point of the resulting scan will experience the same delay with respect to the pump pulse. This scan, shown in Fig. A.11d, provides spectral information and represents the starting point for the determination of materials' transient optical properties.

A.5.3 Retrieval of transient optical properties from THz-TRS data

The raw THz-TRS data shown in the previous section cannot be directly used for the determination of the sample transient optical properties. A first preliminary step towards the extraction of their spectral information is the normalization of the pump-induced changes with respect to the equilibrium reflected field. The equilibrium reference signal is measured before and after each experimental run with the MIR pump blocked and constitutes the normalization for all the delays of the time-resolved measurement. Figure A.12a shows an example of transient EOS with its reference equilibrium signal.

A second delicate measurement that has to be performed before the analysis is

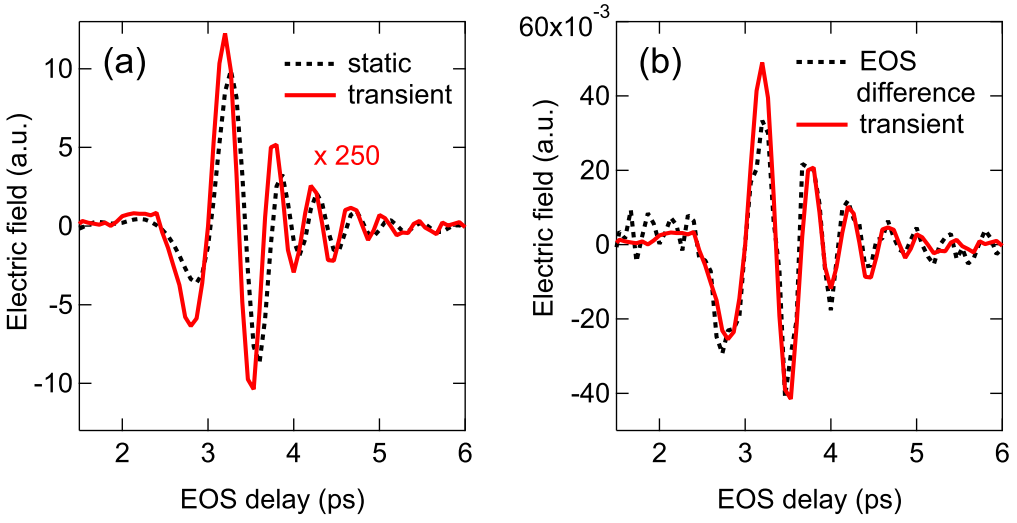

FIGURE A.12: **Transient EOS normalization and sign determination**. Panel (a) shows a comparison between a transient EOS (solid red) at pump arrival time with its reference static signal (dashed black). Panel (b) shows instead a comparison between the same transient EOS of Panel (a) with the corresponding difference between static EOS with and without pump ($\Delta E = E^{pumped} - E^{unpumped}$) at the same pump-probe delay time. This comparison determines the sign of the transient reflectivity changes induced by the pump.

the determination of the absolute sign of the transient reflectivity changes. In our setup we use a freely rotating single chopper and a single lock-in to measure both the equilibrium and the transient fields: in the former case the chopper head goes on the THz generation path, while in the latter it has to be on the MIR pump path. In the two cases the height of the beam with respect to the chopper blades could be slightly different after different alignments and this can induce changes in the optimal inner phase of the lock-inat the two positions, thus making it an unreliable

phase indicator. Our protocol is instead to acquire always with the lock-in phase that maximizes the signal (static or transient) and keep it constant for the whole measurement run. The only unknown is then its sign, and it is determined by comparing the transient EOS with the difference between two series of reference EOS with the pump blocked and unblocked.

If the two traces coincides the transient changes have to be added to the static signal, when flipped they must be subtracted. Once available the normalization spectrum and the sign for the transient changes, the data are Fourier transformed and analyzed as described in this section.

The reflected spectrum from the sample $\widetilde{E}_s(\omega)$ is given by $\widetilde{E}_s(\omega) = \widetilde{r}(\omega)\widetilde{E}_0$, where $\widetilde{E}_0(\omega)$ is the incident electric field and $\widetilde{r}(\omega)$ is the Fresnel reflection coefficient. Since an absolute measurement of $\widetilde{E}_0(\omega)$ is often impractical in reflection geometry, the sample spectrum is usually referenced against the reflected spectrum of a substance with well known, featureless optical properties (e.g. Au mirrors).

The determination of the optical constants at each time delay, and identically in the equilibrium state, is performed by inverting the definition of the Fresnel coefficient $\widetilde{r}(\omega)$ that will depend on the polarization state of the probe field. In Fig. A.13 we briefly recall the two possible polarizations states for an experiment at non-normal incidence geometry. If the electric field E lies in the incidence

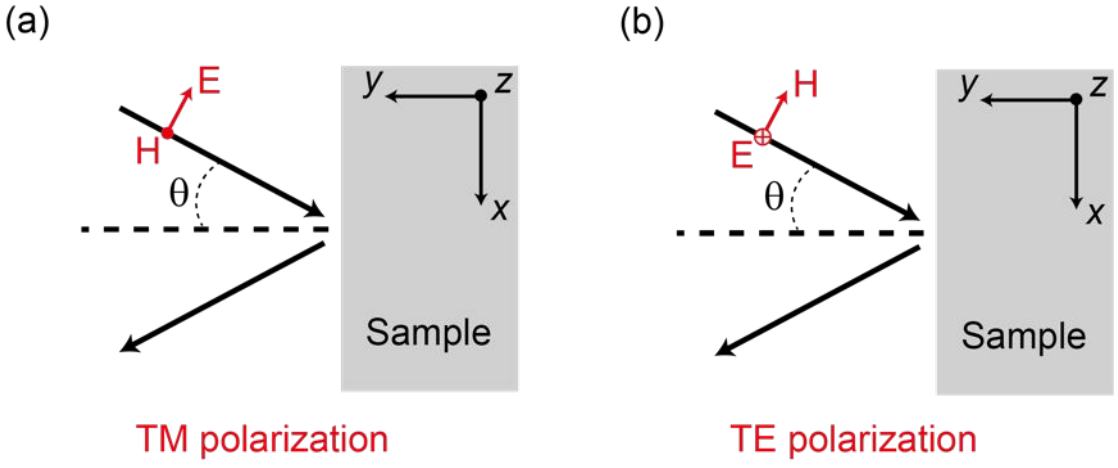

FIGURE A.13: **Definition of the probe field polarization state**. Panel (a)-The polarization state of the probe field is defined as *transverse-magnetic* (TM) if the electric field E of both the incident and reflected beams is polarized in the plane of incidence xy and the magnetic field H is polarized along z. Panel (b)-The opposite case, in which E lies normal to the incidence plane (and thus along z) and H is oriented in-plane, is instead referred as *transverse-electric* (TE) polarization [234, 368, 369].

plane and the magnetic field H is polarized normal to it[6], the polarization state is referred to as *transverse-magnetic* (TM). The opposite case, with E normal to the incident plane is instead referred as *transverse-electric* (TE). In our case, we have a fixed $\theta = 18°$ (reduced to $\theta \sim 8°$ because of refraction in the diamond window) and a p-polarized THz, therefore the relevant polarization state is TM.
The definition of the Fresnel coefficient for the TM polarization at the interface between our diamond window (d) and the sample (s) is

$$\widetilde{r}_{\mathrm{TM}} = \frac{\widetilde{n}_s \cos\theta - \widetilde{n}_d \sqrt{1 - \left(\frac{\widetilde{n}_d \sin\theta}{\widetilde{n}_s}\right)^2}}{\widetilde{n}_s \cos\theta + \widehat{n}_d \sqrt{1 - \left(\frac{\widetilde{n}_d \sin\theta}{\widetilde{n}_s}\right)^2}} \tag{A.12}$$

with $\widetilde{n}_d$ and $\widetilde{n}_s$ being respectively the diamond and sample refractive indexes [234, 368, 369]. The diamond refractive index is considered as constant and equal to 2.37 (see Appendix D). From static reference data collected in the same experimental conditions of the pump-probe experiment but with a conventional FTIR spectrometer the static Fresnel coefficient is calculated.
The differential THz reflectivity measurement at each pump-probe time delay τ probes the pump-induced changes in the frequency dependent Fresnel coefficient through the changes in the reflected field $\widetilde{E}_s(\omega)$ since

$$\frac{\Delta\widetilde{E}_s(\omega,\tau)}{\widetilde{E}_s(\omega)} = \frac{\widetilde{r}_s\,'(\omega,\tau) - \widetilde{r}_s(\omega)}{\widetilde{r}_s(\omega)} \tag{A.13}$$

and thanks to the referencing against the equilibrium $\widetilde{r}_s(\omega)$ the transient Fresnel coefficient is extracted by inverting (A.13)

$$\widetilde{r}_s\,'(\omega,\tau) = \left(\frac{\Delta\widetilde{E}_s(\omega,\tau)}{\widetilde{E}_s(\omega)} + 1\right)\widetilde{r}_s(\omega) \tag{A.14}$$

Since the measured Fresnel coefficient is a complex quantity, $\widetilde{r}_s\,'(\omega,\tau) = |\widetilde{r}_s\,'(\omega,\tau)|e^{i\phi}$, the knowledge of both its real and imaginary parts allows to recalculate the complex time dependent refractive index $\widetilde{n}_s\,'(\omega,\tau) = n_s\,'(\omega,\tau) + i\kappa_s\,'(\omega,\tau)$ and from that all the other optical constants as a function of the energy and of the pump-probe time delay (see appendix for further details).
An important additional element that has been so far neglected is that in MIR pump-THz probe experiments, pump and probe beams may have different penetration depths inside the investigated samples due to the different values of their

[6]Defined by the two propagation vectors of the incident and reflected beams

extinction coefficients $\kappa(\omega)$ at the pump and probe energies. The analysis described so far assumes identical penetration for both the beams. The penetration depth $l_p(\omega)$ is defined as $l_p(\omega) = c/2\kappa\omega$ [234] and is usually larger for low energy photons like the THz probe used in this experiment (see Fig. A.14a). In the

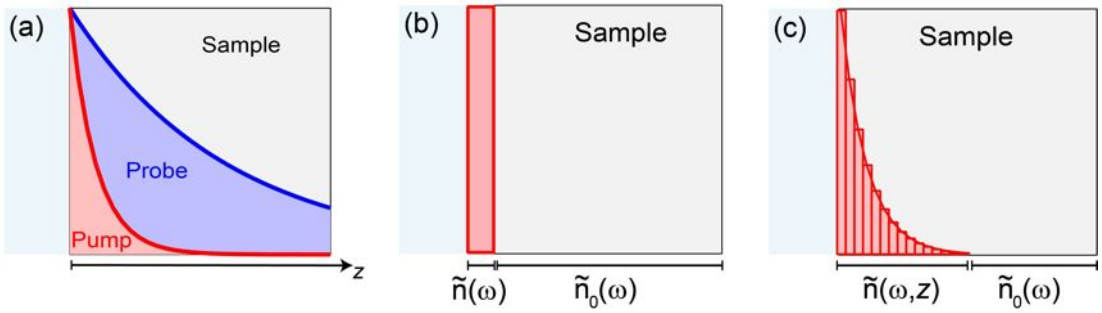

FIGURE A.14: **Penetration depth mismatch and transient optical properties determination**. Panel (a) sketches the penetration depth mismatch between MIR pump (170 meV) and THz probe (5-10 meV) pulses in the case of K_3C_{60} single crystals. Panel (b) shows how the refractive index $\widetilde{n}(\omega)$ of the photoexcited region can be approximated with a homogeneously excited layer (thickness equal to the pump pen. depth) on top of an unperturbed bulk (with refractive index $\widetilde{n}_0(\omega)$). Panel (c) shows instead an alternative modeling based on a series of photoexcited layers with constant refractive index $\widetilde{n}(\omega, z)$) that approaches the unperturbed value $\widetilde{n}_0(\omega)$) as z is increased [48, 50, 370].

following we assume the beam intensity decaying exponentially with the depth z as in Beer's law $I(z) = I_0 e^{-z/l_p}$ [234]. If a significant penetration depth mismatch exist between pump and probe beams (with the probe being more penetrating than the pump), the reflected probe field will contain a mixed response of both perturbed and unperturbed portions of the material and a correct analysis of the pump-induced changes in the optical properties has to disentangle these contributions by introducing a depth dependence in the transient refractive index [48, 50] (and their supplementary information material).

The simplest model accounting for the pump-probe penetration mismatch assumes the photoexcited refractive index as constant with respect to the depth z within a layer of thickness l_p at the surface of the sample (see Fig. A.14b). This physical situation can be imagined as a thin film of photoexcited material at the surface of an unperturbed bulk and is fairly accurate in case the pump penetration depth is much smaller than the probe one. When considering this scenario, the only responsible for the pump-induced changes is the thin layer and the variations of its optical properties will be larger than what probed by the more penetrating THz beam.

In case the penetration mismatch is not large, this approximation is too crude and

the model needs to be improved to take into account the real propagation of both pump and probe beams within the sample. The logical evolution of the thin film approximation is to assume at each time delay the change in the sample refractive index $\widetilde{n}(\omega,\tau)$ maximum at the sample surface and then exponentially approaching the unperturbed one $\widetilde{n}_0(\omega)$ with an exponential profile in the depth z

$$\widetilde{n}(\omega,z) = \widetilde{n}_0(\omega) + \Delta\widetilde{n}(\omega)e^{-z/lp} \tag{A.15}$$

where l_p is the pump penetration depth [48, 50, 370].
The calculation of the optical properties for the excited medium is performed within the transfer-matrix formalism [368] and the starting point is to approximate the exponential excitation profile as a series of thin layers of vanishing thickness δz with constant $\widetilde{n}(z)$ within each layer [48, 50, 370] (and their supplementary information material). The determination of the excited state Fresnel coefficient passes through the evaluation of a global characteristic matrix operator M given by the product of matrices describing each layer, so that $M = \prod_{j=0}^{N} M_j$. For the j-th layer the transfer matrix in the TM polarization is defined as

$$M_j = \begin{bmatrix} \cos(k_j\widetilde{n}_j\delta z) & -\frac{i}{p_j}\sin(k_j\widetilde{n}_j\delta z) \\ -ip_j\sin(k_j\widetilde{n}_j\delta z) & \cos(k_j\widetilde{n}_j\delta z) \end{bmatrix}, \tag{A.16}$$

where $\widetilde{n}_j = \widetilde{n}(\omega, z = j\delta z)$ and $p_j = \cos\theta_j/\widetilde{n}_j$ with θ_j being the angle of incidence of the THz probe light [48, 50, 368, 370]. The term $k_j = k_0\cos\theta_j$ is the component of the probe light propagation vector lying normal to the layer surface and $k_0 = \omega/c$. The layers are set with a thickness δz much smaller than the pump penetration depth and span a sample volume going form the surface to the probe penetration depth $L = N\delta z$.
The elements m_{ij} of the global M matrix completely define the Fresnel coefficient of the excited sample volume for each pump-probe time delay τ as

$$\widetilde{r}\,'_s(\omega,\tau) = \frac{(m_{11} + m_{12}p_L)p_0 - (m_{21} + m_{22}p_L)}{(m_{11} + m_{12}p_L)p_0 + (m_{21} + m_{22}p_L)}. \tag{A.17}$$

The term p_L is calculated at the probe penetration depth, p_0 at the sample surface [48, 50, 370].
Since this equation cannot be analytically solved in the transient refractive index $\widetilde{n}_j$, the determination of the transient optical response occurs through a numerical

optimization of the complex refractive index with a Levenberg-Marquardt algorithm. The quantity of interest for the optimization cycle is the measured transient variation of the reflected field $\Delta\widetilde{E}_s(\omega,\tau)/\widetilde{E}_s(\omega)|_{\text{meas}}$ and, starting from a guessed change in the equilibrium refractive index, it is possible to calculate the expected $\Delta\widetilde{E}_s(\omega,\tau)/\widetilde{E}_s(\omega)\Big|_{\text{calc}}$ with (A.17) and (A.13).
These two quantities define in turn a quality indicator for the modelling procedure

$$Q = \frac{\left| \left.\frac{\Delta\widetilde{E}_s(\omega,\tau)}{\widetilde{E}_s(\omega)}\right|_{\text{meas}} - \left.\frac{\Delta\widetilde{E}_s(\omega,\tau)}{\widetilde{E}_s(\omega)}\right|_{\text{calc}} \right|}{\left| \left.\frac{\Delta\widetilde{E}_s(\omega,\tau)}{\widetilde{E}_s(\omega)}\right|_{\text{meas}} \right|} \tag{A.18}$$

and, after converging to a minimum Q factor, the algorithm gives a fully refined complex refractive index $\widetilde{n}(\omega,\tau)$ that accounts for the observed change in the optical properties [370]. This refractive index is the basis for further analysis discussed in Chapter 5.

A.5.4 Experimental protocol

The A_3C_{60} samples used in our experiments have been synthetized and characterized by Prof. M. Riccó and Dr. D. Pontiroli in the Physics Dept. of Parma University (Italy). The samples are in the form of powders with an estimated average diameter of 100-400 nm. Prior to use for our equilibrium and nonequilibrium measurement, the K_3C_{60} sample batch has been checked with X-ray diffraction and SQUID magnetometry measurements in order to assess the phase purity, powder quality and the T_c. The measurements are presented in Fig. A.15, Panel (a) and (b), respectively. The X-ray diffraction data are reasonably well refined with a single phase fcc - K_3C_{60}, thus indicating a complete phase purity within the experimental uncertainties. From the broadening of the line profile, it has been possible to roughly estimate the average size of the powder grains. The SQUID measurements at zero (ZFC) and 5 Oe (FCC) magnetic fields revealed instead a critical temperature of 19.8 K in agreement with literature findings discussed in Chapter 3, thus excluding possible anomalies in the sample ground state.
Alkali fulleride samples are highly sensitive to oxygen and water content in the environmental atmosphere [371] with a degradation time of a few minutes, therefore extreme care has to be taken during the whole measurement process in order

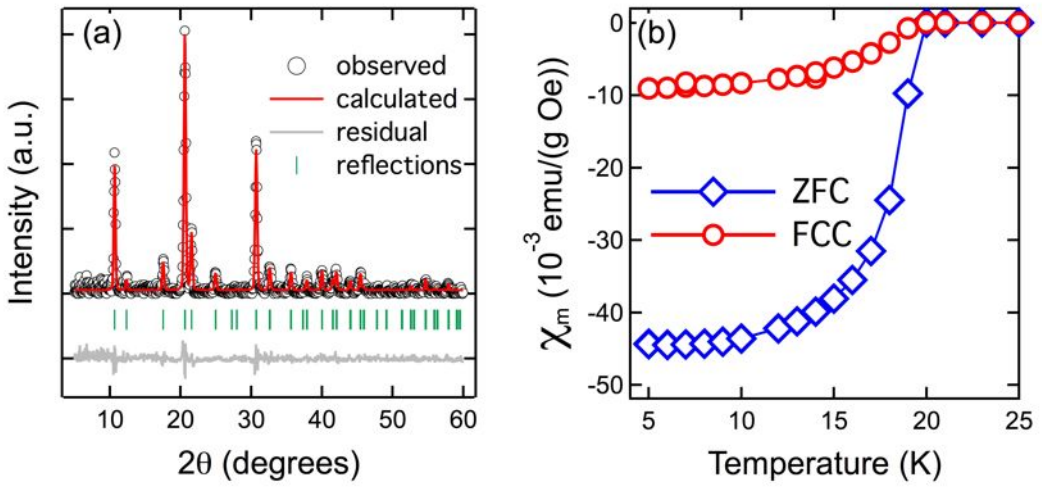

FIGURE A.15: **K_3C_{60} sample characterization**.Panel (a) shows powder X-ray diffraction data for the K_3C_{60} used in this experiment (Batch AJL1) together with a Rietveld structural refinement. Panel (b) shows instead the temperature dependence of the sample magnetic susceptibility with and without magnetic field (FCC-Field-cooled cooling, ZFC-Zero-field cooling). These data have been measured and analyzed by M. Riccó and D. Pontiroli.

to avoid contact with air.

After synthesis, the samples are stored in flame-sealed glass ampoules with Ar content and the preparation for the spectroscopic measurements is performed in a Ar filled glovebox with a constant, monitored level of H_2O and O_2 well below 1 ppm.

In order to perform the spectroscopy measurements on these powders we devised a prototype sample-holder that allows to measure a K_3C_{60} pellet behind a diamond window. The holder has been designed with a double purpose; it protects the sample from exposure to air during the alignment procedures but it is also conceived as an half-diamond anvil cell and works at the same time as a DAC-mockup for imminent THz time-domain measurements under pressure.

An exploded view of the holder and a zoomed section of the holder in measurement condition are reported in Fig. A.16a-b. The diamond anvil used as a window for the experiments is a IIac quality gem (2 mm culet diameter, 1.55 mm thickness, 16 sided, Böhler-Almax cut) mounted on a WC Böhler-Almax seat (12 mm diameter, 4 mm thickness, 84° aperture), suitable also for high pressure experiments up to 2.0 GPa.

The sample is loaded by cumulating the K_3C_{60} powder in the middle of an indium

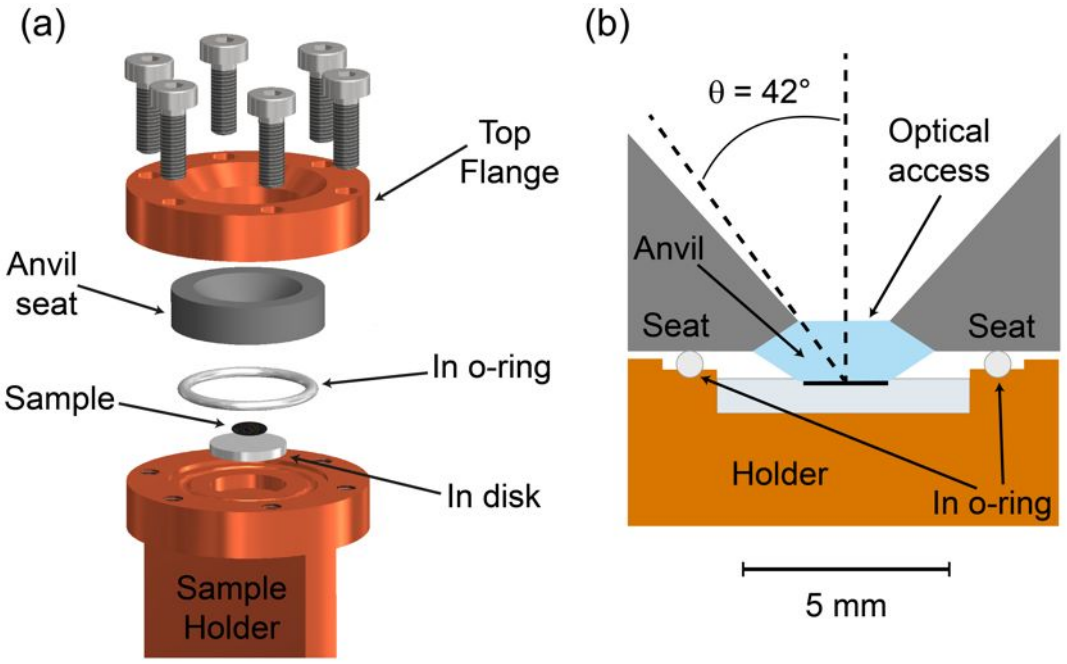

FIGURE A.16: **Sample holder for K_3C_{60} measurements**. Panel (a) shows an exploded view of the sample holder assembly conceived for the MIR pump-THz probe measurements. The lower part of the holder, connecting to the Oxford Optistat CF-V cold finger is not shown. Panel (b) shows a zoomed sketch of the sample holder assembly after closure. The black layer in contact with the anvil is the sample pellet, while the grey disk below is the In disk.

disk (6mm diameter, 1 mm thickness) inserted inside the sample holder inner compartment (see Fig. A.16a) and used to ensure a good thermal contact with the Cu holder. After having prepared the powder, a 1 mm thick indium wire is cut to form a 10 mm diameter o-ring that will ensure the sealing of the compartment and the diamond anvil in its seat is fixed in contact with the sample by tightening an external copper flange (see Fig. A.16b). After tightening, the indium o-ring is completely squeezed between the Cu holder and the seat, while the diamond forms a compact sample pellet with a diameter of 2 mm and a 100 μm thickness, that exhibits a clean optical interface for the spectroscopy measurements.

Once sealed, the sample holder is closed inside an Ar atmosphere in a vacuum-tight tube with CF flanges and is transferred to the MIR pump-THz probe optical setup. The sample is then quickly mounted on the cryostat cold-finger, while, soon after, the alignment with respect to the THz beam and the pump-probe overlap are checked. After 30-40 minutes from the opening of the transfer container the sample, together with the whole THz vacuum box, is evacuated to a pressure lower than $3{\cdot}10^{-4}$ mbar and left until the vacuum stabilizes at 10^{-6} mbar.

Before starting our pump-probe measurements, we monitor the sample condition

by checking whether the superconducting transition can be detected and if a pump-probe signal is present at room temperature. We verified that oxidized samples do not show a pump-probe signal within our noise level and for the same photon energy and excitation levels used in our experiments. We also checked for spurious pump-probe signal coming from the diamond anvil, but we did not detect any.
During each measurement, the reflected equilibrium field of the sample with respect to the reflection coming from the diamond-vacuum interface is monitored, and together with the verification of the superconducting transition in temperature, allows to monitor a possible degradation of the sample. In case the reflected field shows an appreciable decrease, and/or the equilibrium superconducting transition is not observed in the measurement, the time-resolved run is discarder from further evaluation.

Appendix B

Kramers-Kronig relations for reflection data taken through a transparent window

In a standard equilibrium optical spectroscopy experiments, reflectivity data are often acquired through incoherent detectors (MCT or bolometers depending on the spectral range) that measure the intensity I_R of the reflected light, thus losing information about the phase of the electric field. The measured reflectivity of the sample is indeed defined as

$$R(\omega) = \frac{I_r}{I_i} = \frac{\left|\widetilde{r}(\omega)E_i(\omega)\right|^2}{\left|E_i(\omega)\right|^2} = \left|r(\omega)\right|^2 \tag{B.1}$$

where I_i and E_i are intensity and complex field of the incident light, while $\widetilde{r}(\omega)$ is the complex Fresnel reflection coefficient.
Since the extraction of the complex refractive index $\widetilde{N}(\omega) = n(\omega)+ik(\omega)$[1] requires the complete knowledge of the complex Fresnel coefficient one needs to retrieve its frequency dependent phase. This problem is routinely solved by using Kramers-Kronig relations descending from the causality constraint of the response function [234]. In the case of the Fresnel coefficient $\widetilde{r}(\omega) = \sqrt{R(\omega)}e^{i\phi_r(\omega)}$ of a sample in

[1] And, from it, all the other optical constants can be readily obtained.

contact with a vacuum, they can be cast in the following way [234]

$$\ln\left|\widetilde{r}(\omega)\right| = \frac{1}{\pi}\mathcal{P}\int_{-\infty}^{\infty}\frac{\phi_r(\omega')}{\omega'-\omega} \tag{B.2}$$

$$\phi_r(\omega) = -\frac{1}{\pi}\mathcal{P}\int_{-\infty}^{\infty}\frac{\ln\left|\widetilde{r}(\omega')\right|^2}{\omega'-\omega} \tag{B.3}$$

and the complex refractive index follows from

$$\widetilde{r}(\omega) = \frac{1-\widetilde{N}(\omega)}{1+\widetilde{N}(\omega)} \tag{B.4}$$

If we now consider the situation in which the sample is in contact with a transparent window with real and constant refractive index n_w (non-absorbing window), the relation (B.3) will need to be modified. This is exactly the case of reflectivity data under pressure conditions where light is reflected from the interface between the sample and the diamond anvil. The refractive index at the sample-window interface will be now modified in

$$\widetilde{r}_{sw}(\omega) = \frac{n_w-\widetilde{N}(\omega)}{n_w+\widetilde{N}(\omega)} \tag{B.5}$$

The key consideration at this point is that there could be frequencies at which the sample refractive index $\widetilde{N}(\omega)$ could equal the window index n_w, thus producing a singularity in the numerator of phase integral ($\ln|\widetilde{r}_{sw}(\omega)| \to \infty$ for $\widetilde{r}_{sw}(\omega) \to 0$), or equivalently a pole on the imaginary axis. It can be proven that, after a suitable contour integration in the complex plane, the Kramers-Kronig relations have to be modified by introducing an additional phase term [372, 373].
Since $\widetilde{r}(-\omega) = \widetilde{r}^*(\omega)$ must hold for the Fresnel coefficient, we can reformulate eq. (B.3) for a sample-vacuum interface as [257, 372]

$$\phi_r(\omega) = \frac{2\omega}{\pi}\mathcal{P}\int_0^{\infty}\frac{\ln\left|\widetilde{r}(\omega')\right|^2}{\omega^2-\omega'^2}, \tag{B.6}$$

while the corresponding phase relation for a sample-window interface will be [372, 373]

$$\phi_r(\omega) = \frac{2\omega}{\pi}\mathcal{P}\int_0^{\infty}\frac{\ln\left|\widetilde{r}(\omega')\right|^2}{\omega^2-\omega'^2} + \left[\pi - 2\arctan\left(\frac{\beta}{\omega}\right)\right] \tag{B.7}$$

It has to be remarked that if $n_w \to 1$, then $\beta \to \infty$ and we recover the standard phase relation (B.6).

Appendix C

ET-F_2TCNQ equilibrium optical properties: supplementary data

The equilibrium optical measurements reported in Chapter 4 have been performed in two different setups with two different compression protocols. The optical data reported in the chapter are measured with a diamond anvil cell device and CsI as hydrostatic medium, while the data collected in Stuttgart and not shown in the main text are measured in a piston cylinder assembly and Daphne 7373 oil as hydrostatic medium. We report in Fig. C.2 the data coming from these measurements at the 1. Physikalisches Institut of the University of Stuttgart up to a pressure of 1.1 GPa.

These reflectivities present some differences with respect to the other dataset shown in Fig. 4.4, the most important being a dielectric background at low energy (below 400 meV). Since the setup used in this case does not take advantage of a microscope, the surrounding hydrostatic medium (Daphne 7373 oil) contributes to the reflectivity.

Taking this into account, the reflectivity data have been extended with a Drude-Lorentz fit initialized to the ambient pressure ET-F_2TCNQ parameters and the resulting broadband reflectivity has been used for Kramers-Kronig transformations that gave the optical conductivity shown in Fig. C.2b.

The resulting spectra are in full agreement with the ones measured in a different experiment and reported in Chapter 4, showing the same redshift and broadening of the charge-transfer (CT) resonance. We report a comparison between optical conductivity curves collected at similar pressures in these two distinct experimental

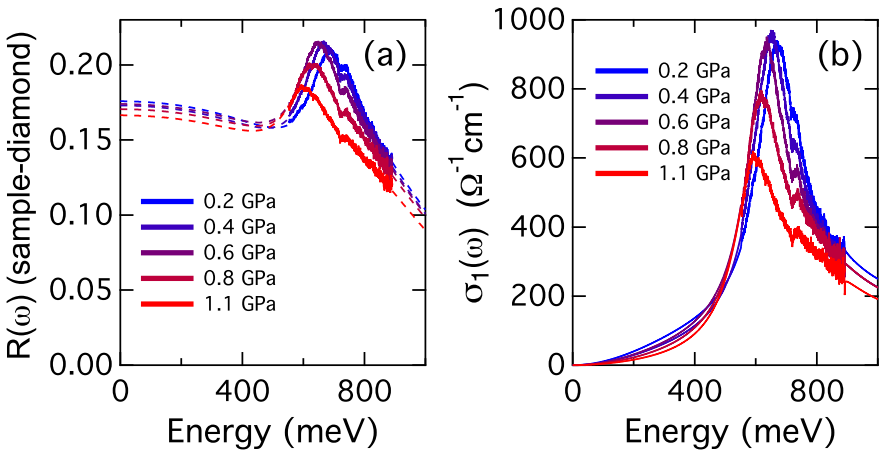

FIGURE C.1: **ET-F_2TCNQ optical properties under pressure-Stuttgart dataset**. ET-F_2TCNQ optical properties along the *a*-axis for selected pressures. Panel (a) shows the reflectivity at the sample-diamond interface, and panel (b) the real part of the optical conductivity $\sigma_1(\omega)$ obtained via a Kramers-Kronig transformation of the data shown in panel (b). Dashed lines of panel (a) are reflectivity extrapolation from a Drude Lorentz fit. A small absorption, coming from residual air in the spectrometer, is present at approximately 730 meV.

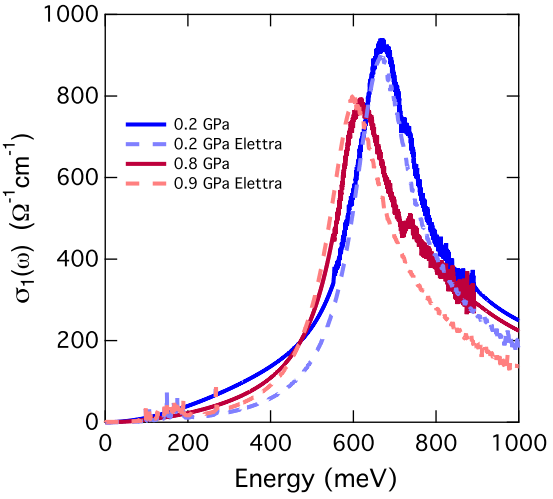

FIGURE C.2: **Comparison between two independent measurements of the ET-F_2TCNQ optical conductivity**. ET-F_2TCNQ optical conductivity along the *a*-axis for selected pressures. Solid lines are data coming from the Stuttgart piston-cylinder device, dashed lines are data collected with a DAC device at SISSI (from Chapter 4).

runs. These data have been analyzed to extract the pressure-dependent effective correlations with the same methods described in Chapter 4.

Appendix D

Ultrafast pulse propagation through a Diamond window

While traveling through a dispersive and transparent material with refractive index n, an ultrafast pulse will experience two important effects [374]:

- an overall *group delay* due to the decrease of the group velocity $v_g = c/n$ with respect to its value in vacuum;
- a chromatic dispersion, and therefore a pulse broadening, due to the frequency dependence of the material refractive index.

This latter effect is particularly crucial in ultrafast spectroscopy because a short pulse with duration Δt will have a certain energy bandwidth $\Delta\nu$ and the minimum pulse duration is achieved only when all the colors contained in such a bandwidth travel with the same group delay [374]. If the pulse satisfies this condition is said to be *unchirped* or *transform-limited*, while if a delay is introduced among different spectral components the pulse duration is inevitably broadened away from the transform limit and the pulse is said to be *chirped* [374]. Since ultrafast spectroscopy experiments under high pressure conditions (or every other ultrafast optical spectroscopy experiments that uses diamond windows) are likely taking advantage of a diamond anvil cell assembly where diamond is the optical window, it is essential to assess the contribution of the diamond window to the broadening of a short pulse upon arrival at the sample surface (see Fig. D.1a). This contribution[1] can be easily estimated from the diamond refractive index as follows. Note that

[1]Not considering possible spatial dispersion effects [374].

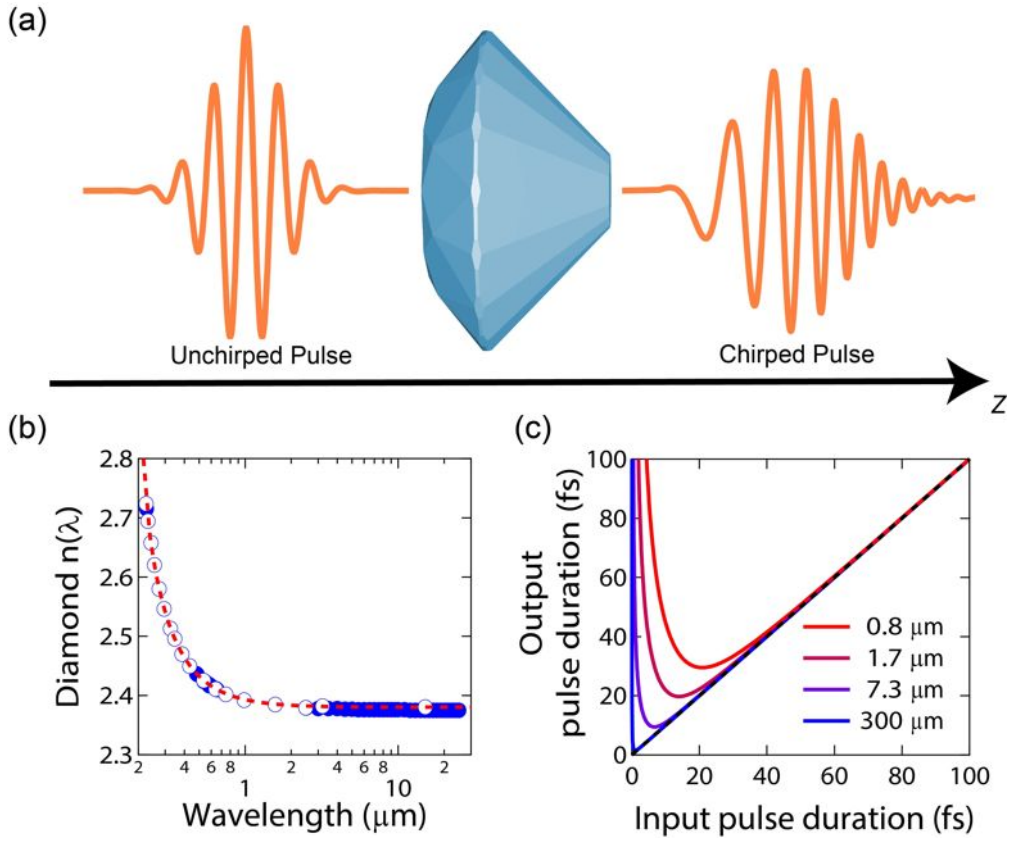

FIGURE D.1: **Ultrafast pulse broadening in a diamond anvil**. Panel (a) depicts the propagation of a few-cycles unchirped pulse through a diamond anvil and the outgoing chirped pulse due to the frequency dependence of the diamond refractive index. Panel (b) shows instead the diamond refractive index (empty circles from Ref. [375], filled circles from Ref. [351]) together with the corresponding Sellmeier equation (red dashed line). Panel (c) shows instead the broadening of an ultrafast pulse as a function of its initial duration for selected center wavelengths and after traveling an anvil with a thickness of 1.55 mm like the ones used in this thesis.

in this section we assume a Gaussian pulse profile and for convention reasons we indicate the photon energies by their corresponding wavelengths, at variance with the main body of this manuscript.

The refractive index of IIac quality diamond has been measured in the visible and infrared regions by several authors [351, 375] (see Fig. D.1b) and can be described (neglecting the multiphonon absorption between 4 and 6 μm [376, 377]) by the Sellmeier equation

$$n(\lambda) = \sqrt{1 + \frac{0.3306\lambda[\mu\text{m}]^2}{\lambda[\mu\text{m}]^2 - 0.030625} + \frac{4.3356\lambda[\mu\text{m}]^2}{\lambda[\mu\text{m}]^2 - 0.011236}} \tag{D.1}$$

The refractive index is quite flat in the visible and infrared range, while it becomes steeper as shorter wavelengths (closer to the electronic band gap) are approached. From the Sellmeier equation, one can derive the key quantity in determining the dispersion-induced pulse broadening, i.e. the Group-Velocity Dispersion coefficient (GVD) that is defined as [374]

$$D_\nu = \frac{\lambda_0^3}{c^2}\frac{d^2 n[\lambda]}{d^2\lambda}\bigg|_{\lambda=\lambda_0} \tag{D.2}$$

and can be conveniently measured in fs^2/mm. Here c is the speed of light in vacuum, while λ_0 is the center wavelength of the light pulse. In the case of IIac diamond one derives the following GVD coefficients for some representative wavelengths used in this thesis

Wavelength (μm)	Energy (meV)	GVD (fs^2/mm)
0.8	1550	1099.53
1.7	730	492.14
7.3	170	113.11
300	4	2.75

TABLE D.1: **IIac diamond GVD coefficients for selected photon wavelengths**. List of group velocity dispersion coefficients for selected photon wavelengths (center lines of the ultrafast pulse) relevant to the experiments described in this thesis.

The GVD coefficient in turn defines the dispersion length $z_0 = \pi\tau_0^2/D_\nu$ (τ_0 being the input pulse duration), namely the propagation distance in the material at which the pulse duration expands by a factor $\sqrt{2}$ [374]. The pulse duration change due to dispersion as the pulse travels a distance z in the medium is then simply given by [374]

$$\tau(z) = \tau_0\sqrt{1+\left(\frac{z}{z_0}\right)^2} \tag{D.3}$$

In Fig. D.1c, pulse broadening curves for selected photon wavelengths and as a function of the incoming pulse duration are shown. The diamond thickness is assumed equal to 1.55 mm as the anvils used in this thesis work.

Diamond anvils induce negligible changes for short pulses in the visible and infrared regions of the electromagnetic spectrum and down to few tens of fs, thus representing a very good window material for ultrafast applications. In the experiment discussed in Chapters 4 and 5, no dispersion effects due to the diamond

anvils have been detected. They are instead expected to become relevant for few fs long pulses in the visible-UV region.

Appendix E

The Mott metal-to-insulator transition

Theoretical description of the transition

One of the most important features of the phase-diagram of a correlated system is the manifestation of a metal-to-insulator transition (MIT) arising from the competition between charge hopping between different lattice sites and Coulomb repulsion between electrons sitting on the same lattice site. Starting from the metallic side of the half-filled phase diagram where charges are delocalized in the lattice and if the temperature is low enough, an increase of the Coulomb repulsion U (and therefore a reduction of W/U) will lead to an electronic localization. The localization stems from the fact that hopping processes involve the creation of double occupancies (also called *doublons*) requiring energies proportional to U, and for large correlation energy values they become energetically unfavorable and rare. This transition, also referred as Mott transition or Mott mechanism, is arising from purely electronic degrees of freedom and leads to insulating states that cannot be predicted in the framework of standard band theory (e.g. V_2O_3, NiO, La_2CuO_4, and Nd_2CuO_4 to name some examples [26]).
One relevant and insightful view on the nature of the MIT is the one emerging from the Dynamical Mean Field Theory (DMFT) picture [110, 111, 378] (see Fig. E.1). DMFT can treat localized (particle-like) and delocalized (wave-like) states on the same footing, therefore it can easily follow the transition[1] between its two

[1] In this section, we discuss only the case of a bandwidth controlled MIT.

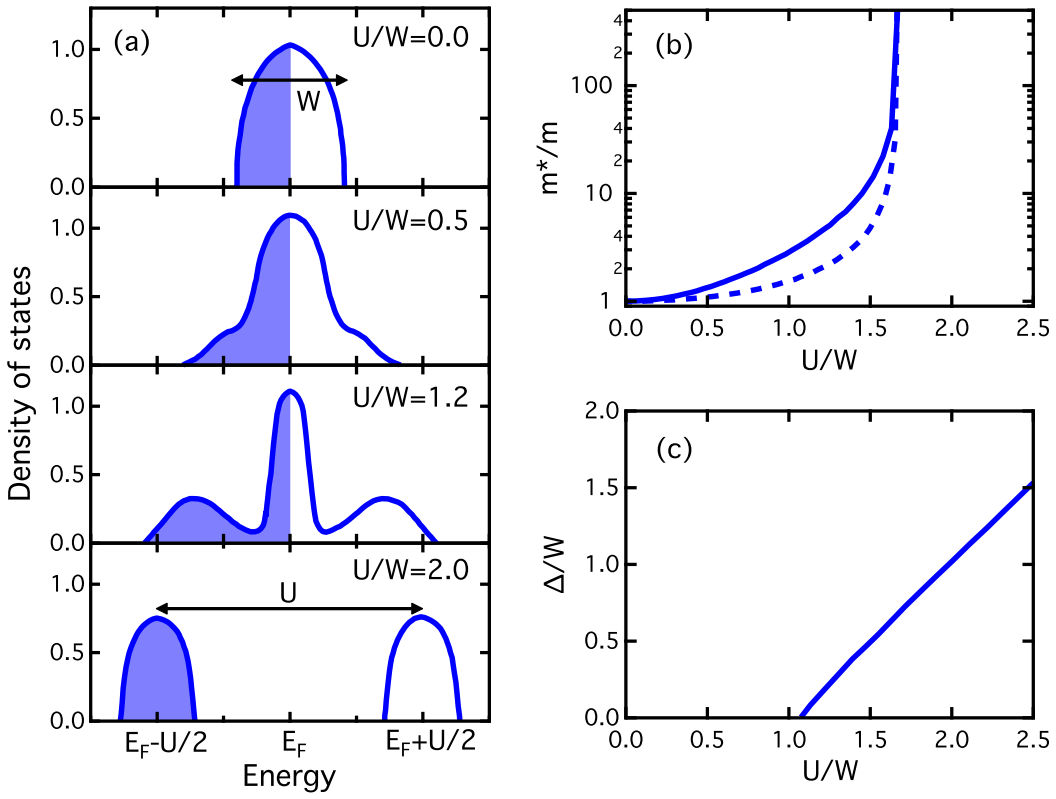

FIGURE E.1: **Metal-to-insulator transition as seen from DMFT**. Panel (a) shows the continuous bandwidth-controlled transition as seen from DMFT calculations at T=0. The electronic DOS evolves from a Fermi-liquid like density at the Fermi level ($U/W = 0$) to an insulating one with well separated lower and upper Hubbard bands ($U/W = 2$) (adapted from [379]). Panel (b) shows instead the diverging effective mass m^*/m towards the transition value of U/W as obtained from iterative perturbation theory (solid) and with a Gutzwiller approach (dashed) (adapted from [111]). Panel (c) shows the gap $\Delta = U - W$ in units of the system bandwidth W as a function of the effective interaction U/W (adapted from [111].)

well known extremes [378, 379]. If we start from the metallic side ($U/W = 0$) (see Fig. E.1a), the density of states presents a single feature at the Fermi level with a bandwidth W and Fermi-liquid theory fully applies [111, 378, 379]. We now introduce a key parameter, in many cases regarded as an order parameter for this phase transition, the *quasiparticle spectral weight* Z, that defines the renormalization of the coherence scale for quasiparticles ${\epsilon_F}^*$. This scale defines the energy (and temperature) below which well-defined (long lived) quasiparticles can exist in the system and it can be shown that ${\epsilon_F}^* \sim Z\frac{W}{2}$ [111]. As U/W is increased, one can observe the gradual appearance of two additional features in the density of states, leading to a three peak structure and a continuous transfer of spectral weight from the quasiparticle peak (carrying a weight Z) to the other two features

(carrying a $1 - Z$ weight). The two additional features are the upper and lower Hubbard bands, broadened by hopping, while the quasiparticle peak in the middle undergoes a narrowing (consistently with the reduction of ${\epsilon_F}^*$) before disappearing completely at $U/W \sim 1.5 - 1.7$ [111]. When the transition is completed, the carriers that for $U/W = 0$ were filling half of the band centered at E_F are entirely filling the lower Hubbard band and are, thus, localized. The Hubbard bands are separated by an energy gap and the state is globally insulating. The carrier localization is evident also in the effective mass, proportional to the reciprocal of Z [111] [2]. As the transition value of the effective interaction U/W is approached, the effective mass diverges due to the blocking effect of the surrounding charges (see Fig. E.1b). As seen in Fig. E.1c the gap Δ opened between the Hubbard bands goes instead linearly with U/W and more precisely, as $\Delta = U - W$ [111].

Optical properties of the paramagnetic phase across the MIT

Since the metal-to-insulator transition involves a massive change in the electronic density of states, experimental probes that couple to the electronic degrees of freedom are particularly sensitive to mobility changes of the materials' charges.
In this thesis work, we focus particularly on optical methods, like infrared optical spectroscopy, but the MIT and correlation effects in general can be naturally studied also with other techniques like photoemission spectroscopy [380–382] and transport measurements [383–385].
A typical infrared optical measurement gives information about the transitions induced by the absorption of one photon with energy $\hbar\omega$, and by spanning the photon energy one can reconstruct the whole ac dielectric constant of the material under investigation [26, 234]. In a correlated material at half filling conditions and in the paramagnetic state, we therefore expect to measure optical responses like the ones depicted in Fig. E.2. In the metallic state ($U/W \sim 0$), the electronic density of states is peaked at the Fermi level, so the only possible excitation mechanism after a photon absorption is the excitation of quasiparticles. In the optical response, seen in the real part of the optical conductivity $\sigma_1(\omega)$, these excitation translate into a Drude peak at zero energy with a width dictated by the electronic scattering rate [234, 257, 386].
As U/W is increased the density of states develops the two additional Hubbard bands and the possible transitions due to photon absorption increase in number.

[2] $m^*/m = 1/Z$, m being the bare electron mass.

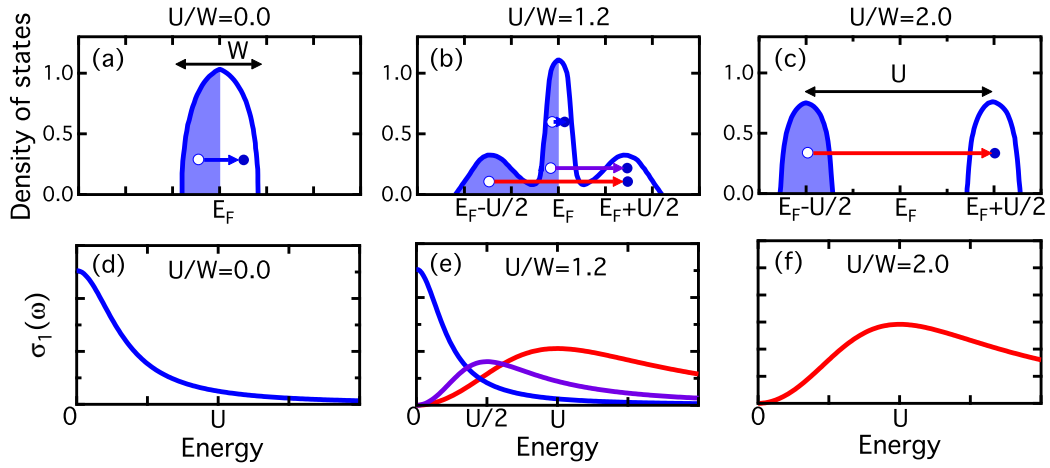

FIGURE E.2: **Optical signatures of the Mott MIT**. Panels (a)-(c) show the density of states as function of the energy with possible optical excitations for different values of U/W (adapted from Ref. [379]). Panels (d)-(f) show instead the corresponding sketch of the expected optical conductivity $\sigma_1(\omega)$ as a function of the incoming photon energy.

At intermediate U/W, for low photon energy we still find a Drude peak with decreased spectral weight but we also start observing higher energy absorptions. One intermediate absorption corresponds to excitations from the quasiparticle peak to the upper Hubbard band and is expected to be positioned at a photon energy equal to $U/2$ (with a width of W) [26]. An additional high energy absorption band is, instead, the one connected to a direct electron excitation from the lower to the upper Hubbard band. In $\sigma_1(\omega)$ this band is positioned at an energy U and has an overall width of $2W$. When the ratio U/W is further increased, the quasiparticle spectral weight is all transferred into the Hubbard bands and the only possible excitation path following direct photon absorption is the one from the lower to the upper Hubbard band. The optical spectrum gets completely gapped as expected for an insulator, with a gap $\Delta = U - W$ [386]. This scenario has been confirmed in a variety of different materials (like V_2O_3, V_3O_5, $SrTiO_3$, $Nd_2CuO_{4-\delta}$, and $La_{2-x}Sr_xCuO_4$, see for example [387], or [26] and references therein), thus strengthening the primary role of optical probes in the investigation of strongly correlated materials.

By inspecting Fig. E.2, we can easily understand how the optical absorption gives a *direct* information on the bandwidth W and on the correlations U in a given system: they can be determined by measuring the gap extension, the position of the Hubbard band and its width, to name a few important accessible informations. Moreover, the optical response, as many other response functions, is subject to a

number of sum-rules [234, 388]. One important partial sum rule is the one connecting the spectral weight of the Drude[3] part of $\sigma_1(\omega)$ to the kinetic energy K of the electrons [26, 389] (and references therein)

$$\int_0^\infty \sigma_{Drude}(\omega)d\omega = -\frac{\pi e^2}{2\hbar^2}\langle K\rangle \tag{E.1}$$

Since the electron kinetic energy (and therefore the Drude spectral weight) can be evaluated from band theory, the ratio K_{exp}/K_{band} between the experimentally determined K_{exp} and the theoretically determined K_{band} gives a quantitative measure of the degree of correlation of a material [389]. If the ratio is close to one the material is weakly or not correlated, if close to zero correlation effects are important and an ideal Mott insulator is positioned as a zero in this particular scale [389]. It is not a case that this ratio resembles the U/W effective interaction, indeed it has been shown that for increasing U, the electron kinetic energy goes to zero as $K \propto 1/U$ [390].

[3]Here we are neglecting possible intraband absorptions due to electron-phonon coupling.

Acknowledgements

Clac! The laser shutter is closed, another day in the laboratory has come to an end. Now I can take off my goggles and write this section that lies in my heart since a long time.

Doctoral studies represent a fundamental period in the formation of a scientist. They last for a period from three to five years, in my case four, and in view of an average life expectancy, this means devoting to them something more than an hour per day, everyday till the end. Together with its scientific endeavour, a PhD (or equivalent formulation) brings in a complex network of human interactions that can significantly modify the quality and the results of this adventure. In my case I have been lucky, therefore I am thanking below all the people that made this possible.

I would like to start by acknowledging my supervisor, Prof. Dr. Andrea Cavalleri, for having trusted in me and in my capabilities as an experimentalist. He shared time and efforts, he gave precious advice throughout these whole four years, on how to select a scientific problem, how to write about results in a meaningful way, but, most importantly, he gave me the opportunity to pursue my research with independence and abundance of resources. I had the opportunity to work in top level group, in a stimulating environment in which I could meet a great fraction of our scientific community. In the laboratory I learned to spot a new frontier in every empty space over our optical tables and I had time to cultivate practical and tacit knowledge of a field (the ultrafast spectroscopy) over which I had no command before.

In addition to Andrea a number of people helped in shaping my work and my formation as a scientist. I could not have made all of this without Dr. Daniele Nicoletti, Dr. Stefan Kaiser and Dr. Matthias C. Hoffmann.

Daniele, thanks for your tips and your advice on how to get here in HH, thanks for the fundamental conversations and for your continuous scientific advice during all the time, when we were still in Geb. 49 as in the last two years. Wherever I will be in the next years, I will tremendously miss you.

Stefan, what to say... it's difficult to condense in a few words all the time and interactions we had in these years. Thank you for your constant, practical help, for all the enormous amount of informations and knowledge that you shared with me, and for all the words of encouragement (very needed in some cases).

Matthias, it's time to thank you for all the support you gave me in the very first

period of my PhD, in teaching me the basics of THz and in all the patience you had in dealing with an optics freshman that had serious problems in aligning even a simple mirror. I will never forget the day we saw the first EOS on my very first setup.
In addition to them I need to thank a couple other people. Thanks to Dr. Stephen Clark for the theoretical support and the constant, patient help during these years. Thanks to Dr. Isabella Gierz, for having involved me in the graphene activities and for all the teaching spanning from graphene physics to the very basics of ARPES. In part of this thesis, as mentioned in the author 's role statement are also heavily involved three other PhD students that shared with me a part of their scientific lives. Rashmi thanks for the long day and nights, the weekends spent in the lab. It was very complex at the beginning to get the things running and the experiment has been quite tough. I hope you enjoyed the time spent together as I did.
Giovanni I want to thank you for the theoretical work you did when we worked together. I strongly appreciated all your efforts and all your patience.
Alice, I must thank you for the outstanding work you did when you joined the fulleride project. It was a tough choice (a difficult experiment, a new setup to build from scratch, a large collaboration already formed) and I appreciated your commitment along this whole year. I hope, if not perfectly symmetrical, to have been at least acceptable as a colleague, but I am looking forward to work together again.
There is then a number of people that shared with me knowledge, instruments, but most importantly a friendly relationship. They have been always around in the most important passages of this adventure, ready to console me in the midst of despair and to celebrate together our achievements. Thanks to Andrea, Cassi, Alberto, Tobia.
Andrea, I am strongly indebted to you for all the times you have been close, closer than others, when I was stuck in a sea of problems. I am struggling to put it in words but I cannot manage to do it effectively (maybe I could say you were "Cartella approved"), but thanks for having been there at the right place, at the right time. Always.
Cassi, we spent 4 years on parallel rails... but sometimes they crossed and I still remember funny moments like the evening you entered the 49 lab to fix my THz problems or the night I nearly fainted when watching you knocking at the office window after the PhD movie screening. I owe you so much from both a scientific and human point of view that I strongly doubt it has been so also in the other

direction. In case not, let me at least warmly thank you.
Tobia, I wanted to thank you for many deep insights you shared with me. I am strongly indebted for a number of crisp observations that day by day revived my engagement in Physics during difficult times.
Alberto thanks for the time spent together, for the weekend running sessions and for the long chats throughout these years.
To conclude with the Hamburg group I wanted to thank Hubertus (I owe you more than a favour) and Regina for all the tips given in these years.
A special mention is for Jörg and all the crazy graphics work done since I joined (and strongly present in this manuscript). You are the best in this business...
Next, I want to thank two close friends that shared hours of video calls with me. Matteo, Fabio, without you two my life would have been worse, much worse and there are no words to express the gratitude for the warmth of a long friendship that crosses borders, extends over thousands of kilometers, that survives the dust of time and the rust of absence. You have been like a Northern star in the fluctuating landscape of my existence and I hope it will be still alike long in the future. I wish you all the best for your research and your life in the next years.
And now a word for someone that is still in Italy and had few, too few possibilities to see me.
Mamma, Sara, in questi anni sono stato lontano per seguire quel sogno che ho sempre coltivato da quando bambino giocavo ad essere uno scienziato. Sono nato così, con un tremendo desiderio di conoscere, di riempire affannosamente di senso ogni singolo secondo, ogni battito di ciglia da qui alla fine.
Vi ringrazio profondamente per aver sopportato la mia assenza, i miei lunghi periodi di lavoro, le sere in cui non mi andava di parlare, l'avervi sovente consegnato la parte peggiore di me. Mi siete mancate tanto, e in questo momento non riesco a esprimere con questi tasti quanto sia forte il desiderio di poter compensare il vuoto che ho lasciato nella vostra quotidianità, nelle parole non dette, negli sguardi e nella mia ingombrante presenza a casa. Non so dirvi se, quando, per quanto tornerò ma sappiate che da qualche parte nel mondo per voi ci sarò sempre.
Vi ringrazio e vi voglio bene.
There is of course a relevant number of people whose influence over the years shaped my personality and that I cannot mention in detail, otherwise this section would become a chapter on its own. I need to thank you for having been like a river that in the long run models even the hardest stones: each interaction, short and fast like falling drops or powerful like roaring falls, contributed to define the

person that now types on this keyboard. Thank you all for having made this possible. I now conclude. It is time to close the laptop as well as this amazing adventure I had here in Hamburg. It is time to move on and, even if with a thrill, to be "[...] strong in will/To strive, to seek, to find, and not to yield." as Lord Tennyson wrote long ago.
Goodbye all.

Bibliography

[1] G Sansone, E Benedetti, F Calegari, C Vozzi, L Avaldi, R Flammini, L Poletto, P Villoresi, C Altucci, R Velotta, S Stagira, S De Silvestri, and M Nisoli. Isolated single-cycle attosecond pulses. *Science*, 314(5798):443–446, 2006. doi: 10.1126/science.1132838. URL `http://www.sciencemag.org/content/314/5798/443.short`.

[2] A L Cavalieri, N Müller, Th Uphues, V S Yakovlev, A Baltuška, B Horvath, B Schmidt, L Blümel, R Holzwarth, S Hendel, M Drescher, U Kleineberg, P M Echenique, R Kienberger, F Krausz, and U Heinzmann. Attosecond spectroscopy in condensed matter. *Nature*, 449(7165):1029–1032, October 2007. doi: 10.1038/nature06229. URL `http://www.nature.com/doifinder/10.1038/nature06229`.

[3] F. Calegari, D. Ayuso, A. Trabattoni, L. Belshaw, S. De Camillis, S. Anumula, F. Frassetto, L. Poletto, A. Palacios, P. Decleva, J. B. Greenwood, F. Martín, and M. Nisoli. Ultrafast electron dynamics in phenylalanine initiated by attosecond pulses. *Science*, 346(6207):336–339, 2014. doi: 10.1126/science.1254061. URL `http://www.sciencemag.org/content/346/6207/336.abstract`.

[4] A Cavalleri, Cs Töth, C Siders, J Squier, F Ráksi, P Forget, and J Kieffer. Femtosecond Structural Dynamics in VO_2 during an Ultrafast Solid-Solid Phase Transition. *Physical Review Letters*, 87(23):237401, November 2001. doi: 10.1103/PhysRevLett.87.237401. URL `http://link.aps.org/doi/10.1103/PhysRevLett.87.237401`.

[5] A Cavalleri, Th Dekorsy, H Chong, J Kieffer, and R Schoenlein. Evidence for a structurally-driven insulator-to-metal transition in VO_2: A view from the ultrafast timescale. *Physical Review B*, 70(16):161102, October 2004. doi:

10.1103/PhysRevB.70.161102. URL http://link.aps.org/doi/10.1103/PhysRevB.70.161102.

[6] A Cavalleri, M Rini, H Chong, S Fourmaux, T Glover, P Heimann, J Kieffer, and R Schoenlein. Band-Selective Measurements of Electron Dynamics in VO_2 Using Femtosecond Near-Edge X-Ray Absorption. *Physical Review Letters*, 95(6):067405, August 2005. doi: 10.1103/PhysRevLett.95.067405. URL http://link.aps.org/doi/10.1103/PhysRevLett.95.067405.

[7] Meng Gao, Cheng Lu, Hubert Jean-Ruel, Lai Chung Liu, Alexander Marx, Ken Onda, Shin-ya Koshihara, Yoshiaki Nakano, Xiangfeng Shao, Takaaki Hiramatsu, Gunzi Saito, Hideki Yamochi, Ryan R Cooney, Gustavo Moriena, Germán Sciaini, and R J Dwayne Miller. Mapping molecular motions leading to charge delocalization with ultrabright electrons. *Nature*, 496(7445):343–346, April 2013. doi: 10.1038/nature12044. URL http://www.nature.com/doifinder/10.1038/nature12044.

[8] P Beaud, A Caviezel, S O Mariager, L Rettig, G Ingold, C Dornes, S-W Huang, J A Johnson, M Radovic, T Huber, T Kubacka, A Ferrer, H T Lemke, M Chollet, D Zhu, J M Glownia, M Sikorski, A Robert, H Wadati, M Nakamura, M Kawasaki, Y Tokura, S L Johnson, and U Staub. A time-dependent order parameter for ultrafast photoinduced phase transitions. *Nature Publishing Group*, 13(10):923–927, August 2014. doi: 10.1038/nmat4046. URL http://www.nature.com/doifinder/10.1038/nmat4046.

[9] Shinichiro Iwai and Hiroshi Okamoto. Ultrafast Phase Control in One-Dimensional Correlated Electron Systems. *Journal of the Physical Society of Japan*, 75(1):011007, January 2006. doi: 10.1143/JPSJ.75.011007. URL http://journals.jps.jp/doi/abs/10.1143/JPSJ.75.011007.

[10] S Wall, D Brida, S R Clark, H P Ehrke, D Jaksch, A Ardavan, S Bonora, H Uemura, Y Takahashi, T Hasegawa, H Okamoto, G Cerullo, and A Cavalleri. Quantum interference between charge excitation paths in a solid-state Mott insulator. *Nature Physics*, 7(2):114–118, December 2010. doi: 10.1038/nphys1831. URL http://dx.doi.org/10.1038/nphys1831.

[11] R D Averitt, G Rodriguez, A I Lobad, JLW Siders, S A Trugman, and A J Taylor. Nonequilibrium superconductivity and quasiparticle dynamics in $YBa_2Cu_3O_{7-\delta}$. *Physical Review B*, 63(14), 2001. URL http://journals.aps.org/prb/abstract/10.1103/PhysRevB.63.140502.

[12] Ryusuke Matsunaga and Ryo Shimano. Nonequilibrium BCS State Dynamics Induced by Intense Terahertz Pulses in a Superconducting NbN Film. *Physical Review Letters*, 109(18):187002, October 2012. doi: 10.1103/PhysRevLett.109.187002. URL http://link.aps.org/doi/10.1103/PhysRevLett.109.187002.

[13] C W Siders, A Cavalleri, K Sokolowski-Tinten, C Toth, T Guo, M Kammler, M H Von Hoegen, K R Wilson, D Von der Linde, and CPJ Barty. Detection of nonthermal melting by ultrafast X-ray diffraction. *Science*, 286(5443): 1340–1342, 1999. URL http://www.sciencemag.org/content/286/5443/1340.short.

[14] K Sokolowski-Tinten, C Blome, C Dietrich, A Tarasevitch, M Horn-von Hoegen, D Von der Linde, A Cavalleri, J Squier, and M Kammler. Femtosecond X-Ray Measurement of Ultrafast Melting and Large Acoustic Transients. *Physical Review Letters*, 87(22):225701, November 2001. doi: 10.1103/PhysRevLett.87.225701. URL http://link.aps.org/doi/10.1103/PhysRevLett.87.225701.

[15] K Sokolowski-Tinten, C Blome, J Blums, A Cavalleri, C Dietrich, A Tarasevitch, I Uschmann, E Förster, M Kammler, and M Horn-von Hoegen. Femtosecond X-ray measurement of coherent lattice vibrations near the Lindemann stability limit. *Nature*, 422(6929):287–289, 2003. URL http://www.exp.physik.uni-due.de/bovensiepen/Publikationen/Sokolowski03Nat422_287.pdf.

[16] Germán Sciaini, Maher Harb, Sergei G Kruglik, Thomas Payer, Christoph T Hebeisen, Frank-J Meyer zu Heringdorf, Mariko Yamaguchi, Michael Horn-von Hoegen, Ralph Ernstorfer, and R J Dwayne Miller. Electronic acceleration of atomic motions and disordering in bismuth. *Nature*, 457(7234):56–59, February 2009. doi: 10.1038/nature07788. URL http://dx.doi.org/10.1038/nature07788.

[17] Y Tokura. Photoinduced phase transition: A tool for generating a hidden state of matter. *Journal of the Physical Society of Japan*, 75(1), January 2006. doi: 10.1143/JPSJ.75.011001. URL http://gateway.webofknowledge.com/gateway/Gateway.cgi?GWVersion=2&SrcAuth=mekentosj&SrcApp=Papers&DestLinkType=FullRecord&DestApp=WOS&KeyUT=000236105300002.

[18] Hirohiko Ichikawa, Shunsuke Nozawa, Tokushi Sato, Ayana Tomita, Kouhei Ichiyanagi, Matthieu Chollet, Laurent Guerin, Nicky Dean, Andrea Cavalleri, Shin-ichi Adachi, Taka-hisa Arima, Hiroshi Sawa, Yasushi Ogimoto, Masao Nakamura, Ryo Tamaki, Kenjiro Miyano, and Shin-ya Koshihara. Transient photoinduced "hidden" phase in a manganite. *Nature Materials*, pages 1–5, January 2011. doi: 10.1038/nmat2929. URL `http://dx.doi.org/10.1038/nmat2929`.

[19] L Stojchevska, I Vaskivskyi, T Mertelj, P Kusar, D Svetin, S Brazovskii, and D Mihailovic. Ultrafast Switching to a Stable Hidden Quantum State in an Electronic Crystal. *Science*, 344(6180):177–180, 2014. doi: 10.1126/science.1241591. URL `http://www.sciencemag.org/content/344/6180/177.short`.

[20] J Bardeen and W H Brattain. The Transistor, a Semi-Conductor Triode. *Physical Review*, 74(2):230–231, 1948. URL `http://link.aps.org/doi/10.1103/PhysRev.74.976.2`.

[21] A Dienst, M C Hoffmann, D Fausti, J C Petersen, S Pyon, T Takayama, H Takagi, and A Cavalleri. Bi-directional ultrafast electric-field gating of interlayer charge transport in a cuprate superconductor. *Nature Photonics*, pages 1–4, June 2011. doi: 10.1038/nphoton.2011.124. URL `http://dx.doi.org/10.1038/nphoton.2011.124`.

[22] M Suda, R Kato, and H M Yamamoto. Light-induced superconductivity using a photoactive electric double layer. *Science*, 2015. doi: 10.1126/science.1261043. URL `http://www.sciencemag.org/content/347/6223/743.short`.

[23] Sir Nevill Mott. *Metal-Insulator Transitions*. Taylor & Francis Ltd., Gunpowder Square, London EC4A3DE, 1997.

[24] Gerald D. Mahan. *Many-Particle Physics*. Plenum, New York, N.Y., 3rd edition, 2000.

[25] Elbio Dagotto. Complexity in Strongly Correlated Electronic Systems. *Science*, 309(5732):257–262, July 2005. doi: 10.1126/science.1107559. URL `http://www.sciencemag.org/cgi/doi/10.1126/science.1107559`.

[26] D Basov, Richard Averitt, Dirk van der Marel, Martin Dressel, and Kristjan Haule. Electrodynamics of correlated electron materials. *Reviews of Modern*

Physics, 83(2):471–542, June 2011. doi: 10.1103/RevModPhys.83.471. URL http://link.aps.org/doi/10.1103/RevModPhys.83.471.

[27] J Rammer. *Quantum Transport Theory*. Perseus Books, New York, United States, 1998.

[28] A J Daley, C Kollath, U Schollwöck, and G Vidal. Time-dependent density-matrix renormalization-group using adaptive effective Hilbert spaces. *J. Stat. Mech.*, 04(cond-mat/0403313):005, 2004. URL http://cds.cern.ch/record/724265.

[29] Steven R White and Adrian E Feiguin. Real-Time Evolution Using the Density Matrix Renormalization Group. *Physical Review Letters*, 93(7): 076401, August 2004. doi: 10.1103/PhysRevLett.93.076401. URL http://link.aps.org/doi/10.1103/PhysRevLett.93.076401.

[30] U Schollwöck. The density-matrix renormalization group. *Reviews of Modern Physics*, 77(1):259–315, January 2005. URL http://journals.aps.org/rmp/abstract/10.1103/RevModPhys.77.259.

[31] J Freericks, V Turkowski, and V Zlatić. Nonequilibrium Dynamical Mean-Field Theory. *Physical Review Letters*, 97(26):266408, December 2006. doi: 10.1103/PhysRevLett.97.266408. URL http://link.aps.org/doi/10.1103/PhysRevLett.97.266408.

[32] Martin Eckstein and Philipp Werner. Thermalization of a pump-excited Mott insulator. *Physical Review B*, 84(3):035122, July 2011. doi: 10.1103/PhysRevB.84.035122. URL http://link.aps.org/doi/10.1103/PhysRevB.84.035122.

[33] Philipp Werner, Naoto Tsuji, and Martin Eckstein. Nonthermal symmetry-broken states in the strongly interacting Hubbard model. *Physical Review B*, 86(20):205101, November 2012. doi: 10.1103/PhysRevB.86.205101. URL http://link.aps.org/doi/10.1103/PhysRevB.86.205101.

[34] Martin Eckstein and Philipp Werner. Photoinduced States in a Mott Insulator. *Physical Review Letters*, 110(12):126401, March 2013. doi: 10.1103/PhysRevLett.110.126401. URL http://link.aps.org/doi/10.1103/PhysRevLett.110.126401.

[35] Hideo Aoki, Naoto Tsuji, Martin Eckstein, Marcus Kollar, Takashi Oka, and Philipp Werner. Nonequilibrium dynamical mean-field theory and its applications. *Reviews of Modern Physics*, 86(2):779–837, June 2014. doi: 10.1103/RevModPhys.86.779. URL `http://link.aps.org/doi/10.1103/RevModPhys.86.779`.

[36] M C Downer and C V Shank. Ultrafast heating of silicon on sapphire by femtosecond optical pulses. *Physical Review Letters*, 56(7):761–764, 1986. URL `http://link.aps.org/doi/10.1103/PhysRevLett.56.761`.

[37] S K Sundaram and Eric Mazur. Inducing and probing non-thermal transitions in semiconductors using femtosecond laser pulses. *Nature Materials*, 1(4):217–224, 2002. URL `http://www.nature.com/nmat/journal/v1/n4/abs/nmat767.html`.

[38] H Okamoto, H. Matsuzaki, T Wakabayashi, Y Takahashi, and T Hasegawa. Photoinduced Metallic State Mediated by Spin-Charge Separation in a One-Dimensional Organic Mott Insulator. *Physical Review Letters*, 98(3), January 2007. doi: 10.1103/PhysRevLett.98.037401. URL `http://link.aps.org/doi/10.1103/PhysRevLett.98.037401`.

[39] Timm Rohwer, Stefan Hellmann, Martin Wiesenmayer, Christian Sohrt, Ankatrin Stange, Bartosz Slomski, Adra Carr, Yanwei Liu, Luis Miaja Avila, Matthias Kalläne, Stefan Mathias, Lutz Kipp, Kai Rossnagel, and Michael Bauer. Collapse of long-range charge order tracked by time-resolved photoemission at high momenta. *Nature*, 471(7339):490–493, March 2011. doi: 10.1038/nature09829. URL `http://www.nature.com/doifinder/10.1038/nature09829`.

[40] J Petersen, S Kaiser, N Dean, A Simoncig, H Liu, A Cavalieri, C Cacho, I Turcu, E Springate, F Frassetto, L Poletto, S Dhesi, H Berger, and A Cavalleri. Clocking the Melting Transition of Charge and Lattice Order in 1T-TaS_2 with Ultrafast Extreme-Ultraviolet Angle-Resolved Photoemission Spectroscopy. *Physical Review Letters*, 107(17), October 2011. doi: 10.1103/PhysRevLett.107.177402. URL `http://link.aps.org/doi/10.1103/PhysRevLett.107.177402`.

[41] M Beck, M Klammer, S Lang, P Leiderer, V V Kabanov, G N Gol'tsman, and J Demsar. Energy-Gap Dynamics of Superconducting NbN Thin Films

Studied by Time-Resolved Terahertz Spectroscopy. *Physical Review Letters*, 107(17):177007, October 2011. doi: 10.1103/PhysRevLett.107.177007. URL http://link.aps.org/doi/10.1103/PhysRevLett.107.177007.

[42] C L Smallwood, J P Hinton, C Jozwiak, W Zhang, J D Koralek, H Eisaki, D H Lee, J Orenstein, and A Lanzara. Tracking Cooper Pairs in a Cuprate Superconductor by Ultrafast Angle-Resolved Photoemission. *Science*, 336 (6085):1137–1139, May 2012. doi: 10.1126/science.1217423. URL http://www.sciencemag.org/cgi/doi/10.1126/science.1217423.

[43] Matteo Rini, Ra'anan Tobey, Nicky Dean, Jiro Itatani, Yasuhide Tomioka, Yoshinori Tokura, Robert W Schoenlein, and Andrea Cavalleri. Control of the electronic phase of a manganite by mode-selective vibrational excitation. *Nature*, 449(7158):72–74, September 2007. doi: 10.1038/nature06119. URL http://www.nature.com/doifinder/10.1038/nature06119.

[44] M Först, C. Manzoni, S Kaiser, Y. Tomioka, Y Tokura, R Merlin, and A Cavalleri. Nonlinear phononics as an ultrafast route to lattice control. *Nature Physics*, 7(11):854–856, August 2011. doi: 10.1038/nphys2055. URL http://www.nature.com/doifinder/10.1038/nphys2055.

[45] M Först, R I Tobey, S Wall, H Bromberger, V Khanna, A L Cavalieri, Y D Chuang, W S Lee, R Moore, W F Schlotter, J J Turner, O Krupin, M Trigo, H Zheng, J F Mitchell, S S Dhesi, J P Hill, and A Cavalleri. Driving magnetic order in a manganite by ultrafast lattice excitation. *Physical Review B*, 84(24):241104, December 2011. doi: 10.1103/PhysRevB.84.241104. URL http://link.aps.org/doi/10.1103/PhysRevB.84.241104.

[46] D Fausti, R I Tobey, N Dean, S Kaiser, A Dienst, M C Hoffmann, S Pyon, T Takayama, H Takagi, and A Cavalleri. Light-induced superconductivity in a stripe-ordered cuprate. *Science*, 331(6014):189–191, 2011. URL http://www.sciencemag.org/content/331/6014/189.short.

[47] A Caviglia, R Scherwitzl, P Popovich, W Hu, H Bromberger, R Singla, M Mitrano, M Hoffmann, S Kaiser, P Zubko, S Gariglio, J M Triscone, M Först, and A Cavalleri. Ultrafast Strain Engineering in Complex Oxide Heterostructures. *Physical Review Letters*, 108(13):1–5, March 2012. doi: 10.1103/PhysRevLett.108.136801. URL http://link.aps.org/doi/10.1103/PhysRevLett.108.136801.

[48] W Hu, S Kaiser, D Nicoletti, C R Hunt, I Gierz, M C Hoffmann, M Le Tacon, T Loew, B Keimer, and A Cavalleri. Optically enhanced coherent transport in $YBa_2Cu_3O_{6.5}$ by ultrafast redistribution of interlayer coupling. *Nature materials*, May 2014. doi: 10.1038/nmat3963. URL `http://www.nature.com/doifinder/10.1038/nmat3963`.

[49] S Kaiser, S R Clark, D Nicoletti, G Cotugno, R I Tobey, N Dean, S Lupi, H Okamoto, T Hasegawa, D Jaksch, and A Cavalleri. Optical Properties of a Vibrationally Modulated Solid State Mott Insulator. *Scientific Reports*, 4, January 2014. doi: 10.1038/srep03823. URL `http://www.nature.com/doifinder/10.1038/srep03823`.

[50] S Kaiser, C R Hunt, D Nicoletti, W Hu, I Gierz, H Y Liu, M Le Tacon, T Loew, D Haug, and B Keimer. Optically induced coherent transport far above T_c in underdoped $YBa_2Cu_3O_{6+\delta}$. *Physical Review B*, 89(18):184516, 2014. doi: 10.1103/PhysRevB.89.184516. URL `http://journals.aps.org/prb/abstract/10.1103/PhysRevB.89.184516`.

[51] R Singla, G Cotugno, S Kaiser, M Först, M Mitrano, H Y Liu, A Cartella, C. Manzoni, H Okamoto, T Hasegawa, S Clark, D Jaksch, and A Cavalleri. Correlation-gap oscillations in an organic Mott-insulator induced by phase locked excitation of local molecular vibrations. *arXiv.org*, September 2014. URL `http://arxiv.org/abs/1409.1088v1`.

[52] Alaska Subedi, Andrea Cavalleri, and Antoine Georges. Theory of nonlinear phononics for coherent light control of solids. *Physical Review B*, 89(22): 220301, June 2014. doi: 10.1103/PhysRevB.89.220301. URL `http://link.aps.org/doi/10.1103/PhysRevB.89.220301`.

[53] Isabella Gierz, Matteo Mitrano, Hubertus Bromberger, Cephise Cacho, Richard Chapman, Emma Springate, Stefan Link, Ulrich Starke, Burkhard Sachs, Martin Eckstein, Tim O Wehling, Mikhail I Katsnelson, Alexander Lichtenstein, and Andrea Cavalleri. Phonon-Pump Extreme-Ultraviolet-Photoemission Probe in Graphene: Anomalous Heating of Dirac Carriers by Lattice Deformation. *Physical Review Letters*, 114(12):125503, March 2015. doi: 10.1103/PhysRevLett.114.125503. URL `http://link.aps.org/doi/10.1103/PhysRevLett.114.125503`.

[54] R Mankowsky, A Subedi, M Först, S O Mariager, M Chollet, H T Lemke, J S Robinson, J M Glownia, M P Minitti, A Frano, M Fechner, N A Spaldin,

T Loew, B Keimer, A Georges, and A Cavalleri. Nonlinear lattice dynamics as a basis for enhanced superconductivity in $YBa_2Cu_3O_{6.5}$. *Nature*, 516 (7529):71–73, November 2014. doi: 10.1038/nature13875. URL `http://dx.doi.org/10.1038/nature13875`.

[55] A Dienst, E Casandruc, D Fausti, L Zhang, M Eckstein, M Hoffmann, V Khanna, N Dean, M Gensch, S Winnerl, W Seidel, S Pyon, T Takayama, H Takagi, and A Cavalleri. Optical excitation of Josephson plasma solitons in a cuprate superconductor. *Nature Materials*, 12(4):1–7, March 2013. doi: 10.1038/nmat3580. URL `http://dx.doi.org/10.1038/nmat3580`.

[56] Ryusuke Matsunaga, Yuki I Hamada, Kazumasa Makise, Yoshinori Uzawa, Hirotaka Terai, Zhen Wang, and Ryo Shimano. Higgs Amplitude Mode in the BCS Superconductors $Nb_{1-x}Ti_xN$ Induced by Terahertz Pulse Excitation. *Physical Review Letters*, 111(5):057002, July 2013. doi: 10.1103/PhysRevLett.111.057002. URL `http://link.aps.org/doi/10.1103/PhysRevLett.111.057002`.

[57] Ryusuke Matsunaga, Naoto Tsuji, Hiroyuki Fujita, Arata Sugioka, Kazumasa Makise, Yoshinori Uzawa, Hirotaka Terai, Zhen Wang, Hideo Aoki, and Ryo Shimano. Light-induced collective pseudospin precession resonating with Higgs mode in a superconductor. *Science*, 345(6201):1145–1149, 2014. doi: 10.1126/science.1254917. URL `http://www.sciencemag.org/content/345/6201/1145.short`.

[58] W Heisenberg. Über den anschaulichen Inhalt der quantentheoretischen Kinematik und Mechanik. *Zeitschrift für Physik*, 43:172–198, 1927. doi: 10.1007/BF01397280.

[59] J J Sakurai. *Modern Quantum Mechanics*. Addison-Wesley Publishing Company Inc., Reading, Massachusetts, revised edition edition, 1994.

[60] C Sohrt, A Stange, M Bauer, and K Rossnagel. How fast can a Peierls-Mott insulator be melted? *Faraday Discussions*, 171:243–257, November 2014. doi: 10.1039/C4FD00042K. URL `http://dx.doi.org/10.1039/C4FD00042K`.

[61] Zala Lenarčič and Peter Prelovšek. Charge recombination in undoped cuprates. *Physical Review B*, 90(23):235136, December 2014. doi: 10.

1103/PhysRevB.90.235136. URL http://link.aps.org/doi/10.1103/PhysRevB.90.235136.

[62] Niels Strohmaier, Daniel Greif, Robert Jördens, Leticia Tarruell, Henning Moritz, and Tilman Esslinger. Observation of Elastic Doublon Decay in the Fermi-Hubbard Model. *Physical Review Letters*, 104(8), February 2010. doi: 10.1103/PhysRevLett.104.080401. URL http://link.aps.org/doi/10.1103/PhysRevLett.104.080401.

[63] Rajdeep Sensarma, David Pekker, Ehud Altman, Eugene Demler, Niels Strohmaier, Daniel Greif, Robert Jördens, Leticia Tarruell, Henning Moritz, and Tilman Esslinger. Lifetime of double occupancies in the Fermi-Hubbard model. *Physical Review B*, 82(22), December 2010. doi: 10.1103/PhysRevB.82.224302. URL http://link.aps.org/doi/10.1103/PhysRevB.82.224302.

[64] Hiori Kino and Hidetoshi Fukuyama. Phase diagram of two-dimensional organic conductors:(BEDT-TTF)$_2$X. *Journal of the Physical Society of Japan*, 65(7):2158–2169, 1996. URL http://journals.jps.jp/doi/abs/10.1143/JPSJ.65.2158.

[65] S Lefebvre, P Wzietek, S Brown, C Bourbonnais, D Jérome, C Méziere, M Fourmigué, and P Batail. Mott transition, antiferromagnetism, and unconventional superconductivity in layered organic superconductors. *Physical Review Letters*, 85:5420, 2000.

[66] M Dressel and N Drichko. Optical properties of two-dimensional organic conductors: Signatures of charge ordering and correlation effects. *Chemical reviews*, 104(11):5689–5715, November 2004. doi: 10.1021/cr030642f. URL http://pubs.acs.org/doi/pdf/10.1021/cr040697x.

[67] B J Powell and Ross H McKenzie. Strong electronic correlations in superconducting organic charge transfer salts. *Journal of Physics: Condensed Matter*, 18(45):R827–R866, October 2006. doi: 10.1088/0953-8984/18/45/R03. URL http://stacks.iop.org/0953-8984/18/i=45/a=R03?key=crossref.06e2ee8cd6b157d1a237691282d111d6.

[68] J Merino, M Dumm, N Drichko, M Dressel, and Ross McKenzie. Quasiparticles at the Verge of Localization near the Mott Metal-Insulator Transition in a Two-Dimensional Material. *Physical Review Letters*, 100(8), February

2008. doi: 10.1103/PhysRevLett.100.086404. URL http://link.aps.org/doi/10.1103/PhysRevLett.100.086404.

[69] Alexey Y Ganin, Yasuhiro Takabayashi, Yaroslav Z Khimyak, Serena Margadonna, Anna Tamai, Matthew J Rosseinsky, and Kosmas Prassides. Bulk superconductivity at 38 K in a molecular system. *Nature Publishing Group*, 7(5):367–371, April 2008. doi: 10.1038/nmat2179. URL http://www.nature.com/doifinder/10.1038/nmat2179.

[70] Y. Takabayashi, A Y Ganin, P Jeglič, D Arčon, T Takano, Y. Iwasa, Y. Ohishi, M. Takata, N Takeshita, and K Prassides. The disorder-free non-BCS superconductor Cs_3C_{60} emerges from an antiferromagnetic insulator parent state. *Science*, 323(5921):1585–1590, 2009. doi: 10.1126/science.1169163. URL http://www.sciencemag.org/content/323/5921/1585.short.

[71] Alexey Y Ganin, Yasuhiro Takabayashi, Peter Jeglič, Denis Arčon, Anton Potočnik, Peter J Baker, Yasuo Ohishi, Martin T McDonald, Manolis D Tzirakis, Alec McLennan, George R Darling, Masaki Takata, Matthew J Rosseinsky, and Kosmas Prassides. Polymorphism control of superconductivity and magnetism in Cs_3C_{60} close to the Mott transition. *Nature*, 466(7303):221–225, August 2010. doi: 10.1038/nature09120. URL http://dx.doi.org/10.1038/nature09120.

[72] J F Kwak. Tetramethyltetraselenafulvalene salts [$(TMTSF)_2X$]: Anisotropy and effective dimensionality of the Fermi surface. *Physical Review B*, 26(8):4789, 1982. URL http://prb.aps.org/abstract/PRB/v26/i8/p4789_1.

[73] T Ishiguro and H Anzai. Organic Superconductors: Present Status and Clue to Future. *Molecular Crystals and Liquid Crystals*, 171(1):333–342, 1989. URL http://www.tandfonline.com/doi/abs/10.1080/00268948908065805.

[74] A Schwartz, M Dressel, G. Grüner, V. Vescoli, L Degiorgi, and T. Giamarchi. On-chain electrodynamics of metallic $(TMTSF)_2X$ salts: Observation of Tomonaga-Luttinger liquid response. *Physical Review B*, 58(3):1261, 1998. URL http://prb.aps.org/abstract/PRB/v58/i3/p1261_1.

[75] J. Moser, M Gabay, P. Auban-Senzier, D Jérome, K. Bechgaard, and JM Fabre. Transverse transport in organic conductors: possible evidence

for a Luttinger liquid. *The European Physical Journal B-Condensed Matter and Complex Systems*, 1(1):39–46, 1998. URL http://www.springerlink.com/index/XNAVPEPH2LR82HQ9.pdf.

[76] H. Seo, C. Hotta, and H. Fukuyama. Toward systematic understanding of diversity of electronic properties in low-dimensional molecular solids. *Chemical reviews*, 104(11):5005–5036, 2004. URL http://pubs.acs.org/doi/abs/10.1021/cr030646k.

[77] A Pashkin, M Dressel, and C Kuntscher. Pressure-induced deconfinement of the charge transport in the quasi-one-dimensional Mott insulator $(TMTTF)_2AsF_6$. *Physical Review B*, 74(16), October 2006. doi: 10.1103/PhysRevB.74.165118. URL http://link.aps.org/doi/10.1103/PhysRevB.74.165118.

[78] Martin Dressel. Ordering phenomena in quasi-one-dimensional organic conductors. *Naturwissenschaften*, 94(7):527–541, May 2007. doi: 10.1007/s00114-007-0227-1. URL http://link.springer.com/10.1007/s00114-007-0227-1.

[79] A Pashkin, M Dressel, M Hanfland, and C A Kuntscher. Deconfinement transition and dimensional crossover in the Bechgaard-Fabre salts: Pressure- and temperature-dependent optical investigations. *Physical Review B*, 81 (12), March 2010. doi: 10.1103/PhysRevB.81.125109. URL http://link.aps.org/doi/10.1103/PhysRevB.81.125109.

[80] S J Blundell and F L Pratt. Organic and molecular magnets. *Journal of Physics: Condensed Matter*, 16(24):R771–R828, June 2004. doi: 10.1088/0953-8984/16/24/R03. URL http://stacks.iop.org/0953-8984/16/i=24/a=R03?key=crossref.220c9563562efae3cd169fc85327fb6f.

[81] Y. Iwasa, K Mizuhashi, T Koda, Y Tokura, and G Saito. Metal-insulator transition and antiferromagnetic order in bis (ethylenedithio) tetrathiafulvalene tetracyanoquinodimethane (BEDT-TTF)(TCNQ). *Physical Review B*, 49(5):3580, 1994. URL http://journals.aps.org/prb/abstract/10.1103/PhysRevB.49.3580.

[82] G. Saito T. Ishiguro, K. Yamaji. *Organic Superconductors*. Springer Verlag, Berlin Heidelberg, 2nd edition, 1998.

[83] Ross McKenzie, J Merino, J Marston, and O Sushkov. Charge ordering and antiferromagnetic exchange in layered molecular crystals of the θ type. *Physical Review B*, 64(8):085109, August 2001. doi: 10.1103/PhysRevB.64.085109. URL http://link.aps.org/doi/10.1103/PhysRevB.64.085109.

[84] D Jérome. Organic conductors: from charge density wave TTF-TCNQ to superconducting $(TMTSF)_2PF_6$. *Chemical reviews*, 104(11):5565–5592, 2004. URL http://pubs.acs.org/doi/abs/10.1021/cr030652g.

[85] D Andres, M Kartsovnik, W Biberacher, K Neumaier, E Schuberth, and H Müller. Superconductivity in the charge-density-wave state of the organic metal α-$(BEDT\text{-}TTF)_2KHg(SCN)_4$. *Physical Review B*, 72(17), November 2005. doi: 10.1103/PhysRevB.72.174513. URL http://link.aps.org/doi/10.1103/PhysRevB.72.174513.

[86] N Drichko, M Dressel, C Kuntscher, A Pashkin, A Greco, J Merino, and J Schlueter. Electronic properties of correlated metals in the vicinity of a charge-order transition: Optical spectroscopy of α-$(BEDT\text{-}TTF)_2MHg(SCN)_4$ (M=NH_4, Rb, Tl). *Physical Review B*, 74(23), December 2006. doi: 10.1103/PhysRevB.74.235121. URL http://link.aps.org/doi/10.1103/PhysRevB.74.235121.

[87] Y Ihara, H Alloul, P Wzietek, D Pontiroli, M Mazzani, and M Riccò. Spin dynamics at the Mott transition and in the metallic state of the Cs_3C_60 superconducting phases. *Europhys. Lett*, 94(3):37007, April 2011. doi: 10.1209/0295-5075/94/37007. URL http://stacks.iop.org/0295-5075/94/i=3/a=37007?key=crossref.29854bb844f8f8edcd8266ba7d1aa0a6.

[88] Y Kurosaki, Y Shimizu, K Miyagawa, K Kanoda, and G Saito. Mott Transition from a Spin Liquid to a Fermi Liquid in the Spin-Frustrated Organic Conductor κ-$(ET)_2Cu_2(CN)_3$. *Physical Review Letters*, 95(17):177001, October 2005. doi: 10.1103/PhysRevLett.95.177001. URL http://link.aps.org/doi/10.1103/PhysRevLett.95.177001.

[89] Sebastian Elsässer, Dan Wu, Martin Dressel, and John A Schlueter. Power-law dependence of the optical conductivity observed in the quantum spin-liquid compound κ-$(BEDT\text{-}TTF)_2Cu_2(CN)_3$. *Physical Review B*, 86(15):155150, 2012. doi: 10.1103/PhysRevLett.99.156402. URL http://journals.aps.org/prb/abstract/10.1103/PhysRevB.86.155150.

[90] Takayuki Isono, Hiromichi Kamo, Akira Ueda, Kazuyuki Takahashi, Motoi Kimata, Hiroyuki Tajima, Satoshi Tsuchiya, Taichi Terashima, Shinya Uji, and Hatsumi Mori. Gapless Quantum Spin Liquid in an Organic Spin-1/2 Triangular-Lattice κ-H_3(Cat-EDT-TTF)$_2$. *Physical Review Letters*, 112(17): 177201, April 2014. doi: 10.1103/PhysRevLett.112.177201. URL `http://link.aps.org/doi/10.1103/PhysRevLett.112.177201`.

[91] D Jérome. The physics of organic superconductors. *Science*, 252(5012): 1509–1514, 1991. URL `http://www.sciencemag.org/content/252/5012/1509.short`.

[92] Arzhang Ardavan, Stuart Brown, Seiichi Kagoshima, Kazushi Kanoda, Kazuhiko Kuroki, Hatsumi Mori, Masao Ogata, Shinya Uji, and Jochen Wosnitza. Recent Topics of Organic Superconductors. *Journal of the Physical Society of Japan*, 81(1):011004, December 2011. doi: 10.1143/JPSJ.81.011004. URL `http://jpsj.ipap.jp/link?JPSJ/81/011004/`.

[93] Jaime Merino and Ross McKenzie. Superconductivity Mediated by Charge Fluctuations in Layered Molecular Crystals. *Physical Review Letters*, 87 (23), November 2001. doi: 10.1103/PhysRevLett.87.237002. URL `http://link.aps.org/doi/10.1103/PhysRevLett.87.237002`.

[94] Moon-Sun Nam, Arzhang Ardavan, Stephen J Blundell, and John A Schlueter. Fluctuating superconductivity in organic molecular metals close to the Mott transition. *Nature*, 449(7162):584–587, October 2007. doi: 10.1038/nature06182. URL `http://www.nature.com/doifinder/10.1038/nature06182`.

[95] Moon-Sun Nam, Cécile Meźière, Patrick Batail, Leokadiya Zorina, Sergey Simonov, and Arzhang Ardavan. Superconducting fluctuations in organic molecular metals enhanced by Mott criticality. *Scientific Reports*, 3, 2013. doi: 10.1038/srep03390. URL `http://www.nature.com/srep/2013/131202/srep03390/full/srep03390.html?message-global=remove&WT.ec_id=SREP-639-20140102`.

[96] H Mayaffre, S Krämer, M Horvatić, C Berthier, K Miyagawa, K Kanoda, and V F Mitrović. Evidence of Andreev bound states as a hallmark of the FFLO phase in κ-(BEDT-TTF)$_2$Cu(NCS)$_2$. *Nature Physics*, 10(12):928–932, October 2014. doi: 10.1038/nphys3121. URL `http://www.nature.com/doifinder/10.1038/nphys3121`.

[97] N.W. Ashcroft and N.D. Mermin. *Solid State Physics*. Saunders College, Philadelphia, 1976.

[98] Eva Pavarini, Erik Koch, Dieter Vollhardt, and Alexander (Eds.) Lichtenstein. *The LDA+DMFT approach to strongly correlated materials: lecture notes of the autumn school 2011, hands-on LDA+DMFT ; autumn school organized by the DFG research unit 1346 dynamical mean-field approach with predictive power for strongly correlated materials at Forschungszentrum Jülich 4-7 October 2011*, volume 1 of *Schriften des Forschungszentrums Jülich. Reihe Modeling and simulation*. Forschungszentrum, Zentralbibliothek, Jülich, 2011. ISBN 9783893367344. URL `http://juser.fz-juelich.de/record/136342`. Record converted from JUWEL: 18.07.2013.

[99] Ken Onda, Hideki Yamochi, and Shin-ya Koshihara. Diverse Photoinduced Dynamics in an Organic Charge-Transfer Complex Having Strong Electron-Phonon Interactions. *Accounts of Chemical Research*, 47(12):3494–3503, December 2014. doi: 10.1021/ar500257b. URL `http://pubs.acs.org/doi/abs/10.1021/ar500257b`.

[100] Daniel Faltermeier, Jakob Barz, Michael Dumm, Martin Dressel, Natalia Drichko, Boris Petrov, Victor Semkin, Rema Vlasova, Cécile Meźière, and Patrick Batail. Bandwidth-controlled Mott transition in κ-(BEDT-TTF)$_2$Cu[N(CN)$_2$]Br$_x$Cl$_{1-x}$: Optical studies of localized charge excitations. *Physical Review B*, 76(16):165113, October 2007. doi: 10.1103/PhysRevB.76.165113. URL `http://link.aps.org/doi/10.1103/PhysRevB.76.165113`.

[101] A Damascelli, Z-X Shen, and Z Hussain. Angle-resolved photoemission spectroscopy of the cuprate superconductors. *Rev. Mod. Phys.*, 75(cond-mat/0208504):473, August 2002.

[102] PA Lee, N Nagaosa, and XG Wen. Doping a Mott insulator: Physics of high-temperature superconductivity. *Reviews of Modern Physics*, 78(1):17–85, 2006.

[103] D Scalapino. A common thread: The pairing interaction for unconventional superconductors. *Reviews of Modern Physics*, 84(4):1383–1417, October 2012. doi: 10.1103/RevModPhys.84.1383. URL `http://link.aps.org/doi/10.1103/RevModPhys.84.1383`.

[104] Matteo Mitrano, Beatrice Maroni, Carlo Marini, Michael Hanfland, Boby Joseph, Paolo Postorino, and Lorenzo Malavasi. Anisotropic compression in the high-pressure regime of pure and chromium-doped vanadium dioxide. *Physical Review B*, 85(18), May 2012. doi: 10.1103/PhysRevB.85.184108. URL `http://link.aps.org/doi/10.1103/PhysRevB.85.184108`.

[105] L Bai, Q Li, S A Corr, Y Meng, C. Park, and S V Sinogeikin. Pressure-induced phase transitions and metallization in VO_2. *Physical Review B*, 2015. doi: 10.1103/PhysRevB.91.104110. URL `http://journals.aps.org/prb/abstract/10.1103/PhysRevB.91.104110`.

[106] Sergey V Ovsyannikov, Dmytro M Trots, Alexander V Kurnosov, Wolfgang Morgenroth, Hanns-Peter Liermann, and Leonid Dubrovinsky. Anomalous compression and new high-pressure phases of vanadium sesquioxide, V_2O_3. *Journal of Physics: Condensed Matter*, 25(38):385401, August 2013. doi: 10.1088/0953-8984/25/38/385401. URL `http://stacks.iop.org/0953-8984/25/i=38/a=385401?key=crossref.aa6179970d0d82fa5ed6c34982b8234f`.

[107] Neil C Hyatt, Joseph A Hriljac, Yuzuru Miyazaki, Ian Gameson, Peter P Edwards, and Andrew P Jephcoat. Structure-compressibility relationships in layered cuprate materials. *Physical Review B*, 65(1):014507, November 2001. doi: 10.1103/PhysRevB.65.014507. URL `http://link.aps.org/doi/10.1103/PhysRevB.65.014507`.

[108] J. Hubbard. Electron correlations in narrow energy bands. *Proceedings of the Royal Society of London. A. Mathematical and Physical Sciences*, 276 (1365):238–257, 1963. URL `http://rspa.royalsocietypublishing.org/content/276/1365/238.short`.

[109] E H Lieb and F Y Wu. Absence of Mott transition in an exact solution of the short-range, one-band model in one dimension. *Physical Review Letters*, 20(25):1445–1448, 1968.

[110] Antoine Georges and Werner Krauth. Numerical solution of the d $=\infty$ Hubbard model: Evidence for a Mott transition. *Physical Review Letters*, 69:1240–1243, 1992.

[111] Antoine Georges, Gabriel Kotliar, Werner Krauth, and Marcelo J Rozenberg. Dynamical mean-field theory of strongly correlated fermion systems and the limit of infinite dimensions. *Reviews of Modern Physics*, 68(1):13, 1996.

[112] M Imada, A Fujimori, and Y Tokura. Metal-insulator transitions. *Reviews of Modern Physics*, 70(4):1039–1263, 1998.

[113] Thomas Pruschke. Antiferromagnetism and metal insulator transition in the frustrated Hubbard model. *Progress of Theoretical Physics Supplement*, 160: 274–295, 2005. URL `http://ptps.oxfordjournals.org/content/160/274.abstract`.

[114] ND Mermin and H Wagner. Absence of ferromagnetism or antiferromagnetism in one-or two-dimensional isotropic Heisenberg models. *Physical Review Letters*, 17(22):1133–1136, 1966.

[115] S Iwai, M Ono, A Maeda, H. Matsuzaki, H Kishida, H Okamoto, and Y Tokura. Ultrafast Optical Switching to a Metallic State by Photoinduced Mott Transition in a Halogen-Bridged Nickel-Chain Compound. *Physical Review Letters*, 91(5):057401, July 2003. doi: 10.1103/PhysRevLett.91.057401. URL `http://link.aps.org/doi/10.1103/PhysRevLett.91.057401`.

[116] J B Torrance, A Girlando, J J Mayerle, J I Crowley, V Y Lee, P Batail, and S J LaPlaca. Anomalous Nature of Neutral-to-Ionic Phase-Transition in Tetrathiafulvalene-Chloranil. *Phys. Rev. Lett*, 47(24):1747–1750, 1981. URL `http://journals.aps.org/prl/abstract/10.1103/PhysRevLett.47.1754`.

[117] Y Tokura, T Koda, T Mitani, and G Saito. Neutral-to-Ionic Transition in Tetrathiafulvalene-P-Chloranil as Investigated by Optical Reflection Spectra. *Solid State Communications*, 43(10):757–760, 1982. URL `http://www.sciencedirect.com/science/article/pii/0038109882909863`.

[118] Alberto Girlando, Franca Marzola, Cesare Pecile, and Jerry B Torrance. Vibrational spectroscopy of mixed stack organic semiconductors: Neutral and ionic phases of tetrathiafulvalene-chloranil (TTF-CA) charge transfer complex. *The Journal of Chemical Physics*, 79(2):1075, 1983. doi: 10.1063/1.445833. URL `http://scitation.aip.org/content/aip/journal/jcp/79/2/10.1063/1.445833`.

[119] Y Tokura, Y Kaneko, H Okamoto, S Tanuma, T Koda, T Mitani, and G Saito. Spectroscopic Study of the Neutral-to-Ionic Phase-Transition in TTF-Chloranil. *Molecular Crystals and Liquid Crystals*, 125(1-4): 71–80, 1985. URL http://www.tandfonline.com/doi/abs/10.1080/00268948508080088.

[120] S Koshihara, Y Tokura, T Mitani, G Saito, and T Koda. Photoinduced Valence Instability in the Organic Molecular-Compound Tetrathiafulvalene-P-Chloranil (TTF-CA). *Physical Review B*, 42(10):6853–6856, 1990. URL http://journals.aps.org/prb/abstract/10.1103/PhysRevB.42.6853.

[121] T Suzuki, T Sakamaki, K Tanimura, S Koshihara, and Y Tokura. Ionic-to-neutral phase transformation induced by photoexcitation of the charge-transfer band in tetrathiafulvalene-p-chloranil crystals. *Physical Review B*, 60(9):6191, 1999. URL http://journals.aps.org/prb/abstract/10.1103/PhysRevB.60.6191.

[122] Shin-ya Koshihara, Yosuke Takahashi, Hiroyuki Sakai, Yoshinori Tokura, and Tadeusz Luty. Photoinduced Cooperative Charge Transfer in Low-Dimensional Organic Crystals. *The Journal of Physical Chemistry B*, 103 (14):2592–2600, April 1999. doi: 10.1021/jp984172i. URL http://pubs.acs.org/doi/abs/10.1021/jp984172i.

[123] S Iwai, S Tanaka, K Fujinuma, H Kishida, H Okamoto, and Y Tokura. Ultrafast Optical Switching from an Ionic to a Neutral State in Tetrathiafulvalene-p-Chloranil (TTF-CA) Observed in Femtosecond Reflection Spectroscopy. *Physical Review Letters*, 88(5):057402, January 2002. doi: 10.1103/PhysRevLett.88.057402. URL http://link.aps.org/doi/10.1103/PhysRevLett.88.057402.

[124] E Collet, M H Lemee-Cailleau, M Buron-Le Cointe, H Cailleau, M Wulff, T Luty, S Y Koshihara, M Meyer, L Toupet, P Rabiller, and S Techert. Laser-induced ferroelectric structural order in an organic charge-transfer crystal. *Science*, 300(5619):612–615, 2003. URL http://scholar.google.com/scholar?q=related:K8iXjv4owYgJ:scholar.google.com/&hl=en&num=20&as_sdt=0,5.

[125] H Okamoto, Y Ishige, S Tanaka, H Kishida, S Iwai, and Y Tokura. Photoinduced phase transition in tetrathiafulvalene-p-chloranil observed in femtosecond reflection spectroscopy. *Physical Review B*, 70(16):165202, October

2004. doi: 10.1103/PhysRevB.70.165202. URL http://link.aps.org/doi/10.1103/PhysRevB.70.165202.

[126] Katsumi Tanimura. Femtosecond time-resolved reflection spectroscopy of photoinduced ionic-neutral phase transition in TTF-CA crystals. *Physical Review B*, 70(14):144112, October 2004. doi: 10.1103/PhysRevB.70.144112. URL http://link.aps.org/doi/10.1103/PhysRevB.70.144112.

[127] H. Okamoto, Y. Tokura, and T. Koda. Optical study of structural phase transition in organic charge-transfer crystals k- and rb-tetracyanoquinodimethane. *Phys. Rev. B*, 36:3858–3867, Sep 1987. doi: 10.1103/PhysRevB.36.3858. URL http://link.aps.org/doi/10.1103/PhysRevB.36.3858.

[128] H Okamoto, K Ikegami, T Wakabayashi, Y Ishige, J Togo, H Kishida, and H. Matsuzaki. Ultrafast Photoinduced Melting of a Spin-Peierls Phase in an Organic Charge-Transfer Compound, K-Tetracyanoquinodimethane. *Physical Review Letters*, 96(3):037405, January 2006. doi: 10.1103/PhysRevLett.96.037405. URL http://link.aps.org/doi/10.1103/PhysRevLett.96.037405.

[129] Hirotaka Uemura, Hiroyuki Matsuzaki, Yukihiro Takahashi, Tatsuo Hasegawa, and Hiroshi Okamoto. Ultrafast Charge Dynamics in One-Dimensional Organic Mott Insulators. *Journal of the Physical Society of Japan*, 77(11):113714, November 2008. doi: 10.1143/JPSJ.77.113714. URL http://jpsj.ipap.jp/link?JPSJ/77/113714/.

[130] Yoshitaka Matsubara, Sho Ogihara, Jiro Itatani, Nobuya Maeshima, Kenji Yonemitsu, Tadahiko Ishikawa, Yoichi Okimoto, Shin-ya Koshihara, Takaaki Hiramatsu, Yoshiaki Nakano, Hideki Yamochi, Gunzi Saito, and Ken Onda. Coherent dynamics of photoinduced phase formation in a strongly correlated organic crystal. *Physical Review B*, 89(16):161102, April 2014. doi: 10.1103/PhysRevB.89.161102. URL http://link.aps.org/doi/10.1103/PhysRevB.89.161102.

[131] Y Kawakami, S Iwai, T Fukatsu, M Miura, N Yoneyama, T. Sasaki, and N Kobayashi. Optical Modulation of Effective On-Site Coulomb Energy for the Mott Transition in an Organic Dimer Insulator. *Physical Review Letters*, 103(6):066403, August 2009. doi: 10.1103/PhysRevLett.103.066403. URL http://link.aps.org/doi/10.1103/PhysRevLett.103.066403.

[132] K Kanoda. Recent progress in NMR studies on organic conductors. *Hyperfine Interactions*, 104(1-4):235–249, 1997. URL `http://link.springer.com/article/10.1023/A:1012696314318`.

[133] M Kasami, T Mishina, and J Nakahara. Femtosecond pump and probe spectroscopy in Bi under high pressure. *physica status solidi (b)*, 241(14): 3113–3116, November 2004. doi: 10.1002/pssb.200405222. URL `http://doi.wiley.com/10.1002/pssb.200405222`.

[134] S Iwai, K Yamamoto, F Hiramatsu, H Nakaya, Y Kawakami, and K Yakushi. Hydrostatic pressure effect on photoinduced insulator-to-metal transition in the layered organic salt α-(BEDT-TTF)$_2$I$_3$. *Physical Review B*, 77(12): 125131, March 2008. doi: 10.1103/PhysRevB.77.125131. URL `http://link.aps.org/doi/10.1103/PhysRevB.77.125131`.

[135] B C Hess, G S Kanner, Z V Vardeny, and G L Baker. High-pressure effects on ultrafast-relaxation kinetics of excitons in polydiacetylene 4BCMU. *Physical Review Letters*, 66(18):2364–2367, 1991. URL `http://link.aps.org/doi/10.1103/PhysRevLett.66.2364`.

[136] T Hasegawa, K. Inukai, S. Kagoshima, T. Sugawara, T. Mochida, S. Sugiura, and Y. Iwasa. Synthesis, structure, and electronic properties of (BEDT-TTF)(F_nTCNQ)(n= 0, 1, 2, 4). *Synthetic Metals*, 86(1-3):1801–1802, 1997. URL `http://www.sciencedirect.com/science/article/pii/S0379677997809101`.

[137] T Hasegawa, S. Kagoshima, T. Mochida, S. Sugiura, and Y. Iwasa. Electronic states and anti-ferromagnetic order in mixed-stack charge-transfer compound (BEDT-TTF)(F_2TCNQ). *Solid State Communications*, 103(8): 489–493, 1997. URL `http://www.sciencedirect.com/science/article/pii/S0038109897002263`.

[138] T. Hasegawa. Private communication. 2010.

[139] Martin R Bryce and Lynne C Murphy. Organic metals. *Nature*, 309, May 1984. URL `http://www.nature.com/nature/journal/v309/n5964/abs/309119a0.html`.

[140] T Hasegawa, T. Mochida, R. Kondo, S. Kagoshima, Y. Iwasa, T. Akutagawa, T. Nakamura, and G Saito. Mixed-stack organic charge-transfer complexes

with intercolumnar networks. *Physical Review B*, 62(15):10059, 2000. URL http://prb.aps.org/abstract/PRB/v62/i15/p10059_1.

[141] M. J. Frisch, G. W. Trucks, H. B. Schlegel, G. E. Scuseria, M. A. Robb, J. R. Cheeseman, G. Scalmani, V. Barone, B. Mennucci, G. A. Petersson, H. Nakatsuji, M. Caricato, X. Li, H. P. Hratchian, A. F. Izmaylov, J. Bloino, G. Zheng, J. L. Sonnenberg, M. Hada, M. Ehara, K. Toyota, R. Fukuda, J. Hasegawa, M. Ishida, T. Nakajima, Y. Honda, O. Kitao, H. Nakai, T. Vreven, J. A. Montgomery, Jr., J. E. Peralta, F. Ogliaro, M. Bearpark, J. J. Heyd, E. Brothers, K. N. Kudin, V. N. Staroverov, R. Kobayashi, J. Normand, K. Raghavachari, A. Rendell, J. C. Burant, S. S. Iyengar, J. Tomasi, M. Cossi, N. Rega, J. M. Millam, M. Klene, J. E. Knox, J. B. Cross, V. Bakken, C. Adamo, J. Jaramillo, R. Gomperts, R. E. Stratmann, O. Yazyev, A. J. Austin, R. Cammi, C. Pomelli, J. W. Ochterski, R. L. Martin, K. Morokuma, V. G. Zakrzewski, G. A. Voth, P. Salvador, J. J. Dannenberg, S. Dapprich, A. D. Daniels, Ö. Farkas, J. B. Foresman, J. V. Ortiz, J. Cioslowski, and D. J. Fox. Gaussian-09 Revision D.01. Gaussian Inc. Wallingford CT 2009.

[142] P Guionneau, C J Kepert, G Bravic, D Chasseau, M R Truter, M Kurmoo, and P Day. Determining the charge distribution in BEDT-TTF salts. *Synthetic Metals*, 86(1-3):1973–1974, 1997. URL http://gateway.webofknowledge.com/gateway/Gateway.cgi?GWVersion=2&SrcAuth=mekentosj&SrcApp=Papers&DestLinkType=FullRecord&DestApp=WOS&KeyUT=A1997WZ98800085.

[143] Alberto Girlando. Charge Sensitive Vibrations and Electron-Molecular Vibration Coupling in Bis(ethylenedithio)-tetrathiafulvalene (BEDT-TTF). *The Journal of Physical Chemistry C*, 115(39):19371–19378, October 2011. doi: 10.1021/jp206171r. URL http://pubs.acs.org/doi/abs/10.1021/jp206171r.

[144] T. Giamarchi. Theoretical framework for quasi-one dimensional systems. *Chemical reviews*, 104(11):5037–5056, 2004. URL http://pubs.acs.org/doi/abs/10.1021/cr030647c.

[145] F Essler, F Gebhard, and E. Jeckelmann. Excitons in one-dimensional Mott insulators. *Physical Review B*, 64(12):125119, September 2001. doi:

10.1103/PhysRevB.64.125119. URL http://link.aps.org/doi/10.1103/PhysRevB.64.125119.

[146] Eric Jeckelmann. Ground-State Phase Diagram of a Half-Filled One-Dimensional Extended Hubbard Model. *Physical Review Letters*, 89(23), November 2002. doi: 10.1103/PhysRevLett.89.236401. URL http://link.aps.org/doi/10.1103/PhysRevLett.89.236401.

[147] Eric Jeckelmann. Optical excitations in a one-dimensional Mott insulator. *Physical Review B*, 67(7), February 2003. doi: 10.1103/PhysRevB.67.075106. URL http://link.aps.org/doi/10.1103/PhysRevB.67.075106.

[148] Masao Ogata and Hiroyuki Shiba. Bethe-ansatz wave function, momentum distribution, and spin correlation in the one-dimensional strongly correlated Hubbard model. *Physical Review B*, 41(4):2326, 1990.

[149] Henk Eskes and Andrzej M Oleś. Two Hubbard Bands: Weight transfer in optical and one-particle spectra. *Physical Review Letters*, 73(9): 1279, 1994. URL http://journals.aps.org/prl/abstract/10.1103/PhysRevLett.73.1279.

[150] H. Okamoto and et al. unpublished. 2007.

[151] Tsutomu Watanabe, Hisatoshi Yokoyama, Yukio Tanaka, and Jun-ichiro Inoue. Superconductivity and a Mott Transition in a Hubbard Model on an Anisotropic Triangular Lattice. *Journal of the Physical Society of Japan*, 75(7):074707, July 2006. doi: 10.1143/JPSJ.75.074707. URL http://journals.jps.jp/doi/abs/10.1143/JPSJ.75.074707.

[152] Hisatoshi Yokoyama, Masao Ogata, and Yukio Tanaka. Mott Transitions and d-Wave Superconductivity in Half-Filled-Band Hubbard Model on Square Lattice with Geometric Frustration. *Journal of the Physical Society of Japan*, 75(11):114706, November 2006. doi: 10.1143/JPSJ.75.114706. URL http://journals.jps.jp/doi/abs/10.1143/JPSJ.75.114706.

[153] Zala Lenarčič and Peter Prelovšek. Ultrafast Charge Recombination in a Photoexcited Mott-Hubbard Insulator. *Physical Review Letters*, 111(1): 016401, July 2013. doi: 10.1103/PhysRevLett.111.016401. URL http://link.aps.org/doi/10.1103/PhysRevLett.111.016401.

[154] H Okamoto, T Miyagoe, K Kobayashi, H Uemura, H Nishioka, H. Matsuzaki, A Sawa, and Y Tokura. Photoinduced transition from Mott insulator to metal in the undoped cuprates Nd_2CuO_4 and La_2CuO_4. *Physical Review B*, 83(12):125102, March 2011. doi: 10.1103/PhysRevB.83.125102. URL `http://link.aps.org/doi/10.1103/PhysRevB.83.125102`.

[155] A Chudnovskiy, D Gangardt, and A Kamenev. Doublon Relaxation in the Bose-Hubbard Model. *Physical Review Letters*, 108(8), February 2012. doi: 10.1103/PhysRevLett.108.085302. URL `http://link.aps.org/doi/10.1103/PhysRevLett.108.085302`.

[156] Philipp Werner, Karsten Held, and Martin Eckstein. Role of impact ionization in the thermalization of photoexcited Mott insulators. *Physical Review B*, 90(23):235102, December 2014. doi: 10.1103/PhysRevB.90.235102. URL `http://link.aps.org/doi/10.1103/PhysRevB.90.235102`.

[157] Felix Hofmann and Michael Potthoff. Doublon dynamics in the extended Fermi-Hubbard model. *Physical Review B*, 85(20), May 2012. doi: 10.1103/PhysRevB.85.205127. URL `http://link.aps.org/doi/10.1103/PhysRevB.85.205127`.

[158] D Golez, J Bonca, L Vidmar, and S A Trugman. Relaxation dynamics of the Holstein polaron. *Physical Review Letters*, 109, December 2012. doi: 10.1103/PhysRevLett.109.236402. URL `http://adsabs.harvard.edu/abs/2012arXiv1209.2586G`.

[159] H W Kroto, J R Heath, S C O'Brien, R F Curl, and R E Smalley. C_{60}: Buckminsterfullerene. *Nature*, 318(6042):162–163, 1985. URL `http://www.nature.com/physics/looking-back/kroto/`.

[160] Olle Gunnarsson. *Alkali-doped fullerides: Narrow-band solids with unusual properties*. World Scientific Publishing Co. Pte. Ltd., 5 Toh Tuck Link, Singapore 596224, 1st edition, 2004.

[161] W I F David, R M Ibberson, J C Matthewman, K Prassides, TJS Dennis, J P Hare, Harold W Kroto, Roger Taylor, and DRM Walton. Crystal structure and bonding of ordered C_60. *Nature*, 353:147–149, 1991. doi: 10.1038/353147a0. URL `http://www.researchgate.net/publication/232753712_Crystal_structure_and_bonding_of_ordered_C60/file/3deec527aa364a2bdd.pdf`.

[162] Peter W Stephens, Laszlo Mihaly, Peter L Lee, Robert L Whetten, Shiou-Mei Huang, Richard Kaner, François Deiderich, and Karoly Holczer. Structure of single-phase superconducting K3C60. *Nature*, 351(6328):632–634, June 1991. doi: 10.1038/351632a0. URL http://www.nature.com/doifinder/10.1038/351632a0.

[163] K M Allen, WIF David, J M Fox, R M Ibberson, and M J Rosseinsky. Molecular Structure of the Fulleride Anions in Superconducting K_3C_{60} and Insulating K_6C_{60} Determined by Powder Neutron Diffraction. *Chemistry of Materials*, 7(4):764–770, 1995. URL http://pubs.acs.org/doi/abs/10.1021/cm00052a023.

[164] I I Mazin, A I Liechtenstein, O. Gunnarsson, O.K. Andersen, V P Antropov, and S E Burkov. Orientational order in A_3C_{60}: Antiferromagnetic Ising model for the fcc lattice. *Physical Review Letters*, 70(26):4142, 1993. URL http://journals.aps.org/prl/abstract/10.1103/PhysRevLett.70.4142.

[165] S Teslic, T Egami, and J E Fischer. Short-Range Antiferromagnetic Orientational Correlations in Rb_3C_{60}. *Physical Review B*, 51(9):5973–5976, 1995. URL http://journals.aps.org/prb/abstract/10.1103/PhysRevB.52.3619.

[166] K-P Bohnen, R Heid, K M Ho, and C Chan. *Ab initio* investigation of the vibrational and geometrical properties of solid C_{60} and K_3C_{60}. *Physical Review B*, 51(9):5805–5813, March 1995. doi: 10.1103/PhysRevB.51.5805. URL http://link.aps.org/doi/10.1103/PhysRevB.51.5805.

[167] Arthur F Hebard. Superconductivity in Doped Fullerenes. *Physics Today*, 45(11):26, 1992. doi: 10.1063/1.881320. URL http://scitation.aip.org/content/aip/magazine/physicstoday/article/45/11/10.1063/1.881320.

[168] O. Gunnarsson. Superconductivity in fullerides. *Rev. Mod. Phys.*, 69:575–606, 1997.

[169] Donald S Bethune, Gerard Meijer, Wade C Tang, Hal J Rosen, William G Golden, Hajime Seki, Charles A Brown, and Mattanjah S de Vries. Vibrational Raman and infrared spectra of chromatographically separated

C_{60} and C_{70} fullerene clusters. *Chemical Physics Letters*, 179(1):181–186, 1991. URL http://www.sciencedirect.com/science/article/pii/000926149190312W.

[170] M G Mitch, S J Chase, and J S Lannin. Variations of Electron-Phonon Coupling in Alkali-Metal-C_{60} Solid-Solutions. *Physical Review B*, 46(6):3696–3699, 1992. URL http://journals.aps.org/prb/abstract/10.1103/PhysRevB.46.7873.

[171] Michael G Mitch, Sabrina J Chase, and Jeffrey S Lannin. Raman scattering and electron-phonon coupling in Rb_xC_{60}. *Physical Review Letters*, 68 (6):883, 1992. URL http://journals.aps.org/prl/abstract/10.1103/PhysRevLett.68.883.

[172] J Winter and H Kuzmany. Landau damping and lifting of vibrational degeneracy in metallic potassium fulleride. *Physical Review B*, 53(2): 655–661, 1996. URL http://journals.aps.org/prb/abstract/10.1103/PhysRevB.53.655.

[173] H Kuzmany, M Matus, B Burger, and J Winter. Raman Scattering in C_{60} fullerenes and fullerides. *Advanced Materials*, 6(10):731–745, 2004. URL http://onlinelibrary.wiley.com/doi/10.1002/adma.19940061004/abstract.

[174] Olle Gunnarsson, Haiko Handschuh, Paul Siegfried Bechthold, Barbara Kessler, Gerd Ganteför, and Wolfgang Eberhardt. Photoemission Spectra of C_{60}^-: Electron-Phonon Coupling, Jahn-Teller Effect, and Superconductivity in the Fullerides. *Physical Review Letters*, 74(10):1875, 1995. URL http://journals.aps.org/prl/abstract/10.1103/PhysRevLett.74.1875.

[175] Kosmas Prassides, John Tomkinsont, Christos Christides, Matthew J Rosseinsky, D W Murphy, and Robert C Haddon. Vibrational spectroscopy of superconducting K_3C_{60} by inelastic neutron scattering. *Nature*, 354:462, 1991. URL http://books.google.com/books?hl=en&lr=&id=h-fMxbYV64YC&oi=fnd&pg=PA169&dq=prassides+(tomkinson+(christides+(haddon+(murphy+nature))))&ots=LzcpneWdPT&sig=jef-ohs-Q-Oet65ridaTybIw77M.

[176] K Prassides, C Christides, M J Rosseinsky, J Tomkinson, D W Murphy, and R C Haddon. Neutron Spectroscopy and Electron-Phonon Coupling in

Alkali-Metal-Doped Fullerides. *EPL (Europhysics Letters)*, 19(7):629–635, 1992. URL http://gateway.webofknowledge.com/gateway/Gateway.cgi?GWVersion=2&SrcAuth=mekentosj&SrcApp=Papers&DestLinkType=FullRecord&DestApp=WOS&KeyUT=A1992JK28400011.

[177] L Pintschovius. Neutron studies of vibrations in fullerenes. *Reports on Progress in Physics*, 59(4):473, 1999. URL http://iopscience.iop.org/0034-4885/59/4/001.

[178] V P Antropov, O. Gunnarsson, and A I Liechtenstein. Phonons, electron-phonon, and electron-plasmon coupling in C_{60} compounds. *Physical Review B*, 48(10):7651, 1993. URL http://journals.aps.org/prb/abstract/10.1103/PhysRevB.48.7651.

[179] B Burk, V H Crespi, A Zettl, and M L Cohen. Rubidium Isotope Effect in Superconducting Rb_3C_{60}. *Phys. Rev. Lett*, 72(23):3706–3709, 1994. URL http://journals.aps.org/prl/abstract/10.1103/PhysRevLett.72.4121.

[180] O. Gunnarsson and G Zwicknagl. Coulomb Pseudopotential, Screening and Superconductivity in C_{60}. *Phys. Rev. Lett*, 69(6):957–960, 1992. URL http://journals.aps.org/prl/abstract/10.1103/PhysRevLett.69.957.

[181] W E Pickett, D A Papaconstantopoulos, M R Pederson, and S C Erwin. Electron-Phonon Coupling in A_3C_{60}-Contributions From Intermolecular Modes. *Journal of Superconductivity*, 7(3):651–655, June 1994. URL http://link.springer.com/article/10.1007/BF00728479.

[182] C Christides, D A Neumann, K Prassides, JRD Copley, J J Rush, M J Rosseinsky, D W Murphy, and R C Haddon. Neutron-scattering study of C_{60}^{n-}(n=3,6) librations in alkali-metal fullerides. *Physical Review B*, 46(18):12088, 1992. URL http://journals.aps.org/prb/abstract/10.1103/PhysRevB.46.12088.

[183] R Zeyher and G Zwicknagl. Superconductivity-Induced Phonon Self-Energy Effects in High-Tc Superconductors. *Zeitschrift Fur Physik B-Condensed Matter*, 78(2):175–190, 1990. URL http://gateway.webofknowledge.com/gateway/Gateway.cgi?GWVersion=2&SrcAuth=mekentosj&SrcApp=Papers&DestLinkType=FullRecord&DestApp=WOS&KeyUT=A1990CK77800003.

[184] II Mazin, SN Rashkeev, VP Antropov, O Jepsen, AI Liechtenstein, and OK Andersen. Quantitative theory of superconductivity in doped C_{60}. *Physical Review B*, 45(9):5114, 1992. URL `http://prb.aps.org/abstract/PRB/v45/i9/p5114_1`.

[185] L Degiorgi, E J Nicol, O Klein, G. Grüner, P Wachter, S M Huang, J Wiley, and R B Kaner. Optical properties of the alkali-metal-doped superconducting fullerenes: K_3C_{60} and Rb_3C_{60}. *Physical Review B*, 49(10):7012, 1994. URL `http://prb.aps.org/abstract/PRB/v49/i10/p7012_1`.

[186] L Degiorgi, G Briceno, M S Fuhrer, A Zettl, and P Wachter. Optical measurements of the superconducting gap in single-crystal K_3C_{60} and Rb_3C_{60}. *Nature*, 369(6481):541–542, 1994. URL `http://www.physics.berkeley.edu/research/zettl/pdf/161.Nature369-Degiorgi.pdf`.

[187] L Degiorgi. The Complete Excitation Spectrum of the Alkali-Metal-Doped Superconducting Fullerenes. *Modern Physics Letters B*, 9(08):445–468, 1995. URL `http://www.worldscientific.com/doi/abs/10.1142/S0217984995000413`.

[188] D Koller, M C Martin, L Mihály, G Mihaly, G Oszlanyi, G Baumgartner, and L Forro. Energy gap in superconducting fullerides: optical and tunneling studies. *Phys. Rev. Lett*, 77:4082–4085, 1996.

[189] M Capone. Strongly Correlated Superconductivity. *Science*, 296(5577): 2364–2366, June 2002. doi: 10.1126/science.1071122. URL `http://www.sciencemag.org/cgi/doi/10.1126/science.1071122`.

[190] J Han, O. Gunnarsson, and V Crespi. Strong Superconductivity with Local Jahn-Teller Phonons in C_{60} Solids. *Physical Review Letters*, 90(16):167006, April 2003. doi: 10.1103/PhysRevLett.90.167006. URL `http://link.aps.org/doi/10.1103/PhysRevLett.90.167006`.

[191] M Capone, M Fabrizio, C Castellani, and E Tosatti. Colloquium: Modeling the unconventional superconducting properties of expanded A_3C_{60} fullerides. *Reviews of Modern Physics*, 81(2):943–958, 2009.

[192] M Schlüter, M Lannoo, M Needels, G A Baraff, and D Tomanek. Superconductivity in alkali intercalated C_{60}. *Journal of Physics and Chemistry of Solids*, 53(11):1473–1485, 1992. URL `http://www.sciencedirect.com/science/article/pii/002236979290240E`.

[193] M Schlüter, M Lannoo, M Needels, G A Baraff, and D Tomanek. Electron-phonon coupling and superconductivity in alkali-intercalated C_{60} solid. *Physical Review Letters*, 68(4):526–529, 1992. URL http://link.aps.org/doi/10.1103/PhysRevLett.68.526.

[194] Steven C Erwin and Warren E Pickett. Theoretical Fermi-surface properties and superconducting parameters for K_3C_{60}. *Science*, 254(5033):842–845, 1991. URL http://www.sciencemag.org/content/254/5033/842.short.

[195] S Satpathy, V P Antropov, O.K. Andersen, O Jepsen, O. Gunnarsson, and A I Liechtenstein. Conduction-band structure of alkali-metal-doped C_{60}. *Physical Review B*, 46(3):1773, 1992. URL http://journals.aps.org/prb/abstract/10.1103/PhysRevB.46.1773.

[196] A P Ramirez, M J Rosseinsky, D W Murphy, and R C Haddon. Specific-heat jump at T c and normal-state magnetic susceptibility of A_3C_{60}. *Physical Review Letters*, 69(11):1687, 1992. URL http://journals.aps.org/prl/abstract/10.1103/PhysRevLett.69.1687.

[197] Katsumi Tanigaki, Mayumi Kosaka, Takahashi Manako, Yoshimi Kubo, Ichiro Hirosawa, Kenshiro Uchida, and Kosmas Prassides. Alkali effects on the electronic states of K_3C_{60} and Rb_3C_{60}. *Chemical Physics Letters*, 240(5):627–632, 1995. URL http://www.sciencedirect.com/science/article/pii/000926149500556J.

[198] V P Antropov, I I Mazin, O.K. Andersen, A I Liechtenstein, and O Jepsen. Dominance of the spin-dipolar NMR relaxation mechanism in fullerene superconductors. *Physical Review B*, 47(18):12373, 1993. URL http://journals.aps.org/prb/abstract/10.1103/PhysRevB.47.12373.

[199] G J Burkhart and C Meingast. High-resolution thermal expansion of superconducting fullerides A_3C_{60} (A=K, Rb). *Physical Review B*, 54(10):R6865, 1996. URL http://journals.aps.org/prb/abstract/10.1103/PhysRevB.54.R6865.

[200] Deming Wang. The spin susceptibility of Rb_3C_{60} probed by Electron Paramagnetic Resonance. *Solid State Communications*, 94(9):767–770, 1995. URL http://www.sciencedirect.com/science/article/pii/0038109895000658.

[201] W H Wong, M E Hanson, W G Clark, G. Grüner, J D Thompson, R L Whetten, S M Huang, R B Kaner, F Diederich, and P Petit. Normal-state magnetic properties of K_3C_{60}. *EPL (Europhysics Letters)*, 18(1):79, 1992. URL http://iopscience.iop.org/0295-5075/18/1/015.

[202] C T Chen, L H Tjeng, P Rudolf, G Meigs, J E Rowe, J Chen, J P McCauley, Jr, A B Smith, III, A R McGhie, W J Romanow, and E W Plummer. Electronic states and phases of K_xC_{60} from photoemission and X-ray absorption spectroscopy. *Nature*, 352:603, 1991. URL http://zernike.eldoc.ub.rug.nl/FILES/root/1991/NatureChen/1991NatureChen.pdf.

[203] W L Yang, V Brouet, X J Zhou, H J Choi, S G Louie, M L Cohen, S A Kellar, P V Bogdanov, A Lanzara, A Goldoni, F Parmigiani, Z Hussain, and Z X Shen. Band Structure and Fermi Surface of Electron-Doped C_{60} Monolayers. *Science*, 300(5617):303–307, April 2003. doi: 10.1126/science.1082174. URL http://www.sciencemag.org/cgi/doi/10.1126/science.1082174.

[204] R L Hettich, R N Compton, and R H Ritchie. Doubly Charged Negative-Ions of Carbon-60. *Phys. Rev. Lett*, 67(10):1242–1245, 1991. URL http://journals.aps.org/prl/abstract/10.1103/PhysRevLett.67.1242.

[205] G Gensterblum, J J Pireaux, P A Thiry, R Caudano, J P Vigneron, P Lambin, A A Lucas, and W Kratschmer. High-Resolution Electron-Energy-Loss Spectroscopy of Thin-Films of C_{60} on Si(100). *Phys. Rev. Lett*, 67(16):2171–2174, 1991. URL http://gateway.webofknowledge.com/gateway/Gateway.cgi?GWVersion=2&SrcAuth=mekentosj&SrcApp=Papers&DestLinkType=FullRecord&DestApp=WOS&KeyUT=A1991GJ64000015.

[206] J De Vries, H Steger, B Kamke, C Menzel, B Weisser, W Kamke, and I V Hertel. Single-photon ionization of C_{60} and C_{70} fullerene with synchrotron radiation: determination of the ionization potential of C_{60}. *Chemical Physics Letters*, 188(3):159–162, 1992. URL http://www.sciencedirect.com/science/article/pii/0009261492900014.

[207] M R Pederson and A A Quong. Polarizabilities, Charge States, and Vibrational-Modes of Isolated Fullerene Molecules. *Physical Review B*, 46 (20):13584–13591, 1992. URL http://journals.aps.org/prb/abstract/10.1103/PhysRevB.46.14257.

[208] V De Coulon, J L Martins, and F Reuse. Electronic structure of neutral and charged C_{60} clusters. *Physical Review B*, 45(23):13671, 1992. URL http://journals.aps.org/prb/abstract/10.1103/PhysRevB.45.13671.

[209] V P Antropov, O. Gunnarsson, and O Jepsen. Coulomb integrals and model Hamiltonians for C_{60}. *Physical Review B*, 46(20):13647, 1992. URL http://journals.aps.org/prb/abstract/10.1103/PhysRevB.46.13647.

[210] Richard L Martin and James P Ritchie. Coulomb and exchange interactions in C_{60}^{n-}. *Physical Review B*, 48(7):4845, 1993. URL http://journals.aps.org/prb/abstract/10.1103/PhysRevB.48.4845.

[211] R W Lof, M A van Veenendaal, B Koopmans, H T Jonkman, and G A Sawatzky. Band Gap, Excitons, and Coulomb Interaction in Solid C_{60}. *Physical Review Letters*, 1992. URL http://zernike.eldoc.ub.rug.nl/FILES/root/1992/PhysRevLettLof/1992PhysRevLettLof.pdf.

[212] P A Brühwiler, A J Maxwell, A Nilsson, N Märtensson, and O. Gunnarsson. Auger and photoelectron study of the Hubbard U in C_{60}, K_3C_{60}, and K_6C_{60}. *Physical Review B*, 48(24):18296, 1993. URL http://journals.aps.org/prb/abstract/10.1103/PhysRevB.48.18296.

[213] Yusuke Nomura, Kazuma Nakamura, and Ryotaro Arita. *Ab initio* derivation of electronic low-energy models for C_{60} and aromatic compounds. *Physical Review B*, 85(15):155452, April 2012. doi: 10.1103/PhysRevB.85.155452. URL http://link.aps.org/doi/10.1103/PhysRevB.85.155452.

[214] A F Hebard, M J Rosseinsky, R C Haddon, D W Murphy, S H Glarum, TTM Palstra, A P Ramirez, and A R Kortan. Superconductivity at 18K in Potassium Doped C_{60}. *Nature*, 350(6319):600–601, 1991. URL http://scholar.google.com/scholar?q=related:S1tYL278IwsJ:scholar.google.com/&hl=en&num=20&as_sdt=0,5.

[215] M J Rosseinsky, A P Ramirez, S H Glarum, D W Murphy, R C Haddon, A F Hebard, TTM Palstra, A R Kortan, S M Zahurak, and A V Makhija. Superconductivity at 28 K in Rb x C 60. *Physical Review Letters*, 66(21):2830, 1991. URL http://journals.aps.org/prl/abstract/10.1103/PhysRevLett.66.2830.

[216] TTM Palstra, O Zhou, Y. Iwasa, P E Sulewski, R M Fleming, and B R Zegarski. Superconductivity at 40 K in cesium doped C_{60}. *Solid State Communications*, 93(4):327–330, 1995. URL http://www.sciencedirect.com/science/article/pii/003810989400787X.

[217] X-D Xiang, J G Hou, G Briceno, W A Vareka, R Mostovoy, A Zettl, V H Crespi, and M L Cohen. Synthesis and Electronic Transport of Single Crystal K_3C_{60}. *Science*, 256(5060):1190–1191, 1992. URL http://scholar.google.com/scholar?q=related:54Hzbvo5Ut8J:scholar.google.com/&hl=en&num=20&as_sdt=0,5.

[218] J G Hou, L Lu, V H Crespi, X-D Xiang, A Zettl, and M L Cohen. Resistivity Saturation in Alkali-Doped C_{60}. *Solid State Communications*, 93(12):973–977, March 1995. URL http://gateway.webofknowledge.com/gateway/Gateway.cgi?GWVersion=2&SrcAuth=mekentosj&SrcApp=Papers&DestLinkType=FullRecord&DestApp=WOS&KeyUT=A1995QK96000003.

[219] W Meissner and R Ochsenfeld. Short initial announcements. *Naturwissenschaften*, 21:787–788, 1933. ISSN 0028-1042.

[220] Michael Tinkham. *Introduction to superconductivity*. Dover Publications Inc., 31 East 2nd Street, Mineola, N.Y. 11501, 2nd edition, 1996.

[221] Z Zhang, C C Chen, and C M Lieber. Tunneling Spectroscopy of M_3C_{60} Superconductors: the Energy-Gap, Strong Coupling, and Superconductivity. *Science*, 254(5038):1619–1621, 1991. URL http://gateway.webofknowledge.com/gateway/Gateway.cgi?GWVersion=2&SrcAuth=mekentosj&SrcApp=Papers&DestLinkType=FullRecord&DestApp=WOS&KeyUT=A1991GV07300037.

[222] R M Fleming, A P Ramirez, M J Rosseinsky, D W Murphy, R C Haddon, S M Zahurak, and A V Makhija. Relation of structure and superconducting transition temperatures in A_3C_{60}. *Nature*, 352:787–788, 1991. URL http://books.google.com/books?hl=en&lr=&id=h-fMxbYV64YC&oi=fnd&pg=PA140&dq=fleming+(ramirez+(rosseinsky+(murphy+(haddon+zahurak))))&ots=LA5qokWeQS&sig=07lHSZtB9D0cSrxOt3-9_MPP48Y.

[223] Otto Zhou, Gavin BM Vaughan, Qing Zhu, John E Fischer, Paul A Heiney, Nicole Coustel, John P McCauley, Jr, and A B Smith III.

Compressibility of M_3C_{60} fullerene superconductors: relation between Tc and lattice parameter. *Science*, 255:833, February 1992. URL http://books.google.com/books?hl=en&lr=&id=h-fMxbYV64YC&oi=fnd&pg=PA159&dq=zhou+(vaughan+(zhu+(fischer+(heiney+coustel)))&ots=LA5qqiZgVS&sig=twYaeY6qU5kpZvnOCLVE8s2IlcE.

[224] C C Chen and C M Lieber. Synthesis of Pure $^{13}C_{60}$ and Determination of the Isotope Effect for Fullerene Superconductors. *Journal of the American Chemical Society*, 114(8):3141–3142, 1992. URL http://pubs.acs.org/doi/abs/10.1021/ja00034a072.

[225] CC Chen and CM Lieber. Isotope effect and superconductivity in metal-doped C_{60}. *Science*, 259(5095):655–658, Jan 29 1993. ISSN 0036-8075.

[226] T W Ebbesen, J S Tsai, K. Tanigaki, H Hiura, Y. Shimakawa, Y. Kubo, I Hirosawa, and J Mizuki. Dopant Isotope Effect on Superconductivity in Rb_3C_{60}. *Physica C: Superconductivity*, 203(1-2):163–166, 1992.

[227] B Burk, V H Crespi, M S Fuhrer, A Zettl, and M L Cohen. Alkali-Metal Isotope Effect in Rb_3C_{60}. *Physica C: Superconductivity*, 235:2493–2494, December 1994. URL http://gateway.webofknowledge.com/gateway/Gateway.cgi?GWVersion=2&SrcAuth=mekentosj&SrcApp=Papers&DestLinkType=FullRecord&DestApp=WOS&KeyUT=A1994QC69600172.

[228] B Burk, V H Crespi, A Zettl, and M L Cohen. Rubidium Isotope Effect in Superconducting Rb_3C_{60}. *Phys. Rev. Lett*, 72(23):3706–3709, 1994. URL http://journals.aps.org/prl/abstract/10.1103/PhysRevLett.72.4121.

[229] B Mitrovic, H G Zarate, and J P Carbotte. The Ratio $2\Delta_0/k_BT_C$ Within Eliashberg Theory. *Physical Review B*, 29(1):184–190, 1984. URL http://journals.aps.org/prb/abstract/10.1103/PhysRevB.29.6187.

[230] L Degiorgi, P Wachter, G. Grüner, S M Huang, J Wiley, and R B Kaner. Optical response of the superconducting state of K_3C_{60} and Rb_3C_{60}. *Physical Review Letters*, 69(20):2987–2990, 1992. URL http://link.aps.org/doi/10.1103/PhysRevLett.69.2987.

[231] Y. Iwasa, K Tanaka, T Yasuda, T Koda, and S Koda. Metallic reflection spectra of K_3C_60. *Physical Review Letters*, 69(15):2284, 1992. URL http://prl.aps.org/abstract/PRL/v69/i15/p2284_1.

[232] Y. Iwasa and T Kaneyasu. Optical study of electronic structures and phonons in alkali-metal-doped C_{60}. *Physical Review B*, 51(6):3678, 1995. URL http://prb.aps.org/abstract/PRB/v51/i6/p3678_1.

[233] D C Mattis and John Bardeen. Theory of the anomalous skin effect in normal and superconducting metals. *Physical Review*, 111(2):412, 1958. URL http://journals.aps.org/pr/abstract/10.1103/PhysRev.111.412.

[234] Martin Dressel and George Grüner. *Electrodynamics of Solids: Optical Properties of Electrons in Matter*. Cambridge University Press, The Edinburgh Building, Cambridge CB2 2RU, United Kingdom, 1st edition, 2002.

[235] G M Eliashberg. Interactions between electrons and lattice vibrations in a superconductor. *Sov. Phys.-JETP (Engl. Transl.);(United States)*, 11(3), 1960. URL http://www.osti.gov/energycitations/product.biblio.jsp?osti_id=7354388.

[236] J Bardeen, LN Cooper, and JR Schrieffer. Theory of superconductivity. *Physical Review*, 108(5):1175–1204, 1957.

[237] C M Varma, J Zaanen, and K Raghavachari. Superconductivity in the fullerenes. *Science*, 254(5034):989–992, 1991. URL http://www.sciencemag.org/content/254/5034/989.short.

[238] Sudip Chakravarty, Martin P Gelfand, and Steven Kivelson. Electronic correlation effects and superconductivity in doped fullerenes. *Science*, 254 (5034):970–974, 1991. URL http://www.sciencemag.org/content/254/5034/970.short.

[239] O. Gunnarsson and G Zwicknagl. Coulomb Pseudopotential, Screening and Superconductivity in C_{60}. *Phys. Rev. Lett*, 69(6):957–960, 1992. URL http://journals.aps.org/prl/abstract/10.1103/PhysRevLett.69.957.

[240] J E Han, E Koch, and O. Gunnarsson. Metal-insulator transitions: influence of lattice structure, Jahn-Teller effect, and Hund's Rule coupling. *Physical Review Letters*, 84(6):1276, 2000. URL http://journals.aps.org/prl/abstract/10.1103/PhysRevLett.84.1276.

[241] Martin Lüders, Andrea Bordoni, Nicola Manini, Andrea Dal Corso, Michele Fabrizio, and Erio Tosatti. Coulomb couplings in positively charged fullerene. *Philosophical Magazine Part B*, 82(15):1611–1647, 2002. doi:

10.1080/136428102100002026. URL http://www.tandfonline.com/doi/abs/10.1080/13642810208220729.

[242] M Lannoo, G A Baraff, M Schlüter, and D Tomanek. Jahn-Teller effect for the negatively charged C_{60} molecule: Analogy with the silicon vacancy. *Physical Review B*, 44(21):12106, 1991. URL http://journals.aps.org/prb/abstract/10.1103/PhysRevB.44.12106.

[243] Assa Auerbach, Nicola Manini, and Erio Tosatti. Electron-vibron interactions in charged fullerenes. I. Berry phases. *Physical Review B*, 49(18):12998, 1994. URL http://journals.aps.org/prb/abstract/10.1103/PhysRevB.49.12998.

[244] S B Fleischer, B Pevzner, D J Dougherty, H J Zeiger, G. Dresselhaus, M S Dresselhaus, E P Ippen, and A F Hebard. Coherent phonons in alkali metal-doped C_{60}. *Applied Physics Letters*, 71(19):2734, 1997. doi: 10.1063/1.120121. URL http://link.aip.org/link/APPLAB/v71/i19/p2734/s1&Agg=doi.

[245] S B Fleischer, B Pevzner, D J Dougherty, H J Zeiger, G. Dresselhaus, M S Dresselhaus, E P Ippen, and A F Hebard. Ultrafast dynamics of superconducting K_3C_{60} and Rb_3C_{60}. *Physical Review B*, 62(2):1366, 2000. URL http://journals.aps.org/prb/abstract/10.1103/PhysRevB.62.1366.

[246] SB Fleischer, EP Ippen, G Dresselhaus, MS Dresselhaus, AM Rao, P Zhou, and PC Eklund. Femtosecond optical dynamics of C_{60} and M_3C_{60}. *Applied Physics Letters*, 62(25):3241–3243, JUN 21 1993. ISSN 0003-6951. doi: {10.1063/1.109086}.

[247] M Mitrano, G Cotugno, S R Clark, R Singla, S Kaiser, J Stähler, R Beyer, M Dressel, L Baldassarre, D Nicoletti, A Perucchi, T Hasegawa, H Okamoto, D Jaksch, and A Cavalleri. Pressure-Dependent Relaxation in the Photoexcited Mott Insulator ET–F2TCNQ: Influence of Hopping and Correlations on Quasiparticle Recombination Rates. *Physical Review Letters*, 112(11):117801, March 2014. doi: 10.1103/PhysRevLett.112.117801. URL http://link.aps.org/doi/10.1103/PhysRevLett.112.117801.

[248] S. I. Anisimov, B. L. Kapeliovich, and T. L. Perelman. Electron emission from metal surfaces under the action of ultrashort laser pulses. *Zhurnal Eksperimental'noi i Teoreticheskoi Fiziki*, 66:776–781,

1974. URL http://www.csa.com/partners/viewrecord.php?requester=gs&collection=TRD&recid=A7430138AH.

[249] P.B. Allen. Theory of thermal relaxation of electrons in metals. *Phys. Rev. Lett*, 59(13):1460–1463, 1987. URL http://link.aps.org/doi/10.1103/PhysRevLett.59.1460.

[250] M Born and R Oppenheimer. Quantum theory of molecules. *ANNALEN DER PHYSIK*, 84(20):0457–0484, 1927. ISSN 0003-3804.

[251] SD Brorson, A. Kazeroonian, JS Moodera, DW Face, TK Cheng, EP Ippen, MS Dresselhaus, and G. Dresselhaus. Femtosecond room-temperature measurement of the electron-phonon coupling constant γ in metallic superconductors. *Physical Review Letters*, 64(18):2172–2175, 1990. URL http://link.aps.org/doi/10.1103/PhysRevLett.64.2172.

[252] L Perfetti, P A Loukakos, M Lisowski, U Bovensiepen, H Eisaki, and M Wolf. Ultrafast Electron Relaxation in Superconducting $Bi_2Sr_2CaCu_2O_{8+\delta}$ by Time-Resolved Photoelectron Spectroscopy. *Physical Review Letters*, 99 (19), November 2007. doi: 10.1103/PhysRevLett.99.197001. URL http://link.aps.org/doi/10.1103/PhysRevLett.99.197001.

[253] C Gadermaier, A Alexandrov, V Kabanov, P Kusar, T Mertelj, X Yao, C. Manzoni, D Brida, G Cerullo, and D Mihailovic. Electron-Phonon Coupling in High-Temperature Cuprate Superconductors Determined from Electron Relaxation Rates. *Physical Review Letters*, 105(25), December 2010. doi: 10.1103/PhysRevLett.105.257001. URL http://link.aps.org/doi/10.1103/PhysRevLett.105.257001.

[254] László Mihály and Michael C Martin. *Solid state physics: problems and solutions; 2nd ed.* Wiley, New York, NY, 2009.

[255] O Svelto. *Principles of Lasers; 4th ed.* Plenum Press, 233 Spring Street, new York, N. Y. 10013, 1998.

[256] P Yu and M Cardona. *Fundamentals of Semiconductors, Physics and Materials Properties, 4th ed.* Springer Verlag, Berlin Heidelberg, 2010.

[257] F. Wooten. *Optical properties of solids.* Academic Press Inc., 111 Fifth Avenue, New York, New York 10003, 1st edition, 1972.

[258] M Rahal, D Chasseau, J Gaultier, L Ducasse, M Kurmoo, and P Day. Isothermal Compressibility and Pressure Dependence of the Crystal Structures of the Superconducting Charge-Transfer Salt (BEDT-TTF)$_2$Cu(NCS)$_2$ [BEDT-TTF= Bis (ethylenedithio) tetrathiafulvalene]. *Acta Crystallographica Section B: Structural Science*, 53(1):159–167, 1997.

[259] E P Wohlfarth. The Energy Band Structure of a Linear Metal. *Proceedings of the Physical Society. Section A*, 66(10):889, 2002. URL `http://iopscience.iop.org/0370-1298/66/10/306`.

[260] Wojciech Grochala, Roald Hoffmann, Ji Feng, and Neil W Ashcroft. The chemical imagination at work in very tight places. *Angewandte Chemie International Edition*, 46(20):3620–3642, May 2007. doi: 10.1002/anie.200602485. URL `http://doi.wiley.com/10.1002/anie.200602485`.

[261] John (Editor) Loveday. *High pressure physics*. CRC press, Taylor & Francis Group, 6000 Broken Sound Parkway NW, Suite 300
Boca Raton, FL 33487-2742, 1st edition, 2012.

[262] Reinhold Egger, C H Mak, and Ulrich Weiss. Quantum rates for nonadiabatic electron transfer. *The Journal of Chemical Physics*, 100(4):2651, 1994. doi: 10.1063/1.466460. URL `http://scitation.aip.org/content/aip/journal/jcp/100/4/10.1063/1.466460`.

[263] S Tornow, R Bulla, F B Anders, and A Nitzan. Dissipative two-electron transfer: A numerical renormalization group study. *Physical Review B*, 78 (3):035434, 2008. doi: 10.1103/PhysRevB.78.035434. URL `http://prb.aps.org/abstract/PRB/v78/i3/e035434`.

[264] A. J. Leggett, S. Chakravarty, A. T. Dorsey, Matthew P. A. Fisher, Anupam Garg, and W. Zwerger. Dynamics of the dissipative two-state system. *Rev. Mod. Phys.*, 59:1–85, Jan 1987. doi: 10.1103/RevModPhys.59.1. URL `http://link.aps.org/doi/10.1103/RevModPhys.59.1`.

[265] Dara P. S. McCutcheon and Ahsan Nazir. Coherent and incoherent dynamics in excitonic energy transfer: Correlated fluctuations and off-resonance effects. *Phys. Rev. B*, 83:165101, Apr 2011. doi: 10.1103/PhysRevB.83.165101. URL `http://link.aps.org/doi/10.1103/PhysRevB.83.165101`.

[266] Bernd T Matthias, Theodore H Geballe, and V B Compton. Superconductivity. *Reviews of Modern Physics*, 35(1):1, 1963. URL `http://rmp.aps.org/abstract/RMP/v35/i1/p1_1`.

[267] J George Bednorz and K Alex Müller. Possible highT_c superconductivity in the Ba−La−Cu−O system. *Zeitschrift Für Physik B-Condensed Matter*, 64 (2):189–193, 1986. URL `http://link.springer.com/article/10.1007/BF01303701`.

[268] Maw-Kuen Wu, Jo R Ashburn, C J Torng, Ph H Hor, Rl L Meng, Lo Gao, Z J Huang, Y Q Wang, and C W Chu. Superconductivity at 93 K in a new mixed-phase Y-Ba-Cu-O compound system at ambient pressure. *Physical Review Letters*, 58(9):908, 1987.

[269] A Schilling, M Cantoni, J D Guo, and H R Ott. Superconductivity above 130 K in the Hg-Ba-Ca-Cu-O system. *Nature*, 363(6424):56–58, 1993. URL `http://www.nature.com/physics/looking-back/schilling/`.

[270] Yoichi Kamihara, Takumi Watanabe, Masahiro Hirano, and Hideo Hosono. Iron-Based Layered Superconductor $LaO_{1-x}F_xFeAs$ ($x = 0.05 - 0.12$) with $T_c = 26$ K. *Journal of the American Chemical Society*, 130(11):3296–3297, March 2008. doi: 10.1021/ja800073m. URL `http://pubs.acs.org/doi/abs/10.1021/ja800073m`.

[271] Hiroki Takahashi, Kazumi Igawa, Kazunobu Arii, Yoichi Kamihara, Masahiro Hirano, and Hideo Hosono. Superconductivity at 43 K in an iron-based layered compound $LaO_{1-x}F_xFeAs$. *Nature*, 453(7193):376–378, April 2008. doi: 10.1038/nature06972. URL `http://www.nature.com/doifinder/10.1038/nature06972`.

[272] J S Schilling. What High Pressure Studies Have Taught Us about High-Tc Superconductivity. *APS Meeting Abstracts*, 2001. URL `http://adsabs.harvard.edu/abs/2001APS..MARS28001S`.

[273] C W Chu, Li Gao, F Chen, Z J Huang, R L Meng, and Y Y Xue. Superconductivity above 150 K in $HgBa_2Ca_2Cu_3O_{8+\delta}$ at high pressures. *Nature*, 365: 323, 1993. URL `http://www.nature.com/nature/journal/v365/n6444/abs/365323a0.html`.

[274] L. Gao, Y. Y. Xue, F. Chen, Q. Xiong, R. L. Meng, D. Ramirez, C. W. Chu, J. H. Eggert, and H. K. Mao. Superconductivity up to 164 k in

hgba$_2$ca$_{m-1}$cu$_m$o$_{2m+2+\delta}$ (m=1, 2, and 3) under quasihydrostatic pressures. *Phys. Rev. B*, 50:4260–4263, Aug 1994. doi: 10.1103/PhysRevB.50.4260. URL http://link.aps.org/doi/10.1103/PhysRevB.50.4260.

[275] Liling Sun, Xiao-Jia Chen, Jing Guo, Peiwen Gao, Qing-Zhen Huang, Hangdong Wang, Minghu Fang, Xiaolong Chen, Genfu Chen, Qi Wu, Chao Zhang, Dachun Gu, Xiaoli Dong, Lin Wang, Ke Yang, Aiguo Li, Xi Dai, Ho-kwang Mao, and Zhongxian Zhao. Re-emerging superconductivity at 48 K in iron chalcogenides. *Nature*, February 2012. doi: 10.1038/nature10813. URL http://www.nature.com/doifinder/10.1038/nature10813.

[276] Nao Takeshita, Ayako Yamamoto, Akira Iyo, and Hiroshi Eisaki. Zero Resistivity above 150 K in $HgBa_2Ca_2Cu_3O_{8+\delta}$ at High Pressure. *Journal of the Physical Society of Japan*, 82(2):023711, January 2013. doi: 10.7566/JPSJ.82.023711. URL http://jpsj.ipap.jp/link?JPSJ/82/023711/.

[277] S Dal Conte, C Giannetti, G Coslovich, F Cilento, D Bossini, T Abebaw, F Banfi, G Ferrini, H Eisaki, M Greven, A Damascelli, D Van Der Marel, and F Parmigiani. Disentangling the Electronic and Phononic Glue in a High-T_C Superconductor. *Science*, 335(6076):1600–1603, March 2012. doi: 10.1126/science.1216765. URL http://www.sciencemag.org/cgi/doi/10.1126/science.1216765.

[278] D Nicoletti, E Casandruc, Y Laplace, V Khanna, C R Hunt, S Kaiser, S S Dhesi, G D Gu, J P Hill, and A Cavalleri. Optically induced superconductivity in striped $La_{2-x}Ba_xCuO_4$ by polarization-selective excitation in the near infrared. *Physical Review B*, 90(10):100503, September 2014. doi: 10.1103/PhysRevB.90.100503. URL http://link.aps.org/doi/10.1103/PhysRevB.90.100503.

[279] M Först, A Frano, S Kaiser, R Mankowsky, C R Hunt, J J Turner, G L Dakovski, M P Minitti, J Robinson, T Loew, M Le Tacon, B Keimer, J P Hill, A Cavalleri, and S S Dhesi. Femtosecond x rays link melting of charge-density wave correlations and light-enhanced coherent transport in $YBa_2Cu_3O_{6.6}$. *Physical Review B*, 90(18):184514, November 2014. doi: 10.1103/PhysRevB.90.184514. URL http://link.aps.org/doi/10.1103/PhysRevB.90.184514.

[280] M Först, R Mankowsky, H Bromberger, D M Fritz, H Lemke, D Zhu, M Chollet, Y. Tomioka, Y Tokura, R Merlin, J P Hill, S L Johnson,

and A Cavalleri. Displacive lattice excitation through nonlinear phononics viewed by femtosecond X-ray diffraction. *Solid State Communications*, 169(C):24–27, September 2013. doi: 10.1016/j.ssc.2013.06.024. URL http://dx.doi.org/10.1016/j.ssc.2013.06.024.

[281] C S Owen and D J Scalapino. Superconducting state under the influence of external dynamic pair breaking. *Physical Review Letters*, 28(24): 1559, 1972. URL http://journals.aps.org/prl/abstract/10.1103/PhysRevLett.28.1559.

[282] G L Carr, R Lobo, J LaVeigne, D H Reitze, and D B Tanner. Exploring the dynamics of superconductors by time-resolved far-infrared spectroscopy. *Physical Review Letters*, 85(14):3001–3004, 2000.

[283] R Lobo, J LaVeigne, D Reitze, D Tanner, Z Barber, E Jacques, P Bosland, M Burns, and G Carr. Photoinduced time-resolved electrodynamics of superconducting metals and alloys. *Physical Review B*, 72(2):024510, July 2005. doi: 10.1103/PhysRevB.72.024510. URL http://link.aps.org/doi/10.1103/PhysRevB.72.024510.

[284] M Beck, I Rousseau, M Klammer, P Leiderer, M Mittendorff, S Winnerl, M Helm, G N Gol'tsman, and J Demsar. Transient Increase of the Energy Gap of Superconducting NbN Thin Films Excited by Resonant Narrow-Band Terahertz Pulses. *Physical Review Letters*, 110(26):267003, June 2013. doi: 10.1103/PhysRevLett.110.267003. URL http://link.aps.org/doi/10.1103/PhysRevLett.110.267003.

[285] Zoltán Mics, Andrea D'Angio, Søren A Jensen, Mischa Bonn, and Dmitry Turchinovich. Density-dependent electron scattering in photoexcited GaAs in strongly diffusive regime. *Applied Physics Letters*, 102(23):231120, 2013. doi: 10.1063/1.4810756. URL http://scitation.aip.org/content/aip/journal/apl/102/23/10.1063/1.4810756.

[286] TTM Palstra, R C Haddon, A F Hebard, and J Zaanen. Electronic Transport Properties of K_3C_{60} Films. *Physical Review Letters*, 1992. URL http://zernike.eldoc.ub.rug.nl/FILES/root/1992/PhysRevLettPalstra/1992PhysRevLettPalstra.pdf.

[287] Bennett H E and J O Porteus. Relation Between Surface Roughness and Specular Reflectance at Normal Incidence. *Journal of the Optical Society*

of America, 51(2):123–&, 1961. URL http://www.opticsinfobase.org/abstract.cfm?uri=josa-51-2-123.

[288] W Zimmermann, E H Brandt, M Bauer, E Seider, and L Genzel. Optical conductivity of BCS superconductors with arbitrary purity. *Physica C: Superconductivity*, 183(1):99–104, 1991. URL http://www.sciencedirect.com/science/article/pii/092145349190771P.

[289] F Gross, B S Chandrasekhar, D Einzel, K Andres, P J Hirschfeld, H R Ott, J Beuers, Z Fisk, and J L Smith. Anomalous temperature dependence of the magnetic field penetration depth in superconducting UBe_{13}. *Zeitschrift Für Physik B-Condensed Matter*, 64(2):175–188, 1986. URL http://link.springer.com/article/10.1007/BF01303700.

[290] J Demsar, R D Averitt, A J Taylor, V V Kabanov, W N Kang, H J Kim, E M Choi, and S I Lee. Pair-Breaking and Superconducting State Recovery Dynamics in MgB_2. *Physical Review Letters*, 91(26):267002, December 2003. doi: 10.1103/PhysRevLett.91.267002. URL http://link.aps.org/doi/10.1103/PhysRevLett.91.267002.

[291] A Rothwarf and B N Taylor. Measurement of recombination lifetimes in superconductors. *Physical Review Letters*, 19(1):27–30, 1967. URL http://link.aps.org/doi/10.1103/PhysRevLett.19.27.

[292] V V Kabanov, J Demsar, and D Mihailovic. Kinetics of a Superconductor Excited with a Femtosecond Optical Pulse. *Physical Review Letters*, 95 (14):147002, September 2005. doi: 10.1103/PhysRevLett.95.147002. URL http://link.aps.org/doi/10.1103/PhysRevLett.95.147002.

[293] G M Eliashberg. Film Superconductivity Stimulated by a High-Frequency Field. *JETP Letters-USSR*, 11(3):114, 1970.

[294] B I Ivlev and G M Eliashberg. Influence of Nonequilibrium Excitations on Properties of Superconducting Films in a High-Frequency Field. *JETP Letters-USSR*, 13(8):333, 1971.

[295] P.W. Anderson and A H Dayem. Radio-Frequency Effects in Superconducting Thin Film Bridges. *Phys. Rev. Lett*, 13(6):195–&, 1964. URL http://journals.aps.org/prl/abstract/10.1103/PhysRevLett.13.195.

[296] A F G Wyatt, V M Dmitriev, W S Moore, and F W Sheard. Microwave-Enhanced Critical Supercurrents in Constricted Tin Films. *Phys. Rev. Lett*, 16(25):1166–&, 1966. URL http://journals.aps.org/prl/abstract/10.1103/PhysRevLett.16.1166.

[297] G Yu, C H LEE, A J HEEGER, N HERRON, and E M MCCARRON. Transient Photoinduced Conductivity in Single-Crystals of $YBa_2Cu_3O_{7-\delta}$-Photodoping to the Metallic State. *Phys. Rev. Lett*, 67(18):2581–2584, 1991. URL http://journals.aps.org/prl/abstract/10.1103/PhysRevLett.67.2581.

[298] G Nieva, E Osquiguil, J Guimpel, M Maenhoudt, B Wuyts, Y Bruynseraede, M B Maple, and Ivan K Schuller. Photoinduced enhancement of superconductivity. *Applied Physics Letters*, pages 1–3, May 1992.

[299] A Kuzmenko, L Benfatto, E Cappelluti, I Crassee, D Van Der Marel, P Blake, K Novoselov, and A Geim. Gate Tunable Infrared Phonon Anomalies in Bilayer Graphene. *Physical Review Letters*, 103(11):116804, September 2009. doi: 10.1103/PhysRevLett.103.116804. URL http://link.aps.org/doi/10.1103/PhysRevLett.103.116804.

[300] David Tománek and Michael A Schluter. Growth regimes of carbon clusters. *Physical Review Letters*, 67(17):2331, 1991. URL http://journals.aps.org/prl/abstract/10.1103/PhysRevLett.67.2331.

[301] N Laouini, O.K. Andersen, and O. Gunnarsson. Analytical molecular orbitals and band structures of solid C_{60}. *Physical Review B*, 51(24):17446, 1995. URL http://journals.aps.org/prb/abstract/10.1103/PhysRevB.51.17446.

[302] Ian D Hands, Janette L Dunn, and Colin A Bates. A complete nearest-neighbor force field model for C_{60}. *The Journal of Chemical Physics*, 120 (15):6912, 2004. doi: 10.1063/1.1683105. URL http://scitation.aip.org/content/aip/journal/jcp/120/15/10.1063/1.1683105.

[303] Peter E Blöchl. Projector augmented-wave method. *Physical Review B*, 50(24):17953, 1994. URL http://journals.aps.org/prb/abstract/10.1103/PhysRevB.50.17953.

[304] G Kresse and J Furthmuller. Efficient iterative schemes for *ab initio* total-energy calculations using a plane-wave basis set. *Physical Review B*, 54(16):11169–11186, 1996. URL http://gateway.webofknowledge.com/gateway/Gateway.cgi?GWVersion=2&SrcAuth=mekentosj&SrcApp=Papers&DestLinkType=FullRecord&DestApp=WOS&KeyUT=A1996VT67500040.

[305] G Kresse and D Joubert. From ultrasoft pseudopotentials to the projector augmented-wave method. *Physical Review B*, 59(3):1758–1775, 1999. URL http://journals.aps.org/prb/abstract/10.1103/PhysRevB.59.1758.

[306] K Parlinski, Z Q Li, and Y Kawazoe. First-principles determination of the soft mode in cubic ZrO_2. *Phys. Rev. Lett*, 78(21):4063–4066, 1997. URL http://journals.aps.org/prl/abstract/10.1103/PhysRevLett.78.4063.

[307] Atsushi Togo, Fumiyasu Oba, and Isao Tanaka. First-principles calculations of the ferroelastic transition between rutile-type and $CaCl_2$-type SiO_2 at high pressures. *Physical Review B*, 78(13):134106, October 2008. doi: 10.1103/PhysRevB.78.134106. URL http://link.aps.org/doi/10.1103/PhysRevB.78.134106.

[308] Paolo Giannozzi, Stefano Baroni, Nicola Bonini, Matteo Calandra, Roberto Car, Carlo Cavazzoni, Davide Ceresoli, Guido L Chiarotti, Matteo Cococcioni, Ismaila Dabo, Andrea Dal Corso, Stefano de Gironcoli, Stefano Fabris, Guido Fratesi, Ralph Gebauer, Uwe Gerstmann, Christos Gougoussis, Anton Kokalj, Michele Lazzeri, Layla Martin-Samos, Nicola Marzari, Francesco Mauri, Riccardo Mazzarello, Stefano Paolini, Alfredo Pasquarello, Lorenzo Paulatto, Carlo Sbraccia, Sandro Scandolo, Gabriele Sclauzero, Ari P Seitsonen, Alexander Smogunov, Paolo Umari, and Renata M Wentzcovitch. QUANTUM ESPRESSO: a modular and open-source software project for quantum simulations of materials. *Journal of Physics: Condensed Matter*, 21(39):395502, September 2009. doi: 10.1088/0953-8984/21/39/395502. URL http://stacks.iop.org/0953-8984/21/i=39/a=395502?key=crossref.c21336c286fa6d3db893262ae3f6e151.

[309] J P Carbotte. Properties of boson-exchange superconductors. *Reviews of Modern Physics*, 62(4):1027, 1990. URL http://rmp.aps.org/abstract/RMP/v62/i4/p1027_1.

[310] Jiří Chaloupka and Giniyat Khaliullin. Orbital Order and Possible Superconductivity in $LaNiO_3/LaMO_3$ Superlattices. *Physical Review Letters*, 100 (1):016404, January 2008. doi: 10.1103/PhysRevLett.100.016404. URL http://link.aps.org/doi/10.1103/PhysRevLett.100.016404.

[311] H Y Hwang, Y. Iwasa, M Kawasaki, B Keimer, N Nagaosa, and Y Tokura. Emergent phenomena at oxide interfaces. *Nature Materials*, 11(2):103–113, February 2012. doi: 10.1038/nmat3223. URL http://dx.doi.org/10.1038/nmat3223.

[312] James M Rondinelli, Steven J May, and John W Freeland. Control of octahedral connectivity in perovskite oxide heterostructures: An emerging route to multifunctional materials discovery. *MRS Bulletin*, 37(03):261–270, March 2012. doi: 10.1557/mrs.2012.49. URL http://www.journals.cambridge.org/abstract_S0883769412000498.

[313] Mohammad A Islam, James M Rondinelli, and Jonathan E Spanier. Normal mode determination of perovskite crystal structures with octahedral rotations: theory and applications. *Journal of Physics: Condensed Matter*, 25(17):175902, April 2013. doi: 10.1088/0953-8984/25/17/175902. URL http://stacks.iop.org/0953-8984/25/i=17/a=175902?key=crossref.0a8fcddf850f5d775dd1277429eec1b9.

[314] Jak Chakhalian, John W Freeland, Andrew J Millis, Christos Panagopoulos, and James M Rondinelli. *Colloquium*: Emergent properties in plane view: Strong correlations at oxide interfaces. *Reviews of Modern Physics*, 86(4):1189–1202, October 2014. doi: 10.1103/RevModPhys.86.1189. URL http://link.aps.org/doi/10.1103/RevModPhys.86.1189.

[315] Alaska Subedi, Oleg E Peil, and Antoine Georges. Low-energy description of the metal-insulator transition in the rare-earth nickelates. *Physical Review B*, 91(7):075128, February 2015. doi: 10.1103/PhysRevB.91.075128. URL http://link.aps.org/doi/10.1103/PhysRevB.91.075128.

[316] Thomas E Weller, Mark Ellerby, Siddharth S Saxena, Robert P Smith, and Neal T Skipper. Superconductivity in the intercalated graphite compounds C_6Yb and C_6Ca. *Nature Physics*, 1(1):39–41, September 2005. doi: 10.1038/nphys0010. URL http://www.nature.com/doifinder/10.1038/nphys0010.

[317] Z H Pan, J Camacho, M H Upton, A V Fedorov, C A Howard, M Ellerby, and T. Valla. Electronic Structure of Superconducting KC_8 and Non-superconducting LiC_6 Graphite Intercalation Compounds: Evidence for a Graphene-Sheet-Driven Superconducting State. *Physical Review Letters*, 106(18):187002, May 2011. doi: 10.1103/PhysRevLett.106.187002. URL `http://link.aps.org/doi/10.1103/PhysRevLett.106.187002`.

[318] E Pavarini, I Dasgupta, T Saha-Dasgupta, O Jepsen, and O Andersen. Band-Structure Trend in Hole-Doped Cuprates and Correlation with $T_{c\,\max}$. *Physical Review Letters*, 87(4):047003, July 2001. doi: 10.1103/PhysRevLett.87.047003. URL `http://link.aps.org/doi/10.1103/PhysRevLett.87.047003`.

[319] M Greiner, O. Mandel, T Esslinger, T.W. Hänsch, and I Bloch. Quantum phase transition from a superfluid to a Mott insulator in a gas of ultracold atoms. *Nature*, 415(6867):39–44, 2002. URL `http://www.telecomb.de/pdf/NatureMottInsulator.pdf`.

[320] Immanuel Bloch. Ultracold quantum gases in optical lattices. *Nature Physics*, 1(1):23–30, October 2005. doi: 10.1038/nphys138. URL `http://www.nature.com/doifinder/10.1038/nphys138`.

[321] Immanuel Bloch and Wilhelm Zwerger. Many-body physics with ultracold gases. *Reviews of Modern Physics*, 80(3):885–964, July 2008. doi: 10.1103/RevModPhys.80.885. URL `http://link.aps.org/doi/10.1103/RevModPhys.80.885`.

[322] Robert Jördens, Niels Strohmaier, Kenneth Günter, Henning Moritz, and Tilman Esslinger. A Mott insulator of fermionic atoms in an optical lattice. *Nature*, 455(7210):204–207, September 2008. doi: 10.1038/nature07244. URL `http://www.nature.com/doifinder/10.1038/nature07244`.

[323] Sebastian Will, Thorsten Best, Ulrich Schneider, Lucia Hackermüller, Dirk-Sören Lühmann, and Immanuel Bloch. Time-resolved observation of coherent multi-body interactions in quantum phase revivals. *Nature*, 465(7295):197–201, May 2010. doi: 10.1038/nature09036. URL `http://dx.doi.org/10.1038/nature09036`.

[324] R Jördens, L Tarruell, D Greif, T Uehlinger, N Strohmaier, H Moritz, T Esslinger, L De Leo, C Kollath, A Georges, V Scarola, L Pollet,

E Burovski, E Kozik, and M Troyer. Quantitative Determination of Temperature in the Approach to Magnetic Order of Ultracold Fermions in an Optical Lattice. *Physical Review Letters*, 104(18), May 2010. doi: 10.1103/PhysRevLett.104.180401. URL `http://link.aps.org/doi/10.1103/PhysRevLett.104.180401`.

[325] S Trotzky, L Pollet, F Gerbier, U Schnorrberger, I Bloch, N V Prokof'ev, B Svistunov, and M Troyer. Suppression of the critical temperature for superfluidity near the Mott transition. *Nature Physics*, 6(12):998–1004, October 2010. doi: 10.1038/nphys1799. URL `http://dx.doi.org/10.1038/nphys1799`.

[326] M Endres, M Cheneau, T Fukuhara, C Weitenberg, P Schauss, C Gross, L Mazza, M C Banuls, L Pollet, I Bloch, and S Kuhr. Observation of Correlated Particle-Hole Pairs and String Order in Low-Dimensional Mott Insulators. *Science*, 334(6053):200–203, October 2011. doi: 10.1126/science.1209284. URL `http://www.sciencemag.org/cgi/doi/10.1126/science.1209284`.

[327] Immanuel Bloch, Jean Dalibard, and Sylvain Nascimbéne. Quantum simulations with ultracold quantum gases. *Nature Physics*, 8(4):267–276, April 2012. doi: 10.1038/nphys2259. URL `http://dx.doi.org/10.1038/nphys2259`.

[328] Manuel Endres, Takeshi Fukuhara, David Pekker, Marc Cheneau, Peter Schauß, Christian Gross, Eugene Demler, Stefan Kuhr, and Immanuel Bloch. The 'Higgs' amplitude mode at the two-dimensional superfluid/-Mott insulator transition. *Nature*, 487(7408):454–458, July 2012. doi: 10.1038/nature11255. URL `http://dx.doi.org/10.1038/nature11255`.

[329] Wolf Weimer, Kai Morgener, Vijay Pal Singh, Jonas Siegl, Klaus Hueck, Niclas Luick, Ludwig Mathey, and Henning Moritz. Critical Velocity in the BEC-BCS Crossover. *Physical Review Letters*, 114(9):095301, March 2015. doi: 10.1103/PhysRevLett.114.095301. URL `http://link.aps.org/doi/10.1103/PhysRevLett.114.095301`.

[330] Robert W Boyd. *Nonlinear optics; 3rd ed.* Academic Press, Amsterdam, 2008.

[331] W Demtröder. *Laser spectroscopy: basic concepts and instrumentation*. Springer Verlag, Berlin Heidelberg, 3rd edition, 2003.

[332] M. Eremets. *High pressure experimental methods*. Oxford University Press, Great Clarendon Street, Oxford OX2 6DP, 1st edition, 1996.

[333] A Jayaraman. Diamond anvil cell and high-pressure physical investigations. *Reviews of Modern Physics*, 55(1):65–108, 1983.

[334] A Jayaraman. Ultrahigh pressures. *Review of Scientific Instruments*, 57: 1013, 1986.

[335] GE Duvall and RA Graham. Phase transitions under shock-wave loading. *Rev. Mod. Phys.;(United States)*, 49(3), 1977. URL `http://www.osti.gov/energycitations/product.biblio.jsp?osti_id=7309112`.

[336] R. J. Hemley, G. L. Chiarotti, M Bernasconi, and L. Ulivi. *(Editors)* High pressure phenomena*Proceedings of the international school of physics "Enrico Fermi", Course CXLVII*. IOS Press, Nieuwe Hemweg 6B 1013 BG Amsterdam, Netherlands, 1st edition, 2002.

[337] J Xu and H Mao. Moissanite: a window for high-pressure experiments. *Science*, 290(5492):783, 2000.

[338] J Xu, H Mao, and R.J. Hemley. The gem anvil cell: high-pressure behaviour of diamond and related materials. *JOURNAL OF PHYSICS CONDENSED MATTER*, 14:11549, 2002. URL `http://iopscience.iop.org/0953-8984/14/44/514`.

[339] W Kaiser and W L Bond. Nitrogen, a major impurity in common type I diamond. *Physical Review*, 115(4):857, 1959. URL `http://prola.aps.org/abstract/PR/v115/i4/p857_1`.

[340] DJ Dunstan. Theory of the gasket in diamond anvil high pressure cells. *Review of Scientific Instruments*, 60:3789, 1989.

[341] K Syassen. Ruby under pressure. *High Pressure Research*, 28(2):75–126, 2008.

[342] Richard A Forman, Gasper J Piermarini, J Dean Barnett, and Stanley Block. Pressure measurement made by the utilization of ruby sharp-line luminescence. *Science*, 176(4032):284–285, 1972. URL `http://www.sciencemag.org/content/176/4032/284.short`.

[343] Jun Liu and Yogesh K Vohra. Sm:YAG optical pressure sensor to 180 GPa:Calibration and structural disorder. *Applied Physics Letters*, 64(25): 3386, 1994. doi: 10.1063/1.111283. URL http://scitation.aip.org/content/aip/journal/apl/64/25/10.1063/1.111283.

[344] H K Mao, J Xu, and P M Bell. Calibration of the ruby pressure gauge to 800 kbar under quasi-hydrostatic conditions. *J. Geophys. Res*, 91(B5): 4673–4676, 1986. URL http://perso.ens-lyon.fr/gilles.montagnac/Download/CED_TIPE/Mao86.pdf.

[345] G C Brown. Fluorescence Lifetimes of Ruby. *Journal of Applied Physics*, 35(10):3062, 1964. doi: 10.1063/1.1713175. URL http://scitation.aip.org/content/aip/journal/jap/35/10/10.1063/1.1713175.

[346] G. J. Piermarini, S Block, J D Barnett, and R A Forman. Calibration of the pressure dependence of the R1 ruby fluorescence line to 195 kbar. *Journal of Applied Physics*, 46(6):2774, 1975. doi: 10.1063/1.321957. URL http://scitation.aip.org/content/aip/journal/jap/46/6/10.1063/1.321957.

[347] Stefano Lupi, Alessandro Nucara, Andrea Perucchi, Paolo Calvani, Michele Ortolani, Luca Quaroni, and Maya Kiskinova. Performance of SISSI, the infrared beamline of the ELETTRA storage ring. *JOSA B*, 24(4):959–964, 2007. URL http://www.opticsinfobase.org/abstract.cfm?uri=josab-24-4-959.

[348] L. Baldassarre. *PhD Thesis, An infrared study of the Metal to Insulator Transition in strongly correlated oxides*. La Sapienza University, Rome, Italy, 2007.

[349] C Marini, E Arcangeletti, and D Di Castro. Optical properties of V_{1-x} Cr_x O_2 compounds under high pressure. *Physical Review B*, 2008. URL http://link.aps.org/doi/10.1103/PhysRevB.77.235111.

[350] A Perucchi, L Baldassarre, P Postorino, and S Lupi. Optical properties across the insulator to metal transitions in vanadium oxide compounds. *JOURNAL OF PHYSICS CONDENSED MATTER*, 21:323202, 2009.

[351] D F Edwards and E Ochoa. Infrared refractive index of diamond. *JOSA*, 71(5):607–608, 1981. URL http://www.opticsinfobase.org/abstract.cfm?&id=58008.

[352] I Kézsmárki, R Gaál, C Homes, B Sípos, H Berger, S Bordács, G Mihaly, and L Forro. High-pressure infrared spectroscopy: Tuning of the low-energy excitations in correlated electron systems. *Physical Review B*, 76(20), November 2007. doi: 10.1103/PhysRevB.76.205114. URL `http://link.aps.org/doi/10.1103/PhysRevB.76.205114`.

[353] DJ Dunstan and W Scherrer. Miniature cryogenic diamond-anvil high-pressure cell. *Review of Scientific Instruments*, 59(4):627–630, 2009.

[354] S. Wall. *PhD Thesis, Photo-induced dynamics in complex materials probed with femtosecond x-rays and few-cycle optical pulses*. St. Johns College, Oxford University, Oxford, United Kingdom, 2009.

[355] C O'Sullivan and J A Murphy. *SPIE Field guide to THz Sources, Detectors and Optics*. SPIE, Bellingham, Washington 98227-0010 USA, 1st edition, 2012.

[356] M Abo-Bakr, J Feikes, K Holldack, P Kuske, W Peatman, U Schade, G Wüstefeld, and H W Hübers. Brilliant, Coherent Far-Infrared (THz) Synchrotron Radiation. *Physical Review Letters*, 90(9), March 2003. doi: 10.1103/PhysRevLett.90.094801. URL `http://link.aps.org/doi/10.1103/PhysRevLett.90.094801`.

[357] E Karantzoulis, G Penco, A Perucchi, and S Lupi. Characterization of coherent THz radiation bursting regime at Elettra. *Infrared Physics and Technology*, 53(4):300–303, July 2010. doi: 10.1016/j.infrared.2010.04.006. URL `http://dx.doi.org/10.1016/j.infrared.2010.04.006`.

[358] D H Auston. Impulse-Response of Photoconductors in Transmission-Lines. *Ieee Journal of Quantum Electronics*, 19(4):639–648, 1983. URL `http://ieeexplore.ieee.org/xpls/abs_all.jsp?arnumber=1071904`.

[359] D H Auston, K P Cheung, and P R Smith. Picosecond photoconducting Hertzian dipoles. *Applied Physics Letters*, 45(3):284, 1984. doi: 10.1063/1.95174. URL `http://scitation.aip.org/content/aip/journal/apl/45/3/10.1063/1.95174`.

[360] N Katzenellenbogen and D. Grischkowsky. Efficient generation of 380 fs pulses of THz radiation by ultrafast laser pulse excitation of a biased metal-semiconductor interface. *Applied Physics Letters*, 58(3):222, 1991. doi: 10.

1063/1.104695. URL http://scitation.aip.org/content/aip/journal/apl/58/3/10.1063/1.104695.

[361] Q Wu and X.C. Zhang. Ultrafast electro-optic field sensors. *Applied Physics Letters*, 68(12):1604, 1996. doi: 10.1063/1.115665. URL http://scitation.aip.org/content/aip/journal/apl/68/12/10.1063/1.115665.

[362] Ajay Nahata, Aniruddha S Weling, and Tony F Heinz. A wideband coherent terahertz spectroscopy system using optical rectification and electro-optic sampling. *Applied Physics Letters*, 69(16):2321, 1996. doi: 10.1063/1.117511. URL http://scitation.aip.org/content/aip/journal/apl/69/16/10.1063/1.117511.

[363] Q Wu and X.C. Zhang. 7 terahertz broadband GaP electro-optic sensor. *Applied Physics Letters*, 70(14):1784, 1997. doi: 10.1063/1.118691. URL http://scitation.aip.org/content/aip/journal/apl/70/14/10.1063/1.118691.

[364] Susan L (Ed) Dexheimer. *THz spectroscopy: principles and applications*. CRC Press, Taylor and Francis group, 6000 Broken Sound Parkway NW, Suite 300, Boca Raton, FL 33487-2742, 1st edition, 2008.

[365] C Kübler, R Huber, and A Leitenstorfer. Ultrabroadband terahertz pulses: generation and field-resolved detection. *Semiconductor Science and Technology*, 20(7):S128–S133, June 2005. doi: 10.1088/0268-1242/20/7/002. URL http://stacks.iop.org/0268-1242/20/i=7/a=002?key=crossref.8537dcd99c3eda1b4187327d7cb39299.

[366] M. C. Hoffmann. *PhD Thesis, Novel Techniques in THz-Time-Domain-Spectroscopy: A comprehensive study of technical improvements to THz-TDS*. Albert-Ludwigs-Universität Freiburg im Breisgau, Freiburg, Germany, 2006.

[367] Martin Van Exter and D. Grischkowsky. Characterization of an optoelectronic terahertz beam system. *Microwave Theory and Techniques, IEEE Transactions on*, 38(11):1684–1691, 1990. URL http://ieeexplore.ieee.org/xpls/abs_all.jsp?arnumber=60016.

[368] M Born and E Wolf. *Principles of Optics*. Cambridge University Press, 7 edition, 1999.

[369] G.R. Fowles. *Introduction to Modern Optics*. Dover Publications Inc., 31 East 2nd Street, Mineola, N. Y. 11501, 2 edition, 1989.

[370] C. R. Hunt. *PhD Thesis, Manipulating superconductivity in cuprates with selective ultrafast excitation*. University of Illinois, Urbana-Champaign, Illinois, United States, 2015.

[371] David R Riley, David Jurbergs, Ji-Ping Zhou, Zhao Jianai, and John T McDevitt. Environmental reactivity characteristics of K_3C_{60} and $YBa_2Cu_3O_{7-x}$ high-temperature superconductor thin films. *Solid State Communications*, 88(6):431–434, 1993. URL `http://cat.inist.fr/?aModele=afficheN&cpsidt=3818925`.

[372] J S Plaskett and P N Schatz. On the Robinson and Price (Kramers-Kronig) Method of Interpreting Reflection Data Taken through a Transparent Window. *The Journal of Chemical Physics*, 38(3):612, 1963. doi: 10.1063/1.1733714. URL `http://link.aip.org/link/JCPSA6/v38/i3/p612/s1&Agg=doi`.

[373] Jennifer A Bardwell and Michael J Dignam. Extensions of the Kramers–Kronig transformation that cover a wide range of practical spectroscopic applications. *The Journal of Chemical Physics*, 83(11):5468, 1985. doi: 10.1063/1.449863. URL `http://link.aip.org/link/JCPSA6/v83/i11/p5468/s1&Agg=doi`.

[374] B E A Saleh and M C Teich. *Fundamentals of Photonics; 2nd ed.* Wiley-Interscience, Wiley Sons Inc., Hoboken, New Jersey, 2007.

[375] Fritz Peter. Über Brechungsindizes und Absorptionskonstanten des Diamanten zwischen 644 und 226 μm. *Zeitschrift für Physik*, 15(1):358–368, 1923. URL `http://www.springerlink.com/index/V346334031J1V445.pdf`.

[376] R Mildren and J Rabeau. *Optical Engineering of Diamond*. Wiley-VCH Verlag & Co. KGaA, Boschstrasse 12, 69469 Weinheim, Germany., 1st edition, 2013.

[377] R Vogelgesang, A D Alvarenga, Hyunjung Kim, A K Ramdas, S Rodriguez, M Grimsditch, and T R Anthony. Multiphonon Raman and infrared spectra of isotopically controlled diamond. *Physical Review B*, 58 (9):5408, 1998. URL `http://journals.aps.org/prb/abstract/10.1103/PhysRevB.58.5408`.

[378] Antoine Georges. Strongly correlated electron materials: Dynamical mean-field theory and electronic structure. *arXiv preprint cond-mat/0403123*, 2004. URL http://arxiv.org/abs/cond-mat/0403123.

[379] Gabriel Kotliar and Dieter Vollhardt. Strongly correlated materials: Insights from dynamical mean-field theory. *Physics Today*, 57(3):53–59, March 2004. doi: 10.1063/1.1712502. URL http://scitation.aip.org/content/aip/magazine/physicstoday/article/57/3/10.1063/1.1712502.

[380] A V Puchkov, M C Schabel, D N Basov, T Startseva, G Cao, T Timusk, and Z-X Shen. Layered ruthenium oxides: From band metal to Mott insulator. *Phys. Rev. Lett*, 81(13):2747–2750, 1998. URL http://journals.aps.org/prl/abstract/10.1103/PhysRevLett.81.2747.

[381] S.-K. Mo, J. D. Denlinger, H.-D. Kim, J.-H. Park, J. W. Allen, A. Sekiyama, A. Yamasaki, K. Kadono, S. Suga, Y. Saitoh, T. Muro, P. Metcalf, G. Keller, K. Held, V. Eyert, V. I. Anisimov, and D. Vollhardt. Prominent quasiparticle peak in the photoemission spectrum of the metallic phase of v_2o_3. *Phys. Rev. Lett.*, 90:186403, May 2003. doi: 10.1103/PhysRevLett.90.186403. URL http://link.aps.org/doi/10.1103/PhysRevLett.90.186403.

[382] Makoto Hashimoto, Inna M Vishik, Rui-Hua He, Thomas P Devereaux, and Zhi-Xun Shen. Energy gaps in high-transition-temperature cuprate superconductors. *Nature Physics*, 10(7):483–495, June 2014. doi: 10.1038/nphys3009. URL http://www.nature.com/doifinder/10.1038/nphys3009.

[383] FJ Morin. Oxides which show a metal-to-insulator transition at the Neel temperature. *Physical Review Letters*, 3(1):34–36, 1959.

[384] A Camjayi, C Acha, R Weht, M G Rodríguez, B Corraze, E Janod, L Cario, and M J Rozenberg. First-Order Insulator-to-Metal Mott Transition in the Paramagnetic 3D System $GaTa_4Se_8$. *Physical Review Letters*, 113(8):086404, August 2014. doi: 10.1103/PhysRevLett.113.086404. URL http://link.aps.org/doi/10.1103/PhysRevLett.113.086404.

[385] Tetsuya Furukawa, Kazuya Miyagawa, Hiromi Taniguchi, Reizo Kato, and Kazushi Kanoda. Quantum criticality of Mott transition in organic materials. *Nature Physics*, 11(3):221–224, February 2015. doi: 10.1038/nphys3235. URL http://www.nature.com/doifinder/10.1038/nphys3235.

[386] M J Rozenberg, G B Kotliar, H Kajueter, G A Thomas, D H Rapkine, J M Honig, and P Metcalf. Optical conductivity in Mott-Hubbard systems. *Phys. Rev. Lett*, 75(cond-mat/9507002):105–117, 1995.

[387] G A Thomas, D H Rapkine, S A Carter, A J Millis, T F Rosenbaum, P Metcalf, and J M Honig. Observation of the gap and kinetic energy in a correlated insulator. *Physical Review Letters*, 73(11):1529–1532, 1994. URL `http://link.aps.org/doi/10.1103/PhysRevLett.73.1529`.

[388] R Kubo. Statistical-Mechanical Theory of Irreversible Processes .1. General Theory and Simple Applications to Magnetic and Conduction Problems. *Journal of the Physical Society of Japan*, 12(6):570–586, 1957. URL `http://journals.jps.jp/doi/abs/10.1143/JPSJ.12.570`.

[389] M M Qazilbash, J J Hamlin, R E Baumbach, Lijun Zhang, D J Singh, M B Maple, and D N Basov. Electronic correlations in the iron pnictides. *Nature Physics*, 5(9):647–650, July 2009. doi: 10.1038/nphys1343. URL `http://dx.doi.org/10.1038/nphys1343`.

[390] D Baeriswyl, J Carmelo, and A Luther. Correlation-Effects on the Oscillator Strength of Optical-Absorption - Sum-Rule for the One-Dimensional Hubbard-Model. *Physical Review B*, 33(10):7247–7248, 1986. URL `http://journals.aps.org/prb/abstract/10.1103/PhysRevB.33.7247`.